Atmospheric Pressure Plasma Jet for the Deposition
of Nanocomposite Antibacterial Coatings

Atmosferische plasmastraal voor de depositie
van antibacteriële dunne lagen uit nanocomposiet

Xiaolong Deng

UNIVERSITEIT
GENT

Universiteit Gent
Faculteit Ingenieurswetenschappen en Architectuur
Vakgroep Toepaste Fysica

Promotoren: Prof. dr. ir. Christophe Leys
               Dr. Anton Nikiforov

Examencommissie:

Prof. Karen De Clerck   Department of Textiles
                             Ghent University, Belgum

Prof. Uroš Cvelbar   Department of Surface Engineering and Optoelectronics
                             Jozef Stefan Institute, Slovenia

Prof. Nathalie De Geyter   Department of Applied Physics
                             Ghent University, Belgum

Dr. Cristina Canal Barnils   Department of Materials Science and Metallurgical Engineering
                             Technical University of Catalonia, Spain

Proefschrift tot het bekomen van de graad van
Doctor in de Ingenieurswetenschappen: Toegepaste Natuurkunde
Academiejaar 2014-2015

勿忘初心

Dankwoord-Acknowledgement

Undertaking this PhD has been a truly tough yet unforgettable experience in my life. It would not have been possible to complete this work without support and guidance that I received from many people. Although words cannot express my gratitude, I will try my best to acknowledge them.

Foremost, I would like to express my sincere gratitude to my supervisor Prof. Christophe Leys, who provided me the opportunity to pursue my PhD degree in his group. As excited I was when I received his invitation, as thankful I am now that I have gotten this chance. I would like to thank him for the continuous support of my PhD study and research, for the encouragement and inspiring discussions.

I would like to gratefully thank my co-promoter Dr. Anton Nikiforov for his help during whole PhD research. He has guided me into the interesting plasma field, taught me all things about plasma science, and constantly encouraged me to participate in conferences and researches in other groups. His observations and comments helped me to establish the overall research direction and to move forward with investigation in depth. He is a person of patience, motivation, and enthusiasm. I could not have imagined having a better advisor and mentor for my PhD study.

My great gratitude is also given to Prof. Rino Morent and Prof. Nathalie De Geyter for their generous support on my research. They have helped me to perform XPS and FTIR measurements, taught me how to correctly analyze the results, and commented on my manuscripts. I am grateful to have such great and experienced experts as my colleagues who are always willing to help me on time.

Much appreciation is given to Prof. Tom Coenye from Department of Pharmaceutical Analysis with whom I started to involve into the amazing field of microbiology. I would like to thank Prof. Uroš Cvelbar (Jozef Stefan Institute, Slovenia) who encouraged and introduced me to participate in an exchange program. Special thanks has to be given to Dr. Danijela Vujosevic and Prof. Vineta Vuksanovic (Institute for Public Health, Montenegro) who hosted me for a one-month research in their lab, and taught me the way to perform good antimicrobial assays.

I would also like to thank all examination committee members, who have accepted to evaluate this work, for their careful review of the thesis and for providing feedback.

I want to thank all my colleagues at the department for the stimulating and

Ghent, June 2015
Xiaolong Deng

Table of Contents

List of Figures

List of Tables

List of Acronyms

A

AA	Acrylic Acid
AC	Alternating Current
APPJ	Atmospheric Pressure Plasma jet
AS	Absorption Spectroscopy
ATR	Attenuated Total Reflectance

B

BE	Binding Energy
BsE	Back-scattered Electrons

C

CL	Cathodoluminescence
CFU	Colony Forming Units

D

DBD	Dielectric Barrier Discharge
DC	Direct Current
DCSBD	Diffuse Coplanar Surface Barrier Discharge

E

EDX	Energy Dispersive X-ray spectroscopy

F

FWHM	Full Width at Half Maximum
FTIR	Fourier Transform Infrared Spectroscopy

G

GAS	Gas Aggregation Cluster Source
GC-MS	Gas Chromatography-Mass Spectrometry
GD-OES	Glow Discharge Optical Emission Spectroscopy

H

HA	Heptylamine
HMDSN	Hexamethyldisilazane
HMDSO	Hexamethyldisiloxane
HV	High Voltage

I

ICCD	Intensified Charge Coupled Device

L

LIF	Laser-Induced Fluorescence

M

MAPP	Maleic Anhydride Plasma-Polymer

MB-MS	Molecular Beam-Mass Spectrometry
MH	Mueller Hinton
MHCD	Microhollow Cathode Discharge
MW	Microwave
MS	Mass Spectrometry
MSA	Mercaptosuccinic Acid

N

NP	Nanoparticle

O

OES	Optical Emission Spectroscopy
OD	Optical Density

P

PBS	Phosphate Buffered Saline
PDMS	Polydimethylsiloxane
PE	Polyethylene
PEN	Polyethylene Naphthalate
PET	Polyethylene Terephthalate
PMMA	Polymethyl Methacrylate
PMT	Photomultiplier Tube
PP	Polypropylene
PTEE	Polytetrafluoroethylene

R

RF	Radio Frequency
RMS	Root Mean Square
RNS	Reactive Nitrogen Species
ROS	Reactive Oxygen Species

S

slm	Standard Liter per Minute
sccm	Standard Cubic Centimeters per Minute
SEM	Scanning Electron Microscopy
SE	Secondary Electrons

T

TEOS	Tetraethoxysilane
TMCTS	Tetramethylcyclotetrasiloxane
TMDSO	Tetramethyldisiloxane

N

UV	Ultraviolet

X

XPS	X-ray Photoelectron Spectroscopy

Nederlandse samenvatting
–Summary in Dutch–

In atmosferische niet-evenwichtsplasma's worden bij omgevingstemperatuur chemische processen geïnitieerd die onder evenwichtsomstandigheden enkel bij hoge temperaturen kunnen doorgaan. Hierdoor hebben deze koude plasma's een brede waaier van toepassingen. Het niet-evenwichtskarakter is afkomstig van het feit dat de elektronentemperatuur, door versnelling van de elektronen in het aangelegde elektrische veld, typisch tussen 10000 K en 50000 K ligt, terwijl de gastemperatuur meestal lager is dan 1000 K. Door botsingen tussen de hoogenergetische elektronen en de moleculen in het gas worden chemisch actieve deeltjes gevormd, zoals ionen, radicalen, reactieve neutrale deeltjes zoals zuurstofatomen, reactieve moleculaire fragmenten, fotonen, geëxciteerde atomen en metastabiele deeltjes. Gedurende de laatste twee decennia werd intensief onderzoek verricht op de ontwikkeling en diagnostiek van koude plasmabronnen en naar het gebruik van koude plasma's in technologische processen en nieuwe toepassingen. Onder de diverse plasmabronnen heeft de atmosferische plasmastraal, die ook in dit werk wordt gebruikt, inmiddels een belangrijke plaats ingenomen. Een intrinsiek voordeel van de plasmastraal is de ruimtelijke scheiding tussen het actieve ontladingsgebied, waar de actieve deeltjes worden gegenereerd, en het uitstroomgebied, waar het te behandelen materiaal zich bevindt. Hierdoor worden ongewenste invloeden van het materiaal op het plasma vermeden. Dit verzekert een stabiele werking van het plasma, terwijl zich een rijke reactiekinetiek kan voordoen in de uitstroomzone. Om dezelfde reden zijn er bij het gebruik van een plasmastraal ook geen beperkingen qua grootte of vorm van het te behandelen voorwerp. Meer specifiek is de atmosferische plasmastraal een veelbelovend werktuig bij toepassingen waar een lage gastemperatuur noodzakelijk is, zoals bij de oppervlaktebehandeling van hittegevoelige materialen of levend weefsel.

Plasmapolymerisatie heeft zich ontwikkeld tot een veelzijdige methode om bepaalde functionele groepen aan te brengen op een brede waaier aan oppervlakken voor uiteenlopende. Plasmapolymeerlagen hebben enkele interessante eigenschappen, zoals een lage porositeit, een hoge graad aan cross-linking, thermische stabiliteit, onoplosbaarheid, chemische inertie en mechanische sterkte. Voor atmosferische plasmatechnologie is er bovendien geen vacuümapparatuur vereist. Andere voordelen zijn een laag energieverbruik en hoge depositiesnelheden. Specifieke troeven van atmosferische plasmastralen zijn de compactheid, de lage investeringskost en de mogelijkheid om voorwerpen met een complexe vorm en

structuur te behandelen. Eén van de relatief nieuwe toepassingsgebieden van plasmapolymeren zijn antibacteriële dunne lagen voor materialen gebruikt in geneeskunde, hygiëne en gezondheidszorg.

Het onderwerp van dit doctoraat is de toepasssing van een atmosferische plasmatechniek voor de depositie van een nanocomposiete antibacteriële dunne laag. Eerst wordt een DC-plasmastraal met stikstof of lucht als draaggas ontworpen en gekarakteriseerd. Vervolgens wordt, gebruik makend van deze plasmabron, de polymerisatie van een organosiliciumfilm bestudeerd. In een volgende stap worden twee nieuwe methodes ontwikkeld voor de depositie van een nanocomposiete, antibacteriële laag op vlakke substraten en op non-woven textielmaterialen. In het laatste deel wordt de opschaling van het depositieproces onderzocht door gebruik te maken van een aangepaste plasmastraaltechniek. De resultaten uit de verschillende delen van het doctoraat worden hieronder samengevat.

De atmosferische niet-evenwichtsplasmabron die voor de beoogde toepassing wordt ontworpen is een DC-plasmastraal die bedreven wordt in stikstof en in lucht. De plasma-eigenschappen worden bepaald in de actieve plasmazone en in de uitstroomzone als functie van de ontladingsstroom en het gasdebiet. Er doen zich twee ontladingsregimes voor: een pulserend regime bij lage ontladingsstroom en een ingesnoerd glimregime bij hogere ontladingsstroom. Door middel van optische emissiespectroscopie worden de reactieve deeltjes geïdentificeerd en worden de gastemperatuur en de vibrationele temperatuur bepaald. Zowel in stikstof als in lucht is de vibrationele temperatuur van de ontlading veel hoger dan de gastemperatuur. Dit is kenmerkend voor een plasma met een hoge thermische niet-evenwichtsgraad. Terwijl de gastemperatuur in het actieve plasma, afhankelijk van de stroomsterkte, tussen 1200 K en 2500 K ligt, daalt de gastemperatuur drastisch tot kamertemperatuur in de uitstroomzone, waar bijgevolg een hittegevoelig substraat kan geplaatst worden. Opmerkelijk is de invloed van het draaggas op het soort langlevende reactieve deeltjes: in de uitstroomzone van de plasmastraal in stikstof wordt O_3 gedetecteerd, terwijl daar voor de plasmastraal in lucht NO wordt gemeten.

Met TMDSO als precursor worden vervolgens organosiliciumfilms afgezet met behulp van de ontworpen DC-plasmastraal. De invloed van de zuurstofconcentratie en het plasmavermogen op de depositiesnelheid en de chemische samenstelling van de film worden in detail onderzocht. De depositiesnelheid stijgt met de zuurstofconcentratie in het draaggas van 172 nm/min (geen O_2) tot 444 nm/min (60 sccm O_2). Dit wordt toegeschreven aan de rol van zuurstof in de effectieve decompositie van het monomeer. Een stijging van het plasmavermogen verhoogt de depositiesnelheid van 273 nm/min bij een vermogen van 18 W tot 493 nm/min bij 30 W. Dit is een gevolg van de toename met het plasmavermogen van de dissociatiegraad van de monomeermolecule. Uit FTIR en XPS metingen blijkt dat ook de verhouding organisch/anorgonisch in de samenstelling van de film kan gestuurd worden door regeling van het plasmavermogen en van de hoeveelheid zuurstof in het draaggas.

Na de karakterisering van de plasmastraal en van de afgezette plasmapolymeerlagen worden twee methodes onderzocht voor de depositie van een dunne

organosiliciumlaag met een specifieke antibacteriële functionaliteit door het incorporeren van zilver-nanodeeltjes. Bij de eerste methode wordt een nanocomposiete film afgezet door een rechtstreekse toevoeging van Ag-nanodeeltjes in het draaggas van de plasmastraal. De morfologie van de film is afhankelijk van de zilverconcentratie aan het oppervlak die op zijn beurt kan geregeld worden via de hoeveelheid Ag-nanodeeltjes in het draaggas. Via XPS worden zilverconcentraties tot 30% gemeten. De resulterende nanocomposiete dunne lagen vertonen antibacteriële eigenschappen tegen *E. coli* en *S. aureus*. De tweede methode is specifiek ontwikkeld voor de depositie van een antibacteriële laag op non-woven PET. Het plasma-geassisteerde proces bestaat uit drie stappen waarbij Ag-nanodeeltjes gefixeerd worden tussen twee organosiliciumlagen, namelijk een reservatielaag (eerste laag) en een barrièrelaag (tweede laag). De resultaten van XPS- en SEM-analyses wijzen op een homogene verdeling van gefixeerde Ag-nanodeeltjes op het PET-oppervlak. Er is vastgesteld dat het variëren van de dikte van de barrirelaag een nauwkeurige methode is om de vrijgave van zilverionen en daardoor de antimicrobiële activiteit van het substraat te sturen. Een barrièrelaag van 10 nm leidt tot een hogere antimicrobiële activiteit dan een barrièrelaag van 50 nm. De stabiliteit van de fixatie van de Ag-nanodeeltjes in de film is onderzocht door een behandeld monster te onderwerpen aan mechanische wascycli. Voor monsters met een barrièrelaag blijft het antibacteriële effect zelfs na tien wascycli behouden. Dit wijst op een effectieve en duurzame immobilisering van de Ag-nanodeeltjes in de matrix van de film. Voor monsters zonder barrièrelaag daarentegen treedt na enkele wascycli een substantiële daling op van de antibacteriële werking.

Tenslotte wordt in het doctoraat een eerste stap gezet in de richting van het opschalen van een plasmadepositietechniek. De daartoe ontwikkelde plasmabron is gebaseerd op een RF-geëxciteerde barrière-ontlading met een breedte van 30 mm. De plasma-eigenschappen worden bepaald met optische en elektrische diagnostieken en met tijdsafhankelijke beeldvorming. Het plasma kan naargelang het RF-vermogen bedreven worden in twee regimes, een diffuus α-regime en een filamentair γ-regime. In het α-regime ontstaat over de ganse breedte van de ontlading een uniforme plasma afterglow met een lengte van 8 mm in omgevingslucht. De gastemperatuur bedraagt 330 K. De homogeniteit van de plasma-emissie in de uitstroomzone is veelbelovend voor de uniforme behandeling van brede substraten. Uit de absolute intensiteit van de continuümstraling wordt een elektronendichtheid van $1{,}9 \pm 1 \times 10^{14}$ cm^{-3} en een elektronentemperatuur van $1{,}75 \pm 0{,}25$ eV berekend. Uit de tijdsgeresolveerde plasma-emissie volgt dat er per halve cyclus van de aangelegde spanning één ontladingspiek optreedt. Uit de beelden gemaakt met een ICCD-camera blijkt dat de emissie van geëxciteerde argondeeltjes geconcentreerd is in de dunne RF-sheath (100-140 μm) ter hoogte van de elektrodes, terwijl de emissie van geëxciteerde OH homogeen verdeeld is in de ruimte tussen de elektrodes.

De veelbelovende resultaten die in het kader van het onderzoek op het vlak van antibacteriële lagen werden verkregen, illustreren de geavanceerde mogelijkheden van atmosferische plasmatechnologie voor de depositie van complexe, functionele dunne lagen.

English summary

Atmospheric pressure non-equilibrium plasmas show a great potential in many practical applications due to their ability to initiate effective gas phase chemistry and energy-intensive processes without elevating gas temperature. In such plasmas, electron temperature is in range of 10000 - 50000 K and is much higher than gas temperature, which is usually below 1000 K. High chemical reactivity of these plasmas is considered to be due to effective production of a wide spectrum of energetic species by electron impact and energy transfer. Such species include charged particles including electrons, ions, and radicals, high reactive neutral species such as oxygen atoms, reactive molecular fragments, photons, excited atomic states and metastable states. In the last two decades, extensive efforts have been given to development and diagnostics of non-equilibrium plasma sources, and use of these plasmas in different technological processes and new application. Among numerous developed plasma sources, atmospheric pressure plasma jets (APPJs) have gained increasing interest because of their intrinsic features. Due to spatial separation of an active discharge region and an afterglow region, plasma avoid undesirable influence of treated object on the discharge, leading to excellent plasma stability in upstream electrode region while enabling rich reaction chemistry within the downstream zone. Besides, capability of remote treatment with plasma jet afterglow provides no restrictions on size and shape of objects in processes. Moreover, cold plasmas generated by plasma jets have bright future in applications where a low gas temperature is necessary, such as treatment of thermal-sensitive materials, cells and living tissues.

Nowadays, plasma polymerization has developed as a versatile method to introduce certain functions onto surface of a wide range of substrates for many applications. These polymerized films are of particular interest due to their excellent properties, such as low porosity, cross-linking, insolubility, thermal stability, chemically inertness and mechanical toughness. Moreover, atmospheric pressure plasma process has the advantage of vacuum equipment elimination, short processing time, low specific energy consumption, and considerably high deposition rates. Use of plasma jets is particularly attractive due to portable designs of plasma sources, low investments and operational costs and capabilities of coating on objects with complex morphology and structure. Among different types of plasma polymers, demands on development of antimicrobial coatings are growing at an extreme rate, especially in medical and hygienical field, and health care sectors.

In this work, plasma jet system have been developed and methods for antibacterial nanocomposite films deposition have been studied. Firstly, an atmospheric

pressure non-equilibrium DC plasma jet with nitrogen/air as working gas is developed and plasma is characterized. Next, organosilicon film polymerization is studied using this DC plasma jet. Afterwards, deposition of antibacterial nanocomposite films by two novel methods on flat and non-woven textile materials is investigated. In the last part, focus has been placed on a large dimensional plasma jet device in order to upscale nanocomposite film deposition process.

The non-equilibrium atmospheric pressure DC plasma jet in nitrogen and air gas is developed and investigated in terms of plasma properties and generation of active species in active zone and afterglow. Effect of gas composition and discharge current on plasma and afterglow properties is studied. Depending on discharge current, two modes of plasma sustainment can be obtained: self-pulsing mode at low discharge current and constricted glow mode at higher discharge current. Optical emission spectroscopy is implemented to analyze reactive species, and to determine gas and vibrational temperature in active zone between the electrodes and in afterglow. Vibrational temperature of nitrogen and air discharge is much higher than gas temperature, which confirms strong non-equilibrium conditions in the plasma. Gas temperature of afterglow decreases dramatically and approaches room temperature along the gas flow downstream where treated object can be placed. A significant difference of long living reactive species in afterglow of N_2 and air plasma jet has been found: O_3 is only produced in afterglow of the N_2 plasma jet, whereas NO is only generated in afterglow of plasma jet with air.

Then, with the DC plasma jet, deposition of organosilicon film is investigated using TMDSO as precursor. Effect of O_2 content and discharge power on film deposition rate and film chemical properties is thoroughly studied. Oxygen content in feed gas can increase deposition rate from 172 nm/min (no O_2) to 444 nm/min (60 sccm O_2) due to effective monomer decomposition by plasma. Increase of discharge power accelerates deposition rate from 273 nm/min at 18 W to 493 nm/min at 30 W due to higher dissociation degree of the monomer molecules. It is shown by FTIR and XPS measurements that the deposited film can be tuned in organic and inorganic component content to specific requirements by variation of oxygen admixing and discharge power.

Next, based on the fundamental work on characterization of plasma jet and polymerization organosilicon films, deposition of antibacterial nanocomposite films by two independent novel methods using the plasma jet system on flat and non-woven textile materials are investigated. First method is proposed to deposit nanocomposite organosilicon thin films with incorporation of AgNPs on flat surface materials. It is a single step plasma jet process, in which AgNPs are directly fed into the DC plasma jet through a feed module. Control of film morphology can be achieved by variation of AgNPs feeding rate. Silver content in the films can be controlled from few percent to more than 30%. These nanocomposite films exhibit antibacterial activity against *E. coli* and *S. aureus* strains. Second method is used for preparation of antimicrobial nano-silver PET fabrics with multilayer structure through a three step process based on atmospheric pressure plasma deposition process. AgNPs are immobilized between two layers of organosilicon films: a reservation layer (1st layer) and a barrier layer (2nd layer). Uniform AgNPs

incorporation on PET surface has been confirmed by XPS and SEM. It is found that variation of barrier layer thickness is a precise method to control release of silver ions and to control antimicrobial activity of the substrate. Samples with 10 nm barrier layer have stronger antimicrobial activity than those with 50 nm barrier layer. Durability of AgNPs bonding in the matrix is also investigated through washing process. For samples with barrier layer, effective immobilization of silver in the matrix is confirmed with stability of antibacterial effect even after 10 washing cycles. However, silver concentration in samples without barrier layer shows significant fluctuation after several washing cycles. Besides, control of antibacterial activity of PET fabrics is obtained by variation of immobilized silver concentration in nano-composite multilayer coatings.

Finally, an approach of large scale plasma deposition on flat and textile materials is initialed through development of a 30 mm wide diffuse RF planar plasma source based on the concept of barrier discharge. Main discharge parameters are determined by electrical diagnostics, emission spectroscopy and time resolved imaging. Two discharge modes, diffuse α mode and filament γ mode, can be sustained in the plasma source depending on RF input power. In diffuse α-mode, brush-shape homogenous plasma afterglow with total length of up to 8 mm can be generated along the slit in ambient air. Gas temperature of afterglow is estimated to be 330 K. Afterglow of the plasma jet shows uniform emission which is very promising for large scale treatment. With absolute calibrated spectroscopy, electron density and electron temperature are estimated from absolute value of the continuum radiation, to be about $1.9 \pm 1 \times 10^{14}$ cm^{-3} and 1.75×0.25 eV respectively. Time resolved intensity of plasma emission indicates that the plasma is sustained through formation of two strong emission peaks appearing in every voltage period. ICCD images show that production of Ar excited states appears in the RF sheath region of 100 - 140 μm close to the electrodes whereas OH(A-X) emission is almost uniformly distributed in the gap.

The promising results obtained in this work, especially concerning preparation of antibacterial nanocomposite materials, demonstrate advanced possibilities of plasma technology for polymerization of complex functional films.

1

Introduction

1.1 Non-equilibrium atmospheric pressure plasma jets

With the ability to achieve high gas phase reactivity without the need for elevated gas temperature, non-equilibrium atmospheric pressure plasma has attracted significant attention for many practical applications in the last two decades. Numerous sources have been investigated to generate such plasmas. Among them, atmospheric pressure plasma jets (APPJs) have gained increasing interest. In a typical APPJ device, plasma is generated between two electrodes inside a nozzle and blown out into the open space by a gas flow to form an afterglow in ambient air. Mostly, afterglows contain abundant reactive species (excited atoms and molecules, radicals, metastables, energy electrons and UV radiation) and exhibit a relatively low gas temperature. Due to spatial separation of active discharge region and afterglow region, plasma jets can avoid undesirable influence of the treated object on generated plasma, leading to excellent plasma stability in the upstream electrode region while enabling rich reaction chemistry within the downstream zone. Besides, capability of remote treatment by plasma jets suggests there is no space limitation of objects in processes. Moreover, cold plasmas have a bright future in applications where low gas temperature is necessary, such as treatment of thermal-sensitive materials, cells and living tissues.

In the last decade, a large number of plasma jets have been developed to generate non-equilibrium plasmas with various configurations and operating parameters. Noble gases, like helium and argon, with mixture of molecular gases like

H_2O, N_2, O_2 and air, are mostly used as working gases. Plasma jets can be sustained by several types of electric sources: direct current (DC) voltage, alternating current (AC) voltage, radio frequency (RF) voltage, microwave voltage and pulsed voltage. Each plasma jet works at its specific conditions (configuration, power, gas), exhibits distinct characterizations and can be used for different applications.

Great advances have been made in developing, understanding and optimizing plasma jets with help of plasma diagnostics, which are a group of methods, instruments and experimental techniques. Important features in plasma jets like plasma discharge mode, voltage-current waveform, present reactive species, gas temperature, electron density, electron temperature, and plasma propagation can be revealed. Up till now, many diagnostic methods have been developed and utilized for characterization of plasma jets, including probe measurements, optical emission spectroscopy, mass spectrometry, intensified charged-coupled device imaging methods, laser induced fluorescent measurements, absorption spectroscopy, plasma probes, acoustic diagnostic and cavity ring-down spectroscopy and so on.

With outstanding features, plasma jets have been extensively investigated for a broad spectrum of potential applications: surface modification, surface cleaning, film deposition, sterilization, food treatment, pollution control, cell treatment, use in medical field and more. These promising applications and bright industrial future also drive fundamental investigation on plasma jets and relative processes.

1.2 Polymerization of basic films and nanocomposite films via plasma jets

Thin films, which are thin material layers ranging from fractions of a nanometer to several micrometers in thickness, have interesting properties that are very different from these of the bulk materials. They are widely deposited on bulk substrates to achieve certain functions on interfaces without change of bulk properties. Films are often used to achieve functions like protecting substrates against corrosion and oxidation, controlled release of drugs and active agents, realizing super-hydrophobic or -hydrophilic surfaces, improving cell adhesion and growth, achieving proper optical/electromagnetic properties, etc. A variety of methods, such as evaporation, sputtering, electrodeposition and sol gel method, have been developed and industrialized to produce thin films with those functions.

Nowadays, plasma polymerization has been developed as a versatile method to deposit thin films onto surfaces of a wide range of substrates. These polymerized films have attracted great interest as they can be pinhole-free, highly cross-linked, insoluble, thermally stable, chemically inert and mechanically tough. Compared to low pressure plasma, atmospheric pressure discharges possess the advantages of vacuum equipments elimination, short processing time, low specific energy con-

sumption, and considerably high deposition rates. Moreover, polymerization processes using atmospheric pressure plasma jets are particularly attractive due to portable designs, local film deposition and capabilities for coating on objects with complex morphologies and structures.

Many types of thin films have been deposited using atmospheric pressure plasma jets system in open air conditions. Because inorganosilicon/organosilicon is one of the primary materials in many applications such as barrier films for packaging, corrosion protection layers, matrixes for composite films and dielectric materials in electronic devices, there is an increasing interest in the deposition of silica-like films using plasma-assisted (also plasma-enhanced) chemical vapor deposition with the help of plasma jets systems. A large variety of commercially available organosilicon monomers have been investigated as possible reactants for plasma polymerization of silicon-inorganic or silicon-organic films. The influence of process parameters, like plasma dissipated power, discharge mode, monomer concentration, gas composition, gas flow rate and position of substrate, on the chemical and morphological properties of deposited films have been widely discussed.

Besides, increasing demands of films with advanced functions, which are difficult satisfied by basic films, have stimulated the development of more complex hybrid or composite films. Among them, antimicrobial coatings are extremely demanded in fields like medical and hygienic materials, water purification and food protection. Currently, preparation of nanocomposite films containing metal nanoparticles (such as silver nanoparticles, copper nanoparticles, zinc oxide nanoparticle) is becoming a new strategy for antibacterial activity. Compared to traditional chemical solution methods, plasma polymerization using plasma jets is a promising approach for fabrication of nanocomposite films with the advantages of gas phase dry processes, short preparation time, and easy use on various substrates.

1.3   Motivations

Although great progress has been made in development of plasma jets, there are still many challenges and barriers that exist in practical applications of plasma jets, for example the wide use of expensive noble gases and small dimension of afterglow. Therefore, research on plasma jets sustained by economic molecular gases, like nitrogen or air, and on plasma jets with relative large dimension is important in the future. First part of the work in this dissertation is to develop plasma jet devices that can generate non-equilibrium plasma using nitrogen/air gases and can generate scaled-up plasmas. Based on these investigations, it aims to contribute to development of more practical plasma jet sources. Meanwhile, emphasis is also made on deposition of basic inorganosilicon films and fabrication

of antibacterial nanocomposite films using a plasma jet. This part of the work is expected to provide new routes for preparation of surfaces with high and lasting antimicrobial activity.

1.4   Outline

In chapter 2, a detailed overview of ongoing research on development of atmospheric non-equilibrium plasma jets, their applications on polymerization of silicon-inorganic and silicon-organic films, and on preparation of antimicrobial materials is presented. Also, research on recent development of up-scaled plasma jet sources is overviewed.

Chapter 3 firstly describes the diagnostic methods applied in this dissertation to reveal the properties of plasma discharges and afterglows in the plasma jet devices. After that, techniques for surface characterization are presented. The third part contains a general introduction of microbiological antimicrobial assays used in this work.

Chapter 4 presents experimental results on generation and characteristics of an atmospheric pressure nitrogen/air DC plasma jet. Discharge mode and visual properties of the plasma jet are investigated. Differences spectra and temperature (gas temperature and vibrational temperature) between N_2 plasma jet and air plasma jet are presented and analyzed. Space-resolved byproduct densities, ozone and nitric oxide, in the afterglow are measured.

In chapter 5 to 7, results of the study are given on plasma deposition of basic organosilicon films and antimicrobial nanocomposite films. In chapter 5, plasma polymerization of organosilicon films by the atmospheric pressure DC plasma jet is investigated. The influence of working parameters, such as oxygen content and dissipated power, on deposition rate and chemical components of deposited films is discussed. This forms the fundamental work for development of nanocomposite films in the next two chapters. In chapter 6, a one step dry process is studied using the plasma jet for deposition of nanocomposite thin films with high concentration of AgNPs. The composition, morphology and antibacterial efficiency of deposited nanocomposite films are carefully analyzed and evaluated. In chapter 7, silver nanoparticles are immobilized on PET non-woven fabrics via a double layer of plasma deposited organosilicon films. Influence of the top layer coating on antibacterial efficiency and release of AgNPs under mechanical stress are investigated. After that, control of incorporated silver content is studied.

In chapter 8, attention is given to development of a RF-DBD plasma jet device with a scaled-up dimension. Plasma parameters, like gas temperature, electron density and electron excitation temperature are studied. Uniformity of the plasma jet is studied by optical emissions of active species. After that, time resolved properties in plasma active region are investigated.

Finally, a general conclusion of the work will be given in the last chapter.

1.5 Publications

1.5.1 Publications in international journals

1. **X. Deng**, A. Y. Nikiforov, E. Ionita, G. Dinescu and C. Leys. "Absolute and relative emission spectroscopy study of 3 cm wide planar radio frequency atmospheric pressure bio-plasma source", *Applied Physics Letters* 107, 053702, (2015).

2. **X. Deng**, A. Y. Nikiforov, T. Coenye, P. Cools, G. Aziz, R. Morent, N. D. Geyter and C. Leys. "Antimicrobial nano-silver non-woven polyethylene terephthalate fabric via an atmospheric pressure plasma deposition process", *Scientific Reports* 5, 10138, (2015).

3. **X. Deng**, A. Y. Nikiforov, D. Vujosevic, V. Vuksanovic, B. Mugosa, U. Cvelbar, N. De Geyter, R. Morent and C. Leys. "Antibacterial activity of nano-silver non-woven fabric prepared by atmospheric pressure plasma deposition", *Materials Letters* 149, 95, (2015).

4. **X. Deng**, C. Leys, D. Vujosevic, V. Vuksanovic, U. Cvelbar, N. D. Geyter, R. Morent and A. Y. Nikiforov. "Engineering of Composite Organosilicon Thin Films with Embedded Silver Nanoparticles via Atmospheric Pressure Plasma Process for Antibacterial Activity", *Plasma Processes and Polymers* 11, 921, (2014).

5. **X. Deng**, A. Y. Nikiforov and C. Leys. "Diffusion and Filamentary Regime of an Atmospheric Pressure DC Plasma Jet in Nitrogen and Air", *IEEE Transactions on Plasma Science* 42, 2452 (2014).

6. **X. Deng**, A. Y. Nikiforov, P. Vanraes and C. Leys. "Deposition of nanosilver-organosilicon composite films using an atmospheric pressure dc plasma jet", *Romanian Reports in Physics* 66, 1088, (2014).

7. **X. Deng**, A. Y. Nikiforov, N. D. Geyter, R. Morent and C. Leys. "Deposition of a TMDSO-Based Film by a Non-Equilibrium Atmospheric Pressure DC Plasma Jet", *Plasma Processes and Polymers* 10, 641, (2013).

8. **X. Deng**, A. Y. Nikiforov, P. Vanraes and C. Leys. "Direct current plasma jet at atmospheric pressure operating in nitrogen and air", *Journal of Applied Physics* 113, 023305, (2013).

1.5.2   Publications in international conferences

1. **X. Deng**, A. Y. Nikiforov, D. Vujosevic, U. Cvelbar and C. Leys. "Nanoparticle incorporated non-woven fabric prepared by atmospheric pressure plasma process for antibacterial property", poster presentation at 22nd International Symposium on Plasma Chemistry, Antwerp, Belgium, July 2015.

2. **X. Deng**, A. Y. Nikiforov and C. Leys. "Preparation of AgNPs non-woven fabrics using an atmospheric pressure Plasma jet system", oral presentation at COST MP1101 meeting on biomedical applications of atmosphheric pressure plasma technology, Istanbul, Turkey, May 2015.

3. **X. Deng**, A. Y. Nikiforov and C. Leys. "Preparation of AgNPs decorated non-woven fabrics using an atmospheric pressure plasma jet", oral presentation at 17th International Congress on Plasma Physcis (ICPP), Lisbon, Portugal, September 2014.

4. **X. Deng**, A. Y. Nikiforov and C. Leys. "Deposition of antibacterial nanocomposite films using an atmospheric pressure nonequilibrium plasma jet", oral presentation at 41st IEEE International Conference on Plasma Science (ICOPS), Washington DC, USA, May 2014.

5. **X. Deng**, A. Y. Nikiforov and C. Leys. "Deposition of thin films using an atmospheric pressure direct current plasma jet", oral presentation at 16th International Conference on Plasma Physics and Applications (CPPA), Bucharest, Romania, June 2013.

6. **X. Deng**, A. Y. Nikiforov, N. D. Geyter, R. Morent and C. Leys. "A nitrogen DC plasma jet and its application for thin films deposition", poster presentation at XXXI International Conference on Phenomena in Ionized Gases, Granada, Spain, July 2013.

7. **X. Deng**, A. Y. Nikiforov and C. Leys. "Characterization of an atmospheric pressure direct current plasma jet operating in nitrogen and air", poster presentation at 40th IOP Annual Spring Conference on Plasma Physics, York, UK, March 2013.

2

Overview of the research field

2.1 Introduction

Low-temperature plasma physics and the technology is truly interdisciplinary as it lies at the confluence of many diverse science and engineering areas, especially physics, chemistry, biomedical engineering and materials science. As one of the most important groups in the family of plasma sources and with distinguishing advantages, plasma jets have attracted extensive attention and have invoked interest in various real applications. In this chapter, a literature review of the development of atmospheric non-equilibrium plasma jets and their applications in polymerization of thin film and synthesis of antimicrobial materials is presented.

2.2 The plasma jets engineering

Plasma, often described as the fourth state of matter, is a quasineutral gas with a mixture of electrons, ions, and neutral particles which are in random movement [1]. Depending on the kind of working gas, the ionization ratio and the pressure, there are many types of plasmas with their own characteristics. According to the balance of electron temperature and gas temperature, plasmas can be divided into two main categories: equilibrium or near equilibrium plasmas and non-equilibrium plasmas. For equilibrium plasmas, also known as thermal plasmas or hot plasmas, the gas temperature equals to the electron temperature. In non-equilibrium plasmas, the electron temperature is much higher than the gas

temperature. One of the most attractive features of the non-equilibrium plasma is the ability to achieve energy-intensive and effective gas phase chemistry without the needs for elevated gas temperature. Such chemical reactivity is considered to be due to a wide spectrum of energetic species generated in the plasma, for example, charged particles including electrons, ions, and radicals, high reactive neutral species such as reactive atoms, reactive molecular fragments, photons, excited atomic states and metastable states. In the last two decades, extensive efforts have been made for increasing understanding of non-equilibrium atmospheric pressure plasma, and its application in a wide variety of fields such as material processing, environmental engineering, food industry, and biomedicine.

Atmospheric pressure non-equilibrium plasma can be generated by various types of plasma sources. This allows the achievement of better performance in specific applications. A dielectric barrier discharge (DBD) is a type of frequently used approach for establishing a non-equilibrium plasma. The plasma is sustained between two electrodes and at least one of them is coved by a dielectric material to avoid the formation of sparks in the discharge gap. With the advantages of maintaining a plasma in an economic and reliable way, DBD plasmas have been extensively investigated and utilized in a number of important applications, including ozone generation [2], pollution control [3], sterilization [4], thin film deposition [5], surface modification and activation of diverse materials, especially polymers [6–8]. However, DBD plasma is typically generated in a geometrically confined space, which is undesirable for many practical applications where a remote plasma without space limitations is needed. Another group of the plasma source, known as non-equilibrium atmospheric pressure plasma jet (APPJ), with an expanding/transporting plasma containing a large amount of reactive species in the effluent, has attracted significant attention. It has exhibited great potential in a broad range of applications, particularly in material process and (bio)medical applications. [4, 9–13] In this thesis, the term 'plasma jet' refer to non-equilibrium atmospheric pressure plasma jet.

2.2.1   Atmospheric pressure plasma jets conception

Generally, a plasma jet consists of a gas nozzle with one, two or even more electrodes. Once a proper gas flow and voltage are applied, plasma can be generated between two electrodes inside the nozzle and blown out into the open space by a gas flow to form an afterglow or plume. This afterglow is formed by the transport of plasma generated metastables and radicals. Due to this intrinsic merit, a plasma jet can be spatially divided into an active plasma region, where the electric field is used for the generation of the discharge, and an afterglow region, where plasma generated active species can be used for remote treatment of the objects or plasma polymerization of the objects or plasma polymerization and film deposi-

tion. The spatial separation of the plasma generation and the plasma treatment can prevent the undesirable influence of the treated object on plasma, leading to excellent plasma stability in the upstream electrode region while enabling rich reaction chemistry within the downstream zone.

A considerable number of plasma jets exhibit very low temperature afterglow, mostly close to room temperature. Hence, they are also called low temperature or cold plasma jets. Since a low gas temperature is essential in many specific applications, cold plasmas have a bright future in applications, such as treatment of thermal-sensitive materials or living tissues. In fact, plasma medicine, which directly uses plasma jets to treat microorganisms, living tissues or cells, has emerged as a prospective field over the last few years. It exhibits great potential as a new treatment approach in the medical field [14, 15].

To realize future industrial applications, plasma jets must simultaneously achieve both high plasma stability and high effective non-equilibrium reaction chemistry [16]. However, this is a big challenge because a stable plasma is often sustained with inert gases (mostly Ar and He) whereas chemically reactive gases are demanded for efficient reactions. Additionally, many plasma jets are working in what is called "a glow mode", which can easily transfer due to a variety of instabilities to the arc mode when a high power is dissipated in the plasma. Moreover there are other barriers in the way of plasma jets in practical applications, such as small dimensions of APPJs (typically few millimeters) and the use of expensive noble gases. All these challenges and limitations have driven research and exploration in this domain, which is outlined in the following sections.

2.2.2   Methods for excitation and sustention of plasma jet

Till now, a large number of plasma jets with various constructions, operating parameters and plasma characterizations such as electron temperature, density and gas temperature have been reported. Typical operating parameters include working gas, dissipated power, driven voltage, gas flow rate and electrode configuration. Many categories of plasma jets can be made using the above parameters as the reference. Each plasma jet works at its specific conditions (configuration, power, gas . . .), exhibits distinct characterizations and can be used for different applications.

According to the configurations, plasma jets can be divided into two main categories. One is the cross-field jet whose electric field is perpendicular to its flow field. The other is referred as the linear-field jet with the electric field parallel to its flow field [16]. Based on the principle of afterglow formation, plasma jets can be distinguished by remote plasma jets, in which the afterglow is potential free, and active plasma jets, in which the afterglow contains a substantial amount of free and high energetic electrons [9]. In the latter case, the substrate must be considered as a second or third electrode, which means that the afterglow is not potential

free. According to the working gases used, there are noble gas plasma jets using helium or argon, and molecule gas plasma jets using nitrogen or air [17]. The way of electrical excitation and sustain has been mostly adopted for the classification of plasma jets: direct current (DC) plasma jets, alternating current (AC) plasma jets, radio frequency (RF) plasma jets, microwave (MW) plasma jets and pulsed DC plasma jets [18]. Since a great number of plasma jets have been developed through the years, only a few typical plasma jets will be reviewed and discussed in this section. The classification for the discussed plasma jets is based on the frequency range of the power supplies used to ignite and sustain them.

2.2.2.1 Direct current plasma jets

With the advantages of simple external electric circuit and high reproducibility, DC plasmas have been widely used in industry. Under atmospheric pressure, one of the major challenges of stable DC plasma generation is the difficulty in preventing the glow-to-arc transition. This transition occurs as a sudden sharp rise of discharge current from a few milliamperes in a glow discharge mode to amperes in an arc discharge mode. Electronic and thermal instabilities are accused as the sources of the glow-to-arc transition in DC plasmas [19]. Several methods have been used to suppress those instabilities in DC plasmas, which promote the developments of stable non-equilibrium DC plasma jets [20–22].

Typically, DC plasma jets are generated in a cylinder structure with an inner HV electrode and a ground electrode at the nozzle. Dudek et al. [23] reported a DC plasma jet needle source which consists of a shaped pin as the HV electrode and a metallic conical cylinder as the ground electrode and the gas channel shown in figure 2.1 (a). Nitrogen gas with a flux up to 20 standard liters per minute (slm) was used as the working gas. The glow discharge mode was characterized by high emission intensity in a small region near the cathode tip and low emission intensity in the afterglow region. Despite the temperature of the active plasma zone near the cathode tip being up to 950 K, the gas temperature in the effluent flow was reduced to less than 400 K by the effective thermal-conductivity of the feed gas. A DC plasma jet with comparable structure was utilized for the inactivation of Escherichia coli (*E. coli*) and its four kinds of single-gene knockout mutants [24].

Another plasma jet with an inner electrode configuration that can operate in air and nitrogen was reported by Xian et al. [25, 26]. The schematic diagram of the device is shown in figure 2.1 (b). The DC plasma jet device consists of a quartz tube with an inner stainless steel needle in the tube, and a grounded copper ring at the outlet of the tube. The center need (HV electrode) was connected in parallel with a capacitor to a DC power supply through a 1 MΩ resistor. When air or nitrogen flows through the tube and a sufficient HV (few kV), a discharge was ignited between the electrode gap and a plasma plume was launched through the hole of the copper ring into the surrounding air. Two distinct discharge modes
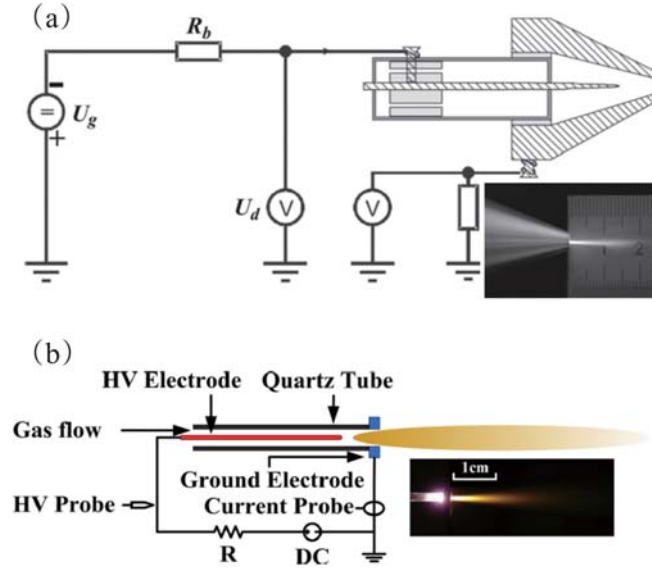
Figure 2.1: Schematic of typical DC plasma jets: (a) the plasma jet device developed by Dudek et al. [23].; (b) the plasma jet device developed by Xian et al. [26].

were founded in the DC jets: self-pulsing mode and DC operation mode. The gas temperature of the plume in self-pulsing mode was lower than that in the DC mode and dropped to less than 323 K at a distance of 2 mm.

A non-equilibrium DC plasma jet source based on the concept of microhollow cathode discharge (MHCD) were reported by Kolb et al. [27], with the configuration shown in figure 2.2. In this configuration, a stable discharge was generated with a DC high voltage by confining the glow discharge in a hollow cathode geometry with dimensions of the order of 1 mm in order to avoid the glow-to-arc transition. The MHCD jet consists of an insulated-separated electrode system, in which the cathode and anode have holes with the same diameter of 0.2-0.8 mm. A ballast resister of 51 kΩ was connected between the DC power supply and the HV electrode in order to limit the discharge current. When air or any other operating gas was ejected into the anode channel and a DC voltage (400 - 600 V in their work) was loaded on the electrodes, a plasma could be sustained at glow discharge mode with a 1 - 2 cm afterglow. According to their report, the gas temperature of the afterglow at the distance of 5 mm was less than 328 K. Abundant reactive species, such as O, OH, NO, and ozone, were identified with high concentrations in the afterglow, and could be used for biomedical applications, such as fungal decontamination on sensitive surfaces. A DC MHCD jet with slight modification of configuration was reported by Zhu et al. [28]. The discharge transition between

self-pulsing mode and normal glow mode was observed as well. Promising results were reported on using the DC jet in versatile applications, such as teeth whitening, root canal treatment, inactivation of Bacillus subtilis (*B. subtilis*) spores in water [29–32].

In addition, DC plasma jets with an active plasma afterglow have also been reported. Wu et al. [33] developed a DC plasma jet device with an active plasma afterglow. As schematically shown in figure 2.3 (a), the afterglow of the jet device was characterized by a homogeneous large cross-section. The plasma jet device consists of a stainless steel needle, which is inserted into a quartz tube and connected to a DC power supply through a ballast resistor, and a ground plate, which is put few mm away from the nozzle. Air was used as the working gas. The gas temperature of the plasma was estimated around 300 - 350 K. It was demonstrated that the plasma and afterglow properties were strongly dependent upon the nozzle-object distance and the gas flow rate. They suggested that the residual charges trapped on the inner surface of the quartz tube were responsible for the formation of large cross-section plasma afterglow.

Recently, Jiang et al. [34] developed a DC non-equilibrium plasma jet using argon as the working gas. The schematic diagram of the plasma jet device is depicted in figure 2.3 (b). The device consists of a cylindrical rod as the anode in a quartz tube and a ground metal spring cathode which is 5 mm away from the nozzle. From the analysis of OH and N_2 molecular emission spectrum, the rotational and vibrational temperatures of the plasma were estimated to be 810 K and 2200 K respectively. An interesting physical phenomenon was found: the

Figure 2.2: Atmospheric pressure DC plasma jets with microhollow cathode discharge configuration [27].

Figure 2.3: Atmospheric pressure DC plasma jets with a configuration of remote ground electrodes: (a) the DC plasma device developed by Wu et al. [33]; (b) the plasma device developed by Jiang et al. [34].

anode glow, which often exists in traditional DC glow discharges, was absence in their device. This observation was attributed to the ambipolar diffusion of electrons from the vicinity of the anode into the positive column.

2.2.2.2 Alternating current plasma jets

Several plasma jets powered by alternating current (AC) have been developed as DBD plasma jets or DBD-like plasma jets [17]. One of the earliest non-equilibrium AC plasma jets was reported by Teschke et al. [35]. It consists of a quartz glass tube with two ring electrodes on the outer side of the tube and with helium flowing through the tube. Figure 2.4 depicts the jet configuration. The application of a sinusoidal voltage with a peak value of 7 kV at a frequency of 13 kHz resulted in the generation of a plasma which consumed 4 W of electrical power and propagated to the surrounding air. The plasma discharge was at a glow-like mode. Although the plasma appeared homogeneous, the discontinue characterization with bullet-like discharge volumes was found for the first time by fast imaging technique. They noticed that the orientation of HV-ground electrode was essential. A downstream afterglow was developed with an HV front electrode and grounded rear electrode, whereas an inner glow against gas flow was formed by a vice versa connection of the electrodes.

However, the effect of electrode orientation on plasma propagation was absent in the plasma jet device developed by Lee et al., which consists of an inner extra floating inner electrode [36]. The plasma jet was driven by a high voltage sinusoid at frequency of 20 kHz. The inner floating electrode was a cylinder perforated by several capillary holes of 1 mm diameter. It was used to enhance the local electric field as well as facilitate plasma ignition at low voltage. From the spectra of the second positive nitrogen bands, the rotational and vibrational temperature of the plasma was estimated to be 290 K and 2500 K respectively. When used in
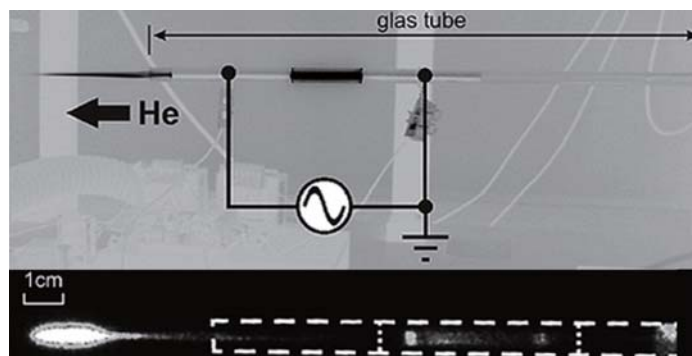
Figure 2.4: Configuration of plasma jets based on DBD structure and the plasma propagation in a bullet form [35].

combination with hydrogen peroxide (H_2O_2), this plasma jet exhibited a strong teeth bleaching effect and removing coffee or red wine stains from extracted teeth [36, 37]. AC plasma jets with a single ring electrode as the HV electrode were studied by Li and Walsh [38, 39]. In their device, the electrode was arranged 20 mm away from the edge of the nozzle, and was driven by a high sinusoidal voltage of 52 kHz. The working gas (He, Ne, and Ar) was passed through the tube. The discharge in the tube was ignited at downstream region, but extended to upstream region at a high voltage. It was found that the gas flow rate shown strong effects on the length of the plasma afterglow [38]. Three distinct operating modes, namely the chaotic mode, the bullet mode and the continuous mode were observed in the plasma device [39]. By increasing dissipated power after the plasma ignition, the plasma jet evolved through these three modes of distinct difference with abrupt mode transition.

Another widely used configuration in AC plasma jets was made of one inner electrode in a dielectric tube. A typical AC plasma jet with a pin and a ring electrodes was reported by Sarani et al. [39]. In the schematic shown in figure 2.5, the HV inner electrode is a tungsten rod of 0.5 mm diameter with half spherical shape and is placed inside a quartz capillary. The ground ring electrode is placed 40 mm away from the HV electrode and 20 mm away from the edge of the capillary. Mixture gases of Ar and H_2O was used as the working gas. It was found that the water content exhibited a significant impact on plasma properties. The maximum intensity of OH radicals in the plasma was observed with the mixture of 0.05% of H_2O. It was found that the rotational temperature of afterglow in case of pure argon is around 625 K and 1100 K for maximum concentration of water. Diverse applications of the plasma jets were studied: inactivation of Staphylococcus aureus (*S. aureus*) biofilms, surface modification of Poly-ξ-Caprolactone and polypropylene [40–42]. Recently, the jet with small modifications have been used for the

treatment of the inner wall in small polyethylene tubes (inner diameters from 0.28 mm to 2.45 mm) and for the surface activation of polyethylene to enhance the hydrophilicity by Onyshchenko and Van Deynse, respectively [43, 44].
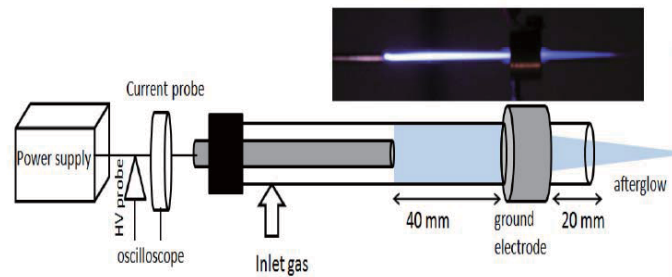
Figure 2.5: AC plasma jet with pin and ring electrodes developed by Sarani et al. [39].

Lu et al. [45] developed an AC plasma jet which can generate a plasma afterglow up to 11 cm. The inner HV electrode was inserted in a quartz tube with tip end closed and put in a big quartz tube. The ground ring electrode was attached to the outer surface of the big quartz tube. A homogeneous plasma was generated using helium as the working gas. The gas temperature of the plasma afterglow was about 300 K with 10 W dissipated power. Besides this, the use of a metal tube as the inner HV electrode was reported by Chen et al. [46]. Argon was the working gas for their device. They utilized an electrolyte solution of potassium chloride (KCl) remaining in the outer layer as of the other electrode for the purpose of cooling down the dielectric efficiently and improving the power efficiency. With 60 W dissipated power, the gas temperature of plasma afterglow was measured as lower than 320 K by an infrared thermometer. This plasma jet was applied for the fabrication of highly sensitive nanostructured bio-substrate for DNA probe immobilization, and for coating of acrylic acid polymer on silk fibers [46, 47].

A nitrogen microplasma jet driven by 20 kHz AC voltage was developed by Hong and Uhm [48]. The device consists of two electrodes with a hole having a diameter of 500 μm, which are attached to the double surfaces of a centrally perforated dielectric disk with a same size hole in the center. An afterglow with a length up to 6.5 cm and a temperature below 300 K was produced by this microplasma jet. Using swarm parameters of electron, the electron temperature and density were estimated to be 0.56 eV and 1.71×10^{13} /cm^3, respectively.

2.2.2.3   Radio frequency plasma jets

Radio frequency (RF) high voltage is one of the most frequently used methods for the excitation and sustentation of plasmas. A large number of RF-driven plasma jets have been designed and utilized in many fields through the years.
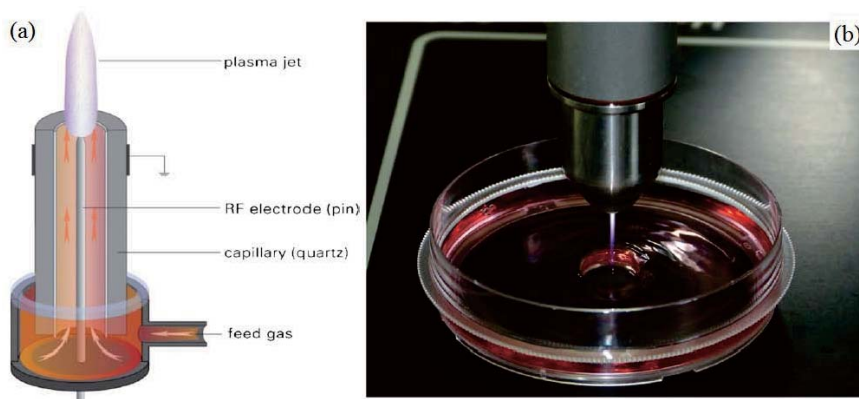
Figure 2.6: Schematic setup of the APPJ plasma source (kINPen 09) (left); a photograph of the plasma jet used for treatment of HaCaT cells in a culture dish (right) [52].

One of the earliest non-equilibrium RF plasma jet was reported by Koinuma et al. [49]. Based on a simple coaxial DBD configuration, the device consists of a HV needle electrode inside a quartz tube, and a cylindrical grounded electrode surrounding the tube. The influence of mixing ratio of the working gases on the stability of the discharge was studied. It was found that the mixing conditions for generating stable discharge were Ar/He = 0% - 30%, CF_4/He = 0% - 5%, H_2/He = 0% - 4% and NF_3/He = 0% - 1%. Instability or even extinguishing of plasma discharge occurred when the introduced working gases exceeded the above concentration ranges. This plasma jet was used for silicon etching, rubber treatment and fullerenes production [49–51].

Recently, the kINPen 09 source was developed by the researchers at INP Greifswald, [9]. The schematic diagram of the device is depicted in figure 2.6. The plasma jet consists of a pin-type HV electrode (diameter = 1 mm) in the centre of a quartz capillary (inner diameter = 1.6 mm), and a grounded anode surrounding the tube. With Ar flowing through the capillary and a radio frequency voltage (1 - 5 kV, 1.5 MHz) coupled to the central electrode, a plasma was generated at the top of the centered electrode and expanded to the surrounding air outside the nozzle. The temperature at the tip of the plasma afterglow (length up to 12 mm) was lesser than 310 K. With the CE marking, many preclinical studies have been performed for potential medical applications, such as the antimicrobial efficacy against biofilms, medical critical yeasts and bacteria cultures. Further, treatment impact on human HaCaT keratinocytes cells and Murine epithelial cells mHepR1 has also been analysed, [9, 52–54]. Additionally, the plasma jet has been used for the deposition of Zn-containng films [55].

As one can see, DBD based RF plasma jets share a very similar configuration with many AC plasma jets. In order to understand the difference between the
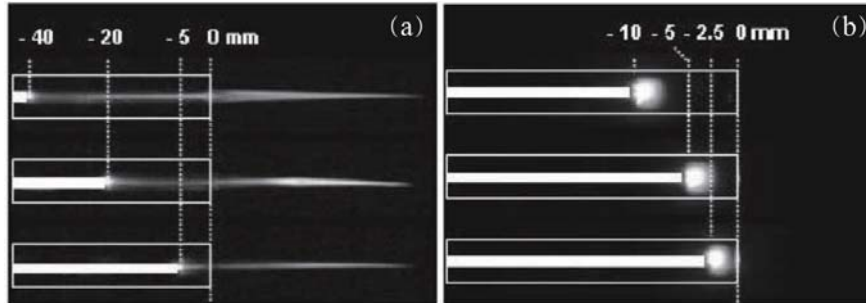
Figure 2.7: Comparison of a plasma jet excited by two different frequency: (a) 50 kHz; (b) 13.56 MHz [56].

plasma jets driven by a AC voltage and by a RF voltage, Kim et al. [56] reported a comparative study on a plasma jet under voltages with two different input frequencies (50 kHz and 13.56 kHz). The plasma jet had a single electrode with helium as the working gas. They found that the input frequency significantly effected plasma characterization, such as the appearance, the electrical property the gas temperature and the spectra property. Figure 2.7 depicts a visual comparison of the plasma jet under two driven frequencies. In general, the plasma jet revealed a long cylindrical shape with low frequency, but roughly a spherical shape with RF frequency. Results of current waveform and optical emission measurement indicated that the discharge was more continuous in time for RF plasma in contrast to AC plasma. The dissimilarity in RF discharge and AC discharge was attributed to the mobility variation of electrons and ions in fast changes electric fields.
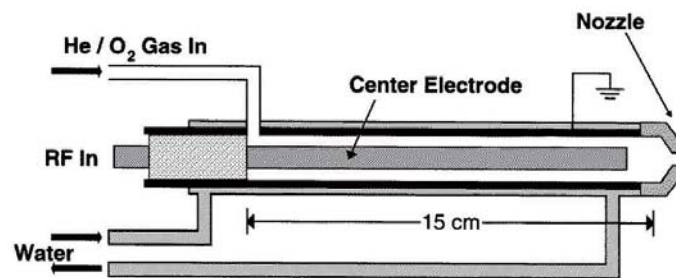
Figure 2.8: Schematic of the atmospheric pressure RF plasma jet with coaxial metal electrode [57].

Another typical type of RF plasma jets has the coaxial configuration of an HV inner electrode and a grounded outer electrode [57, 58]. Figure 2.8 depicts the schematic diagram of the plasma jet. A mixture of helium and other reactive molecule gases, such as oxygen, was fed through the annular space between the

two electrodes. Unlike plasma jets with DBD configuration, this plasma jet did not require any dielectric material between the electrodes to create stable plasma. The sustaining power for the plasma jet ranged from 40 W to 500 W. Special designed water cooling system was used to keep the jet from overheating. The gas temperature of afterglow was in the range of 100 to 150 ^{o}C. By introducing organosilicon precursor (tetraethoxysilane in their work) to the nozzle at the end of the plasma jet, SiO_2 films were deposited on a silicon substrate which was put 1.7 cm away from the nozzle. It was found that the film growth rate decreased with the increase of sample temperature and increased with the rise of dissipated power [58]. Other than that, material etching (Kapton, silicon dioxide, tantalum and tungsten) of the plasma jet was studied with a gas mixture of helium, oxygen and carbon tetrafloride (CF_4). From the analysis of the gas composition during the process, they suggested that the etching was mainly caused by chemical mechanisms [57].

Various plasma jets based on the above concept have been developed. For example, a helium RF glow discharge plasma jet with the coaxial metal electrodes was developed for biomaterials treatment [59]. With a dissipated power of 10 - 120 W, the gas temperatures ranged from 297 to 337 K on the axis of the plasma jet at 2.0 mm downstream. The genetic effect of the plasma jet acting on a loopful recombinant plasmid was reported. It was found that the chains of the plasmid DNA was broken after a 30 s plasma treatment. More significant genetic effects were observed in the plasma jet treatment with a high helium flow rate, a high RF power input, or/and short distance between the nozzle and the sample. They noticed that the chemically active species, instead of heat, ultraviolet radiation (UV), intense electric field, and/or charged particles, broke the double chains of the plasmid DNA.

In addition, RF voltage has also been used for microplasma jets. A microscale atmospheric pressure plasma jet (μ-APPJ) with a small discharge volume ($1 \times 1 \times 30$ mm^3) between two stainless steel electrodes and quartz glass side walls was reported by Schulz-von der Gathen et al.(see figure 2.9) [60, 61]. This special design makes the plasma region and the afterglow region easily accessible for optical diagnostics. Helium was used as the working gas. With a RF power between 10 W to 20 W, the device generated a homogeneous stable glow discharge (γ-mode discharge), and formed an afterglow at temperature of 303 K. When a small amount of molecular oxygen or nitrogen was mixed to the helium flow, high densities of reactive oxygen species and nitrogen species were produced. Those reactive species was expected to promote bactericidal activity for the plasma [62]. Further on, Niermann et al. [63] investigated the influence of typical intruding impurities (air diffusion from the front nozzle) and of impurities originating from gas system in the microplasma jet systems on the energy transfer processes of discharge in the plasma jet. In order to avoid the self-destruction at high powers, a modified μ-APPJ with a wedge electrode configuration instead of a coplanar one
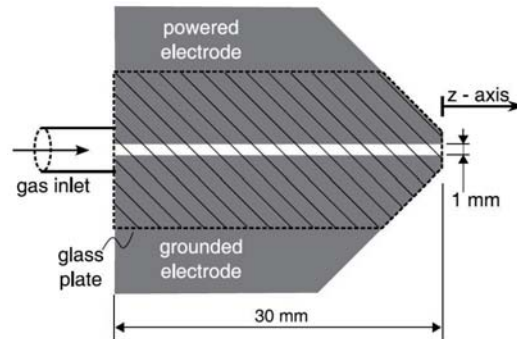
Figure 2.9: schematic of a microscale atmospheric pressure RF plasma jet developed by Schulz-von der Gathen et al. [60].

was developed by Schroder et al. [62, 64]. With such a wedge-shaped electrode configuration, the device exhibited a self-pulsing behavior. This phenomenon was characterized by the dynamical constricted "γ-mode-like" discharges, which was firstly ignited at the gas inlet, and then propagated with the gas flow towards the nozzle, and finally distinguished. It was found that helium metastables induced processes such as Penning ionization and pooling reactions played an important role in the sustainment and the propagation dynamics of the constricted discharge.

Besides exciting by a single frequency voltage, plasma jets can also be sustained by two voltage waves as widely used as in low pressure capacitively coupled plasmas [65]. Zhou et al. [66] developed a dual-frequency argon plasma jet with a coaxial configuration: a central pin electrode (driven by a 50 kHz voltage) in a quartz syringe and a copper ring electrode (driven by 2 MHz voltage) near the tube nozzle. The plasma jet was demonstrated to possess the advantages of low frequency and high frequency plasma jets: namely a long plasma plume and a high electron density respectively. It is noticeable that the plasma jet exhibited low ignition voltages and a large controllable range for gas temperatures. In addition, a helium plasma jet device with spatially separated dual-frequency excitations was developed by Cao et al. [67]. Their device consists of three electrodes, namely an upperstream capillary electrode recessed within a quartz tube, a ring electrode (driven by a 30 kHz voltage) wrapped around the quartz tube near the tube nozzle and a downstream plate electrode placed downstream from the tube nozzle (driven by a 5.5 MHz voltage). They suggested the possibility of separate, but not necessarily independent, control of plasma plume length, plasma density and gas temperature in their jet.

2.2.2.4   Microwave plasma jets

Atmospheric pressure microwave plasma sources (mostly at a frequency of 915 MHz or 2.45 GHz) are gaining increasing interest for many industrial applications, such as gas purification, decomposition of gaseous pollutants, sterilization, food preservation, living cells treatments, surface modification, hydrogen production, plasma-assisted combustion, and etc [68, 69]. However, most of those plasmas are characterized with high gas temperature (typically as high as few thousands Kelvin). Recently, some microwave plasma jets with a low gas temperature have been reported for biomedical applications. In general, one can clearly distinguish between plasmas formed at the tip of the electrodes supplied with microwave energy and plasmas generated through the electromagnetic energy transfer from standing waves in suitable resonator structures.
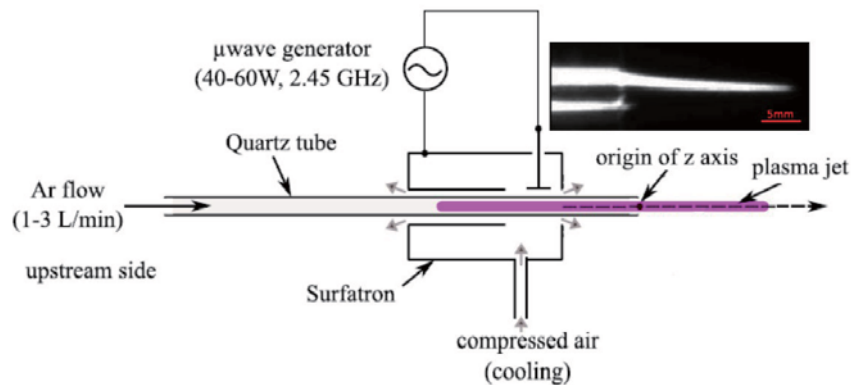
Figure 2.10: Schematic view and a photo of a microwave argon plasma jet based on a standard surfatron structure [70].

Wattieaux et al. developed a microwave argon plasma jet based on a standard surfatron structure (see figure 2.10) [70]. A quartz tube with 4 mm inner diameters was surrounded by a surfatron cavity with a 2 cm length extending in the downstream side out of this cavity. Argon gas was fed through the tube as the working gas. Microwave at 2.45 GHz was supplied from a generator and coupled to the argon gas by the applicator of the surfatron, where surface microwave was generated, leading to the ignition of gas discharge inside the quartz tube. In their experiment, the microwave power was set between 40 W and 60 W. The temperature of the afterglow at 30 mm away from the outlet was below 325 K. The potential biocide species like ozone, atomic oxygen and UVC were analyzed and quantified thus emphasizing promising potential biocide effect on the bacteria treatment. It was found that, comparing to atomic oxygen and UV radiation, ozone was identified as the main germicidal active species produced by the device.

   Choi et al. [71, 72] developed a portable microwave-excited plasma jet using a coaxial transmission line resonator for biomedicine applications. In this system, matching network is not required. As shown in figure 2.11, the resonator was made of a quarter wavelength of coaxial line, which was connected to a SMA connector for feeding power. The device had an electrically open at one end and a short circuit at the other end. It was found that a metal tip in the device could reduce the plasma ignition power to lower than 2.5 W. The gas temperature at the downstream of the APPJ stayed less than 320 K during 5 min of continuous operation. Acceleration of blood coagulation was observed with the plasma treatment: the blood coagulation occurred within 20 s of plasma treatment in vitro and within 1 min in vivo [71]. They also pointed out that the blood coagulation with treatment by the microwave plasma jet was twice faster than that by a low frequency plasma jet [73].

   Na et al. [74] developed a microwave plasma jet source with coaxial structure for the inactivation of fungal spores. The plasma jet was excited by 2.45 GHz microwave and sustained at low energy regime (0.8 W - 1.6 W). Inhibition effects on fungal growth depended on the several parameters like electric power, pulse widths and fed gases. They also noticed that different fungal species exhibited different levels of response to the plasma treatment. A small coaxial microwave plasma torch was developed by Stonies et al. [75] for gaseous species detection as an element specific detector in gas chromatography. In addition, Shimizu et al. [76] developed an atmospheric low-temperature microwave plasma torch with special designed electrode system. By using 2.2 slm of Ar gas flow and 85 W
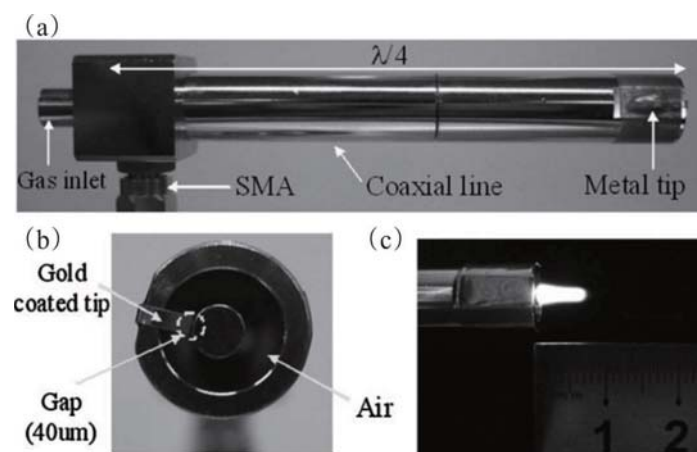
Figure 2.11: The configuration of a plasma device based on a coaxial transmission line resonator operating at 900MHz (a) side view, (b) front view, (c) with plasma on [71].

of microwave power, the device exhibited a strong bactericidal effect against microorganisms. They suggested that the UV radiation from the plasma device was one major agent killing bacteria. Besides, they also mentioned there were other mechanisms involving in the antibacterial process. Further clinical trials of argon plasma treatments on infected wounds were conducted with its follow-up devices (MicroPlaSter series) [77].

2.2.2.5 Pulsed plasma jets

Several plasma jets have been developed using pulsed excitation methods. Comparing to the AC, DC or RF discharge, a pulsed discharge is a typical over-voltage discharge, which can provide a high instantaneous power density to accelerate electrons and boost ionization processes. Also, short duration discharges in a pulsed source can reduce the heat accumulation, which is the main cause of thermal instability [78]. Pulsed DC voltages are mostly with amplitude of few kV, with a pulse width of few nanoseconds or microseconds and with a repetition rate of few kHz.

A portable nanosecond DC pulsed plasma jet with a similar configuration as the DC plasma jet in figure 2.1 was developed by Walsh and Kong [79]. The pulsed plasma jet consists of a center HV needle electrode with a sharpened end and a coaxial conical metallic ground electrode. Air was fed through the device at the rate of 10 slm as the working gas. When a pulsed voltage with 150 ns full width half maximum (FWHM) and a repetition rate of 5 kHz was introduced, the discharge occurred with more than 40 kW of the peak dissipated power but only around 1 W of the average dissipated power. The plasma jet was characterized with a gas temperature of 1850 ± 50 K in the active region and of 320 K in the afterglow region. It was noticeable that the copper material of the HV electrode was eroded in the plasma discharge, and deposited on a downstream substrate. This phenomenon was further investigated in a non-thermal plasma jet for the synthesis of copper particles by Lazea-Stoyanova et al. [80].

Lu et al. [81] developed a single electrode plasma jet device driven by a sub microsecond pulsed DC voltage. As schematic shown in figure 2.12 (a), the plasma source consists of a single wire electrode inside a quartz tube with one closed end. The quartz tube along with the HV electrode was inserted into a hollow barrel of a syringe. Helium was the working gas in this device. A plasma afterglow up to 4 cm long was formed with the applied voltage (magnitude 9 kV, pulse frequency 1 kHz, FWHM 800 ns). The gas temperature of the afterglow was estimated about 300 K. From the electric measurement of the circuit, there were two distinct discharge current pulses in each applied voltage pulse. The second discharge was due to the accumulation of charges on the surface of quartz tube during the first discharge. Also, they measured the afterglow current which exhibited one pulse in a voltage pulse. This current pulse could reach hundreds milliamperes range and

not change at different diagnostic position in the afterglow. The behavior of the plasma afterglow was similar with that of the ionization wave [81]. However, in Karakas's DC pulsed plasma jet, there were two afterglow current pulses in one voltage pulse [82]. The deviation of the measurement is probably due to the use of different configurations.

Lu et al. [83] also noticed that the voltage and width of the DC pulses exhibited significant effects on the afterglow length, whereas the pulse frequency, gas flow rate, and nozzle diameter exhibited less effect on the afterglow length. They
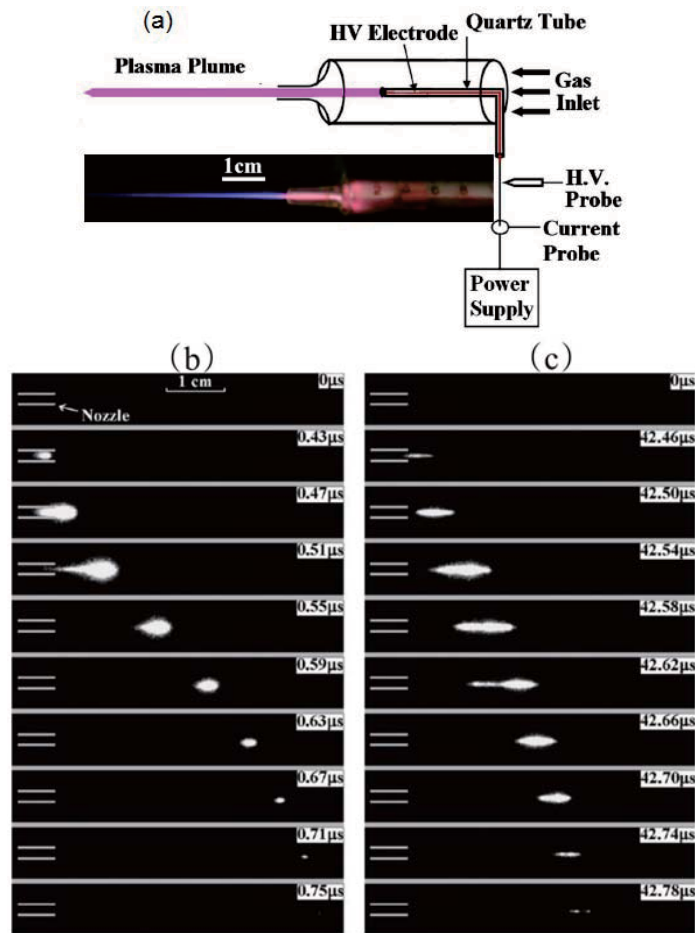
Figure 2.12: (a) a plasma jet device driven by a submicrosecond pulsed dc voltage developed by Lu et al. [81]; (b) and (c) the fast shown images of the bullet propagation of the plasma jet driven by pulsed voltage and sine-wave voltage with a repetition rate of 4 kHz respectively [85].

pointed out that the propagation of plasma afterglow was directly related to the integrated total charge, rather than peak current of the primary discharge. Figure 2.12 (b) depicted the propagation of plasma afterglow in the form of plasma bullets in the open air [84]. The bullet reached the biggest size at the moment of the highest bullet velocity and the strongest N_2^+ emission (391.4 nm). Additionally, a comparison study of the plasma jet excited by DC pulse (8 kV, 800ns and 4 kHz) and sine-wave voltage (16 kV and 4 kHz) was reported [85]. In general, the pulsed plasma exhibited a stronger optical emission, a larger discharge current, and a lower gas temperature than that in sine-wave plasma jet. The propagations of plasma bullets in DC pulsed plasma jet and sine-wave plasma jet are shown in figure 2.12 (b) and (c) respectively. The plasma bullets propagated with maximum velocity at around 2.4×10^5 m/s for pulsed voltage and 1.3×10^5 m/s for sine-wave voltage, and to a longer distance in the open air in the pulsed DC excitation case.

Recently, due to their potential advantages in sustaining plasma with low energy and low temperature, even short high voltage pulses (around 100 ns or less) have been used to ignite plasma jets. A plasma jet using unipolar pulse voltage with magnitude of 6 kV and width of 140 ns was reported by Jiang et al. [86]. As schematic shown in figure 2.13, the plasma jet device consists of concentric tubular electrodes separated by a ceramic cylindrical structure. Mixture of He and 1% of O_2 were fed the device. It was found that the polarization of the transient electric field near the device nozzle exit affected the dynamics of the plasma plumes, resulting in the differences of the plume length and propagation velocity.

A comparison study of a helium plasma jet source sustained by nanosecond
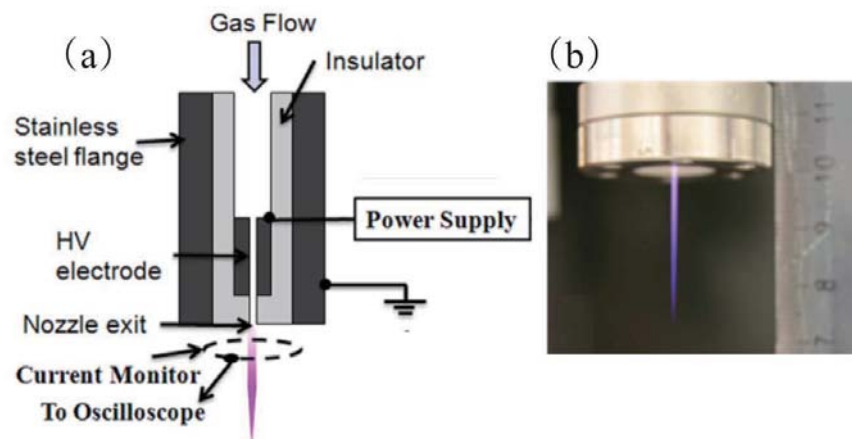
Figure 2.13: (a) schematic of nanosecond pulsed plasma jet developed by Jiang, et al., (b) photograph of the plasma jet excited with +6 kV, 140 ns pulses at 1.5 kHz [86].

pulse voltage (rise time 70ns, pulse width 100 ns, repetition rate 1 kHz) and microsecond pulse voltage (rise time 300 ns, pulse width 5 μs, repetition rate 1 kHz) voltage was reported by Zhang et al. [78]. Although consuming less energy, plasma sustained in nanosecond pulse voltage exhibited longer plume length, larger instantaneous power per pulse and stronger optical emissions than that in microsecond pulse voltage. It was explained by the formation of large density initial electrons and fast ionization in nanosecond pulse plasma jet.

2.2.3   Atmospheric pressure plasma jets up-scale

As mentioned above, plasma jets have been extensively studied for many practical applications which has opened various new and fast growing interdisciplinary research fields, such as surface modification, thin film deposition, medical therapy, nanoparticle synthesis [42, 87–92]. However, the dimensions of developed APPJs nozzles are mostly very small (sub-millimeter to several millimeters), which is a major deficiency and limitation for some large-scale applications, such as some cases in surface modification, film deposition and biomedical applications [93–95]. To overcome the barrier, some exploratory researches have been conducted in the last decade to develop a large-scale atmospheric pressure plasma source. In general, two main strategies have been reported to obtain an up-scale plasma jet source in an open space: (1) plasma jet arrays that consist of a number of ordinary size plasma jets; (2) plasma jets with large cross sections. Even though plasma sources based on surface discharge (SD) can also generate large size plasma in an open environment, they are not included in this section. The reason is that plasma generated by SD sources is confined in a thin layer near the surface instead of extending to open space [96–98]. In the following paragraphs, an overview on the two strategies for the development of up-scale plasma sources will be presented.

2.2.3.1   Atmospheric pressure plasma jet arrays

One straightforward approach to enlarge the overall dimension of plasma jets is combining many small plasma jet sources together as a jet array. There are one-dimension (1D) and two-dimension (2D) arrangements of identical plasma jets.

Cao et al. [99] reported an 1D jet array with the assembling of 10 glow discharge plasma jets in an acrylic cassette. The schematic diagram of the array is shown in figure 2.14. Each individual plasma jet unit consists of a glass tube wrapped by a copper tube, which is connected to the power supply through an individual ballast resistor (510 kΩ). The array device has a dimension of 3.2 cm width from the first to the last jet. This jet array was sustained by a voltage of 3 kV and 30 kHz, with helium flowing through each tube unit. Time and space uniformity of the plasma jet array were achieved and attributed to a self-adjustment mechanism among individual jets, which was facilitated by individual ballast in
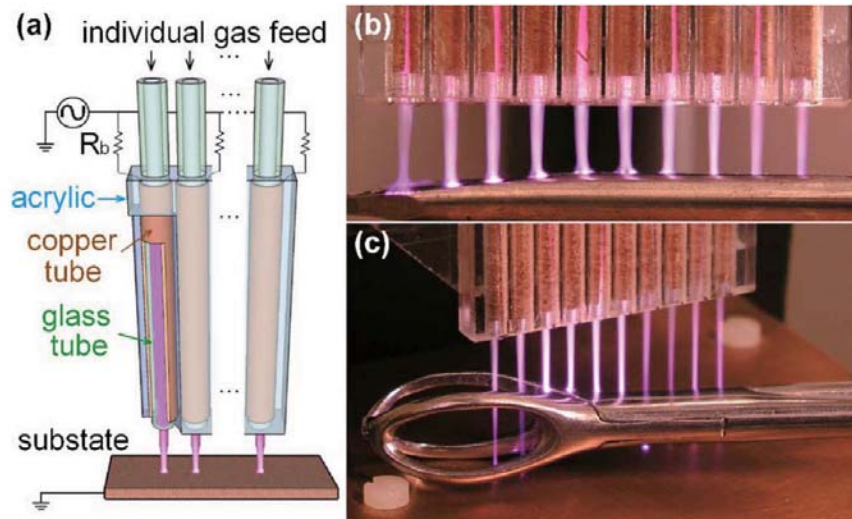
*Figure 2.14: (a) schematic of a ten-jet atmospheric pressure linear array with individual
ballasts, (b) image with the flat surface of a screwdriver as the substrate, (c)
image with a surgical tissue forceps as the substrate [99].*

the system and by spatial redistribution of surface charges in each tube. Also, Kim
et al. [100] developed an 1D plasma jet array, which consists of 16 tungsten pin
wire electrodes, Teflon tubes, and quartz tubes with a pencil-shaped nozzle. Each
wire was covered with a Teflon tube except a short tip. A pulsed bipolar source was
connected to the tungsten wires. Unlike Cao's array where helium was separately
introduced to each individual plasma jet tubes, the gas in this array was firstly fed
to a chamber and then delivered to each jet units. The ground copper electrode was
covered with a quartz plate and put 4 mm away from the nozzles. The propaga-
tion of plasma bullets in individual gas channels and interaction between adjacent
plasma afterglows were studied through fast imaging technique.

Pei et al. [101] developed a simple 1D jet array with the linear arrangement
of ten syringe needles. Those needles were connected to a large glass tube that
guided the gas flow. All needles were connected to a pulsed DC power supply
through a capacitor and a resistor. It was found that the plasma afterglow on both
edges initiated earlier than that in the middle of the plasma jet array. The propaga-
tion speed of the plasma bullets on both edges of the plasma array was higher than
that in the middle of the plasma array. They also reported another plasma jet array
for the generation of a homogenous large-scale plasma glow [33]. The elemental
plasma jet unit (depicted in figure 2.3 (a)) was characterized with a uniform after-
glow. When five of jet units were linearly arranged, the afterglows of individual
jets were emerged, leading to the formation of a homogenous afterglow.

Plasma jet arrays with 2D arrangement of elemental plasma jets have also been reported by many groups. A two-dimensional plasma jet array with seven identical plasma jets in a honeycomb configuration was reported by Nie et al. [95]. The schematic diagram of the 2D array device is shown in figure 2.15. Each individual jet consists of a central HV capillary electrode in a quartz tube. The center-to-center distance between two adjacent quartz tubes is 3.55 mm. Helium was used as the working gas and separately fed into each channel at a flow rate of 2.14 slm. The electric diagnostics of the jet array suggested that the six outer channels were simultaneously broken down and before the central channel's ignition. Fast images were employed to analyze the time resolve dynamics of the array in a full period of the voltage. It was found that the central jet was firstly ignited in a negative half cycle of the voltage, whereas the six surrounding jets were ignited in a positive half cycle. They further developed a 37-channel honeycomb-shaped array (see figure 2.15 (c)) and suggested that there was no fundamental limitation to scale up the plasma jet array with this configuration [102]. Fan et al. [103] also reported an honeycomb-shaped plasma jet array, but with seven single electrode plasma jets as the elemental unit. A repelling phenomenon of the six surrounding jets was observed in this device. Unlike the kinetics in Nie's array, a synchronized operation and temporal jet-uniformity of all individual jets during the whole voltage cycle was observed. This deviation was probably due to the different configurations of electrode system.

Due to the direct jet-to-jet coupling in plasma jet arrays within a honeycomb structure, two working modes were found in a 2D plasma jet array under different gas flow conditions, i.e. an intense plasma mode and a well-collimated plasma mode [104–106]. Based on optical emission spectroscopy, the plasma array in an intense plasma mode exhibited strong intensity of many active species, and had higher electron energy than those in a well-collimated mode. The jet-to-jet coupling was explained as electric coupling of charged particles instead of optical or chemical coupling. Besides, they also proposed an upgrade 19-channel array which generated a much higher emission than the 7-channel array [104]. Based on this, they suggested that the 2D jet array at an intense plasma mode was useful for applications requiring the high energetic plasmas. In addition, the 2D jet array at a collimated plasma mode was used for the growth of multiple-stack high-density ZnO nanoflower/nanorod structures on polyethylene naphthalate (PEN) substrates [107].

In addition to arrays of individual plasma jets, a novel structure of close-packed plasma jet array based on microchannels was developed by Sun et al. [108]. The packed array, which was molded into a transparent, lightweight, and flexible polymer, consisted of as many as 64 microchannels unit. The diameter of a microchannel was 350 μm. One main benefit of this design was the possibility to increase the number of microchannels without the jet-jet interactions. Further on, clinical stud-
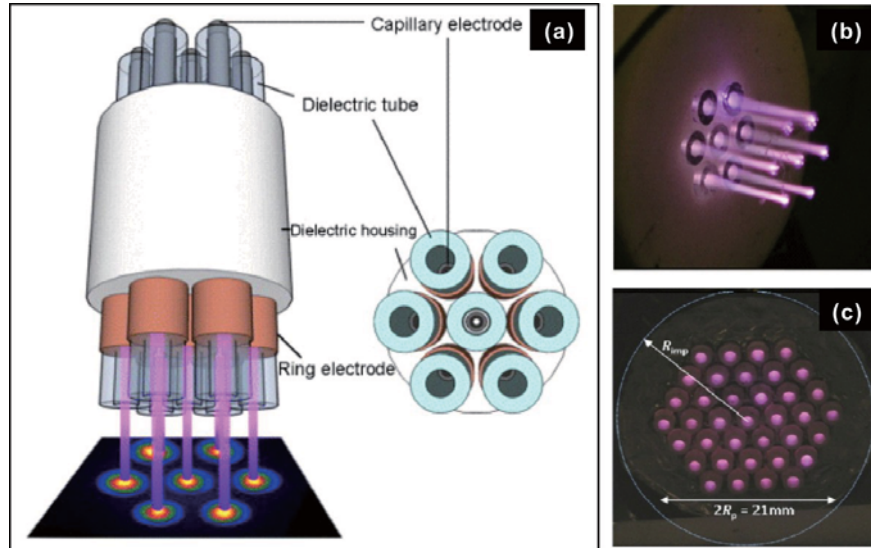
Figure 2.15: (a) Schematic of the seven-jet array arranged in a honeycomb configuration with both side view (left) and end view (right) [95], (b) Image of a seven-channel honeycomb array in an atmospheric helium flow, (c) Image of a 37-jet array [102].

ies on acute epidermal wounds in Sprague-Dawley rats found that a 40 s exposure to an plasma array per day could accelerate healing of the wounds [109].

It is well known that a plasma is inherently a nonlinear medium [110]. The coupling behavior caused by jet-jet interactions in plasma arrays is widely existed and makes operation of multi-source plasma devices non-trivial [111]. Therefore, it is necessary to have a better understanding on those jet-jet interactions, which has attracted more attentions recently. The influence of voltage amplitude, voltage frequency and gas flow rate on the characteristics of an atmospheric pressure jet array were reported by Qian et al. [112]. Besides, a small amount of O_2 additive into a three-jet array exhibited a positive effect on the length and the spatial uniformity of the plasma jets [113]. Ghasemi et al. [114] investigated the interaction between adjacent plasma afterglow in an 1D plasma array by Scalieren imaging technique. Once the discharges were ignited, a significant reduction in the length of the laminar flow region was observed. This was mainly due to the gas heating in the jet channel. Meanwhile, the strong repulsion between charged streamer channels in the array caused a significant divergence of the plasma afterglow, which could lead to a non-uniform treatment.

2.2.3.2 Atmospheric pressure plasma jet with a large cross section

Besides plasma jet arrays, plasma jets with large cross section have been considered as another approach to upscale a plasma jet source.

An atmospheric pressure plasma jet with 10 cm × 0.15 cm cross section was reported by Park et al. as one of the earliest cold atmospheric pressure plasma jet with large cross section [115]. The device was based on simple parallel metal electrode structure. Stable discharge was generated with 13.56 MHz radio frequency voltage and large helium flow (50 slm). By mixing 1% oxygen in helium, absolute concentration of ozone and atomic oxygen in the discharge and the effluent region were analyzed. The discharge in the plasma device exhibited two working modes: α mode and γ mode [116].
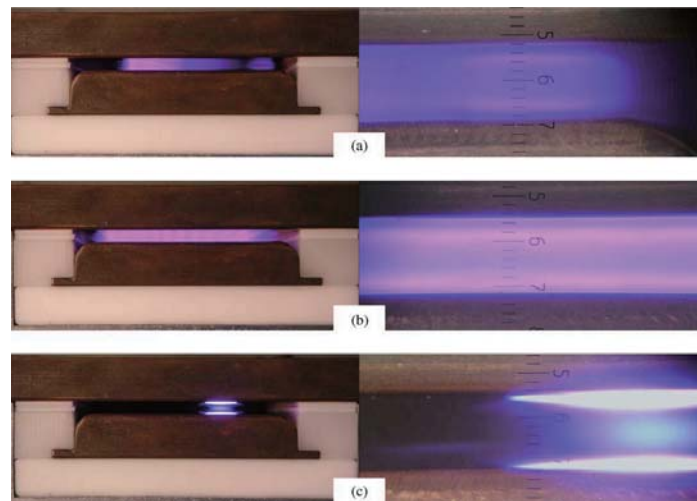
Figure 2.16: Photographs of the gap for various RF input powers of Laimer's plasma device operated with helium at gap spacing of 2.5 mm (full size and zoom in pictures on left side and right side respectively): (a) 140 W, (b) 360 W and (c) 440 W. Grounded counter electrode is on top, RF powered electrode is below [19].

Laimer et al. [19, 117, 118] reported visual and electric properties of these two discharge modes in a RF plasma jet device, which consists of two parallel metal electrodes similar to Park's device. α mode (see figure 2.16 (a) and (b)) was characterized as stable uniform glow-like discharge that partially or fully covered the electrodes. However, γ mode (see figure 2.16 (c)) was identified as localized discharge that covered a small fraction of the electrode surfaces. Unfortunately, there was limited information on the property of the afterglow, which is extremely important for applications.

A cold plasma brush consisting of a gas compartment and two cylindrical metallic electrodes was developed by Duan et al. [93, 119]. When sufficient DC
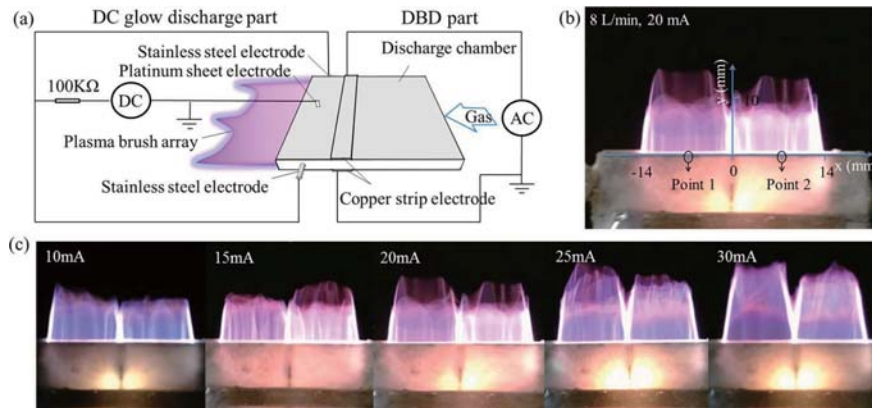
Figure 2.17: (a) Schematic diagram of a plasma brush array with two plasma brushes; (b) and (c) shown images of the array with different currents at 8 L/min [121].
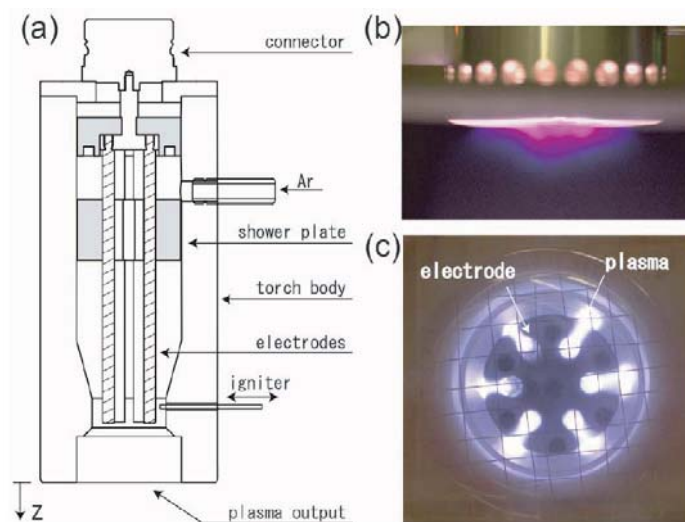
Figure 2.18: Schematic view of the plasma torch system and produced plasma: (a) plasma torch, (b) plasma plume below the torch, (c) plasma produced between the electrodes and the cylinder [76].

voltage and argon flow were applied, plasma was generated between the electrodes and launched to open air with a dimension of 10 -15 mm in width, 1 mm in thickness and 15 - 20 mm in length. A ballast resistor was connected with an electrode to suppress electric field fluctuations and to restrain electrical current in the discharge. After that, a DBD reactor was added to the plasma device as a preionization source to improve performance of the system [120]. The aim of this design

was to achieve efficient plasma generation by reduction of ignition potential, sustaining voltage, plasma dissipated power and Joule heat. In order to further extend dimension, an array was developed by integrating a pair of plasma brushes in parallel [121]. As schematically shown in figure 2.17, this device consists of a central ground platinum sheet electrode and two high voltage electrodes on both sides of the gas chamber. Measured with emission spectroscopy, the plasma was near-symmetrical in lateral direction of the plasma brush. Recently, a transverse magnetic field was employed to the brush to improve performance of the DC plasma [122]. Owing to electron drift in the $\mathbf{E} \times \mathbf{B}$ field, collisions of electrons with molecules in plasma and afterglow were significantly enhanced, which could simultaneously enlarge plasma dimension and improve plasma uniformity and stability. In addition, self-pulsing phenomenon of discharge in a DC plasma brush was studied by temporal and spatial resolved measurement of discharge voltage, current and emission intensity [123]. The formation of the afterglow was caused by the movement of pulse generated plasma, which propagated at speed of same order as the gas flow. The pulse discharges in the DC brush were attributed to dynamics of voltage between the electrodes due to plasma propagation. They found that frequency of pulse discharge was dominated by gas flow rate and discharge power.

Lu et al. reported a plasma brush driven by sub-microsecond voltage pulses [94]. The source consists of two blades (nozzle of 25 mm × 1 mm), which simultaneously functioned as channel for the gas flow and as the high voltage electrode. Helium was used as working gas. Based on I-V characterization and fast imaging, they found that discharge dynamics of the plasma sources were dependent on the electrode gap.

A microwave plasma torch (also known as MicroPlaSter) was developed with a configuration of six stainless steel electrodes inside a metal cylinder with diameter of 35 mm (see figure 2.18) [76]. It was the first plasma source used for clinical trials with patients, especially on dermatology [13, 124]. It was found that a daily 5 minutes plasma exposure led to significantly lower bacterial load compared to the control wounds [125, 126].

2.3 Polymerization of thin films using atmospheric pressure plasmas

Use of atmospheric pressure plasma jets has been intensively studied for many applications, including biomedicine [125, 127], food treatment [128, 129], modification and activation of material surface [44, 130], destruction of organic components [131, 132], synthesis of nanoparticles/nanocomposites [133, 134], etc. Among these applications, one of the most promising fields is plasma polymerization,

which is a subject of this thesis.

2.3.1   Plasma polymerization process

Nowadays, plasma polymerization is a versatile method to render certain functions onto the surface of a wide range of substrates for many applications [135–138]. These polymerized films have attracted great interest due to their excellent properties, such as pinhole-free, highly cross-linked, insoluble, thermally stable, chemically inert and mechanically tough [135]. Plasma polymerization in low pressure systems has been extensively investigated over decades. However, a low pressure process means high cost and difficult to batchwize process. Plasma polymerization at atmospheric pressure has the advantages of elimination of vacuum equipments, possibility of industrial integration, and high deposition rates. Therefore, many efforts have been given to develop and characterize atmospheric pressure plasma deposition systems.

Generally, organic monomer precursors (vapor, aerosol, or gas) have to be introduced into the plasma zone with working gases (usually helium, argon, or nitrogen) in plasma polymerization processes. These monomer molecules will react with reactive plasma species, and be converted into several molecular fragments and atomic species, which then recombine on the substrate surface and device components, and deposit in form of thin films. Functionality of plasma deposited films is mainly determined by the nature of the used precursor monomers [138, 139]. A variety of organic precursors has been investigated to obtain thin films with certain functions. For more information about atmospheric pressure plasma polymerization, detailed reviews can be found in [89, 139–142] and references cited therein.

Considerable attention has been given to plasma polymerization of silicon-inorganic and silicon-organic films for several purposes like vapor and gas barrier creation [143], wear and friction reduction [144], corrosion protection [145], biocompatibility [146] and hydrophobicity of surfaces [147]. A large variety of organosilicon monomers with attractive features, like sufficient volatile at room temperature, relatively low-toxicity, non-flammability, cheapness and commercial availability, have been employed as possible reactants for plasma polymerization of silicon-inorganic or silicon organic films [148]. Figure 2.19 depicts six of the most frequently used organosilicon monomers in atmospheric pressure plasma processes.

Morent et al. [135, 138, 148] reported a typical plasma polymerization process using a DBD plasma reactor with hexamethyldisiloxane (HMDSO) as precursor. Ar or Ar/air mixture was used as working gas. The liquid precursor was vaporized by passing Ar gas through a vessel before introduction to the reactor. Polymerized HMDSO films were deposited on polyethylene terephthalate (PET) surfaces. In-
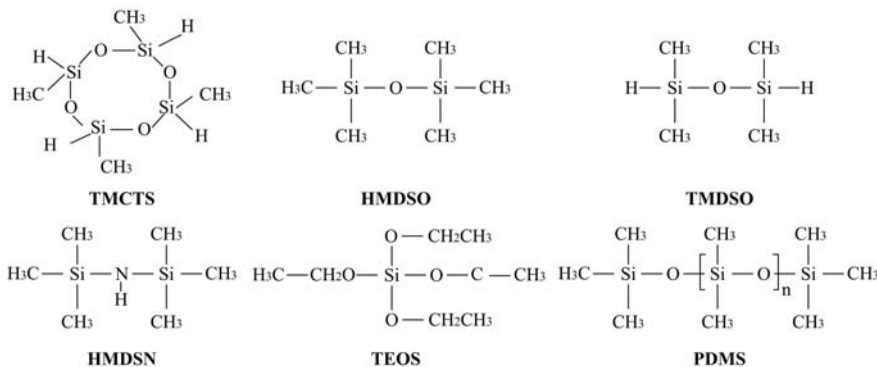
Figure 2.19: Commonly used monomers for the plasma deposition of SiO$_2$ coatings. With TMCTS = tetramethylcyclotetrasiloxane, HMDSO = hexamethyldisiloxane, TMDSO = tetramethyldisiloxane, HMDSN = hexamethyldisilazane, TEOS = tetraethoxysilane, PDMS = polydimethylsiloxane.

fluence of air content on chemical structure and surface morphology of deposited films were investigated [135, 148]. They noticed that deposition rate and chemical structure of plasma polymerized films were strongly affected by plasma discharge power and monomer concentration [138]. In the process with pure argon, plasma polymerization led to formation of quite homogeneous and hydrophobic thin films with high degree of linearization of monomer precursor (Si-O-Si chains and high retention of Si-CH$_3$ bonds). Whereas, the thin films deposited with Ar/air mixture exhibited a rough and hydrophilic surface with chemical structure closely related to silica. With increase of monomer concentration or of discharge power, growth rate of the deposits increased and reacted to maximum value. Any further increase of either parameter could slow down deposition rate. These results were explained with Yasuda's controlling parameter W/FM, where W is dissipated power of plasma, F is monomer flow rate, and M is molecular weight of the monomer, respectively [138, 149]. Additionally, plasma polymerization of polymethyl methacrylate (PMMA) and polyacrylic acid were reported using this type of DBD plasma deposition system [150–152].

Reuter et al. [153] studied deposition of carbon-free SiO$_2$-like thin films by a layer-by-layer process, in which very thin films were deposited from Ar/HMDSO or N$_2$/HMDSO plasma (only 3 s plasma-on time) and treated afterwards by pure N$_2$ DBD plasma for 30 s. Comparing to films deposited without N$_2$ plasma treatment, which were characterized by rich existence of carbon groups, films deposited with nitrogen plasma treatments exhibited dense and silicon oxide like features without any carbon related features. Carbon removal effect in N$_2$ plasma treatment was attributed to surface reactions of N$_2$ plasma generated excited species (metastables, ions, or possible photons) with surface bonded carbon.

Recently, use of pulsed plasma electrical excitation in atmospheric pressure plasma deposition processes has been reported to improve quality and reduce roughness of deposits [154–156]. Boscher et al. [156] studied the effect of electrical excitation on morphology and electrochemical properties of films in a nitrogen plasma using HMDSO as precursor. In spite of a lower average power, films from pulsed excited processes were grown in higher degree of cross-linking and equivalent deposition rate as that from continuous wave excited plasma processes. It is interesting to note that films grown with pulsed modulated signals exhibited a five times polarization resistance than the ones growth with a continuous wave electrical excitation.

Atmospheric pressure plasma polymerization has been extensively used to obtain many advanced functional materials. However, a gap exists between mechanism understanding and practical applications. In order to have better control over deposition processes, considerable attention has been given to kinetics and mechanisms in deposition processes. One of the widely accepted explanations is based on the concept of "atomic polymerization" [157]. In plasma polymerization process, monomer molecules are extensively fragmented to small components, which then randomly recombine, rearrange, and are fragmented again. Thus, unlike conventional polymers, plasma polymers generally exhibit a high degree of cross-linking and disorder (see figure 2.20). In a low pressure plasma process, collisions between monomer molecules and electrons, which induce breaking of a chemical bond and formation of two radicals, dominate the excitation mechanism for activated monomer. However, reactions involving high energy metastables have to be considered in an atmospheric pressure process [89].
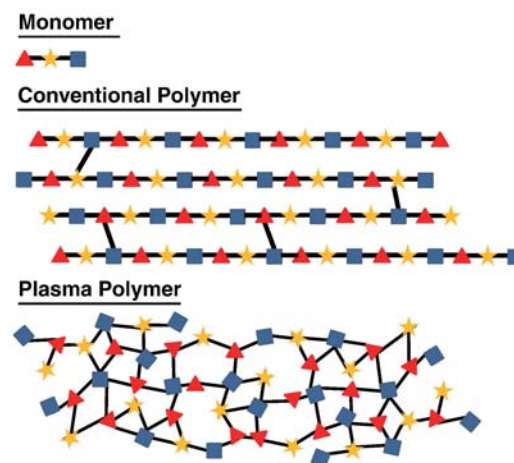
Figure 2.20: Schematic comparison between conventional polymers and plasma polymers with same monomer [89].

One method to analyze a plasma deposition process is by characterizing films which are deposited with different conditions (discharge power, monomer concentration, gas composition). Giving an indication of power input per molecule, the Yasuda's parameter (W/FM ratio), which was firstly used in a lower pressure plasma process, has been often adopted as an important reference in atmospheric pressure plasma processes to explain dependence of deposition rate on some external parameters [138, 149, 158–161]. It is suggested that, in a plasma polymerization process, low W/FM values result in less monomer fragmentation and high probability of retaining functionalities, whereas higher values stimulate dissociation of monomer molecules and promote fragmentation. However, Kakaroglou et al. [161] pointed out that the Yasuda parameter ignores discharge kinetics, which also strongly affect plasma deposition mechanisms and deposits. They found that, under same W/FM parameters, films with different morphologies, different thicknesses and different chemical structures were deposited using a plasma reactor under different discharge mode: glow discharge and filament discharge. It was demonstrated that morphology and chemistry of plasma polymerized films were extensively dependent on many parameters in plasma processes, such as discharge mode, reactive species distribution, reactor geometry, dissipated power, voltage frequency,monomer concentration, working gas, flow rates . . .

Recently, direct insights into reactions in gas phase plasmas have been performed by techniques like Gas Chromatography-Mass Spectrometry (GC-MS) [162–164], Molecular Beam-Mass Spectrometry (MB-MS) [165], and Fourier Transform Infrared Spectroscopy-absorption spectroscopy (FTIR-AS) [166]. In an atmospheric pressure DBD plasma process using HMDSO as precursor, Fanelli et al. [163, 164] analyzed exhaust gases by GC-MS to assess monomer depletion and to quali-quantitative determine by-products formed in the process. As an interesting observed result, HMDSO depletion in the plasma process with oxygen was always lower than that without oxygen. This indicated that adding oxygen to the plasma process did not improve monomer activation/utilization. According to their explanation, oxygen addition in the process led to a more filamentary discharge, which reduced plasma volume for HMDSO activation. Also, oxygen addition strongly influenced chemistry of deposits and composition of exhaust gases. Meanwhile, they suggested that silanols in deposited films were formed through heterogeneous (plasma-surface) reaction during film growth, instead of in gas phase plasma [163, 164]. Vinogradov et al. [166] reported their FTIR-AS investigation on a deposition process using HMDSO as the precursor. It was noticeable that four main radicals were produced in plasma: $(CH_3)_3SiO$, $Si(CH_3)_3$, $(CH_3)_3SiOSi(CH_3)_2$, and CH_3. They also suggested that the $(CH_3)_3SiO$ radical could be an important reacting agent in the film deposition process.

2.3.2   Thin film polymerization by plasma jets

Compared to polymerization processes within a volume-confined plasma, like typical DBD plasmas, polymerization processes using atmospheric pressure plasma jets are particularly attractive due to portable designs and capabilities to treat objects with complex morphologies and structures.

Hicks et al. [58, 167] reported one of the earliest investigations on plasma polymerizations using an atmospheric pressure plasma jet device (with jet configuration shown in figure 2.7). An oxygen and helium gas mixture was fed into the device. Precursor (TEOS) was introduced by passing a channel of helium gas through a bubble container, and mixing with the plasma at the end of the jet nozzle. Thin films were deposited on silicon substrates which were located 1.7 cm downstream of the outlet. Highest deposition rate in their experiment was 302 ± 25 nm/min with a monomer partial pressure of 0.2 Torr and dissipated power of 400 W. It was found that deposition rate increased with increase of RF dissipates power and oxygen pressure, and decreased with increase of sample temperature. Influence of precursor injecting positions on deposited films was investigated by Lommatzsch and Ihde [168]. They used a commercial AC plasma jet using HMDSO as precursor. Two positions with vertical separation of 4 mm were tested in the experiments. According to their work, these two positions were arranged at transition phase between the excited volume plasma and relaxing afterglow. Thin films with different structures and compositions were obtained at different precursor injecting positions. Those functional differences in the final films were attributed to the different precursor fragmentation extent due to strong relaxation of the volume plasma and different residence times in afterglow plasma [168].

Plasma polymerizations of organosilicon films using plasma jet sources with coaxial pipe configuration have also been extensively studied. Raballand et al. [169] reported the deposition of organosilicon and silicon oxide-like films at room temperature using an atmospheric pressure argon microplasma jet without addition of oxygen. In their system, the plasma jet consists of a stainless steel capillary, which serves as HV electrode and gas channel for precursor (HMDSO), and a ceramic tube, which serves as main gas channel. Silicon substrates were put 1 mm away from the end of the jet nozzle. When flow rate of precursor channel reduced to below 0.1 standard cubic centimeters per minute (SCCM), chemical composition of deposited films changed abruptly from organic composition to an inorganic silicon oxide composition. Deposition of carbon-free SiO_2 film without adding oxygen was attributed to reactions which were initiated by dissociative ionization of HMDSO and followed by ion-induced polymerization [169]. Huang et al. [170] reported growth of organosilicon film using a coaxial plasma jet with HMDSN as precursor. The plasma device consists of an inner quartz capillary, which serves as working gas channel, and a quartz tube, which serves as gas channel for oxygen and precursor. Plasma was firstly generated inside the capillary, then mixed with

precursors near the nozzle, and propagated to the surface of polycarbonate substrates. Surface properties of the deposited films were affected by parameters like plasma dissipated power, substrate position and oxygen flow rate [170, 171].

Schafer et al. [172–176] deposited carbon-free silicon oxide films with a non-thermal RF capillary jet system. The plasma jet source is configured with an inner capillary and an outer quartz capillary, which is wrapped by two ring electrodes. The inner capillary serviced as gas channel for precursors. Self-organized discharge patterns were observed in this device and could be controlled by external parameters, such as dissipated power, gas flow rate, electrode distance and driven frequency [174]. It was found that the locked mode in the jet device was a distinctive discharge regime in which homogeneous and symmetric thin films were deposited. Influence of oxygen and precursor concentration on film chemistry and on their radical gradients over the profile was studied. It was found that the static deposition profile (the footprint) of the plasma deposits was influenced by working parameters and geometry parameters [173]. The deposited film footprint could be shaped from a ring form reflecting the tube dimension to a parabolic profile.
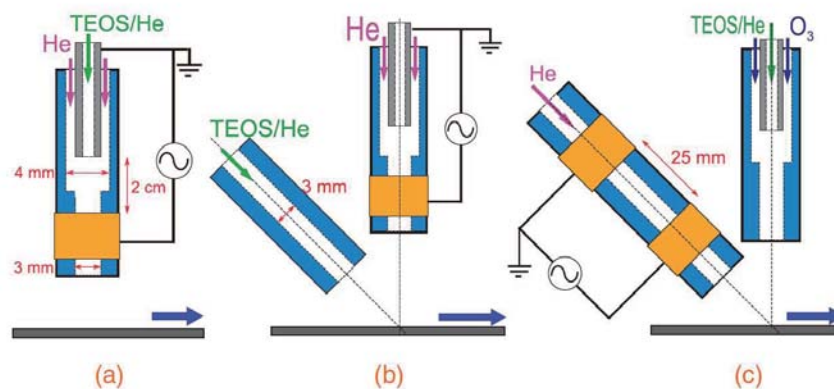
Figure 2.21: *Schematics of the plasma jet deposition system reported by Ito et al.: (a) coaxial configuration, (b) crossed configuration with vertical plasma jet and tilted TEOS supply, and (c) crossed configuration with tilted plasma jet and vertical TEOS supply [177].*

Ito et al. [177] reported deposition of SiO_2 films with a coaxial helium plasma jet using TEOS as precursor (see figure 2.21). For a comparative study, two modified systems were developed with different crossed configurations: one consists of a vertical plasma jet with a 45 degrees tilted TEOS supply nozzle (figure 2.21 (b)) and the other consists of a tilted plasma jet with vertical TEOS supply nozzle (figure 2.21 (c)). The plasma jet was powered by a bipolar impulse power supply with a frequency of 2.5 to 15 kHz. It was found that the deposition rate increased with the driving frequency in all three configurations. A higher deposi-

tion rate was observed with the tilted jet configuration (figure 2.21 (c)), which was attributed to longer interaction distance caused by plasma spreading along the substrate surface. They also suggested that adding ozone to the process could increase deposition rate. In addition, the apparatuses were also used for deposition of ZnO films with bio(octane-2,4-dionato) zinc $(Zn(OD)_2)$ as source material [178].

2.4 Plasma engineering of antimicrobial materials

Among different types of plasma polymers, demands on development of antimicrobial coatings are growth at an extreme rate in many fields, such as medical and hygienic materials, water purification and food protection [179–182]. In medical field, infections associated with medical devices, especially with medical surgical tools and supporting parts, are responsible for at least 1.5 % to 7.2 % post-operational complications [183, 184]. The earliest and essential event in pathogenesis of a biomaterial related infection is attachment of microorganisms to the surface [185]. This event produces extracellular polysaccharides, causes formation of a biofilm which can protect bacteria from antibiotics and host body's innate defence system, and eventually results in infections [186, 187]. Many methods have been reported on development of antimicrobial materials. In general, two main strategies can be distinguished: "passive" non-fouling strategy and "active" antibacterial strategy [187]. The former one is to prevent attachment of bacteria on material surfaces by grafted polymer coating or by designed micro-/nano-patterns [188,189]. Whereas the latter one aims to kill microorganisms existing on the material surface and in the surrounding biological milieu by elution of antibacterial compounds from the materials [190–194]. A variety of promising methods have been purposed for the fabrication of biomaterials with one of these two effects or with both effects [195]. Plasma-based strategy is a suitable and versatile approach that is transferable between a large range of different materials at a low temperature without any need of specific substrate or any chemical solvents. In this section, recent development of antimicrobial functional materials based on plasma methods will be overviewed.

2.4.1 Plasma assisted surface grafting of antibacterial components

Plasma has been widely used as a pretreatment step to activate or modify material surfaces, which can improve efficiency of grafting or incorporating antibacterial components onto surfaces.

Due to their natural antibacterial/antifungal properties, chitosan and its derivatives have been widely used in biomedical materials. Chang et al. [196] used plasma pretreatment to promote grafting of chitosan on polyester fabrics to obtain
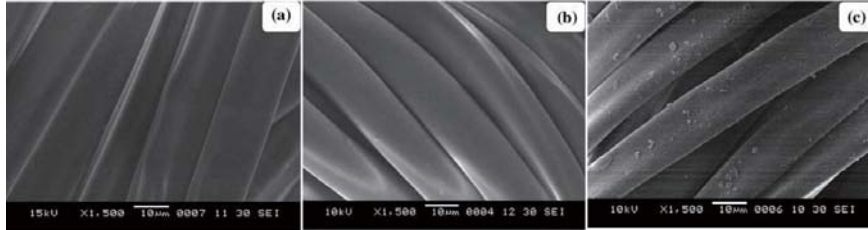
Figure 2.22: SEM images of PET surface: (a) before plasma treatment and without chitosan deposition, (b) before plasma treatment and with chitosan deposition, and (c) after plasma treatment and with chitosan deposition [197].

antibacterial activity. In their work, fabrics were firstly pretreated by Ar/O$_2$ DBD plasma for surface activation, then exposed to atmosphere for further oxidization, and finally immersed in chitosan solvents for chitosan grafting. It was found that the modified fabrics not only exhibited strong antibacterial activity against *B. subtilis* and *S. aureaus*, but also shown a good biocompatibility with fibroblasts cells. They also pointed out that the time of plasma pretreatment was the major factor that determined antibacterial efficiency of modified fabrics. In addition, grafting of chitosan onto the surface of woven poly(ethylene terephthalate) (PET) materials and polyethylene (PE) films with air DBD plasma pretreatments was reported by Theapsak et al. [197, 198]. Figure 2.22 presents SEM images of untreated and treated PET surfaces under different conditions. As one can see, no chitosan was incorporated on the raw PET surface (figure 2.22(b)). However, after plasma pretreatment, chitosan was successfully deposited on the PET surface (figure 2.22(c)). The results further confirm the importance of plasma surface pretreatment.

Besides chitosan, many other natural compounds, like nisin peptides, thymol and herbs, have also been grafted onto plasma-treated polymer surfaces to obtain an antibacterial material. Three types of plasma pretreatment, namely nitrogen plasma modification, argon/oxygen plasma modification and plasma-induced grafting of acrylic acid (AA), were used to incorporate nisin peptides onto the surface of low density polyethylene (LDPE) films [199]. It was found that nisin adsorption onto the surface was strongly affected by many factors: type of surface, hydrophobic and hydrophilic interactions, surface charge, surface topography . . . The antibacterial activity of nisin-functionalized films was dominated by distribution and amount of nisin on the surfaces. In general, samples with hydrophilic feature, low electrostatic surface charge, and/or granular structures showed stronger absorption capability of nisin, and exhibited stronger antibacterial activities. One has to keep in mind that general antibacterial efficiency of surfaces should be considered as the combined effect of many factors instead of any single one. Duday et al. [200] used plasma polymerized organosilicon coatings as a reactive layer for the immobilization of nisin onto steel surfaces. In addition to effective bacterial

reduction, the organosilicon-based surfaces were also very stable under several cleaning conditions.

Recently, there has been growing interest in using metal components as antimicrobial agents. In most cases, metal components like silver, copper and zinc in form of ions, nanoparticles, microparticles etc., are adopted because of their pronounced oligodynamic and biocidal activity. Silver-loaded cotton/polyester fabrics with antimicrobial activity were prepared by Kostic et al. [201] by a two-step process: the raw fabrics were exposed to air DBD plasma for surface activation, and then immersed into an aqueous silver nitrate solution for silver sorption. It was demonstrated that both treatment time and aging time strongly affected silver ion sorption of the fabrics. Maximum silver sorption was found 7 days after plasma treatment of the fabrics. Antimicrobial activity of the silver-loaded fabrics was determined after one or two washing cycles with laundry detergent. In spite of a slight decrease after the first washing cycle, antimicrobial activity of the silver-loaded fabrics was stable afterwards. This method was intended to be used in preparation of specific textiles like rubber footwear lining with antimicrobial activity and improved wearing comfort. In addition, a similar method was used to prepare antimicrobial viscose fabrics with incorporation of silver or copper ions using $AgNO_3$ solution and $CuSO_4$ solution respectively [202]. It is interesting to note that water sorption of DBD treated samples exhibited no change after 6 months. Sorption of silver ions increased up to 100% after 7 days aging, whereas that of copper ions decreased with any further aging.

Due to large surface-to-volume ratio and small size, many metal or metal-based nanoparticles, such as silver nanoparticles, copper nanoparticles, gold nanoparticles, and zinc oxide nanoparticles, have merged up as a new generation of antibacterial agent for diverse applications [203–206]. Vu et al. [203] incorporated silver nanoparticle (AgNP) onto the surfaces of polyamide 6.6 (PA) fabrics by a two-step process: raw fabrics were pretreated by an air DBD plasma for surface activation, and then immersed into AgNPs dispersions for AgNPs incorporation. It was confirmed that plasma pretreatment could remarkable increase dispersed AgNPs content on the fabrics surface. Dispersions with three sizes of AgNPs (10 nm, 20 nm and 50 nm) were prepared to study the effect of nanoparticles size on their adsorption in plasma pretreated PA fabrics. It was found that AgNPs in small size exhibited high adsorption in the fiber surfaces. In addition, AgNPs were also incorporated onto cotton textiles with help of CF_4 plasma pretreatment [206]. Plasma treatment preserved the color and mechanical properties of cotton textiles, and stimulated adhesion of silver nanoparticles on the fabric surface due to plasma etching effect. Recently, Taheri et al. [207, 208] developed a sophisticated method to obtain silver nanoparticle based antibacterial coatings, in which AgNPs were capped with mercaptosuccinic acid (MSA) in solvent processes, and then grafted onto an allylamine plasma polymerized (AApp) surface. AgNPs were incorpo-

rated in the plasma polymers by electrostatic immobilization of nanoparticles functionalized by carboxyl acid groups to an amine group rich interlayer prepared by plasma deposition. MSA surfactant could also reduce oxidation rate of AgNPs, and prolong lifetime of functional coatings. Besides effective antibacterial activity, films exhibited no toxicity to primary fibroblast cells and no significant effect on innate immune cell function.

Comparative study of the effect of different plasma pretreatments, air DBD plasma pretreatment and air diffuse coplanar surface barrier discharge (DCSBD) plasma pretreatment, on incorporation of gold nanoparticles (AuNPs) to polypropylene (PP) nonwoven materials were studied by Radic et al. [204]. It was found that DCSBD plasma treatment introduced more hydrophilic functional groups, whereas DBD plasma treatment exhibited more pronounced morphology change of the surface. Compared to grafting of oxygenated functionalities, increase of roughness and "porosity" of the surface, caused by stronger plasma etching was the main reason for a large impregnation of AuNPs on the samples.

2.4.2   Plasma polymerization of antibacterial nanocomposite films

Besides grafting antimicrobial agents to material surfaces, materials with antibacterial activity can also be obtained by deposition of antibacterial nanocomposite films onto material surfaces. Nanocomposite films, with incorporation of antibacterial nanoparticles into a polymerized matrix film, have been developed by various methods. The method of plasma polymerization has been explored and represented as a new but effective approach to induce antimicrobial activity to material surfaces. Nanoparticles can be incorporated by methods like sputtering of bulk metal, on-site reducing of surface attached metal cation, and introducing into plasma phase directly. In general, two types of nanocomposite films have been reported in literature: films with nanoparticles incorporated in the full matrix, and films with multilayer structure.

The first type of nanocomposite films, mostly synthesized by simultaneously incorporating nanoparticles with matrix growth, is characterized by a full spread of nanoparticles in the whole nanocomposite film. Deposition of silver nanocomposite thin films based on organosilicon matrix have been well studied by associating plasma polymerization and simultaneous silver sputtering in a single step process using HMDSO as precursor by Despax et al. [209–215]. In their setup, a silver RF-power electrode was subjected to argon plasma as silver nanoparticle source. Balance between silver sputtering and plasma polymerization was monitored through a pulsed HMDSO mass flow rate. Nanocomposite films with silver content of 0 to 32.5 at.% were obtained under different plasma process conditions. Film properties, like silver content, nanoparticle size and matrix composition, could be controlled through processing parameters, like HMDSO pressure, plasma dissipated

power, and bias voltage [212]. Under certain operation conditions, AgNPs were homogeneously distributed inside the bulk matrix and exhibited as different volume fragments (See figure 2.23). For nanocomposite films with different silver concentrations, the ageing process in saline solution exhibited two different ageing mechanisms: for coatings with low silver contents (7.5 at.%), silver amount decreased at the surface but coating thickness was not changed, whereas for the coatings with high silver contents (20.3 at.%), matrix erosions were observed with silver content reduction [214].
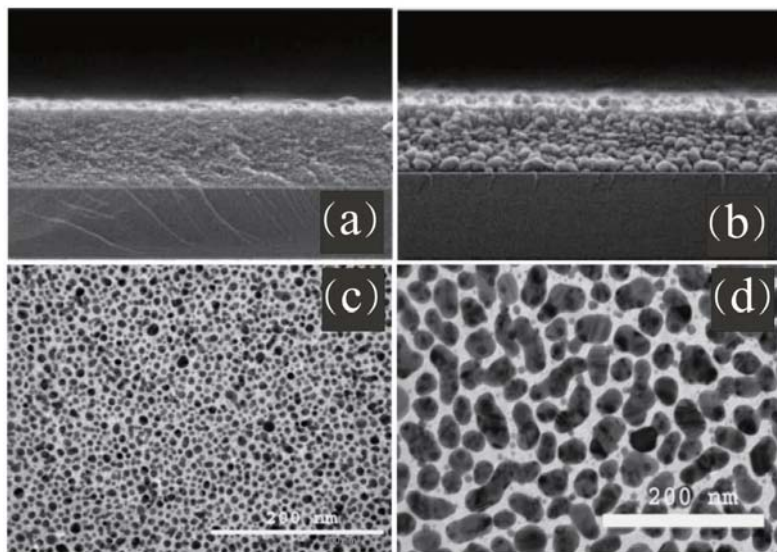
Figure 2.23: (a) and (b) SEM images of the cross section of bulk materials with low and big silver volume fraction, (c) and (d) TEM images of nanocomposite materials with low and big silver volume fraction [209].

Besides organosilicon, functional hydrocarbon was also used as matrix for incorporation of AgNPs to obtain a nanocomposite coating [216–219]. Nanocomposite films were deposited by simultaneously sputtering silver electrode and polymerizing films with CO_2/C_2H_4 or NH_3/C_2H_4 as gas monomers. It was found that silver content, AgNPs morphology and their distribution in the matrix were dominated by parameters like plasma dissipated power, gas ratio and coating thickness [216]. An increase in CO_2/C_2H_4 ratio in the process led to increased silver content but small particles in the coatings. High power input in the process led to increase of incorporated silver content and big size particles in the coatings. In general, the nanocomposite coatings released most bound Ag and yielded an antibacterial burst within the first day when they were immersed in water. They suggested that the release kinetics of silver from these nanocomposite coatings in

deionized water were influenced by silver content, AgNPs morphology and distribution. Meanwhile, the type of monomer mixture, CO_2/C_2H_4 or NH_3/C_2H_4, also affected silver release kinetic property of the nanocomposite coatings [217].

Besides silver, other metals like copper and platinum were also used as sputtering electrodes for the deposition of nanocomposite films [220, 221]. Daniel et al. synthesized an antibacterial nanocomposite of copper containing organosilicon thin film on stainless steels [220]. They suggested that antimicrobial activity was strongly dependent on the incorporated copper content in the nanocomposite coatings.

Electrode sputtering and plasma polymerization can also be spatially separated for deposition of nanocomposite films as suggested by Peter et al. [222]. In their device, silver clusters were generated in a gas aggregation cluster source (GAS), and directed as a focused beam into the downstream plasma region, incorporated into nanocomposite films. The main advantage of this method is the avoidance of complex interference between sputtering (for generation of AgNPs) and plasma polymerization (for the formation of matrix). Therefore, two processes above could be independently controlled. They also pointed out that this system can realize a rapid deposition of composite materials with various metal concentrations.

Additionally, atmospheric pressure plasma jet systems have been used for the deposition of antibacterial nanocomposite coatings, as reported by Beier et al. [223, 224]. Silver nanocomposite films were directly deposited on glass surfaces using an open air plasma jet system, in which HMDSO was fed as organosilicon precursor and silver nitrate solution was sprayed silver source. AgNPs were in situ generated in the plasma region and incorporated into the downstream films. It was suggested that, instead of silver oxide, mainly pure silver nanoparticles were created by the plasma. AgNPs, with various sizes up to about 100 nm, were homogeneously incorporated into the plasma polymers. In washability tests, the nanocomposite films showed a significant removal of loose particles at the first few washing cycles, and then exhibited a diffusion process of silver ions at later washing cycles. The diffusion of silver ions was suggested to contribute long term antibacterial activity. Recently, this method was used for three types of textiles to obtain antibacterial wound dressing materials [224].

As mentioned at the beginning of this section, there is a second approach to obtain nanocomposite antibacterial films, which is based on a multilayer concept, mostly with three layers in a sandwich structure [225–232]. In such structure, antibiotic nanoparticles are enclosed between two polymer layers.

Vasilev et al. [227] developed a tunable antibacterial triple-layer coating based on amine plasma polymer films loaded with silver nanoparticles. As schematically shown in figure 2.24 (a), a 100 nm thick n-heptylamine (HA) plasma polymer film was firstly deposited on substrates, then was loaded with AgNPs which was syn-

thesized by local reduction of silver ions through solvent reactions, and finally covered by another thin layer of HA plasma polymer [227]. The amount of loaded AgNPs was determined by the immersion time of samples in silver nitrate solution, by the time of reduction reactions and by the thickness of the first HA plasma polymer. The release of silver ions from the nanocomposite films could be controlled by the thickness of the second HA plasma polymer. They found that, with appropriate thickness of the second HA plasma polymer, the nanocomposite films were feasible to maintain efficient antibacterial activity and to support the growth of mammalian cells as shown in figure 2.24 (b) and (c) [229].

Besides HA polymers, polymers like polytetrafluoroethylene (PTEE) and organosilicon have also been used to obtain multilayer nanocomposite coatings. Alissawi et al. [225, 226] deposited two layers of PTEE films to immobilize an AgNPs layer, which was deposited on the first PTEE layer by thermal evaporation from an alumina crucible. They found that strong dependence of silver ion release on the particles' size leads to significant redistribution of the composite morphology and suppression of silver ions release with time. Due to the polymer hydrophobicity, the second layer (also known as barrier layer) of PTEE film exhibited insufficient water uptake which made high Ag ions release difficult. Later on, plasma polymerized HMDSO films were used to replace the second layer of PTEE films for nanocomposite films [225]. They suggested that water uptake property of nanocomposite films was strongly dependent on chemistry and thickness of HMDSO coatings. In general, a high Ag ion release occurred in films with
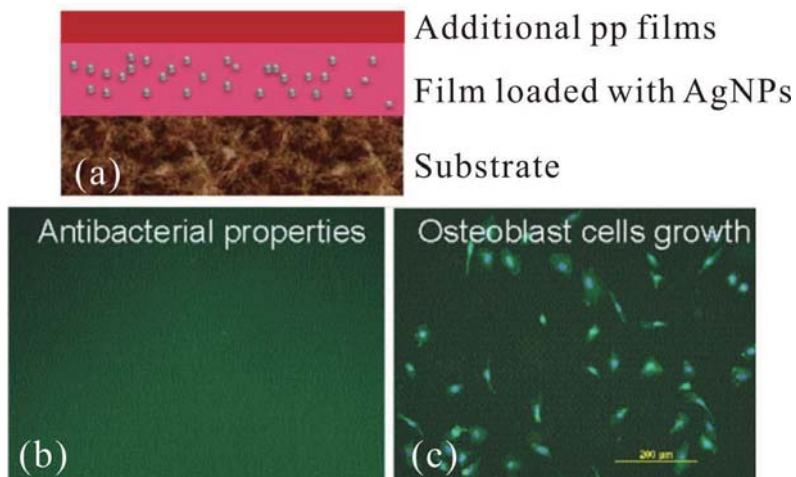
Figure 2.24: (a) Schematic of the multilayer films [227]. (b) Complete inhibition of bacterial adhesion by the nanocomposite films [230]; (c) growth of osteoblastic cells on the nanocomposite films [229].

high oxygen content and small thickness.

Based on multilayer plasma polymers, a type of mechanically responsive bioactive biomaterials was reported by Airoudj et al. [231, 232]. Silver nanoparticles, as antibacterial agent reservoirs in the materials, were trapped between two maleic anhydride plasma-polymer (MAPP) films. They suggested that silver ions were released through diffusion processes over the barrier layer. Tensile strength generated cracks within the plasma polymer overlayer which could be used as diffusive channels for silver ion species. Tailored release of silver ions was achieved by mechanically reversible fragmentation in the plasma deposited polymer top-layer. Release of silver ions was reduced when the material returned to its initial length due to closure of cracks. Additionally, they reported interesting effects of ageing and sterilization methods on these multilayer coatings [230]. It was found that the autoclave sterilization method influenced surface structure significantly, but exhibited no influence on chemical characters. Whereas electron beam sterilization method decreased O/C elemental concentration ratio in the films, but shown no influence on topographic changes. A better antibacterial efficiency against planktonic bacteria was observed for the materials after electron beam irradiation.

2.5 Conclusions

Due to distinguished features, such as achieving strong reactivity without elevation of gas temperature and spatially dividing active plasma region and afterglow region, non-equilibrium plasma jets have received significant attention. As described in this review chapter, numerous non-equilibrium low temperature plasma jets have been designed, analyzed and applied for a broad spectrum of applications in the last years. Many new features of plasma jets, like discharge modes and plasma bullets, have been revealed and been better understood. Although great progress has been made, there are still many challenges and barriers that exist in developments and practical applications of plasma jets, for example the wide use of expensive noble gases and the small dimensions of plasma. Therefore, research on plasma jets sustained by economic molecular gases, like nitrogen or air, and on plasma jets with a relative large dimension are important in the future.

Besides, plasma engineering based on non-equilibrium plasma jets for thin film polymerization and nanocomposite film deposition has emerged and is expected to be an efficient approach over traditional methods. Many interdisciplinary works on plasma engineering with material science and biological science have to be done in the future.

3

Methods for plasma characterization and surface analysis

3.1   Introduction

In this thesis, two atmospheric pressure plasma jet devices have been designed and characterized through various plasma diagnostics. Also, application of the plasma jets for plasma polymerization of organosilicon thin films and of nanocomposite films on flat substrates and non-woven fabrics has been investigated using surface characteristic methods and microbiologic assays. This chapter gives an introductory overview of plasma diagnostics, a theoretical overview of different physical and chemical techniques for surface characterization, and a general introduction of microbiological antimicrobial assays used in this thesis. Operation details and experimental parameters are not given in this chapter, and can be found in corresponding later chapters.

3.2   Plasma diagnostics

In order to evaluate performance of a plasma and to further optimize plasma jets for scientific and practical applications, it is important to investigate plasma features, such as voltage-current waveforms, presented reactive species, gas temperature, electron density, electron temperature, plasma propagation, etc. Those parameters can be obtained through plasma diagnostics, which are a group of methods,

instruments and experimental techniques. Up till now, many diagnostic methods have been developed and utilized for the characterization of plasma jets, including current-voltage measurements, optical emission spectroscopy (OES), mass spectrometry (MS), intensified charged-coupled device (ICCD) imaging methods, laser induced fluorescent (LIF) measurements, absorption spectroscopy (AS), plasma probes, acoustic diagnostic and cavity ring-down spectroscopy. More information about plasma diagnostics can be found in [17, 233–235] and references cited therein. In this section, only the diagnostic methods implemented in this thesis will be introduced.

3.2.1   Optical Emission Spectroscopy

Optical emission spectroscopy (OES), with the advantages of non-invasive, easy to implement and fast measurement, is one of the most used techniques in plasma diagnostics to characterize plasma discharges. Method of OES is passively based on plasma emitted light in UV-visible region. In a plasma, massive collisions of gas-phase particles with electrons excite the particles to higher electronic states. Relaxation of those excited particles to lower energy states leads to the emission of photons. The emitted photon energy is equal to the difference between excited and lower energy state and corresponds to the wavelength of spectral lines. Therefore, OES has been extensively employed to identify excited reactive species and transitions in plasmas. Figure 3.1 depicts prominent emission systems in most nitrogen plasma, which occur due to electransition between the ro-vibrational levels of the triplet states of molecule nitrogen: $C^3\Pi_u$, $B^3\Pi_g$, and $A^3\Pi_u$, where the state A is metastable. Next to that, transitions between ionized nitrogen states are also widely present in a nitrogen-contained discharge.

Besides qualitative analysis, quantitative studies are often conducted with OES, especially for determination of rotational temperature (T_{rot}) and vibrational temperature (T_{vib}) of some reactive molecules or radicals in plasmas. In atmospheric pressure plasmas, rotational temperature T_{rot} has been supposed to be equal to gas temperature (T_{gas}) based on the assumption that molecules in rotational states and surrounding neutral gases molecules are in equilibrium due to the frequent collisions among heavy particles [236, 237]. Gas temperature is one of the most important plasma parameters for application of plasma jets, especially in treatment of thermal sensitive materials, living tissues and biological objects. Spectra comparison between synthetic and experimental rotational spectra bands, mostly NO(A-X), N_2(C-B), OH(A-X) or N_2^+(B-X), is a most used way to estimate gas temperature [238, 239]. Synthetic spectra can be calculated numerically and simulated by programs such as Specair and Lifbase [240–242].

However, it is necessary to note that the assumption above is not always the case for plasmas under conditions in which the Boltzmann distribution of rota-

tional levels is deformed. Non-Boltzmann behavior of OH(A-X) transition has been observed in many plasma jets with a noble gas (He/Ar) as carrier gas [39, 84, 243–245]. Non-Boltzmann vibrational-rotational population of OH radicals in an Ar plasma jet is explained with the different generation mechanisms of excited species with various rotational quantum numbers. OH excitation at low rotational levels would be due to direct electron impact excitation whereas at high rotational levels, the excitation would be due to direct dissociation of water molecules [39]. In such non-Boltzmann conditions, Boltzmann plot method with a two- or three-temperature fitting routine has been applied for the estimation of rotational temperature. The rotational population distribution is approximated by two or three superimposed Boltzmann distributions [246–248]. A two-temperature rotational population distribution of OH(A-X) was observed in a He plasma source, in which the rotational temperature of N_2(C-B) was corresponding to the small temperature parameter [246]. However, distinguished difference between estimated rotational temperatures of N_2(C-B) and OH(A-X), with T_{rot} = 600 K for N_2 and 330 K for OH, was found in an Ar plasma jet by Xiong et al. [249]. This deviation was due to a relatively high rotational distribution of N_2, which was caused by the easy energy transfer from argon metastable Ar(4s) to the ground state nitrogen (N_2(X)) molecules. Therefore, a comprehensive consideration is necessary to obtain a correct gas temperature in a plasma source.
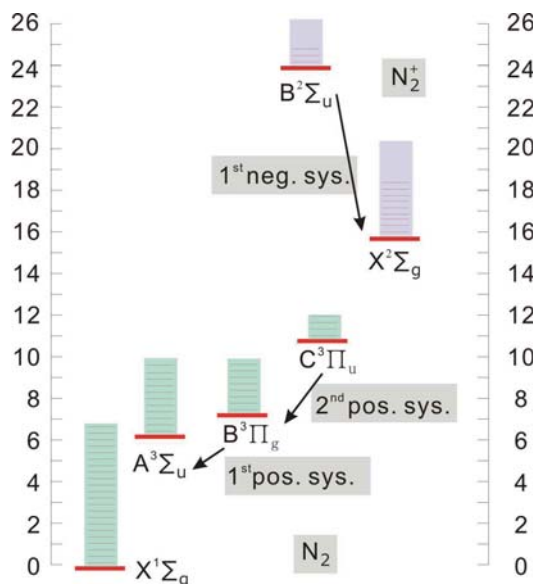
Figure 3.1: Energy level diagram for molecular nitrogen and molecular ionized nitrogen species

Vibrational temperature T_{vib}, which is often used to characterize plasmas containing molecular species, is another important parameter in a plasma. Since population of excited vibrational levels proceeds via electron excitations, vibrational temperature T_{vib} provides a valuable insight into plasma activity, particularly in energy transfer from high-energy electrons to cold heavy species [250]. Thus, vibrational temperature T_{vib}, as an indicative factor, provides useful information on chemical activity of the discharge. Vibrational temperature T_{vib} is readily derived from the (relative) intensity distribution of vibrational bands, which belong to a given electronic transition and differ in vibrational quantum numbers. Spectral bands of N_2(C-B), OH(A-X) and N_2^+(B-X) are often used to determine T_{vib} [251–253].

Besides, other plasma parameters, like electron temperature (T_e), electron density (n_e) or density of reactive species, can also be obtained from OES. Line intensity method, which is based on the intensities of two emission lines of the same kinds of atoms or ions, can be used to calculate electron temperature [254]. Meanwhile, a Boltzmann plot of a series of atomic emission lines is also a good way to obtain electron temperatures [246, 255, 256]. Absolute OES measurement is a useful way for plasma diagnostics under certain conditions. Electron density can be determined using absolute measurements of continuum radiations [257, 258]. Electron temperature of an argon plasma in a DBD plasma jet can be determined by a combination of absolute line intensity measurements with a collision radiative model (CRM) [259]. Besides, broadening of atomic lines is a well-known method to determine electron density [260]. Starking broadening of hydrogen lines (H_α, H_β, H_γ), caused by Coulomb interaction between the light emission atoms and electrons, has been used to estimate electron density (n_e) of the plasma in plasma jets by many groups [235]. It is necessary to note that van der Waals broadening should be taken into account under certain conditions (low electron densities, low gas temperatures, atmospheric pressure) since it is in the same order of magnitude as Starking broadening [261–264]. In addition, concentrations of metastable (Ar(1s5) and Ar(1s3)) and resonant species (Ar(1s2) and Ar(1s4)) in a cold Ar plasma jet were determined by a profile analysis of self-absorption broadening [265].

3.2.2 Mass spectrometry

With the ability to identify and quantify compounds, mass spectrometry (MS) is a well developed and invaluable analytical technique across a broad range of applications in physical, chemical, and biological fields. The intersection of plasma and mass spectrometry has been proven to be a fruitful area and possessing great potential for both scientific and industrial communities. On the one hand, many plasma sources have been implemented as ion sources in mass spectrometry for

different purposes, and enhance performance of mass spectrometers [266]. On the other hand, mass spectrometry has been employed as a powerful tool to characterize plasmas due to their advantages, such as high sensitivity, possibility to identify positive and negative species and possibility to analysis ground state species [267]. Mass spectrometry has been widely used to measure ionic species in capacitively coupled discharges at low pressures up to a few Torr [268–270]. Also, a few mass spectrometric studies have been made for atmospheric pressure plasmas.
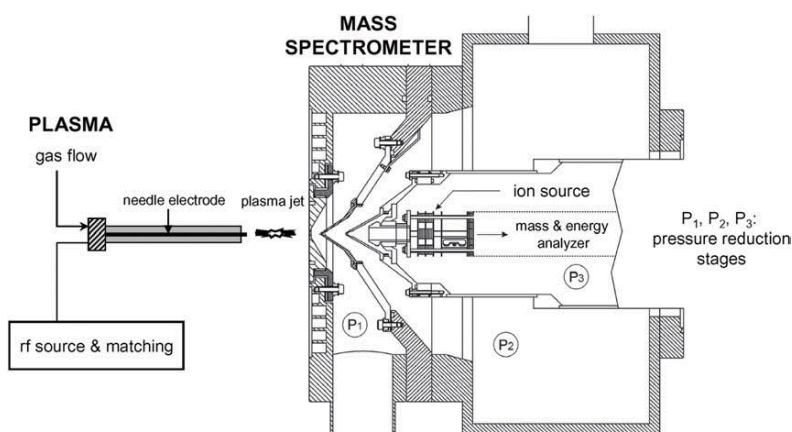
Figure 3.2: A schematic view of the plasma needle and an molecular beam sampling mass/energy analyzer system [275].

Formation and evolution of negative ions in an atmospheric pressure corona discharge in ambient air was analyzed by mass spectrometry [271, 272]. In RF excited atmospheric pressure glow discharges with mixture of helium and water, the positive and negative ion fluxes toward the electrode were investigated as a function of water concentration and discharge power by mass spectrometry [273]. Plasma was generated by a parallel electrode system; using a copper circulate plate as the HV electrode and the inlet plate of a mass spectrometer as the ground electrode.

Recently, mass spectrometry has been used to diagnose plasma jets by simply aligning plasma jets with the orifice of a mass spectrometer with a small distance. Oh et al. measured positive and negative ions in an atmospheric-pressure plasma jet using Molecular beam mass spectrometry [274]. In their experiment, a variation of different traces gases (Ar, N_2, and O_2) was added to the downstream of main helium flow. It was found that ionic composition in the plasma afterglow was strongly affected by those additional gases. Besides, the concentrations of reactive oxygen and nitrogen species (ROS/RNS) in a radiofrequency medical plasma needle were determined by means of threshold ionization mass spectrometry, as

shown in figure 3.2 [275]. Similar method was used to monitor the production of atomic oxygen, ozone and nitrogen in a radiofrequency micro-atmospheric pressure plasma jet [61,276]. A rotating skimmer was used to realize a pulsed gas flow from atmosphere into the pumping system of the mass spectrometer. In all above reports, influence of mass spectrometer on plasma jet, especially afterglows, is not discussed. Moreover, the spatial characterization of afterglows is rarely discussed.

3.2.3   Techniques for temporal analysis

Since plasmas in plasma jets are generated by an external electric field and with the application of a gas flow, development of breakdown and propagation of plasma along the jets are temporal functions of working parameters, such as electric field, and gas flow rate. Therefore, temporal diagnostics of plasma jets are crucially important to understand physical mechanisms of the plasma discharge. Following paragraphs will present an overview on the often used techniques for temporal diagnostics of atmospheric pressure plasma jets.

An intensified charge-coupled device (ICCD) camera is an extremely sensitive and fast imaging device that operates with a very high speed gate (high speed shutter with an integration time as fast as 2 ns) to capture transient phenomena. In the last twenty years, intensified charge-coupled device (ICCD) camera has achieved a great advance and acted as a versatile and powerful diagnostic tool in many fields. In 2005, Teschke et al. firstly reported the discrete nature of plasma propagation in a plasma jet by means of ICCD imaging [35]. They found that plasma afterglow, which appeared continuous to naked eyes, was in fact made up of fast moving plasma volume (also known as plasma bullet). The dynamic properties like propagation velocity (estimated as 1.5×10^4 m/s), shape (donut) and size of the plasma bullets (few mm) were also investigated from the ICCD images. After that, extensive investigations on this new discovered phenomenon have been carried out to reveal mechanisms and properties of plasma bullets in various plasma jets. Influence of working parameters, such as electrode geometry, driven voltage waveform (amplitude and frequency), gas components (He, Ar or their mixture with molecule gases), gas flow rate and surrounding gases, on dynamics and physical properties of plasma bullets has been experimentally studied by ICCD method [17, 86, 277–279, 279–281]. It is interesting to note that a huge difference between plasma bullet velocities of two air plasma jets were reported by Xian et al. [25] and Lacoste et al. [282], with a velocity of 230 m/s and of 4×10^5 m/s respectively. This deviation is probably caused by the different excitation voltage of those two plasma jets. According to Lu et al., plasma bullets are guided ionization waves moving in a thin column of a jet of plasma forming gases expanding into ambient air [283]. Those waves are repetitive and highly-reproducible and propagate along the same path.

Besides fast imaging, ICCD camera has also been simultaneously used as a versatile detector with the combination of other components. A high resolution spectrometry system, by combining an ICCD camera with a monochromator, have been widely used for many purposes, such as recording optical emission for OES method [265], recording fluorescence light for LIF method [284], and recording scattering signals for laser scattering methods (Thomson, Rayleigh and Raman scattering) [285]. A grating-ICCD camera system, which is based on two dispersion gratings and an ICCD camera, was developed to study the time- and space-resolved propagation behavior of excited radicals (OH, N_2, Ar) in an argon plasma jet [249].

With the capability of high sensitivity and ultra-fast response, photomultiplier tubes (PMT) have been widely used with monochromator as a detector to record time resolved emissions at a specific wavelength [286, 287].

3.3   Surface characterization

3.3.1   Scanning Electron Microscopy

Scanning electron microscopy (SEM) is one of the most versatile instruments to reveal morphology and chemical composition of surfaces. According to the resolution criteria from Abbe's diffraction theory, the limit of resolution depends on the wavelength of the illumination source. In the case of light (optical) microscope where visible light is used, the resolution limit is more than 200 nm with a maximum magnification of about 1000 ×. Using a medium with a shorter wavelength than visible light is a straight way to enhance the resolution of a measurement. Invented approximately 50 years ago, SEM has been developed as a mature technique and applied widely in many scientific fields to unveil the surface morphology of samples with a resolution as great as 0.1 nm and a magnification of 500,000 ×.

Typically, SEM operates at a high vacuum environment. An electron beam is generated by a suitable source, accelerated through high voltage, collimated and focused by electromagnetic lenses and scanned across the sample surface by electromagnetic deflection coils. In SEM measurement, interaction of primary electron beam with surface generates signals containing secondary electrons, backscattered electrons, Auger electrons, characteristic X-ray radiation and visible light (see figure 3.3). All those signals can be collected and analyzed to obtain a wealth of information about the sample's properties, including morphology, microstructure and composition.

Secondary electrons (SE), which are produced as a result of incident primary electron beam's interaction with electrons of atoms present in the sample, provide information on the surface topography of the sample. Back-scattered electrons (BsE) are essentially primary incident electrons that turn back from the sample
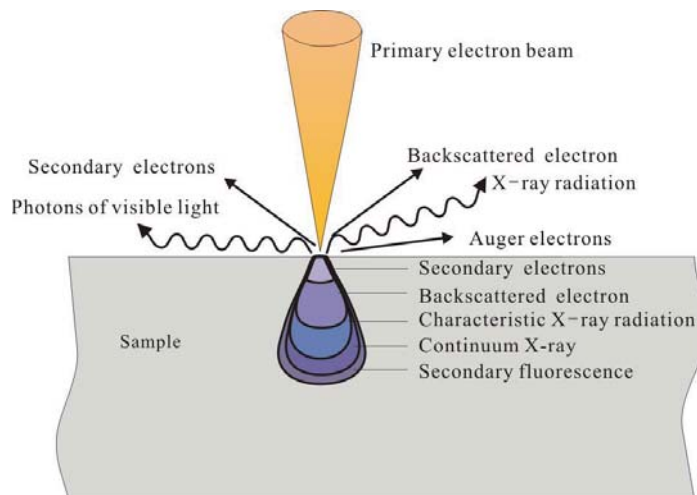
Figure 3.3: Scheme of electron beam-sample interactions in SEM

due to large angle elastic scattering and the large number of scattering events. These BsE provide important information on the topography, crystal orientation and atomic contrast (relative atomic number of the elements) of the sample. X-rays are generated by inelastic collisions of the incident primary electrons with inner-shell electrons of the atoms present in the sample, and have energy characterizing the elements that emitted them. The technique is widely known as energy dispersive X-ray spectroscopy (EDX), which can be used to obtain qualitative and quantitative chemical information about the atoms present in the sample. Light luminescence, which carries information about defect structure, can be collected by photomultiplier and imaged as cathodoluminescence (CL).

In a SEM measurement, limited or non-conductive material samples (such as ceramic, polymers) will accumulate electrostatic charges at the surface when they are scanned by electron beams. Therefore, it is necessary to coat the sample with an ultrathin layer of electrically conducting material, such as gold, gold/palladium alloy, platinum, osmium, iridium, tungsten, chromium, or graphite. These coatings can be easily performed by a plasma sputter coater. In this work, SEM method has been implemented to reveal the surface morphology of nanocomposite coatings. Since two different SEM devices have been used in this thesis, details of SEM settings will be given in the corresponding chapters.

3.3.2   Fourier Transform Infrared spectroscopy

Fourier transform infrared spectroscopy (FTIR) is a sensitive chemical analysis method. Although it is capable of characterizing some inorganic compounds,

FTIR is particularly used for identification of organic chemicals in a whole range of applications. An infrared (IR) absorption spectrum represents a fingerprint of a sample with absorption peaks that correspond to frequencies of vibrations in bonds between atoms of the material. Since different bonds are unique combinations of atoms, no two compounds produce the exact same infrared spectrum. With the ability to offer both qualitative and quantitative analysis, FTIR has been frequently used in polymer science, thin film analysis, petrochemical engineering, pharmaceutical industry, food analysis and so on.

The principle of FTIR spectroscopy is to excite molecular vibrations by exposing a sample to an infrared beam. The measured infrared absorption spectrum corresponds to the vibration spectrum of composing molecules. The vibrational energy (usually expressed as wavenumbers) is determinedly by the molecular composition, such as atoms involved in the bond, nature of the bond (single, double), surrounding atoms (hydrogen bonding), and structure (C=C cis or trans), . When exposed to infrared radiation, molecules in the sample selectively absorb radiation of specific wavelengths which causes the change of dipole moment of sample molecules. Consequently, vibrational energy state of molecules is transferred from ground state to excited states. Frequency of an absorption peak is determined by the vibrational energy gap. Number of absorption peaks is related to the number of vibrational freedoms of the molecule. Intensity of an absorption peak is related to the change of dipole moment and the possibility of the transition of energy levels. Therefore, by analyzing the infrared spectrum, one can readily obtain abundant chemical structure information of a molecule. Most molecules are infrared active except some homonuclear diatomic molecules such as O_2, N_2 and Cl_2 due to the zero dipole change in the vibration and rotation of these molecules. Commonly used range for infrared absorption spectroscopy is 4000 to 400 cm^{-1} because radiation absorption of most organic compounds and inorganic ions is within this region.

Nowadays, attenuated total reflectance (ATR) is the most used FTIR sampling
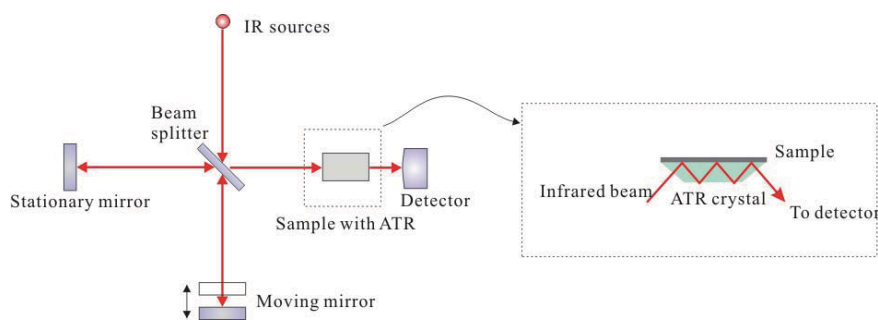
Figure 3.4: Schematic diagram of FTIR-ATR system

tool because it overcomes most challenging aspects in traditional infrared analyses, namely sample preparation and spectral reproducibility. Figure 3.4 is a diagram of a FTIR-TR spectrometer, which commonly consists of an IR light source, an interferometer, a sample compartment, an ATR accessory, a detector, and a computer. The IR source generates radiation which passes through the interferometer and passes through the ATR crystal with a high refractive index (typically germanium, Thallium Bromoiodide, or zinc serenade) where the sample has been contacted. The internal reflectance at the sample surface creates an evanescent wave that extends beyond the surface of the crystal into the sample with a depth of only a few micrometers (0.5 μm - 2 μm). The beam is then collected by a detector as it exits the crystal. Eventually, the signal is transferred to a computer in which Fourier transformation is carried out [288].

FTIR measurement in this work is performed using a commercial BrukerTensor 27 spectrometer purged with dry, CO_2 free air to obtain infrared absorption spectra. The spectrometer is equipped with a single reflection ATR accessory (MIRacleTM, Pike Technologies) using a germanium (Ge) crystal as internal reflection element. The FTIR spectra are recorded using a liquid nitrogen cooled MCT (mercury-cadmium-telluride) detector with resolution of 4 cm^{-1} and are the result of 32 scans.

3.3.3   X-ray Photoelectron Spectroscopy

X-ray photoelectron spectroscopy (XPS), also known as electron spectroscopy for chemical analysis (ESCA), is a well-established quantitative surface technique that is capable of providing elemental and chemical state information from a 5 to 10 nm layer of a solid surface. The principle of XPS is based on the photoelectric effect, a phenomenon discovered by Hertz in 1887 and outlined by Einstein in 1905. In photoelectric theory, the concept of photons is used to describe the escape of electrons from a surface when the electrons absorb energy from electromagnetic radiation with short wavelengths. The emitted electrons are called photoelectrons. In the 1950s, Kai Siegbahn et al. recorded the first high-energy-resolution XPS spectrum of cleaved sodium chloride using a high resolution spectrometer and a Cu Ka X-ray source [289].

As schematic shown in figure 3.5, when an X-ray with a known energy (hν) interacts with an atom on the surface, a photoelectron can be emitted via the photoelectric effect (figure 3.5). Next, kinetic energy (E_k) of the emitted electron is measured. Thus, atomic core level binding energy (E_b) of the atom, which is related to the Fermi level (E_f) of the sample, can be determined using following equation:

$$E_b = h\nu - E_k - \Phi \tag{3.1}$$

Where Φ is the work function of the spectrometer.
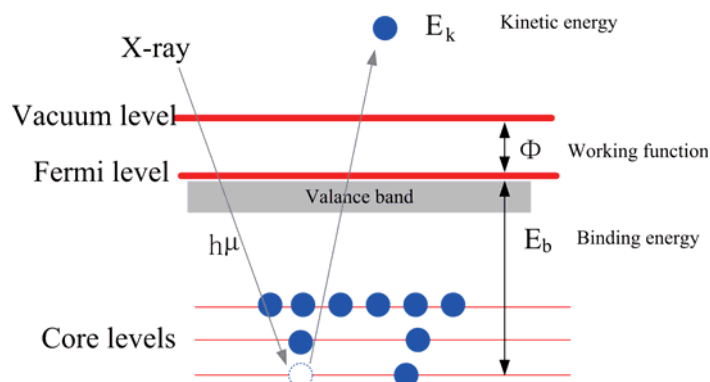
Figure 3.5: Schematic diagram of FTIR-ATR system

Each atom in the surface has core electrons with a characteristic binding energy that is conceptually, not strictly, equal to the ionization energy of the electrons. Different elements that exist on the surface can be determined through identification of XPS peaks at characteristic binding energies. All elements except hydrogen and helium present in samples can be identified. Concentration of each element present at the surface can be quantified by integrating the corresponding XPS peaks. Besides, chemical state of surface elements can be analyzed because the binding energy of an atom is sensitive to the chemical environment of the atom. An increased binding energy will be observed in the core electrons of the atoms when they are bound to strong electron withdrawing groups. Conversely, decreased binding energies will be measured in the core electrons of atoms when they withdraw electrons from their neighboring atoms. Chemical states and concentrations of the surface elements can be found by deconvolution analyses of the corresponding peaks.

It is necessary to keep in mind that, in a XPS measurement, only the top atoms within 10 nm of the surface can be analyzed. The measurement range is the escape depth of the emitted photoelectrons. The emitted photoelectrons underneath that range are scattered by colliding or by interacting with other atoms with loss of energy.

XPS measurements in this thesis are performed on a Versaprobe II system (Physical Electronics (PHI), USA) equipped with a monochromatic Al K X-ray source (hν = 1486.6 eV) operating at 23.3 W. The pressure in the analyzing chamber is maintained below 10^{-6} Pa during analysis and photoelectrons are detected with a hemispherical analyzer positioned at an angle of 45° with respect to the normal of the sample surface. The obtained elements were quantified with Multipak software using a Shirley background and applying the relative sensitivity

factors supplied by the manufacturer of the XPS instrument. C1s spectrum (285.0 eV) was used to calibrate the energy scale. The deconvolution of high resolution peaks were conducted using Gaussian-Lorentzian (G-L ratio is set between 80% to 100%) peak shapes and the full-width at half maximum (FWHM) of each line shape was constrained between 1.3 and 1.8 eV.

3.4   Antimicrobial test
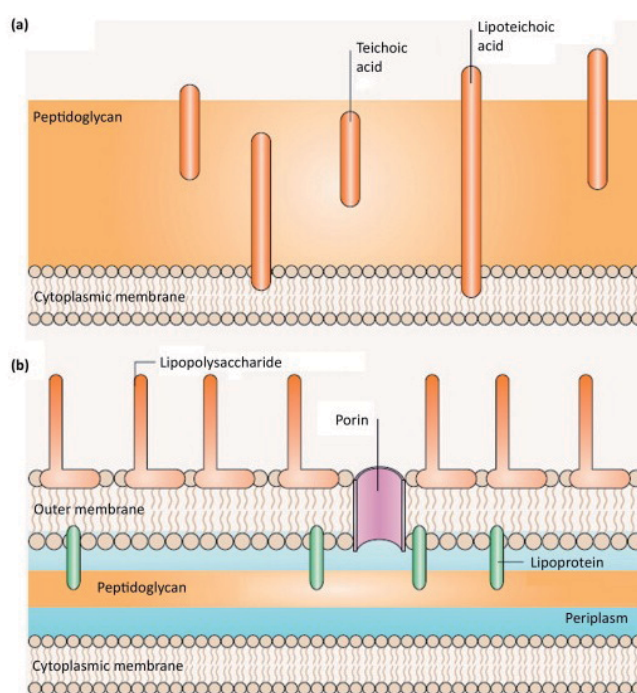
Figure 3.6: Bacterial cell structure: (a) A Gram-positive bacterial cell wall (b) A Gram-negative bacterial cell wall [290].

As one will see in chapter 6 and chapter 7, novel functional materials containing nanoparticles with antibacterial activity are synthesized based on plasma processes. To evaluate bactericide activity, those materials have been tested by method of plate count and method of bacterial growth curve. According to structure, components, and functions of the bacteria cell wall, bacteria can be divided into two main categories: Gram-positive bacteria and Gram-negative bacteria (see figure 3.6) [290]. The wall of Gram-positive cells is composed of a thick and multi-layered peptidoglycan sheath outside of the cytoplasmic membrane. However, Gram-negative cell walls, which are composed of an outer membrane linked by

lipoproteins to thin and single-layered PG, are more complex, both structurally and chemically. In this thesis, antibacterial activity against typical Gram-positive and Gram negative bacteria has been tested due to the fact that both types of bacteria are compared in medical practice.

3.4.1 Plate count method

Plate count method is a conventional and reliable approach to estimate the number of cells present based on their ability to give rise to colonies under specific conditions of nutrient medium, temperature and time. The counting with colony forming units (CFU) assumes that every colony is separated and founded by a single viable microbial cell. It is one of the most used methods to quantitatively evaluate the antimicrobial efficiency of materials against microorganisms. An introduction of the procedure is presented in following paragraphs.

As schematically shown in figure 3.7, the quantitative antimicrobial test in this work is based on an inoculate and recover concept. All experiments are conducted within a laminar flow workstation. Before application of the assay, all samples are sterilized by a 30 minutes UV exposure. The bacterial suspension of 0.5 McF ($\sim$ 1.5×10^8 CFU/ml) for each bacterium is diluted with sterile phosphate buffered saline (PBS) to certain concentrations (10^4, 10^5 and 10^6 CFU/ml in this work). Afterwards, the samples are transferred into the bacterial cultures, and then incubated at 37 ^oC for 24 h. After well vortexed, the suspension which was treated with the films in above test was pipetted out and tenfold serially diluted. At the end, a small volume of each delution was re-plated on three agar plates, which were incubated at 37 ^oC for 24 - 48 h for colony forming counts.
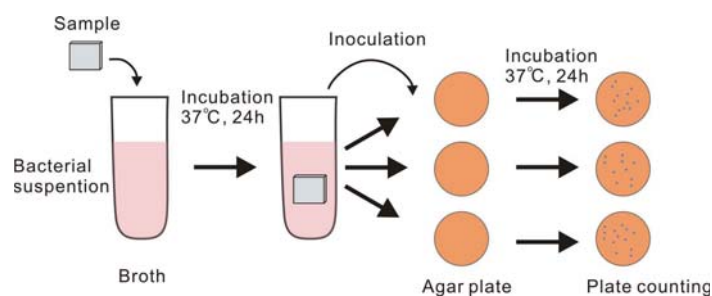
Figure 3.7: Schematic diagram of the protocol of the plate count method in this work

Bactericidal efficiency of the samples against microorganisms is calculated by following formula:

$$R(\%) = \frac{B - A}{B} \times 100\%$$

(3.2)

Where A is CFU per millilitre for the medium with the treated substrate after incubation, and B is CFU per millilitre of the medium with the control samples after incubation.

3.4.2 Bacterial growth curve

Growing in a liquid culture medium, bacteria display a uniform growth curve, as expressed in logarithmic number of bacteria over time. As shown in figure 3.8, a typical bacterial growth curve can be divided into four major phases: lag phase, exponential phase, stationary phase and decline phase. These phases reflect the physiologic state of the microorganisms in the culture at that particular time, and provide a clue to understand the kinetic details of the growth or inhibition [291]. Mostly, three main microbial growth kinetic parameters can be estimated from growth curves as follows: (a) lag time is estimated from the duration of the lag phase, (b) the specific cell growth rate during the exponential growth phase is calculated using:

$$dX(t)/dt = \mu X(t) \tag{3.3}$$

where X(t) is the cell concentration of bacteria in the medium, is the specific growth rate of bacteria (h^{-1}), and t is time (h) [292]. The final cell concentration (C_f) was estimated by optical density at stationary phase as suggested by J. Han, and D. Chung [292, 293].
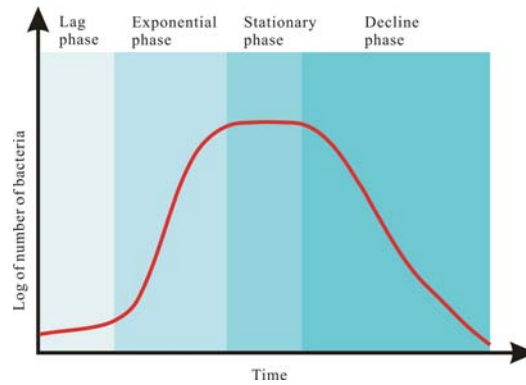
Figure 3.8: A typical growth curve for a bacterial population in a batch culture

In this work, the bacterial growth kinetics in liquid broth was studied using optical density (OD600) of cultured medium, which is often used as a measurement of the cell concentration in a suspension. One piece of specimen was transferred into a culture broth (9 ml), which was inoculated with a volume of *E. coli* (cell concentration of 10^5 CFU/ml) or *S. aureus* (cell concentration of 10^5 CFU/ml)

culture, and then incubated at 37 ^{o}C. The culture was sampled (200 μl) periodically during the incubation period to obtain a microbial growth profile. The optical density of each sampled medium was measured at the wavelength of 600 nm using an UV/Vis photometer (BioPhotometer plus, Germany) to represent the cell concentration of microorganism in the medium.

4

Characteristics of an atmospheric pressure DC plasma jet

4.1 Introduction

As overviewed in chapter 2, numerous non-equilibrium low temperature plasma jets have been developed for different applications. In most cases about generation and sustention of stable plasma jets, noble gases like helium or argon are used to prevent constriction of discharges and the overheating of treated samples. However, use of expensive working gases hinders plasma jet systems from many practical applications. Moreover, molecules gases like oxygen and nitrogen are required to generate important reactive species. Therefore, non-equilibrium plasma jets using nitrogen or air as working gas are extremely attractive. Many reactive species with long life time can be generated in nitrogen plasma jet and air plasma jet: various N_2 metastables, nitric oxide (NO), nitrous oxide (N_2O), ozone (O_3), atomic oxygen (O) and singlet oxygen ($^1O_2$) [294]. Generation of N_2 or air plasma jets with a glow like mode has been discussed by many groups [21, 22, 295]. The role of discharge parameters on stability of plasma jets has been analyzed. In order to generate and sustain a stable plasma jet with nitrogen or air, one must avoid glow-to-arc transitions in the discharge, which can be caused by thermal accumulation or electrical instability. One method to stabilize a plasma is to decrease heating instability of the discharge by high gas flow [296, 297]. In addition, use of DC voltage for excitation of plasma jets is interesting due to use of simple and highly stable external circuits. Glow-to-arc transition of DC discharge can be sup-

pressed by use of an appropriate ballast resistor and work of the plasma jet can be stabilized by continuous removal of heat from the active plasma region using a gas flow.

In this chapter, a stable atmospheric pressure DC plasma jet using nitrogen and air is developed and investigated in terms of plasma properties and generation of active species in active zone and afterglow. Influence of working gases (nitrogen or air) and discharge current on plasma parameters and afterglow properties are studied. Electrical diagnostics show that discharge can be sustained in two different operating modes. Optical emission spectroscopy (OES) is employed to analyze excitation and transition of reactive species in the plasma jet. Gas temperature and vibrational temperature of the N_2 jet in active zone and in the afterglow are determined by means of emission spectroscopy, based on fitting spectra of N_2 second positive system and by the Boltzmann plot method respectively. Spectra and temperature differences between N_2 plasma jet and air plasma jet are presented and analyzed. Spatially resolved distribution of emission intensities of many excited species along the jet axis is described. Space-resolved ozone and nitric oxide densities in afterglow are measured. Ozone density, which is formed in afterglow of nitrogen plasma jet, is quantitatively detected by an ozone monitor. Density of nitric oxide, which is generated only in air plasma jet, is determined by means of mass-spectroscopy.

4.2   Experimental details

The atmospheric pressure DC plasma jet is schematically shown in figure 4.1. The discharge is generated between pin to mesh electrodes inside a quartz tube with an inner diameter of 5 mm. The distance between the pin and the mesh is 14 mm. The anode is made of a fine-meshed metallic grid and placed at the tube outlet. The cathode, which is manufactured from a tungsten rod (diameter 2 mm) with a conically sharpened tip, is connected to the negative polarity of a DC high voltage power supply (Technix) through a ballast resistor (880 kΩ). The discharge current ranges from 5 to 30 mA. A gas flow (nitrogen or air), flowing through the tube by the control of a mass flow controller (MKS PR4000), blows the plasma generated active species and is used to remove the heat and leads to the formation of an afterglow.

The current and discharge voltage are recorded by means of a Tektronix TDS 200 digital oscilloscope with a high voltage probe (Tektronix P6015A). A shunt resistor (100 Ω) is used to measure the electrical current of the system. The optical emission spectrum is collected through fiber optics connected to spectrometers. The overview spectra of discharge and afterglow in the rage of 250 - 800 nm are recorded using an Avantes spectrometer (AvaSpec-2048, resolution 0.5 nm). The high resolution spectra in the range of 300 - 350 nm are obtained with
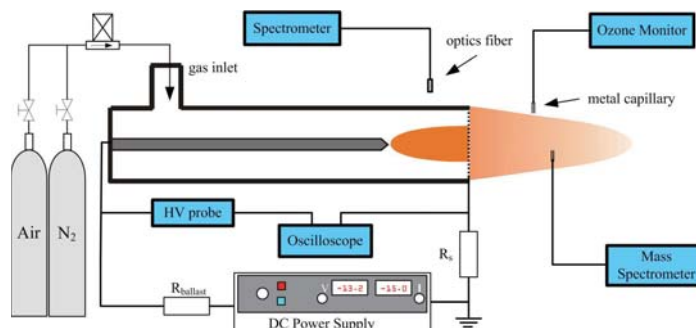
Figure 4.1: Scheme of the DC plasma jet operating in N_2 or dry air

another Avantes spectrometer (AvaSpec-3048, resolution 0.05 nm). Both optical systems are calibrated with a tungsten ribbon lamp and the instrumental function is obtained with an Ar low pressure lamp (Pen-Ray). The ozone generation in the afterglow of the jet is measured with an ozone monitor (Envitec 450). The axial distribution of ozone in the afterglow is detected by changing the distance between the monitor inlet and the anode. The spatial resolution of the system is limited by the size of the inlet and estimated to be 1 mm. Generation of NO by the plasma is measured by a quadrupole mass-spectrometer (Hiden HAL/3F-RC) with a home-made atmospheric pressure inlet system. First stage of the mass-spectrometer inlet system is a capillary that determines the spatial resolution of the measurements of 1.6 mm. To quantify the yield of NO, a known premixed gas mixture of NO/dry air is used to calibrate the mass-spectrometer.

4.3   Results and Discussion

4.3.1   Electrical properties of the discharge

An application of high voltage to the electrodes leads to breakdown of the gas and formation of plasma. The main electron involved reactions in the active zone of N_2 plasma include nitrogen ionization $N_2 + e \rightarrow N_2^+ + 2e$, formation of nitrogen metastables: $N_2 + e \rightarrow N_2(A^3\Pi_u, B^3\Pi_g, C^3\Pi_u) + e$, and electron impact dissociation with generation of atomic N in the states ^4S, ^2D and ^2P (Paschen notation) [298]. Ionization of O_2, $O_2 + e \rightarrow O_2^+ + 2e$, plays an important role in the sustainment of plasma in air. The electron attachment in the three body reactions $2O_2 + e \rightarrow O_2^- + O_2$, with a cross-section of 1.3×10^{-18} cm^2, $O_2 + e + N_2 \rightarrow O_2^- + N_2$, and the reaction of dissociative attachment $O_2 + e \rightarrow O + O^-$ starts to be the main mechanism of electron losses in air plasma [299]. The presence of O_2 results in the generation of atomic oxygen because of the electron impact dissociation reactions Eqs. 4.1 and 4.2, and excited molecular oxygen by the reactions

Eqs. 4.3 and 4.4 [298, 300]:

$$O_2 + e \rightarrow O(^3P) + O(^3P) + e \tag{4.1}$$

$$O_2 + e \rightarrow O(^3P) + O(^3D) + e \tag{4.2}$$

$$O_2 + e \rightarrow O_2(a^1\Delta) + O(^3P) + e \tag{4.3}$$

$$O_2 + e \rightarrow O_2(b^1\Sigma) + e \tag{4.4}$$
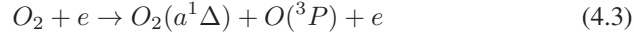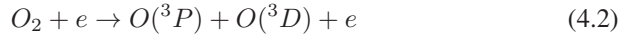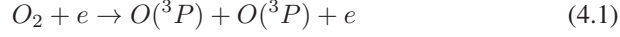
Self-sustainment of the DC jet is determined by equivalence of the ionization and recombination processes, and leads to the current density: $J = n_e e \nu_e$. The average voltage-current characteristics of the N_2 plasma and air plasma are presented in figure 4.2. For both working gases (N_2 and air), there are two operating modes. In the self-pulsing mode the V/I characteristic has a negative slop. A change for slope is observed when the discharge is transferred to the glow-like stable mode at a discharge voltage and current of 4 kV and 10 mA, as shown in figure 4.2. In this stable mode, weak negative slope indicates that the discharge voltage slightly depends on the discharge current for both gases. The sharp increase in current with a slow change in voltage corresponds to the formation of a stable and diffuse plasma without oscillation of the current. The phenomenon of mode changing also has been observed for underwater DC discharge [301]. Both modes are also different in visual appearance.
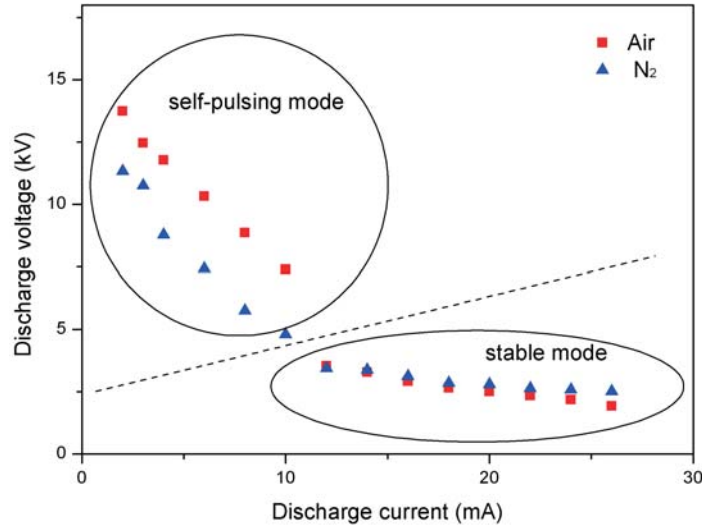
Figure 4.2: Time average voltage/current characteristic of N_2 and air discharge

At low current level (<5 mA), the discharge is sustained in a form of short current pulses with a duration of about 15 ms, as shown in figure 4.3 (a). Since

the voltage-current waveforms of nitrogen plasma and air plasma are similar to each other, only the typical waveforms of nitrogen plasma are presented in figure 4.3. Time-resolved measurement reveals that the voltage applied on the electrodes drops to -12 kV after a slow decline to -4 kV during 4 ms. After a short period of 3-4 ms during which the voltage is constant, it decreases again until the moment when the breakdown stops. The frequency of the regular self-pulsing mode is determined by the RC time of the electrical circuit. Increasing the average current (more than 10 mA) generates a glow discharge with constant current and voltage, as shown in figure 4.3(b).
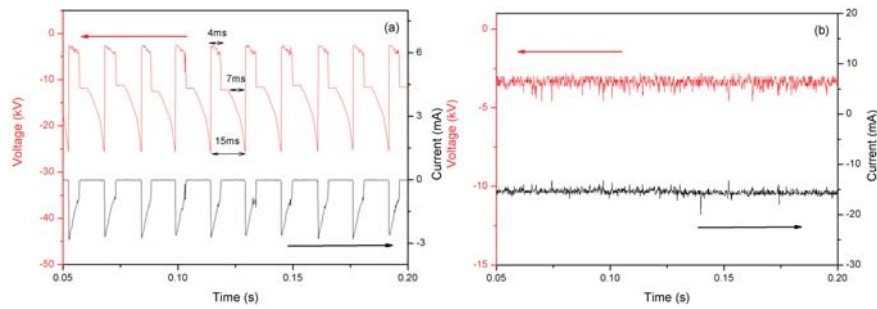
Figure 4.3: Voltage, current waveforms in N_2 plasma in self-pulsing (a) and stable regimes (b) at average current of 5 mA and 15 mA respectively.

4.3.2   Visual view of the plasma jet

In this section, the visual characterization of nitrogen and air plasma jet at various discharge currents and gas flow rates were studied. Images were taken by a Canon 50D digit camera.

Figure 4.4 (a) shows the discharge region of the plasma jet with various discharge currents in nitrogen and air, respectively. The plasma is ignited in vicinity of the electrode tip in nitrogen, and spread towards the anode with rise of discharge current. However, air plasma is directly formed in the whole region at a relatively high threshold voltage and current. As one can see, discharge in both gases at low current is formed by small filaments, which gradually converts to diffused plasma with rise of discharge current. At low average current, discharge consists of a narrow filament with a pink or salmon color and with diameter of 0.1 - 0.3 mm moving around the cathode tip. Current increase to 10 mA results in formation of diffuse plasma with a blue glowing region of 1-3 mm close to the cathode tip. At discharge current of 25 mA, discharge diameter is almost equal to inner diameter of the quartz tube and filaments are not visible anymore. For a gas with a known electron mobility, estimation of the discharge diameter allows us to determine electrons concentration from $J=n_e e \nu_e = n_e e \mu_e E$, where J is the current

density, e is the elementary charge, E is the electrical field in V cm^{-1}, and μ_e is the electron mobility in nitrogen or air. Accordingly, electron density in the active zone of the nitrogen jet is estimated at 1.1×10^{21} m^{-3} whereas it is 0.91×10^{21} m^{-3} in air due to slightly higher electron mobility in air. At low discharge current, expected electron density should be higher because of discharge constriction into narrow filaments. Figure 4.4 (b) reveals influence of flow rate on the discharge region. At low flow rate of 2 slm (1.7 m/s), both discharges are generated in diffuse mode, which is characterized with a relative homogeneous discharge. With increasing flow rate, the plasma column expands and fills the whole tube volume as shown in the figure at 15 slm (12.7 m/s). However, formation of filaments starts to place, especially in N$_2$ when gas flow rate is higher than 10 slm (8.5 m/s).
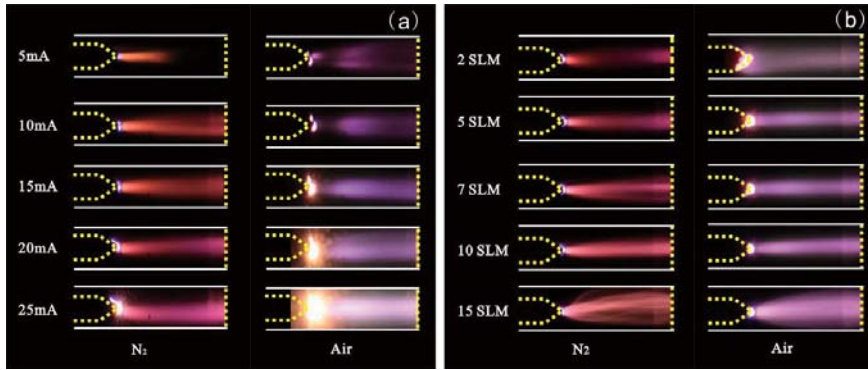
Figure 4.4: Photographs of the discharge region of the DC plasma jet under different conditions: (a) N$_2$ and air discharge at various discharge currents; (b) N$_2$ and air discharge at various gas flow rates.

Because of possible application of the DC jet for remote treatment of different objects and polymers we investigated the influence of gas flow and discharge current on afterglow. Figure 4.5 indicates the afterglow profile depends on gas flow rate, discharge current and gas composition. According to results of emission spectroscopy which will be presented in section 4.3.3, afterglow was formed by N$_2$ metastables from the active region and emission is generated due to collision of excited molecules with surround N$_2$. In general, length of afterglow is longer for the nitrogen plasma jet than for the air plasma jet. Plasma jet afterglows at different discharge currents for nitrogen and air are presented in Figure 4.5 (a). For discharge at low current, afterglow length of nitrogen and air plasma is about 10 mm. With rise of discharge current, it extends to 20 mm and 15 mm for N$_2$ and air jet respectively. Figure 4.5 (b) shows the relationship between gas flow rate and afterglow length. Appearance of pink afterglow at gas flow on N$_2$ up to 10 slm is probably attributed to electronic transitions from high vibrational levels of B$^3\Pi_g$, as well as to the C$^3\Pi_u \rightarrow$ B$^3\Pi_g$ transitions (second positive system of

nitrogen) [302]. Afterglow length is less than 5 mm with 2 slm flow rate for both gases. It grows steadily to more than 20 mm in N_2 jet and 15 mm in air jet with increasing gas flow rate till the moment when laminar regime is transformed into turbulence which is observed at flow rate of about 15 slm. Hence due to intensive mixing with ambient air, afterglow became shorter to about 15 mm and 10 mm in N_2 jet and air jet, respectively.

Figure 4.5: Photographs of the afterglow of the DC plasma jet under different conditions: (a) N_2 and air discharge at various discharge currents; (b) N_2 and air discharge at various gas flow rates.

4.3.3   Diagnostics of the active zone of the discharge

4.3.3.1   Overview of the emission spectra

Diagnostics of the plasma active zone has been carried out by means of optical emission spectroscopy (OES). OES is the most common technique used in plasma diagnostics, especially in the UV-Visible region for determining vibrational and rotational distribution functions of electronically excited states in molecular plasmas [241, 250]. Typical survey spectra between 250 nm and 800 nm in the plasma regions for N_2 discharge and air discharge are shown in figure 4.6 (a) and (b) respectively. The spectrometer used in the measurements is calibrated by standard tungsten ribbon lamps. Both plasmas are generated at 14 mA current, which in-

dicates a stable mode (figure 4.2). In N_2 and air discharge, the emission of the second positive system of the nitrogen molecule ($N_2(C^3\Pi_u \rightarrow B^3\Pi_g)$, 281.4 nm - 497.6 nm), the first negative system of the nitrogen molecular ion ($N_2^+(B^2\Sigma_u \rightarrow X^2\Sigma_g)$, 329.3 nm - 586.5 nm) and first positive system of the nitrogen molecule ($N_2(B^3\Pi_g \rightarrow A^3\Pi_u)$, 503.1 nm - 800 nm) are the main contributions to the spectra. Besides nitrogen vibrational emission, the nitric oxide γ-system ($NO(A^2\Sigma \rightarrow X^2\Pi)$, 250-300.8 nm) is observed only for the plasma in air. In comparison with the N_2 plasma, the emitted intensity from the vibrational transitions $N_2(B^3\Pi_g \rightarrow A^3\Pi_u)$ and $N_2^+(B^2\Sigma_u \rightarrow X^2\Sigma_g)$ is lower in air plasma.
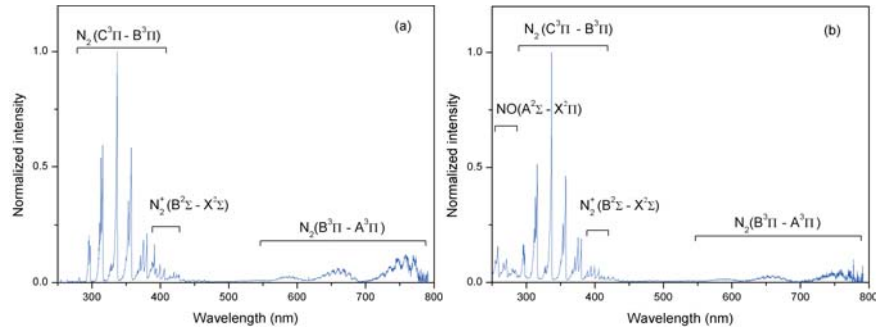
Figure 4.6: A comparison of the emission spectra of DC discharge at air flow and nitrogen flow: (a) Plasma generated by nitrogen discharge at 14 mA; (b) Plasma generated by air discharge at 14 mA.

According to Akishev [22], the vibrationally excited molecules determine the excitation and de-excitation processes in low-current discharge. For the discharge at current greater than 10-15 mA, the energetic electrons and interparticle collision processes play a more important role in the dynamic balance of the charged species and excitation processes in plasma. The intensive N_2 molecular bands in the spectra indicate that discharge generates abundant metastable electronic excited nitrogen molecules and ionized species, such as $N_2(A)$, $N_2(B)$, $N_2(C)$, $N_2(a)$, N_2^+, etc [22, 303, 304]. Due to the relatively low excitation energy (6.17 eV), direct electron impact excitation by reaction Eq. 4.5 and the collisions between vibrational nitrogen molecules by reaction Eq. 4.6 contribute to the population of the excited state $N_2(A)$:

$$e + N_2(X^1\Sigma_g) \rightarrow N_2(A^3\Pi_u) + e \quad\quad\quad (4.5)$$

$$N_2(\nu_1) + N_2(\nu_2) \rightarrow N_2(A^3\Pi_u) + N_2(X^1\Sigma_g) \quad\quad\quad (4.6)$$
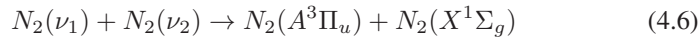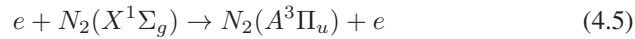
Besides direct electron impact excitation and the collisions between vibrational nitrogen molecules, the excited state $N_2(B)$ is partly populated by the pooling reaction of the metastable state $N_2(A)$. From the spectra of both discharges, the

strongest emission is observed at the second positive system of nitrogen $N_2(C^3\Pi_u$ $\rightarrow B^3\Pi_g)$ which means the mechanism of the excitation process for $N_2(C)$ is mainly the direct electron impact excitation and the pooling reaction of the nitrogen metastable state:

$$N_2(A^3\Pi_u) + N_2(A^3\Pi_u) \rightarrow N_2(C^3\Pi_u) + N_2(X^1\Sigma_g) \qquad (4.7)$$
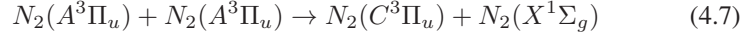
4.3.3.2 Vibrational and rotational temperature measurements

Since chemical properties depend exclusively on the molecular orbital nature, which is modified by electronic excitation created by plasma, population of excited vibrational levels proceeding via electron excitation provides a valuable insight in plasma activity, particularly in energy transfer from electrons to cold heavy species. Thus, vibrational temperature T_{vib}, like an indicative factor, provides useful information on chemical activity of the discharge. Vibrational temperature can be estimated by Boltzmann plot method, which is introduced in following paragraphs.

Theoretically, intensity of the a emission line can be expressed as [305]:

$$I_{v'v''} = h\nu v_{v'v''} A_{v'v''} N_{v'} \qquad (4.8)$$

Where v', v" are used to denote vibrational quantum of upper level and lower level respectively. $v_{v'v''}$ is the wave number of emission, $A_{v'v''}$ is the corresponding Einstein's transition probability, and $N_{v'}$ is the upper level density of the molecule.

Vibrational energy of a vibrational state v is:

$$E_v = \omega_e(v' + \frac{1}{2}) - \omega_e x_e(v' + \frac{1}{2})^2 + \omega_e y_e(v' + \frac{1}{2})^3 + \cdots \qquad (4.9)$$

Where ω_e, $\omega_e x_e$, and $\omega_e y_e$ are vibrational constants [306]. For plasma at local thermal equilibrium, upper level molecules will be populated with a Boltzmann distribution:

$$N_{v'} = N_0 e^{-E'_v/kT_{vib}} \qquad (4.10)$$

WhereE'_v is the rotational energy at vibrational v level, N_0 is atomic density, k is the Boltzmann constant, T_{vib} is the vibrational temperature.

Combining the above three formulas Eqs. (4.8,4.9 and 4.10), one can obtain following equation:

$$ln\frac{I_{v'v''}}{v_{v'v''}A_{v'v''}} = ln(hcN_0) - \frac{E'_v}{kT_{vib}} \qquad (4.11)$$

Therefore, vibrational temperature T_{vib} can be estimated from this function due to the linear relationship between $\ln(I_{v'v''}/v_{v'v''}A_{v'v''})$ and E'_v. Overpopulation of N_2 vibrational degrees indicates a high vibrational temperature (T_{vib}) of N_2 species. Three vibrational bands, $\Delta v = 1$ (1-0, 2-1, 3-2), $\Delta v = -1$ (0-1, 1-2, 2-3), and $\Delta v = -2$ (0-2, 1-3, 2-4) are used in the Boltzmann plot method. Wavelengths and transition probabilities of each vibrational transition are listed in Table 4.1 [307]. A typical Boltzmann plot of relative intensity distribution levels for the second positive system $N_2(C^3\Pi_u \rightarrow B^3\Pi_g)$ is plotted in figure 4.7 (a).

Sequence $\Delta v = v'-v''$	Vibrational transition $v'-v''$	Wavelength λ (nm)	Transition probability $A_{v'v''}(10^6 s^{-1})$
	1 - 0	315.8	10.27
+1	2 - 1	313.5	8.84
	3 - 2	311.5	5.48
	0 - 1	357.6	7.33
-1	1 - 2	353.6	4.61
	2 - 3	349.9	1.46
	0 - 2	394.2	2.94
-2	1 - 3	399.7	4.10
	2 - 4	405.8	3.37

Table 4.1: Vibrational transitions of $N_2(C^3\Pi_u \rightarrow B^3\Pi_g)$ for vibrational temperature [307].

The gas temperature in the active plasma zone (in the interelectrode gap) of the DC plasma jet is determined by analysis of the rotational structure of a nitrogen molecular band in the second positive system, namely the 0-0 vibrational band of $N_2(C^3\Pi_u \rightarrow B^3\Pi_g)$) emission at $\lambda = 337.1$ nm. The synthetic spectrum is calculated by Specair 2.2 program. A typical fitting procedure of the spectra for nitrogen plasma at 12 mA is presented in figure 4.7 (b).

For both air plasma and nitrogen plasma, figure 4.8 shows the results of the gas temperature T_{gas} and the vibrational temperature T_{vib} as a function of the discharge current. The vibrational temperatures T_{vib} for both discharges are much higher than the gas temperatures T_{gas}, which suggest a strong deviation from thermal equilibrium plasma. Compared to N_2 plasma, air plasma has a low vibrational temperature T_{vib} and a high gas temperature T_{gas}. The gas temperature of air plasma is approximately 300 K higher than the one of nitrogen plasma. Considering the high oxygen content of 21 % in dry air, this heating effect is probably explained by a more effective energy transfer from electrons to molecular O_2 through excitation of vibrational and rotational levels of oxygen, which leads to the heating of the gas due to effective energy relaxation processes in the presence of O_2 [308]. Both T_{vib} and T_{gas} strongly depend on the discharge current. T_{gas} is linearly increasing from 1300 K to 2750 K (N_2 plasma) and from 1750 K to 3000 K (air

plasma) at nearly the same slope rate with an increase of the current from 4 mA to 30 mA. T_{vib}, however, presents a nonlinear relationship with discharge current for both discharges. For air discharge, T_{vib} reaches a peak value of 4800 K at 8 mA
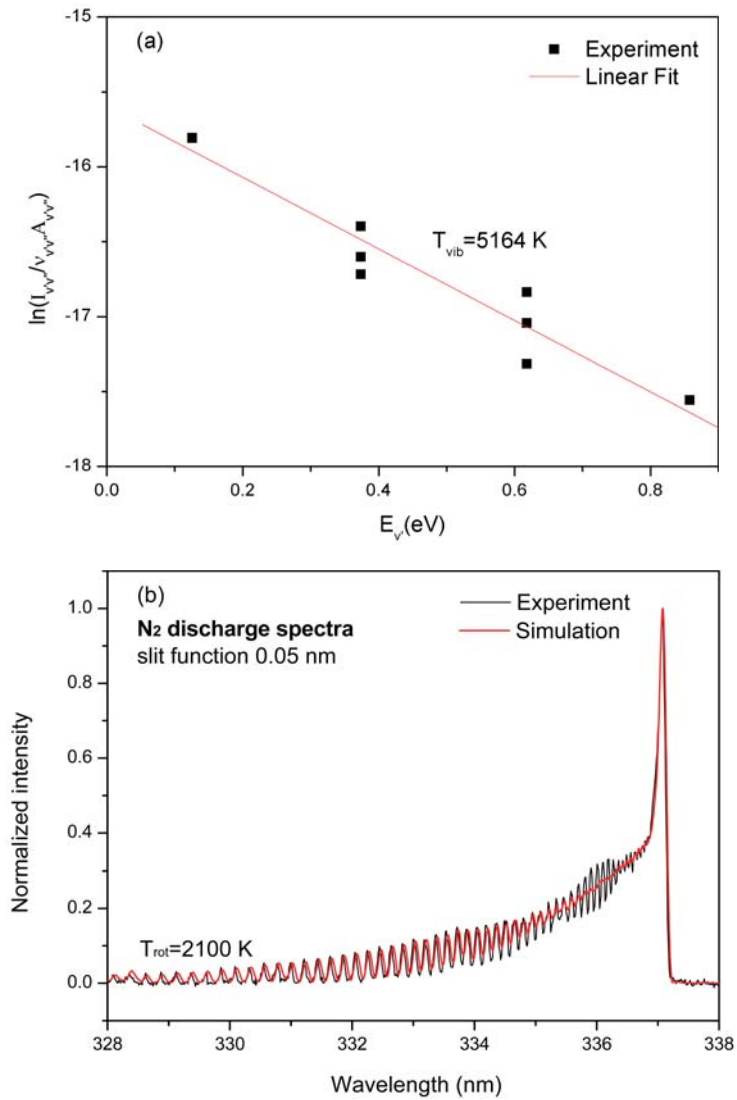
Figure 4.7: (a) Typical Boltzmann plot of N_2 vibrational distribution. Three vibrational band series are chosen: $\Delta v = 1$ (1-0, 2-1, 3-2), $\Delta v = -1$ (0-1, 1-2, 2-3), and $\Delta v = -2$ (0-2, 1-3, 2-4); (b) Determination of gas temperature by fitting procedure of experimental spectrum with calculated spectrum of $N_2(C^3\Pi_u \rightarrow B^3\Pi_g)$. The plasma is generated in nitrogen flow at 14 mA

and slightly drops to 4100 K at the maximum current. In N_2 plasma, the current for maximum T_{vib} (6050 K) is shifted to 10 mA and T_{vib} decreases to about 4800 K at highest current (30 mA). The approach of T_{vib} towards T_{rot} at high current indicates the thermalization of the discharge and the transformation of glow to arc plasma.
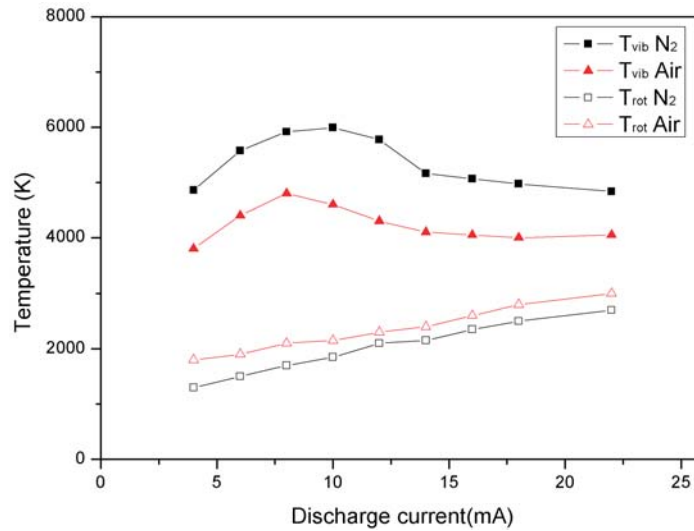
Figure 4.8: Rotational and vibrational temperature in the active zone of the nitrogen and air discharge for different discharge current. Error of T_{vib} is in the range of $\pm$ 200 K and of T_{gas} is about $\pm$ 50 K.

4.3.4   Diagnostics of the afterglow of the DC jet

4.3.4.1   Emission spectroscopy of the discharge afterglow

A distinguished advantage of an atmospheric pressure plasma jet is the fact that the available plasma volume is not limited to the gap between the electrodes. Besides the chemical reactive radicals and the metastable molecules generated in the discharge and blown out, species with long life time, e.g. O_3, can be formed in the afterglow of the jet. Typical survey spectra of the afterglow are presented in figure 4.9. The spectrum of the afterglow of N_2 discharge (figure 4.9 (a)) shows similarities with one measured in the active zone (figure 4.6 (a)), with only a difference in band intensities. On the other hand, a remarkable difference is observed between the spectra of afterglow and the ones of the active zone in air plasma, see figure 4.9 (b) and figure 4.6 (b). The strongest bands of the air jet in the active zone and the afterglow are dominated by the N_2 emission and NO emission respectively. There is no NO emission in the spectra of the N_2 plasma afterglow. The behavior

of the most intensive bands current is presented for both plasmas as a function of discharge current in figure 4.10 (a), (b).
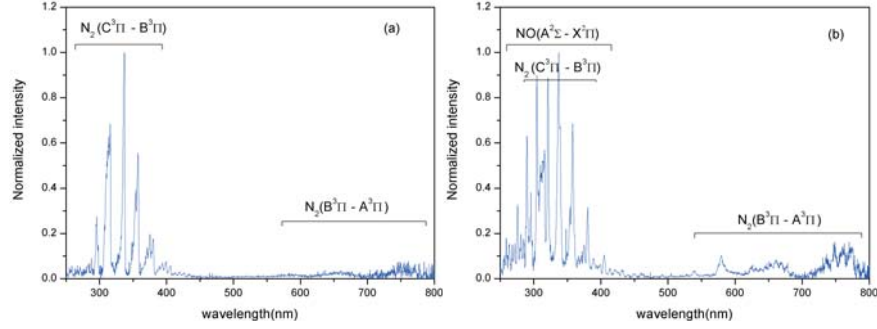
Figure 4.9: Emission spectra of the plasma afterglow (5 mm above the nozzle) of nitrogen (a) and air (b). Plasma generated with discharge current of 14 mA, flow rate is 8 slm.
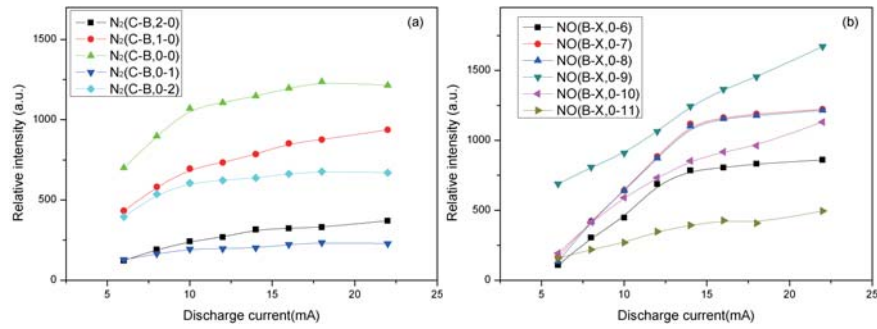
Figure 4.10: The relative intensity of the strongest bands in N_2 (a) and air (b) as a function of the discharge current.

Based on OES results, it can be assumed that the afterglow of the N_2 jet mostly consists of N_2 metastables that are formed in the active zone and transported to the afterglow because of a sufficiently long life time. This is confirmed by figure 4.10 (a), where the non-linear increasing of the bands intensities with increasing of the current correlates with the results of the vibrational temperature measurements in the active zone, see figure 4.8 for N_2 with the maximum of T_{vib} 6050 K around 10 mA current. The main difference between active zone and afterglow of air plasma is the increase of the NO bands intensity in the afterglow of the former. We have to note that the vibrational temperature of the species in the afterglow of the N_2 plasma is higher than in the afterglow of air plasma. The former is about 3600 K at 6 mA, furthermore increases to 4600 K in the current range of 14-18 mA and then drops to 4200 K at 25 mA. At the same time, T_{vib} of air plasma afterglow does

not exceed 1800 K. From a technological point of view for biomedical treatment, the used plasma source has to satisfy requirement of low gas temperature of the afterglow along with the high deviation from thermal equilibrium. The spatial resolved gas temperature measurements have been carried out with 1 cm resolution by the same technique as in part 3.2.2 and the results are presented in figure 4.11 (a) and (b). The temperature of the gas drops down from 2000 K in the active zone to almost room temperature in the afterglow of both plasmas on the distance of 1 cm from the nozzle. This decrease is observed mainly due to the mixing of plasma with surrounding air and due to the heat transfer to the metal grid placed at the end of the nozzle. The decrease of the temperature in air plasma afterglow is smoother, which agrees with a fact that air plasma is closer to thermal equilibrium.
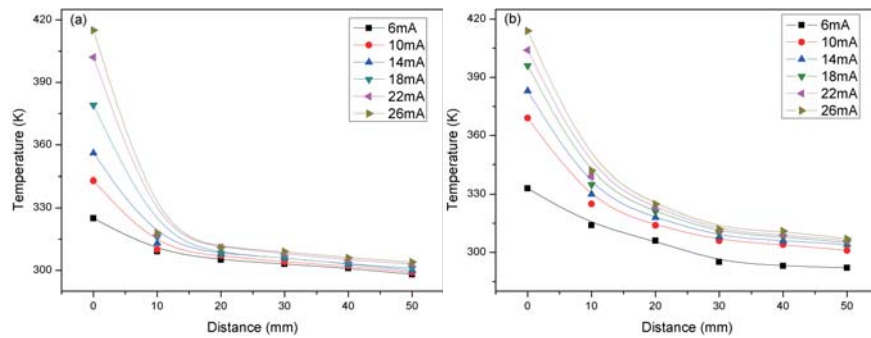
Figure 4.11: Spatial distribution of the gas temperature in the discharge afterglow for (a) N_2 discharge and (b) air discharge. Error of the measurements is about 50 K.

4.3.4.2 Mass-spectroscopy of NO and ozone monitoring
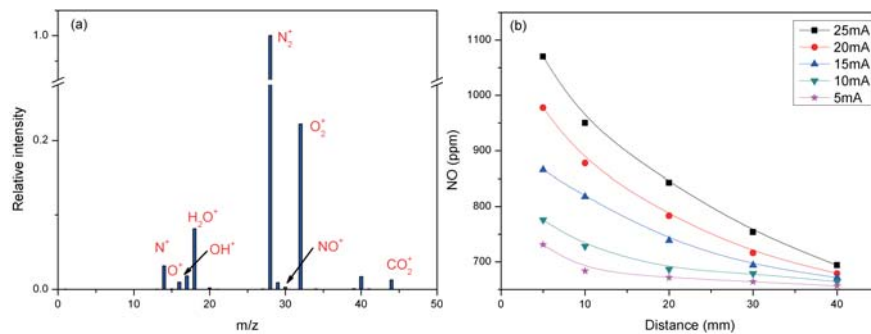
Figure 4.12: (a) Mass-spectra of the air discharge afterglow (discharge current 14 mA); (b) spatially resolved NO measurements along the gas flow as a function of the discharge current.

In the present study, diagnostics of the afterglow have been focused on long living species, especially the two species NO and O_3, which are considered to be important in biomedical applications of plasma jets. For air plasma, the evidence of NO generation in the active zone is confirmed by the emission from the nitric oxide γ-system NO($A^2\Sigma \rightarrow X^2\Pi$) transition in the UV range. NO in the ground state is measured by mass-spectroscopy with preliminary calibration. A typical mass-spectrum of air plasma is presented on figure 4.12 (a), together with spatially resolved NO measurements along the gas flow in the afterglow region, figure 4.12 (b). Mass-spectroscopy shows only one new stable component - NO in the afterglow of the air discharge. The maximal achievable density of NO is about 1080 ppm at a current of 25 mA. NO concentration is decreasing linearly with the decline of the discharge current. The decrease of the NO concentration in the afterglow is mainly explained by dilution of the feed gas as NO is formed in the active zone of the discharge. Nitrogen oxide is not observed in the afterglow of the N_2 plasma even at the highest current of 30 mA. In the discharge area, the electron impact dissociation of N_2 and O_2 molecules leads to the formation of atomic oxygen (reaction Eqs. 4.1, 4.2 and 4.3) and the breaking of the strong bond in the N_2 molecule by vibrational excitation and dissociation. Effective generation of NO in air plasma can be explained by so-called thermal NO through the Zel'dovich reactions [1, 309]:

$$N + O_2 \rightarrow NO + O(^3P) \tag{4.12}$$

$$N_2 + O \rightarrow NO + N \tag{4.13}$$
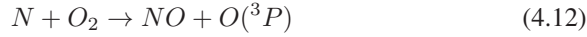
which leads to formation of NO with consumption of atomic N or O. The NO yield has strong a temperature dependence and the NO generation is intensively reduced at $T_{gas} < 2000$ K. NO in the ground state can also be formed in case of non-equilibrium plasma by the reactions Eqs. 4.14 and 4.15 involving atomic nitrogen.

$$O_2(b^3\Sigma) + N \rightarrow NO + O(^3P) \tag{4.14}$$

$$N(^2D, ^2P) + O_2 \rightarrow NO + O(^3P, ^3D) \tag{4.15}$$
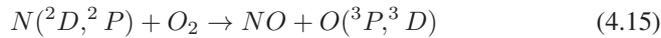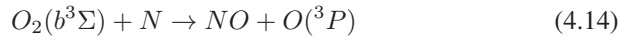
The excited state of NO, on the other hand, is mainly provoked by nitrogen and oxygen metastable states, such as $N_2(A^3\Pi_u)$, $N_2(B^3\Pi_g)$, $O_2(a^1\Delta)$ and $O_2(b^3\Sigma)$ as in reaction 4.16 and 4.17

$$N_2(A^3\Pi_u, B^3\Pi_g) \rightarrow N_2 + NO \tag{4.16}$$

$$O_2(a^1\Delta, b^3\Sigma) + NO \rightarrow O_2 + NO \tag{4.17}$$
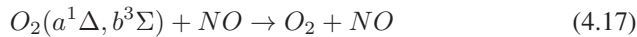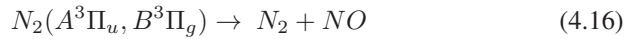
We expect the reason for the absence of NO in the N_2 plasma jet is the low dissociation degree of N_2 in the afterglow due to reaction 4.14. Therefore, the

yield of NO by reactions Eqs. 4.14, 4.16 and 4.17 is negligible. At the same time, generation of NO in the active zone as in air discharge is impossible due to the absence of oxygen. In contrast to air plasma, a high density of O_3 is observed in the afterglow of N_2 discharge. The spatial distribution of O_3 in the afterglow of N_2 discharge is presented in figure 4.13.
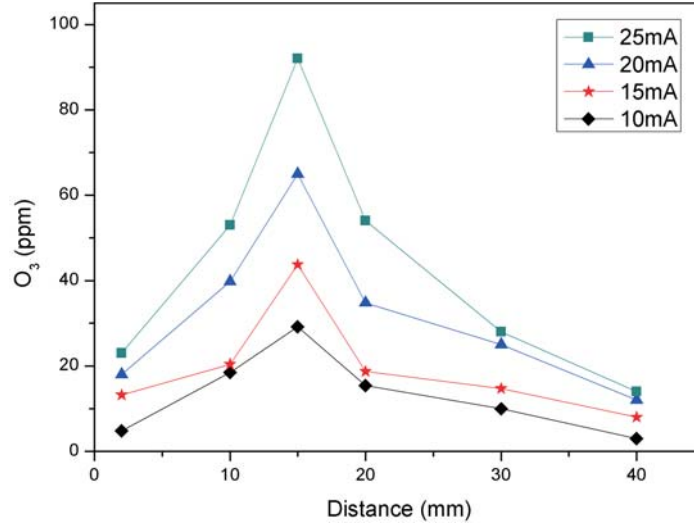
Figure 4.13: The distribution of O_3 along the afterglow as a function of the current for N_2 discharge.

The mechanism of ozone generation at high pressure is dominated by three-body processes, i.e. reactions [304]:

$$O + O_2 + O_2 \rightarrow O_3 + O_2 \tag{4.18}$$

$$O + O_2 + N_2 \rightarrow O_3 + N_2 \tag{4.19}$$
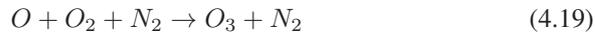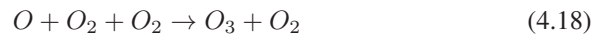
This shows that ozone generation in the plasma mainly depends on the generation of atomic oxygen. The contribution of N_2 discharge to O_3 formation is mostly due to the formation of O atoms by atomic nitrogen and electronically excited nitrogen molecules. According to [300], the contribution of N atoms can take up about 10 % to the total production of atomic oxygen and hence ozone generation. The most significant contribution to the formation of atomic oxygen, and thus ozone, is caused by the reactions of electronically excited nitrogen molecules:

$$N_2(A^3\Pi_u) + O_2 \rightarrow N_2(X^1\Sigma_g) + O + O \tag{4.20}$$

$$N_2(B^3\Pi_g) + O_2 \rightarrow N_2(X^1\Sigma_g) + O + O \qquad (4.21)$$
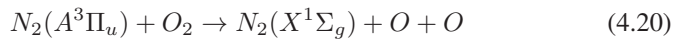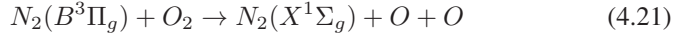
There are two main reasons for the absence of ozone in the afterglow of air discharge. Firstly, a high concentration of nitrogen oxides completely stops the generation of O_3 by means of the discharge poisoning effect, which is related to fast reactions of O atoms with NO by the mechanism O+NO+M $\rightarrow$ NO$_2$+M. When the NO concentration exceeds the threshold value with about 0.1 %, the reaction of atomic oxygen with nitrogen become faster than reactions with molecular oxygen, with the formation of ozone [300]. Secondly, the gas temperature in the active zone of air plasma is too high and thermal dissociation of O_3 starts to play an important role. So, even if ozone molecules already formed in the discharge, they will dissociate.

4.4   Conclusions

A DC plasma jet in N_2 and air flow is investigated in terms of electrical parameters and efficiency of active species generation in afterglow. Depending on discharge current, two modes of plasma sustainment are determined. At low average current I <5 mA, discharge is sustained in self-pulsing regime and at a current higher than 10 mA, plasma behaves as a glow discharge without voltage and current oscillations. Vibrational and gas temperature of the plasma jet are determined from emission spectroscopy for active zone and afterglow. Vibrational temperature T_{vib} of both discharges are much higher than gas temperature T_{gas}, which indicates that the plasmas are far away from thermal equilibrium. As indicated by higher T_{vib} and lower T_{gas}, N_2 plasma shows strong deviation from thermal equilibrium. Use of air (21% O_2) results in decrease of T_{vib} and increase of T_{gas} in comparison with N_2 discharge. It is revealed that T_{vib} and T_{gas} strongly depend on discharge current. For both discharges, T_{gas} is linearly increasing from 1300 to 2750 K (N_2 plasma) and from 1750 to 3000 K (air plasma) with current increase to 30 mA at nearly a same slope rate. However, T_{vib} of both discharges presents a nonlinear relationship versus discharge current. Approach of T_{vib} to T_{rot} at high current indicates discharges thermalization and transfer of glow to arc plasma. Afterglow of N_2 and air plasmas is characterized by gas temperature almost equal to room temperature and still high vibrational temperature (up to 4600 K in N_2 on 5 mm distance from the nozzle). Afterglow emission of the N_2 plasma jet is produced by N_2 metastables. Afterglow spectrum of air plasma jet is dominated by NO emission. Afterglow of the plasma jets is characterized in terms of long living species production - O_3 and NO. NO is only detected in the air plasma jet at concentration up to 1100 ppm (25 mA current) and O_3 is only found in the afterglow of the N_2 plasma jet. Absence of NO in the N_2 plasma jet is because of the low dissociation

degree of N_2 molecules in the afterglow. Absence of O_3 in air jet is expected to be caused by two reasons: high concentration of NO in the air plasma completely stops O_3 generation by means of discharge poisoning effect and thermal dissociation of O_3 starts to play an important role due to high gas temperature of active zone.

5

Plasma polymerization of organosilicon films using the DC plasma jet

5.1 Introduction

Nowadays, considerable attention has been given to plasma polymerization of silicon-inorganic and silicon-organic films due to their wide applications as functional coatings for packaging, biomedical materials, optical components, et al. [310, 311]. Generally, plasma deposited films are characterized as amorphous, insoluble, highly cross-linked, highly heat and corrosion resistant and very adhesive to different substrates [312]. Compared to low pressure processes which are costly and difficult to process batchwize, atmospheric pressure processing provides advantages of elimination of vacuum equipment, ability of integration for industrial production, and high deposition rates [313]. Atmospheric pressure plasma jet process for thin-film deposition is particularly attractive, and such plasma process can deposit thin-film coating without reactor chamber size limitations, can provide treatment for 3D objects can avoid influence of substrate on plasma.

There are substantial works on deposition of diamond-like films using DC plasma jets [314, 315]. However, few works have been reported on the deposition of silicon-containing films using a DC plasma jet, even less work using plasma jet with nitrogen. This can be explained by the fact that DC discharge at atmospheric pressure inclines to transfer from glow discharge to arc [22]. This arc results in

very high temperature and hence hinders application of DC jet for heat-sensitive materials. As shown in chapter 4, an atmospheric pressure non-equilibrium nitrogen/air plasma jet driven by DC power has been designed and characterized with strong plasma region and low temperature afterglow by continual removal of heat from the active plasma region using gas flow and by stabilizing glow-to-arc transformation using ballast resistors. This characterization indicates the great capability for efficient plasma polymerizations on thermal sensitive materials. Therefore, it is interesting to investigate plasma polymerization process of the DC plasma jet.

$$\text{H}-\underset{\underset{\text{CH3}}{|}}{\overset{\overset{\text{CH3}}{|}}{\text{Si}}}-\text{O}-\underset{\underset{\text{CH3}}{|}}{\overset{\overset{\text{CH3}}{|}}{\text{Si}}}-\text{H}$$
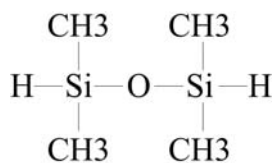
Figure 5.1: The chemical structure of TMDSO which is the organosilicon precursor in the plasma process

In this chapter, research on deposition of silicon-containing films by atmospheric pressure nitrogen DC plasma jet using tetramethyldisiloxane (TMDSO) as gaseous precursor is presented. Chemical structure of TMDSO is presented in figure 5.1. Properties of obtained coatings will be discussed in detail using profilometry, Fourier transform infrared spectroscopy (FTIR) and X-ray photoelectron spectroscopy (XPS). The chapter is organized as follows: after description of experimental details in section 2, presentation and discussion of experimental results related to different working conditions is presented in section 3. Finally, section 4 presents a summary of the presented results.

5.2 Experimental details

5.2.1 Experimental set-up

Schematic diagram of the plasma deposition system is shown in figure 5.2. It comprises the DC plasma jet as described in chapter 4 and placed within a cylindrical chamber. Plasma is generated between a pin and a fine-meshed metallic grid inside a quartz tube with an inner diameter of 5 mm. The cathode, which is manufactured from a 2 mm tungsten rod with a conically sharpened tip, is connected to the negative polarity of a direct current high voltage power supply through a ballast resistor. By switching on an electric field between these two electrodes, the plasma is ignited. A nitrogen gas flow flowing through the tube blows the active species as well as heat through the mesh outside the tube leading to the formation of an afterglow.
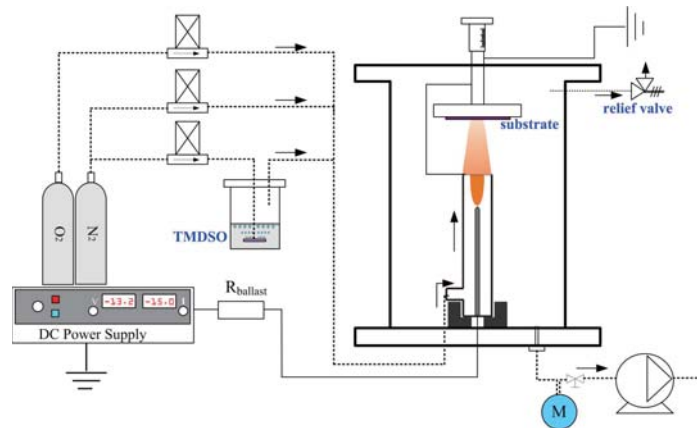
Figure 5.2: Schematic diagram of the deposition system with an atmospheric pressure DC plasma jet.

The substrate, which is a silicon wafer with a size of 10 mm $\times$10 mm and a thickness of 523 μm, is placed on the adjustable sample holder. The distance between the mesh and the substrate is kept constant at 10 mm. Actually, thermal sensitive polymers, such as PP and PET, have also been used as substrates and successfully been deposited with organosilicon films as depositing on silicon. To simplify the experiment and measurement, only silicon wafer are used as substrates in this chapter.

After introduction of the substrate, the chamber is pumped down to 0.1 kPa by a rotary vane pump and then filled with nitrogen to a pressure of 101 kPa. A continuous nitrogen flow remains during the deposition process while the pressure in the chamber is maintained at atmospheric pressure by a relief valve. Once atmospheric pressure is reached, TMDSO, which is vaporized by passing nitrogen through a bubble system at a temperature of 18 ^{o}C, is added to gas flow. The total nitrogen gas flow of the jet is maintained at 7000 sccm. The deposition is carried out with different oxygen and precursor mixtures: the precursor is kept constant by a fixed diluting nitrogen flow rate of 5 sccm, while the oxygen flow is varied between 0 and 60 sccm (0-8571 ppm) to study the influence of oxygen addition on the deposition process. The amount of TMDSO, which can be calculated by taking into account the vapor pressure of the precursor, is 0.9 sccm (129 ppm) in the gas flow. The ratio O_2/TMDSO thus varies from 0 to 66. The diluting nitrogen gas flow was limited to 5 sccm to prevent possible formation of microparticles in the gas phase. It is known that a high concentration of precursor leads to gas phase nucleation resulting in a decrease in film quality and film uniformity [141]. In this chapter, the process is carried out with a discharge power of 18 W, 22.5 W, and 30 W.

5.2.2 Film characterization

A mechanical profilometer Dektak 150 from Veeco is used to measure the thickness of the deposited films. In order to obtain the thickness, substrates are partially masked before the deposition process. After deposition, the height difference between the deposited and non-deposited region gives the thickness of the films.

The chemical structure of the deposited films is obtained using Fourier transform infrared spectroscopy (FTIR). The commercial spectrometer is employed as introduced in section 3.3.2. The FTIR spectra shown in the chapter are ATR corrected for the wavelength dependence of the penetration depth and are normalized on the Si-O-Si peak at 1020 cm^{-1}.

X-ray photoelectron spectroscopy (XPS) is performed for characterization surface chemistry of deposited films as described in section 3.3.3. The pressure in the analyzing chamber is maintained below 10^{-7} Pa during analysis and the diameter of the analyzed area is 100 μm. Survey (0-1100 eV) and high resolution spectra are recorded at a pass energy of 117.4 eV and 29.35 eV respectively.

5.3 Results and discussion

5.3.1 Film measurement

Before discussing the actual film thickness results, it is important to mention that the films deposited in this work are solid films presenting interference fringes. In addition, no white powder agglomerations have been observed on the samples. Due to the relationship of thickness with the physical film properties, film thickness is a very important parameter in several applications [316]. Figure 5.3 shows the development of thickness as a function of processing times for the deposited films at various oxygen flow rates and discharge powers. The data clearly show a linear correlation between deposition time and film thickness, which is in accordance with the work by Morent et al. [138] and Yang et al. [171]. By linear analysis, the deposition rates can be estimated from the slope of the regression lines and the results are presented in Table 5.1. The coefficient of determination R^2 indicates that the regression lines fit the data well.

As shown in Table 5.1, the deposition rate is estimated at 172 nm/min when the process is carried out in a pure nitrogen atmosphere. The introduction of 20 sccm oxygen to the nitrogen atmosphere significantly accelerates the deposition rate up to 352 nm/min. A further raise in O_2 content to 60 sccm increases the deposition rate to 444 nm/min. This increasing deposition rate will be explained in the following paragraph. Due to electron impact collision and ionization of the added oxygen, substantial oxygen metastables and oxygen atoms are generated in the plasma region. Moreover, it has also been shown that the density of electrons present in the discharge increases with increasing oxygen content [317]. These oxygen metasta-
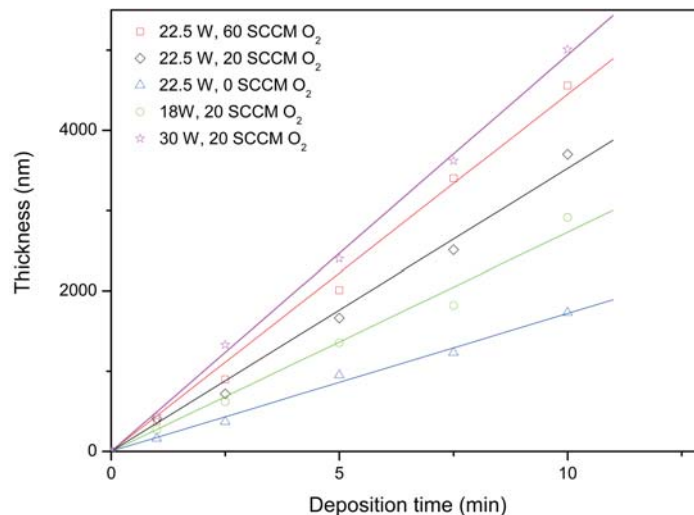
Figure 5.3: Film thickness as a function of deposition time for various working parameters.

bles, oxygen atoms and electrons can react with the monomer leading to a more pronounced monomer fragmentation and intensive formation of active species at higher oxygen amounts [171] which can result in a higher deposition rate.

According to the data shown in Table 5.1, the discharge power of the plasma jet also has a significant influence on the deposition rate. The deposition rate is only 273 nm/min for a discharge power of 18 W, but this deposition rate increases to 352 nm/min for a discharge power of 22.5 W. An even higher deposition rate of 494 nm/min is achieved at the highest discharge power (30 W). These results clearly show that an increasing discharge power accelerates the deposition process. A higher discharge power, which is caused by an enhanced electric field, results in an increasing electron density and thus a higher number of collisions between electrons and TMDSO. As a result, more radicals are formed in the gas phase,

Oxygen (sccm)	Power (W)	Deposition rate (nm/min)	R^2
0	22.5	172	0.9933
20	22.5	352	0.9921
60	22.5	444	0.9955
20	18	273	0.9860
20	30	493	0.9985

Table 5.1: The deposition rate and coefficient of determination R^2 of the regression lines for various oxygen flows and discharge powers.

which can initiate the polymerization processes and thus result in higher deposition rates. The higher deposition rate at higher discharge power could also be partly due to a small expansion of the plasma region at higher powers. This expansion increases the TMDSO residence time in the plasma zone which can result in a higher degree of TMDSO conversion.

The deposition rates obtained here can be compared with the ones acquired by other researchers performing TMDSO plasma polymerization. For example, Huang and Yu [318] measured a film thickness of approximately 750 nm after a deposition time of 25 min, suggesting a deposition rate of 30 nm/min. On the other hand, very large deposition rates up to 1000 nm/min have been observed by Nowling et al. [319] in an atmospheric pressure RF discharge. Other deposition parameters like deposition area, precursor amount, should however be taken into account to enable an objective comparison between the deposition rates of various plasma deposition systems.

5.3.2 FTIR measurement
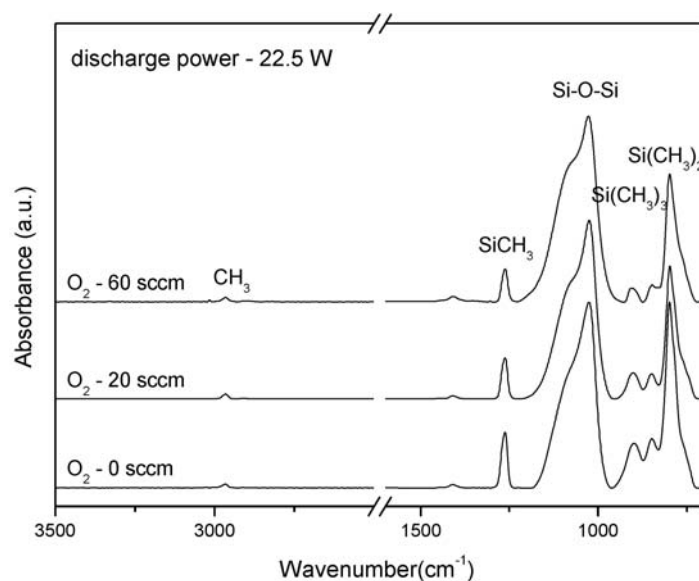
Figure 5.4: FTIR spectra of films deposited by the DC plasma jet at various oxygen flows.

The chemical structure and the chemical bonds present in the deposited films are examined by FTIR spectroscopy. Large differences can be found in the chemical composition of the deposited thin films by infrared absorption spectra. The FTIR spectra of the films deposited with various oxygen flow rates (0 sccm, 20 sccm and 60 sccm) are shown in figure 5.4. This figure clearly shows that the deposited

films exhibit strong absorption bands at 2965 cm^{-1}, 1260 cm^{-1}, 1020 cm^{-1}, 850 cm^{-1} and 800 cm^{-1}. The absorption band at 2965 cm^{-1} is due to CH$_3$ symmetric and asymmetric stretching vibrations while the absorption band at 1260 cm^{-1} can be attributed to CH$_3$ deformation vibrations and symmetric bending in Si-CH$_3$ groups [158, 320]. The strongest absorption band around 1020 cm^{-1} is caused by Si-O-Si asymmetric stretching vibrations [135, 148]. The absorption band at 850 cm^{-1} indicates Si-C stretching vibrations [158, 174]. The absorption band at 800 cm^{-1} can be assigned to CH$_3$ stretching vibrations and rocking vibrations in Si-(CH$_3$)$_2$ groups [320]. Bands at 800 cm^{-1}, 850 cm^{-1}, 1260 cm^{-1} and 2965 cm^{-1} thus indicate the retention of methyl groups in the deposited films. The organic/inorganic characteristics of the deposited films can be evaluated by means of FTIR. It has been shown in [321] that the absorption peak integral of methyl deformation vibrations in Si-CH$_3$ at 1260 cm^{-1} is an indicator of bonds correlated with carbon containing groups in the film. The absorption peak of Si-O-Si stretching vibrations at 1020 cm^{-1} is considered as a reference. A parameter, i.e. a relative ratio r(SiCH$_3$)representing the organic content of the deposited films can be calculated by the following equation [322]:

$$r(SiCH_3) = \frac{\int SiCH_3(1260cm^{-1})}{\int SiOSi(1020cm^{-1})} \tag{5.1}$$

The FTIR spectra in figure 5.4, which show the chemical changes of the films with oxygen flow rate, indicate different film formation processes during deposition. When deposition is carried out in pure nitrogen, the film shows strong absorption bands at 1260 cm^{-1} and 800 cm^{-1}, which can be attributed to CH$_3$ deformation vibrations, symmetric bending in Si-CH$_3$ groups and Si-C stretching vibrations and Si-CH$_3$ rocking vibrations in Si-(CH$_3$)$_2$ respectively. The introduction of oxygen (20 sccm) into the nitrogen atmosphere decreases the two above mentioned absorption peaks. In addition, the absorption peak at 850 cm^{-1} which is due to Si-C stretching also decreases. Based on these FTIR spectra, the ratio r(SiCH$_3$) can be calculated for different oxygen concentrations. This ratio is 0.065 in the pure nitrogen discharge and decreases to 0.048 and 0.032 when 20 and 60 sccm oxygen are respectively added to the nitrogen gas. This result thus clearly indicates that the deposited films have a lower carbon content when oxygen is added to the plasma phase. The reduction in silicon-carbon bonds is mainly due to the fact that oxygen addition urges the fragmentation of monomer molecules and increases the oxidation reactions in the deposition process. According to Lin et al. [321], the shape of the absorption band around 1020 cm^{-1} reveals the subtle relationship between oxygen and silicon contents: while the FTIR spectra of oxygen-rich films show a band shift towards higher wavenumbers, the oxygen-poor films have an absorption band at lower wavenumbers. This conclusion is in accordance with the results obtained in this work: the Si-O-Si peak is located at 1024 cm^{-1} after pure

nitrogen deposition, while it shift to higher wavenumbers (1026 cm^{-1} at 20 sccm oxygen deposition and 1034 cm^{-1} at 60 sccm oxygen deposition), indicating the formation of an oxygen-rich film at higher oxygen amounts.

Figure 5.5 shows the FTIR spectra of films deposited at various discharge powers (18 W, 22.5 W and 30 W) with a constant oxygen flow rate of 20 sccm. The absorption bands mentioned in the previous paragraph are also presented in the FTIR spectra of the films deposited at various plasma discharge powers. When the discharge power is increased from 18 W to 22.5W, the absorption bands at 1260 cm^{-1} and 800 cm^{-1} due to methyl deformation vibrations, symmetric bending in Si-CH$_3$ groups and Si-C stretching vibrations respectively, clearly decrease. However, a further increase in discharge power shows a negligible change of the above mentioned absorption bands. The ratio r(SiCH$_3$) has also been calculated for the FTIR spectra shown in figure 5.5 and is was found that this ratio decreases from 0.094 at 18 W to 0.048 at 22.5 W and 0.046 at 30 W. This result thus indicates a decrease in carbon content with increasing discharge power. Based on figure 5.5, it was also found that the Si-O-Si peak shifts to higher wavenumbers when the discharge power is increased showing that the films contain a higher oxygen content at higher discharge powers.
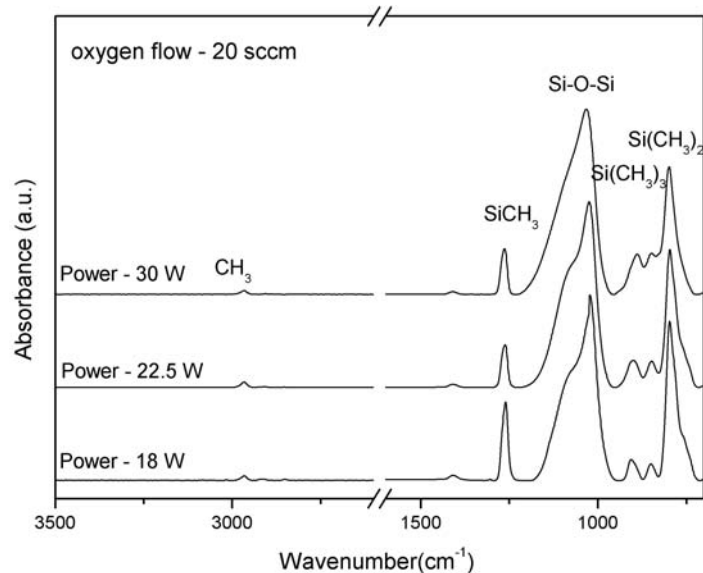
Figure 5.5: FTIR spectra of films deposited by the DC plasma jet at various discharge currents.

5.3.3   XPS measurement

Chemical bonds that are present in the thin films can be qualitatively analyzed using FTIR spectra. However, the limitation of FTIR in quantification and the co-existing of different bonds at similar wavenumbers require further investigation. Therefore, besides FTIR, XPS measurements have been carried out to quantify the chemical composition of the deposited films. Low-resolution XPS survey spectra are acquired to reveal information on the relative amounts of elements present in the films. As shown in a typical spectrum in figure 5.6, survey spectra indicate that oxygen (O), carbon (C) and silicon (Si) are present in the films, while no nitrogen (N) can be found on the deposited films. The absence of nitrogen in the film is in close accordance with the results obtained by Massines et al [323]. These researchers have examined the plasma polymerization of hexamethyldisiloxane in a nitrogen discharge containing different amounts of oxidizer gas (N_2O). An incorporation of nitrogen in the deposited films has only been observed in the absence of the oxidizer gas. In the experimental set-up, a small amount of molecular oxygen is always present in the discharge since it is very difficult, if not impossible, to ensure that the deposition process occurs in a completely air-free environment. This oxygen presence will inhibit the incorporation of nitrogen, which can explain the absence of nitrogen in the deposited films.
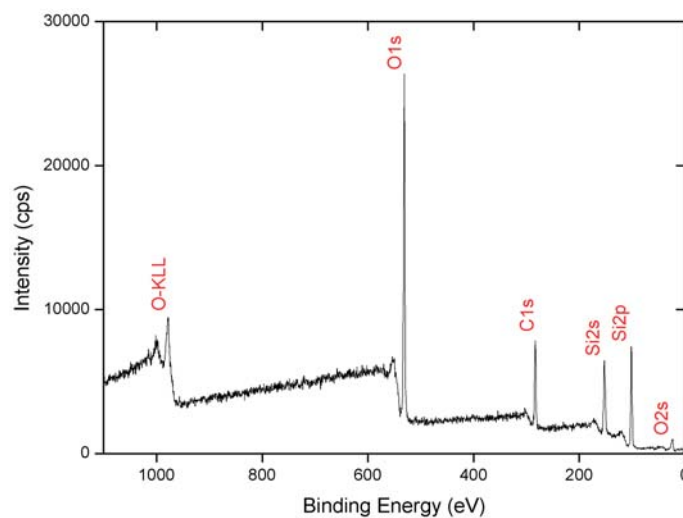
Figure 5.6: A typical XPS survey spectrum of a deposited film. The film is deposited with 20 sccm O_2 at 15mA discharge current.

Table 5.2, which presents the atomic composition of the deposited films obtained with various deposition parameters, shows a strong correlation with the FTIR results shown in figure 5.3 and 5.4. As can be seen from the data, the film

Oxygen (sccm)	Power (W)	O (%)	C (%)	Si (%)
0	22.5	40.5	35.6	23.9
20	22.5	48.0	28.0	24.0
60	22.5	53.5	25.4	21.1
20	18	44.4	31.0	24.6
20	30	50.2	26.3	23.5

Table 5.2: Atomic percentage of deposited films for various oxygen flow rates and discharge powers.

deposited in nitrogen (without O_2) contains 35.6% of carbon and 40.5% of oxygen. An introduction of 20 sccm of O_2 into the discharge atmosphere decreases the carbon content to 28% and increases the oxygen percentage to 48%. A further increasing in O_2 flow rate to 60 sccm results in the deposition of an oxygen-rich film comprising 53.5% of oxygen. One can therefore conclude that O_2 addition increases the oxygen content of the film and a high O_2 flow thus results in an oxygen-rich coating, which is in accordance with the results obtained in the FTIR results section.

The chemical composition of the films, which are deposited at various discharge powers, is also presented in Table 5.2. The film deposited at 18 W exhibits a high carbon proportion of 31% and a low oxygen percentage of 44.4%. Increasing the discharge power to 22.5 W results in a steady decrease of carbon content to 28% and a rise in oxygen content to 48%. A further increase in discharge power to 30 W results in a slightly lower carbon content and a higher oxygen content. It can be concluded that an increasing discharge power tends to increase the oxygen content of the deposited films combined with a decrease in carbon content. Also these XPS findings are in agreement with the previously mentioned FTIR results. This oxygen increase with increasing discharge power can be explained as follows: with increasing discharge power, more activated oxygen species are present in the discharge, which can react with the monomer molecules. More interactions between oxygen species and the monomer molecules can thus occur at higher power. Since these oxygen plasma species are very effective in removing CH_3 groups from the monomer molecules and replacing them by oxygen atoms, higher discharge powers can thus lead to a higher oxygen content in the deposited films.

Table 5.2 also clearly shows that the amount of silicon in the deposits is neither affected by oxygen addition nor by discharge power. This is most likely due to the fact that the activated plasma species mostly interact with the CH_3 side groups of the monomer and not with the Si-O-Si backbone.

To obtain further insight into the chemical bonds present in the deposited films,

curve deconvolution of the high resolution Si2p peaks is carried out by CasaXPS software. In order to carry out the deconvolution of the Si2p peak only 4 components (see figure 5.7) have been considered [135, 324]: a component at a binding energy of 101.5 eV due to a $(CH_3)_3SiO$ unit, a component at a binding energy of 102.2 eV due to a $(CH_3)_2SiO_2$ unit, a component at a binding energy of 102.8 eV due to a CH_3SiO_3 unit and a component at a binding energy of 103.4 eV due to a SiO_4 unit. A variation in the position of each peak of 0.1 eV has been considered acceptable. The full width at half maximum (FWHM) of the fitted Si2p components is kept constant at 1.6 ± 0.1eV and the Gaussian to Lorentzian ratio is kept constant at 30% for all peaks.
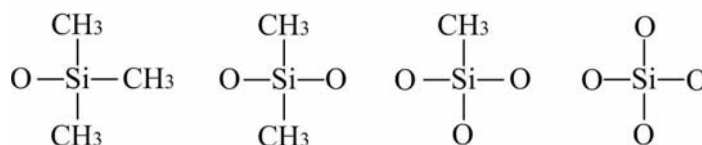
Figure 5.7: Structure of 4 fragments used in XPS deconvolution analysis [324].

Figure 5.8 shows the deconvolution of the high resolution Si2p peaks of the plasma-polymerized films deposited in two extreme working conditions: a pure nitrogen atmosphere at 22.5 W and a nitrogen with 20 sccm O_2 discharge at 30 W. For the film deposited in pure nitrogen, the Si2p peak can be fitted with three peaks as shown in figure 5.8 (a). The biggest peak at 102.1 eV is due to the $(CH_3)_2SiO_2$ unit, while two small peaks at 102.5 eV and 103.4 eV correspond to CH_3SiO_3 and SiO_4 content respectively. On the other hand, the film deposited with the 20 sccm oxygen flow (figure 5.8 (b)) shows a low content of $(CH_3)_2SiO_2$ unit at 102.1 eV. The peaks at 102.5 eV and 103.4 eV which are due to CH_3SiO_3 and SiO_4 content are larger and clearly show the higher content of these content when oxygen is present in the discharge gas.

The concentration of the different silicon units (the four component peaks of Si2p as mentioned above) for various oxygen flow rates is summarized in Table 5.3. There is a negligible amount of $(CH_3)_3SiO$ unit (less than 1%) in all deposited films, which is expected since the TMDSO molecule (chemical structure shown in figure 5.1) does not contain any of these units. Once introduced into the plasma region, the monomer containing $(CH_3)_2SiO_2$ units is bombarded by ions and excited species resulting in the loss of methyl groups and the dissociation into fragments leading to the creation of other chemical units in the deposited films.

Table 5.3 clearly shows that there are three main components $((CH_3)_2SiO_2$, CH_2SiO_3, and $SiO_4)$ in all films. The film deposited in a pure nitrogen atmosphere contains a high amount of $(CH_3)_2SiO$ unit (59.2%), which indicates that the film exhibits chemical characteristics similar to the monomer. With the ad-
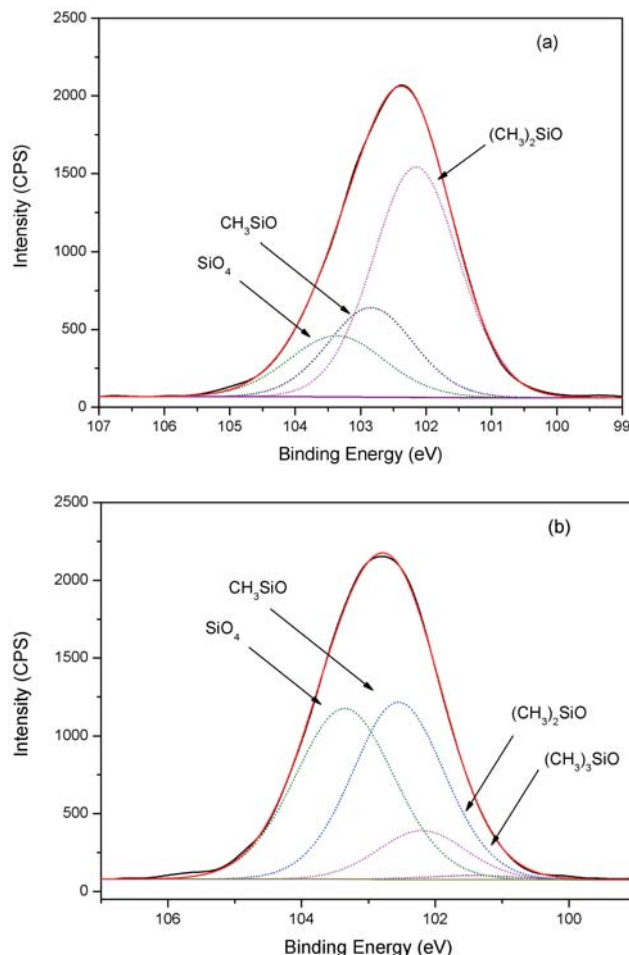
Figure 5.8: Deconvoluted Si2p peaks of thin films deposited at the following conditions: (a) pure nitrogen with a discharge power of 22.5 W, (b) nitrogen and 20 sccm oxygen flow with a discharge power of 30W.

dition of a 20 sccm oxygen flow, the deposited film shows a gradual decrease in $(CH_3)_2SiO_2$ unit to 35.9% and a considerable increase in SiO_4 unit percentage to 44.8%. An increase of the oxygen flow to 60 sccm further declines the concentration of the $(CH_3)_2SiO_2$ unit to 24.4% and increases the proportion of the SiO_4 unit to 63.5%. The films deposited in the pure nitrogen atmosphere retain a high content of $(CH_3)_2SiO_2$ unit which indicates a low dissociation level of the monomer. Introduced O_2 molecules are dissociated into oxygen atoms and/or excited into metastables into the plasma region which in turn enable the oxidation of the $(CH_3)_2SiO_2$ unit into CH_3SiO_3 and SiO_4 unit. Therefore, one can conclude

Oxygen (sccm)	Power (W)	$(CH_3)_3SiO$ (101.5 eV)	$(CH_3)_2SiO_2$ (102.1 eV)	CH_3SiO_3 (102.8 eV)	SiO_4 (103.4 eV)
0	22.5	0	59.2	23.1	17.7
20	22.5	0.6	35.9	18.7	44.8
60	22.5	0.4	24.5	11.6	63.5
20	18	0.4	38.5	34.2	26.9
20	30	0.1	12.4	43.0	45.5

Table 5.3: Concentration (in %) of different silicon bonds in the plasma deposited films for various oxygen flows and various discharge powers.

that the participation of O_2 in the deposition process changes the deposits from high carbon monomer polymerization films to high oxygen composition films, and a higher oxygen composition in the films can be achieved by an increasing oxygen flow.

The component proportion of the films deposited under various discharge powers is present in Table 5.3 as well. When the plasma jet operates at 18 W, the deposited film consist of 38.5% $(CH_3)_2SiO_2$, 34.2% CH_3SiO_3 and 26.9% SiO_4. Increasing the discharge power to 22.5 W reduces the amount of CH_3SiO_3 unit to 18.7% and increases the SiO_4 unit concentration to 44.8%. The percentage of $(CH_3)_2SiO_2$ unit slightly decreases to 35.9%. A further increase in discharge power to 30 W leads to a drastic decrease of $(CH_3)_2SiO_2$ unit to 12.4% and a significant raise in CH_3SiO_3 unit concentration to 43.0%, while the amount of SiO_4 unit remains steady at approximately 44.5%.

For the deposition process at high discharge power, there is an increase of energy for excited molecules and atoms, which intends to boost dissociation and oxidization processes for monomer molecules and fragments. When the discharge power rises from 18 W to 22.5 W, the amount of SiO_4 unit increases due to the oxidation of the CH_3SiO_3 units. A further increase of the discharge power to 30 W results in an increasing amount of CH_3SiO_3 units due to the oxidation of $(CH_3)_2SiO_2$ units while the concentration of SiO_4 units shows negligible changes. This indicates that the ability of SiO_4 units formation is limited.

5.4   Conclusions

In this chapter, thin film deposition on silicon wafers using an atmospheric pressure nitrogen DC plasma jet with TMDSO as precursor is discussed. Effect of O_2 content and plasma discharge power on film growing speed and chemical properties of the films is thoroughly investigated. The developed plasma source is capable of depositing controllable films with high deposition rates. Oxygen content in feed gas can increase deposition rate from 172 nm/min (no O_2) to 444 nm/min (60

sccm O_2) due to effective monomer decomposition by the plasma. Precise control of deposition rate can also be achieved by variation of discharge power. Increase of discharge power accelerates deposition rate from 273 nm/min at 18 W to 493 nm/min at 30 W in a mixture with 20 sccm O_2. This effect can be explained by increased electron density and thus higher dissociation degree of TMDSO at higher discharge powers. As a result, more radicals are formed in gas phase, which can initiate polymerization processes and thus lead to higher deposition rates. Chemical structure of the films is investigated by FTIR spectroscopy and XPS analysis. Both techniques reveal complex film chemical composition. Formation of an organic film can be partially suppressed by increase of discharge power and increase of oxygen content in the feed gas. XPS survey spectra show oxygen content increase from 40.5% without O_2 admixture to feed gas up to 54.4% at an O_2 flow rate of 60 sccm. A similar trend of oxygen-rich film formation is also observed with increasing discharge power. High resolution XPS spectra show that films consist of $(CH_3)_x SiO_y$ (x=1,2) contents (up to 82%) and low amount of SiO_4 content ($< 18\%$) when no O_2 is added to the feed gas. Film chemical composition can be tuned to more inorganic structure by admixture of O_2 which results in an increase of SiO_4 content to 63.5% in optimal deposition conditions.

<div align="right">**6**</div>

Deposition of composite organosilicon thin films with embedded silver nanoparticles

6.1 Introduction

Atmospheric pressure plasma process can not only be employed for polymerization of thin films with pure chemical or physical feature, such as basic organosilicon thin films as described in chapter 5, but also can be utilized for synthesis of more complex hybrid or composite films with advanced properties which are difficultly satisfied by deposition of simple films. Nanocomposite films and coatings, invented with the development of nanotechniques, have gained considerable attention due to their unique physical and chemical properties [325, 326]. There is currently growing interest in synthesis of nanocomposite films by atmospheric pressure plasma process for advance functional materials, especially for functional materials with antibacterial property [182, 187].

To obtain active antimicrobial activity, antibiotic needs to be incorporated in the surface of materials. Molecular antibiotics traditionally used to against bacteria face several disadvantages, including worldwide emergency of antibiotic resistance, difficulty to be incorporated into many materials and sensitivity to harsh environments during many industrial processes [327]. Inorganic nanosized compounds present strong antibacterial activity at low concentration due to their high surface area to volume ratio and unique chemical and physical properties [328].

Currently, incorporation of metal nanoparticles (such as silver nanoparticles, copper nanoparticles, zinc oxide nanoparticle) is becoming a new strategy for improving antibacterial activity because of their pronounced biocidal activity and higher stability under extreme conditions [328–330].

Silver is well known for its intrinsic antimicrobial property and silver nanoparticles (AgNPs) have merged up as a new generation of antibacterial with diverse medical applications [328]. Unfortunately, emergence of cytotoxicity and genotoxicity of silver nanoparticles goes against some practical applications in human body [331, 332]. Considering above concerns, it is important to fabricate antibacterial surfaces with firm loading of AgNPs. In this way, release of silver nanoparticles to the microenvironment is limited and silver ions are only released locally. This system combines the benefits of antibacterial properties and suppresses potential hazardous influence of silver nanoparticles.

Recently, nanocomposite embedded AgNPs films with antibacterial activity have been reported by many groups. Besides multistep wet chemical solution methods, low pressure plasma processes by associating plasma polymerization and sputtering in single step have been reported as reviewed in chapter 2 [209, 211, 211–213, 215–218, 231]. As with most of low pressure technologies, used method has limitation on the size of samples, applicability to flat materials without pores and low deposition rate of some nm/min [209]. Moreover, high investment and maintenance costs limit use of the proposed method to applications where high quality of deposited films with high control of deposition is required. Therefore, it would be significantly interesting to fabricate nanocomposite thin films in a way that combines efficiency and price of chemical methods with high load of AgNPs in a single step technology, as is achieved by low pressure sputtering.

In this chapter, an original one step dry process is developed using atmospheric pressure plasma jet for deposition of nanocomposite thin films with high concentration of AgNPs. Composition, morphology and antibacterial efficiency of deposited nanocomposite films are carefully analyzed and evaluated. Nanocomposite film growth will be discussed as well.

6.2   Experimental details

6.2.1   Plasma deposition process

The nanocomposite films are deposited using an atmospheric pressure plasma deposition system with a nitrogen direct current (DC) plasma jet as shown in figure 6.1 (a). As one can see in chapter 4, the plasma is generated between a pin and a mesh electrode placed in a quartz tube. Investigation based on optical emission spectroscopy revealed that plasma contains abundant excited states of nitrogen molecules ($N_2(A^3\Pi_u$, $B^3\Pi_g$, $C^3\Pi_u$)) and ionized species $N_2^+(B^2\Sigma_u$, $X^2\Sigma_g$). In

this work, the plasma is generated with a fixed power at 22.5 W and a total flow rate at 7 slm. As shown in figure 6.1 (b), the afterglow, extending to the open air of about 20 mm, is characterized by a fast decrease of the temperature with the distance. The substrate is put 10 mm away from the nozzle, where the gas temperature decreases to 310 K which is practical for thermo sensitive biomaterials.

The deposition process, based on the plasma polymerization of organosilicon films in chapter 5, is performed on Si wafers. The substrate is cleaned with ethanol in ultrasonic bath for 20 minutes and dried before the deposition. The atmospheric pressure DC plasma generated in N_2 with admixing of O_2 and TMDSO as the organosilicon precursor is used for the deposition. The thickness of the films in this work is 700 nm. Silver nanoparticles (Sigma Aldrich) of 100 nm size with a purity of 99.5% (trace metal basis) are used through experiments as purchased. The independent N_2 flow is passing through an AgNPs feeding module which is a narrow tube filled with silver nano-particles used for the introduction of nanoparticles into the plasma reactor. It has to be noted that in first step we also tried to use suspension of AgNPs in 3 different solvents (H_2O, ethanol, TMDSO) with
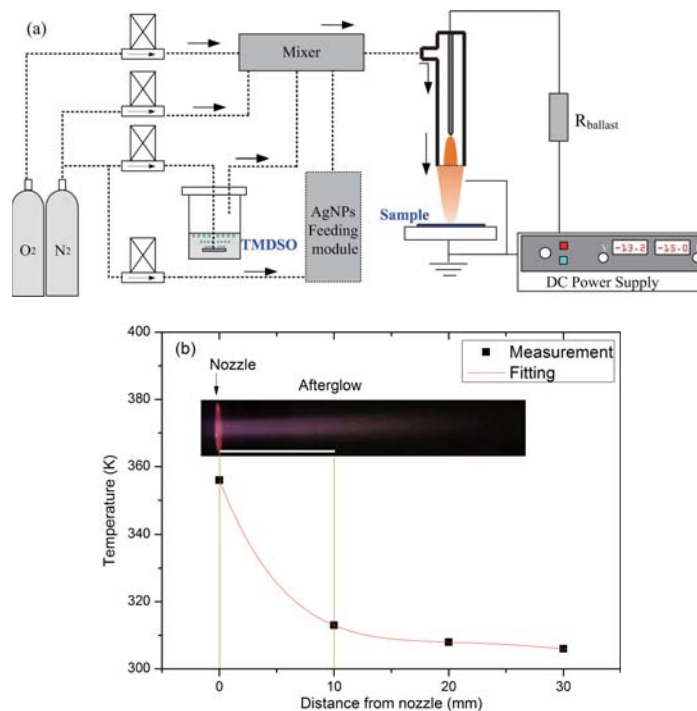
Figure 6.1: (a) Scheme representing the atmospheric pressure plasma deposition system for nanocomposite films manufacturing and (b) temperature distribution in the afterglow of the plasma system obtained with emission spectroscopy.

ultrasonic atomization but the using of solvents leads to very low concentration of AgNPs in the films and also high concentration of solvent in the feed gas made the plasma unstable with high gas temperature. Correspondingly, in the present work the system with powder of AgNPs inside of container is used through the all experiments. This system is very reliable, cheap and provides a high flow of particles in the plasma zone so high content of AgNPs can be obtain in the deposited film. In order to prevent agglomeration of AgNPs only dry N_2 with 0% humidity is used in the system. The amount of AgNPs is controlled by a flow rate of the gas passing the tube. In following sections, sample 1, sample 2, sample 3 and sample 4 are corresponding to the thin films deposited with a gas flow rate passing the AgNPs feeding module at 100 sccm, 500 sccm, 1000 sccm and 1500 sccm, respectively.

6.2.2   Film characterization

The top surface chemistry of the films is determined by X-ray photoelectron spectroscopy (XPS) on a Versaprobe II system as described in section 3.3.3. The pressure in the analyzing chamber is maintained below 10^{-7} Pa during analysis and the diameter of the analyzed area is 100 μm. Survey (0-1100 eV) and high resolution spectra are recorded at a pass energy of 117.4 eV and 29.35 eV respectively.
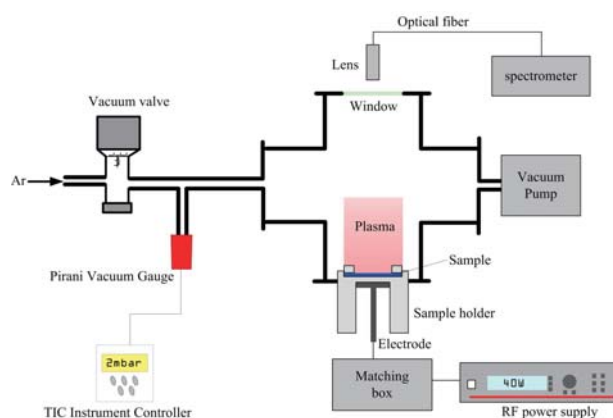
Figure 6.2: Schematic diagram of the experimental set-up for RF-GD-OES

The silver content of the nanocomposite samples and the depth profile is investigated by glow discharge optical emission spectroscopy (GD-OES) using a Grimm-type glow discharge source powered by a radio frequency (RF) power supply (Advanced Energy Cesar, USA). The scheme of the GD-OES setup is shown in figure 6.2. Argon is used as working gas. After introducing a sample to the sample stage, the chamber is pumped to 10^{-3} mbar and then flushed by argon for 3 min to eliminate the background gases. The plasma is generated in 2 mbar argon

atmosphere at a power of 40 W. The emission spectra are collected by a spectrometer (Ocean Optics S2000, USA) with a resolution of 0.2 nm. The calibration is done by measurement of a set of standard samples with known Ag content.

SEM analysis is performed in order to investigate the morphology of AgNPs in the samples. The samples are Au coated with a Baltec SCD005 Sputter Coater (Bal-Tec AG, Principality of Liechtenstein) in order to avoid a charge effect. The deposited films are studied by a FEI XL30 scanning electron microscope (FEI, Netherlands) equipped with a LaB6 filament and with an energy dispersive X-ray spectroscopy detector (EDAX, The Netherlands).

6.2.3 Antibacterial assay

The antibacterial tests are performed with cultures of Escherichia coli (*E. coli*, ATCC 25922) and Staphylococcus aureus (*S. aureus*, ATCC 25923). The antibacterial activity of AgNPs was evaluated with Mueller-Hinton (MH) agar disc diffusion and macrodilution method. Test solution with 0.5 McFarland (approx. 1.5×10^8 CFU/ml) is used as a standard of turbidity for *E. coli* and *S. aureus* strains. All tests are repeated 3 times for statistical averaging.

6.3 Results and Discussion

As known, plasma film deposition starts with chain breaking and dissociation of monomer molecules of the precursor and thereby creating radicals. These radicals recombine with each other, form cross-linking structures and finally are deposited on the substrate. In the present study we used a mixture of TMDSO with O_2 resulting in the composition of the film close to inorganic SiO_2. In chapter 5, it was shown by XPS and FTIR measurements that deposited films without AgNPs consists of < 55 % of O. The deposition rate can be controlled by the oxygen content in the feed gas and can be varied from 172 nm/min (no O_2) up to 450 nm/min (60 sccm O_2) due to effective monomer decomposition by the plasma. In previous experiments we observed formation of white micro-particles on the surface of the deposited film at an O_2 concentration in the feed gas higher than 60 sccm. Therefore, the flow rate of O_2 has been fixed at 20 sccm in this work. The concentration of TMDSO, O_2, flow rate and plasma power are fixed through all the experiments and allows manufacturing the coating at 350 nm/min deposition rate on Si.

6.3.1   Chemical composition of the film

6.3.1.1   XPS measurement

XPS technique, which uses an electron beam to probe 1-10 nm of surfaces, is mostly used for identification of component elements, and is also used for analysing the chemical state of atoms. In this work, it is used to investigate the chemical constituents of the films at the top surface within 10 nm. Figure 6.3 presents the XPS spectra for a control film without AgNPs and two nanocomposite films fabricated at different feeding conditions. The survey spectrum indicates that the control film is composed of oxygen, carbon and silicon with corresponding XPS peaks O1s, C1s, Si2s, and Si2p and no N signal is detected even though N_2 plasma is used for the deposition.
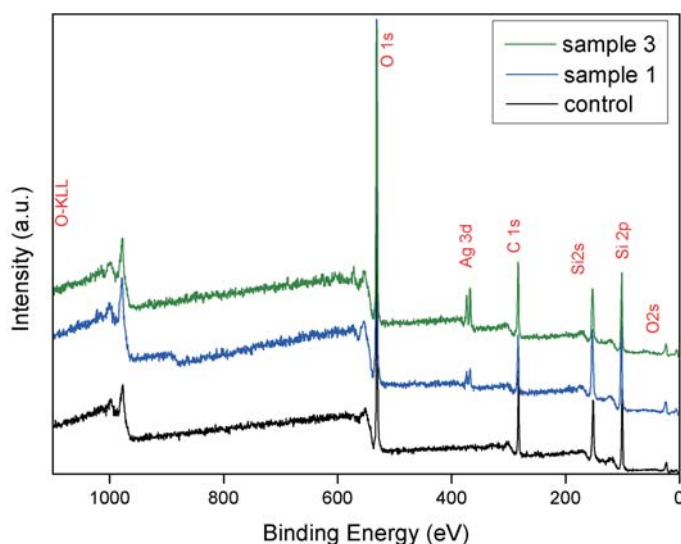
Figure 6.3: Survey spectra of the control sample and 2 nanocomposite films (a); a deconvolution of Si2p peak for the control sample (b). The binding energies are referenced to C1s (285eV).

With the introduction of AgNPs into the plasma, the characteristic doublet peak of Ag3d is observed in the XPS survey spectra shown in figure 6.4. In the figure, it is shown that with the increase of gas flow rate from 100 sccm (sample 1) to 1000 sccm (sample 3), the intensity of Ag3d peak increases which indicates that the control of AgNPs co-deposition can be achieved by variation of gas flow rate through the feeding module. The high resolution spectra of the Ag3d peaks reveal that the binding energies of Ag3d5/2 and Ag3d3/2 of the silver nanoparticles are between 367 eV and 370 eV and between 374 eV and 375.5eV, respectively. A spin-orbit separation of Ag3d5/2 and Ag3d3/2 peaks is 6.0 eV indicating the presence of

metallic silver nanoparticles in the film. The energies are in good agreement with the reported values for the binding energies of silver nanoparticles [203]. While comparing to the binding energy of Ag3d5/2 for bulk metal Ag at 368.2 eV, a positive chemical shift observed for Ag3d5/2 suggests that silver nanoparticles are oxidized during the deposition process. According to [333], the peak of Ag3d5/2 at 367.8 eV can be deconvoluted into two components: Ag metallic and AgO at binding energy of 368.5 eV and 367.7 eV, respectively. The analysis of the decomposed Ag3d peak in figure 3 (a) reveals that the AgNPs embedding in the film consists of about 82% of Ag and 18% of AgO. It is also confirmed by the peak shift of O1s from 531.6 eV in the control film to 532.2 eV in the nanocomposite films presented in figure 6.4 (b) which is attributed to oxidation of silver. Therefore, the silver nanoparticles embedded in the films consist of metallic silver at the core and the surface of AgO. The atomic concentration of elements in the control film and in the nanocomposite films is presented in Table 6.1. As one can see, the element percents exhibit slight different between the control samples in table 6.1 and the sample in table 5.2 with 20 sccm of oxygen and 22.5 W discharge power. This can be explained by the change of deposition environments, from a pure nitrogen background in chapter 5 to an open space deposition background in this work. With introduction of AgNPs into the process, the films present the increasing content of oxygen that raise from 46.1% to 63.5%, and the decrease in carbon content that declines from 26.7% to as low as 4.3%, indicating that silver is prone to oxidation process.
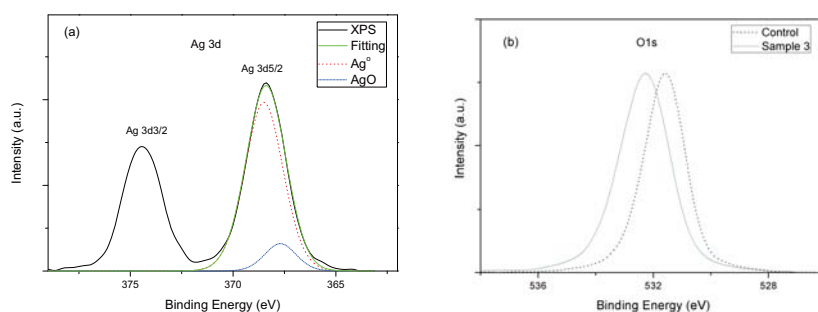
Figure 6.4: (a)High resolution XPS spectra of Ag3d with respective deconvolution of Ag3d5/2 peak;(b) the comparison of high resolution spectra of O1s between the control sample and a nanocomposite sample

Unfortunately, the results of XPS measurements of Ag content in the films are strongly dependent on the distribution of nanoparticles inside the film. The e-beam of XPS machine is used to probe 1-10 nm of the surface and therefore, the concentration of nanoparticles with a size of 100 nm obtained by XPS can undergo high underestimation, as mentioned elsewhere [203]. Moreover, measurement of a depth profile of the composite films by combining a sequence of ion gun etch

	Ag [at.%]	Si [at.%]	C [at.%]	O [at.%]
control	0	25.7	29.8	44.5
Sample 1	0.4	26.8	26.7	46.1
Sample 2	2.0	28.6	12.2	57.2
Sample 3	4.3	27.5	6.9	61.3
Sample 4	7.6	24.6	4.3	63.5

Table 6.1: Atomic percentage of the different samples.

cycles alternated with XPS measurements is accompanied by unavoidable and un-controllable "matrix effect" because of the high energy of sputtering ions (typically 3-5 keV) in the XPS device [334]. "Matrix effect" can result in the removal of an entire nanoparticle during sputtering step, leaving a cavity on the surface for the next XPS measurement step which makes analysis of results difficult or even impossible.

6.3.1.2   GD-OES measurement

One way to overcome the limitation of XPS method due to "matrix effect" is the use of glow discharge optical emission spectroscopy (GD-OES) [335]. In the GD-OES, the plasma is initiated when a high potential is applied between the electrodes. The scheme of the technique is presented on figure 6.5. The positive ions (argon ions in the setup) are attracted toward the sample surface, strike the sample surface with an energy of 10-50 eV and cause the release of surface material into the gas phase. Upon entering the gas phase environment of the glow discharge, the sputtered materials are excited by the plasma. Finally, the excited atoms or ions come back to the fundamental energy level, and emit a characteristic photon. The emitted photons, whose energy is characteristic for a chemical element's energy level, are then collected by a spectrometer. This allows to quantify the elemental composition of the material. In comparison with XPS, which measures the sample surface, RF-GD-OES is based on the detection and quantification of sample species within the plasma. Among the advantages of the GD-OES are the simplicity of the technique and the low cost of the analysis.

As shown in the spectra by figure 6.6, emission bands around 337.1 nm and 336 nm are due to the emission from background reactions of nitrogen second positive system N_2(C-B) and the transition of NH(A-X), respectively. A comparison between the control sample (without AgNPs introduced into the layer) and the composite layers (with AgNPs introduced into the film) indicate the existence of two new emission lines for the hybrid samples, at 328.1 nm and 338.3 nm, respectively. These lines appear due to the transition of 5p $\rightarrow$ 5s for silver ions (Ag I). According to the mechanism of the RF-GD-OES, the silver emission lines indicate
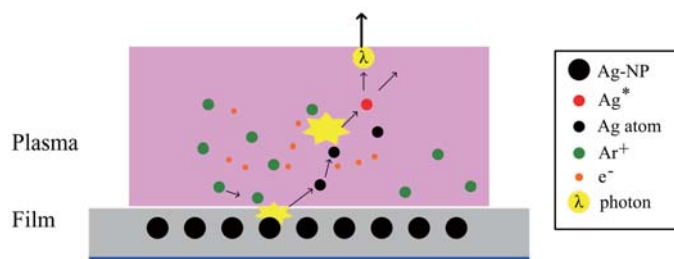
Figure 6.5: Diagrammatic sketch of the mechanism in the GD-OES

the presence of silver in the hybrid films. Because of a higher transition probability and stronger emission, the emission at 328.1 nm is considered for further analysis. Due to high rate of the sputtering during GD-OES measurement, the intensity of the Ag signal as a function of the sputtering time can be used to characterize the depth distribution of Ag in the films.
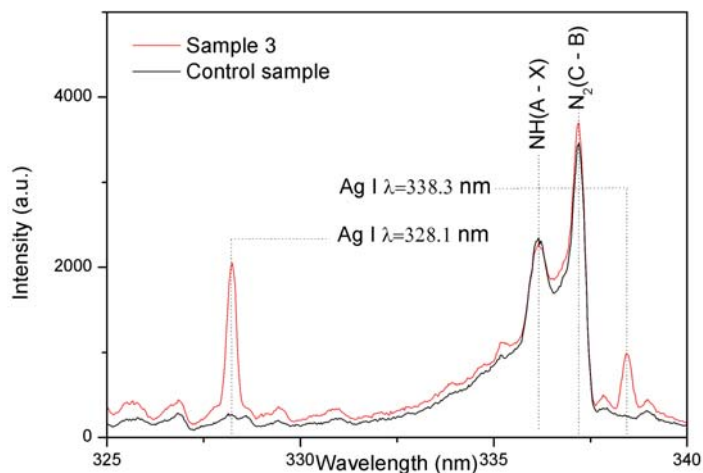
Figure 6.6: Emission spectra of RF-GD-OES. The control sample was obtained without the introduction of AgNPs. The sample were deposited with 1000 sccm flow rate of carrying gas.

Therefore, time-resolved measurements of Ag I line at 328.1 nm during the sputtering of the target are used in order to measure the depth profile of AgNPs in the deposited films. The results for two samples are shown in figure 6.7 where increase of the signal at first 60 s is believed to be time required for gas heating and formation of a sputtering crater. A GD-OES experiment consists of two steps: a) formation of the sputtering crater, heating of sputtering zone and heating of the working gas and b) uniform sputtering of the material from the crater. As widely
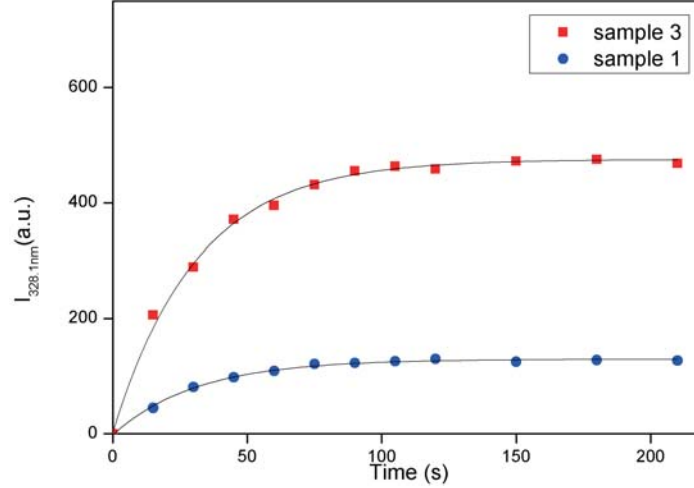
Figure 6.7: The intensity of Ag I line at 328.1 nm as a function of process time. Background pressure 2 mbar, discharge power 40 W.

accepted, only the results from the second step can be used for the characterization of elements distribution in the sample [335]. Therefore, only signal intensity after delay time of 60 s is used in the paper for analysis of Ag distribution. The stable emission intensity after the initialization period demonstrates a uniform distribution of silver in both samples. We would like to note that in GD-OES experiments the size of analyzed surface is about 20 mm^2 and so the method is not sensitive to presence of clusters of μm size in the film. The method gives a space averaged value of Ag distribution.

In GD-OES, the emission intensity of an atomic line is proportional to the product of the concentration of the corresponding element of the sample. For a recorded signal, the emission line from element *i* is given by [335]:

$$I_i = k_i S_i R_i c_i q_i + b_i \qquad (6.1)$$

where k_i is the instrumental detection efficiency, S_i is the correction for self-absorption, R_i is the emission yield, c_i is the content of element *i*, q_i is the sputtering rate, b_i is the background term.

The emission of Ag I presented in figure 6.7, is used to determine the silver content in the films after the calibration. The calibration is made by means of the use of samples with known density of Ag. Ag content of tested samples is given in figure 6.8. As we can see, the concentration of silver in the matrix increases gradually with the rise of feeding gas flow rate, which provides a convenient way to control the composition of the films. Moreover, the content of silver which is a key factor that determines the antibacterial activity of the coating can reach 32%,
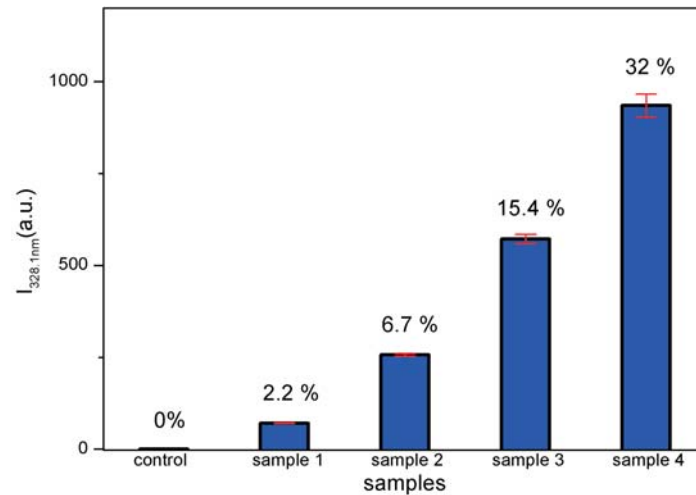
*Figure 6.8: The results of silver content in the samples using GD-OES with absolute cal-
ibration by standards. The used emission line is at 328.1 nm, chamber back-
ground pressure 2 mbar.*

which is higher than that provided by other methods.

6.3.2   The morphology of films and AgNPs distribution

A series of SEM images in figure 6.9 shows the morphology of nanoparticles in the
films. For a low feeding gas rate in the process as shown in figure 6.9, AgNPs are
separated and homogenously embedded into the matrix. The size of the particles is
about 100-500 nanometer. Figure 6.10 is an example of a high resolution image of
single cluster from the sample 1. As we can see, the cluster has a dimension of 700
nm and consists of small particles which have a diameter of about 200 nm. SEM
images confirm slight aggregation of nanoparticles in the clusters. Meanwhile, it
is also shown that the clusters are separated quite well from each other. With the
increase of feeding flow rate to 500 sccm and 1000 sccm the amount of AgNPs
on the top of the coating grows gradually with the formation of bigger clusters i.e.
figure 6.9 (b) and (c). Further increase of the feeding flow rate to 1500 sccm leads
to significant aggregation and results in the formation of clusters up to several mi-
crometers in size as shown in figure 6.9 (d). Clusters area analysis is presented
in figure 6.11. For the samples with less than 15% content of Ag that deposited
with low feeding flow rates, the clusters area is smaller than 10 μm^2. However,
for the content of Ag higher than 30% formation of large area agglomerates is ob-
served.   The SEM image of a typical cluster (from sample 3) and corresponding
EDX spectrum are presented in figure 6.12. As shown in figure 6.12 (a), the clus-

ters are formed by an aggregation of small spherical particles with a diameter of around 1 μm which is ten times larger than the size of the nanoparticle used in the work. The structure of outer shell of particles has many small cracks and pores which are believed to provide the way for Ag^+ to be released from the films. The EDX analysis (figure 6.12 (b)) revealed that core of the clusters consists of AgNPs. Moreover, the EDX mapping in figure 6.12 (c) further confirms presence of silver only in clusters. EDX mapping of O in figure 6.12 (d) shows that the intensity of O is much stronger in the clusters than that at the surrounding film. This can be explained by oxidation of AgNPs which is in accordance with XPS result.

Based on XPS and SEM results a diagram of the processes occuring during plasma deposition process is presented in figure 6.13. In the plasma region the precursor molecules are dissociated in a chain of collisions with active species formed by the discharge. When AgNPs are introduced, they are oxidized by atomic O formed in the plasma and concurrently TMDSO fragments are recombined on their surface which results into the film growth directly on AgNPs. As soon as AgNPs have been completely covered by silicon oxide, no further oxidation of Ag is possible. Nanoparticles and clusters at various sizes are transported by the gas flow together with active species in the discharge afterglow where particles and fragments continue deposition process leading to the formation of large and
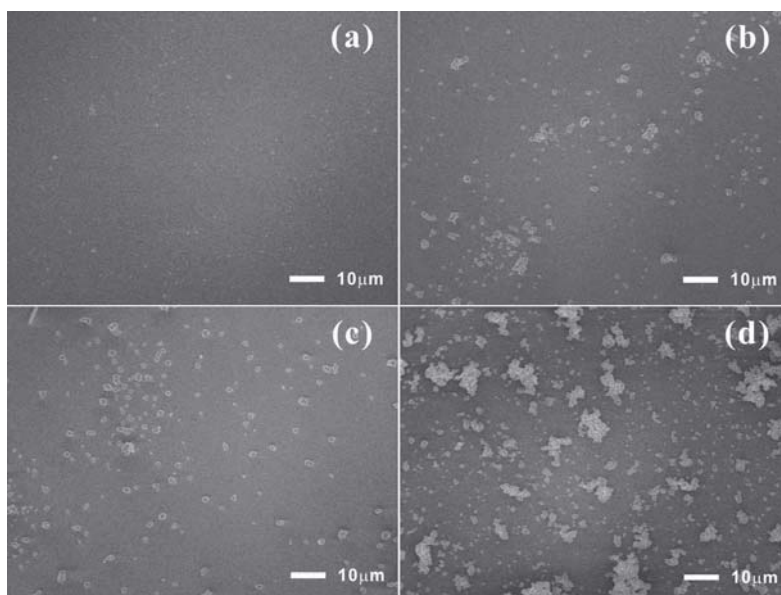
Figure 6.9: SEM image of nanocomposite films embedding various contents of AgNPs: figure (a), (b), (c), and (d) are corresponding to sample 1, 2, 3 and 4, respectively. Accelerating SEM voltage 2 kV.
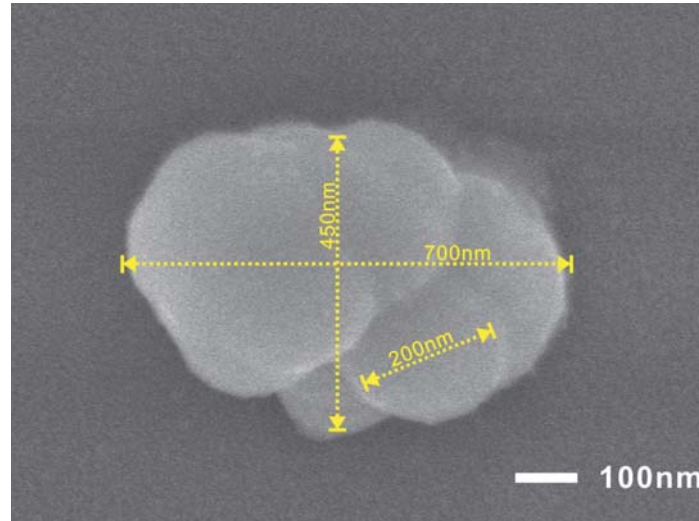
Figure 6.10: high resolution SEM image of a typical cluster embedded in the samples.
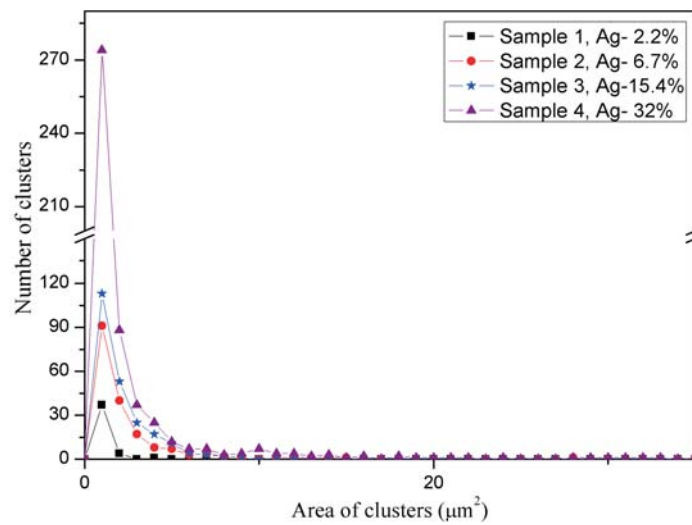
Figure 6.11: Clusters analysis of the SEM results for silver containing films. Isolated clusters of area larger than 30 μm^2 are still observed for the sample 4 (not shown on the figure).

irregular clusters. As mentioned above, the coating of AgNPs has a number of imperfections (cracks, pores, open places), hence the release of Ag ions is possible from the films by controlling the process through changing the deposition parameters. Two parameters are expected to significantly affect the imperfections in the
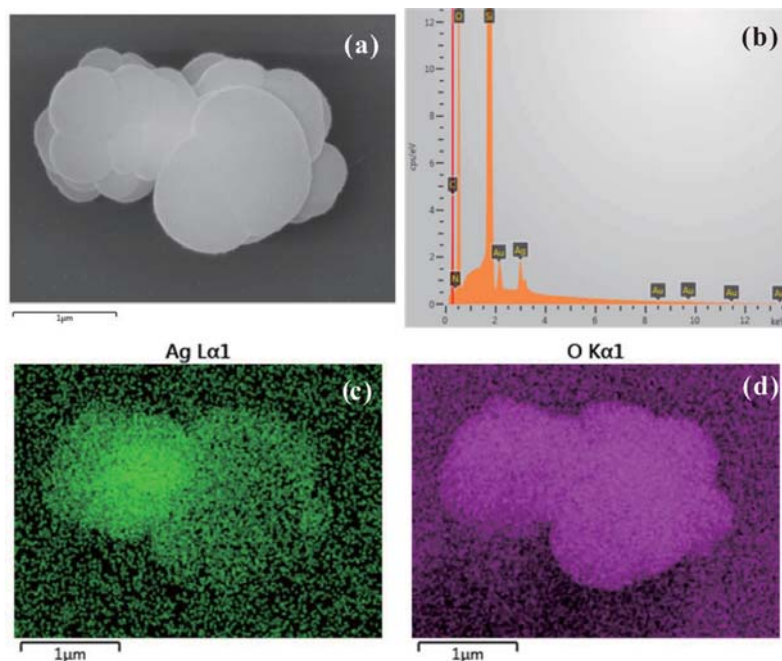
Figure 6.12: SEM results and the corresponding EDX mapping of a typical cluster. Accel-erating SEM voltage 8 kV. Presence of Au is due to pre-coating of samples with gold performed in order to suppress the charge effect.

coatings of AgNPs: the total gas flow and the plasma discharge power. The total gas flow rate determines the residual time of AgNPs inside of the plasma region, thus determining the deposition of silicon oxide on the AgNPs, and therefore controlling the capability of silver release. The discharge power can be used to control the temperature gradient between the plasma region and the afterglow which is responsible for a thermal stress on the surfaces of the particles. This leads to the generation of imperfections due to the breaks of the film.

6.3.3   Antibacterial assay

The antibacterial properties of the nanocomposite films based on AgNPs are assessed with *E. coli* and *S. aureus* as the representatives of Gram-negative bacteria and Gram-positive bacteria, respectively. Standard procedure of disk diffusion method with 19 hours incubation of MH agar plates was shown to be not representative for tests of the films due to the high concentration of bacteria and long release time of Ag ions from the films. So, the test procedure has been adapted in the present work by macrodilution method by making bacterial suspension of
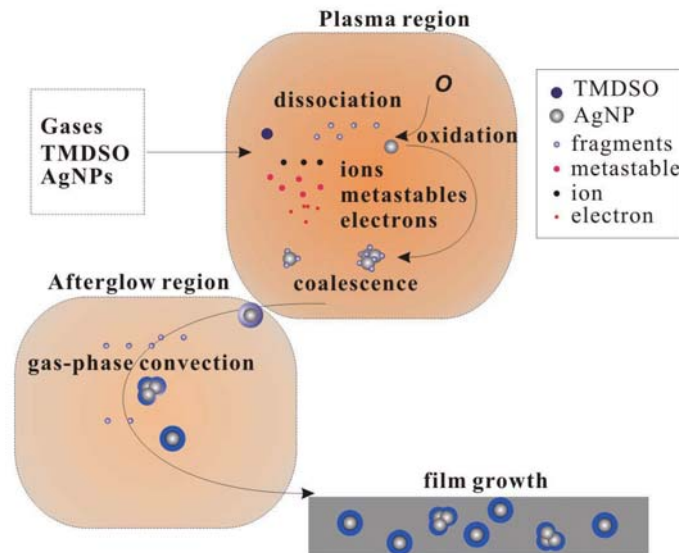
Figure 6.13: Schematic diagram of the atmospheric pressure plasma deposition process with AgNPs.

isolated colonies selected from MH agar plate in saline solution to lower concentration. Specifically, the test solution of 0.51 McF (1.5×10^8 CFU/ml) for *E. coli* and 0.50 McF for *S. aureus* is diluted with sterile saline to concentration of about 10^3 CFU/ml. The bacterial solutions were incubated for 19 hours at 37 ^{o}C and 100 μl from each solution were spread on three MH plates. The bacterial colonies were counted the next day. The same procedure is used for the plasma deposited films which are immersed into the bacterial solution before incubation.

The results of the test for the case of film with 6.7% AgNPs load are presented in figure 6.14. As expected the antibacterial effect is increased with the increasing of AgNPs content in the films. For all tested films higher reduction of *E. coli* was observed. At very low bacterial concentration only 5.6 times reduction of *E. coli* was found and with increase of AgNPs load in the film to 15.4% the plates did not exhibit any growth after the incubation. The *S. aureus* bacterium has shown higher resistance against silver. Even with high load of AgNPs the CFU reduction was 80 times, which shows lower efficiency of Ag against Gram-positive microorganisms. The observed effect of higher resistance of Gram-positive *S. aureus* versus *E. coli* is in agreement with results of others [336, 337]. It was suggested that the antimicrobial effects of AgNPs could be associated with characteristics of certain bacterial species [338]. The lower efficacy of the AgNPs against *S. aureus* derives
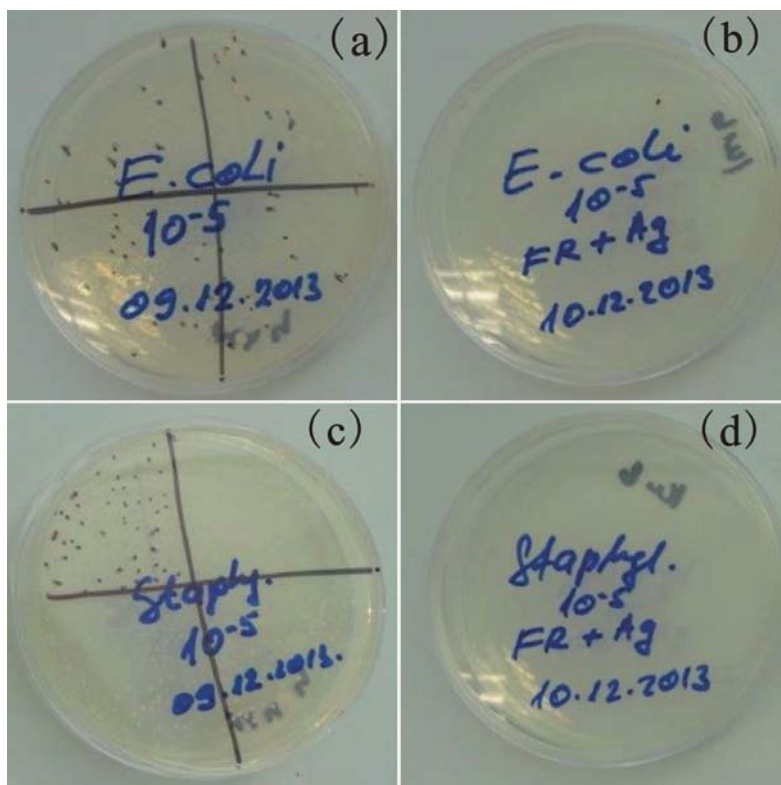
Figure 6.14: Schematic diagram of the atmospheric pressure plasma deposition process with AgNPs.

from the differences in cell wall structure and permeability compared with *E. coli*, but still, the effect is distinguishable even for *S. aureus* [336].

Figure 6.14 Visual representation of antibacterial test results of *E. coli* and *S. aureus*: (a) Control plate with *E.coli*; (b) plate with *E.coli* and the sample with 6.7% concentration of AgNPs in the film; (c) Control plate with *S. aureus*; (d) plate with *S. aureus* and the sample with 6.7% concentration of AgNPs in the film. Distinctive capabilities to deposit thin films on various substrates (such as silicon wafers, soft materials, polymers and metals) at atmospheric pressure plasma with no limitation on dimensions makes it a promising strategy for functionalization of biomaterials.

6.4   Conclusions

Nanocomposite organosilicon thin films with incorporation of AgNPs have been fabricated using original atmospheric pressure plasma process. It is shown that control of morphology of AgNPs in the films can be achieved by variation of Ag-NPs feeding rate. Silver content in the films can be controlled from few percent to more than 30%. Particles growth from nanosize to big clusters in deposited films is proposed to be due to aggregation of AgNPs and deposition of organic fragments during deposition. Antibacterial assays of films performed by macrodilution method using *E. coli* and *S. aureus* strains demonstrate antibacterial activity of deposited coatings. The developed method of plasma co-deposition at atmospheric pressure can be applied as a low cost substitution for processes done under vacuum conditions for various medical materials ranging from metallic to polymer surfaces providing a new class of antibacterial coatings.

7

Preparation of antimicrobial nano-silver non-woven fabric via an atmospheric pressure plasma deposition process

7.1 Introduction

In chapter 5 and chapter 6, non-equilibrium plasma jet has been employed for deposition of organosilicon films and nanocomposite films on silicon wafer or polymers, which have a simple flat surface. In practical applications, however, many materials with more complex topology structures, like non-woven materials, have been widely used. Non-woven polyethylene terephthalate (PET) has been used in a wide range of applications due to its outstanding characteristics such as excellent mechanical strength and good chemical stability [339]. In recent years, a lot of attention has however been paid to achieve more multifunctional performance of PET fabrics, especially in the health and hygienic field. For this purpose, PET fabric treated with antimicrobial agents has been extensively studied and results indicate capability of preventing pathogenic microorganisms growth, such as bacteria, fungi, algae,... [340–342]. Incorporation of nanosized inorganic compounds, such as silver nanoparticles and copper nanoparticles, which are characterized by strong antibacterial activity at low concentration due to their high surface area to volume ratio and unique chemical and physical properties, becoming a new

strategy for improving antibacterial activity because of their pronounced biocidal activity and higher stability under extreme conditions [328].

In the past, different strategies have already been proposed and investigated for incorporation of silver nanoparticles on a fabric. Deposition of a metallic silver film on PET fabrics has been studied using magnetron sputtering and an ion-beam-assisted deposition process [343–345]. Dipping-pad-drying for silver finishing of non-woven fabrics using colloidal silver have also been applied [346, 347]. Some of the above mentioned methods are however based on reactions in liquid medium and require surfactants, reducing agents or templates for the synthesis of silver nanoparticles, resulting in inevitable presence of impurities in the final products [348]. Moreover, due to poor adhesion between organic fabrics and inorganic particles caused by their difference in surface energy, surface modification of fabrics or nanoparticles is important or even essential when incorporating nanoparticles [349]. In addition, weakly bonded AgNPs will affect antibacterial efficiency and even cause potential cytotoxicity [331]. The film deposition method on non-woven fabrics with immobilized antimicrobial nanoparticles is of great interest but has not been tested before. Plasma polymerization is a very promising deposition technique because of environmental safeness, sustainability and high deposition rate coupled with good film adhesion to different substrates. Moreover, materials with various topology structures, flat or complex 3D objects, can be used as substrate.

In this chapter, PET non-woven fabrics with antimicrobial properties will be produced by firmly immobilizing silver nanoparticles via a double layer of plasma deposited organic films. In order to have a better understanding of the capability of the proposed process, chemical composition and morphology of silver decorated fabrics will be characterized by X-ray photoelectron spectroscopy (XPS) and scanning electron microscopy (SEM) respectively. Antimicrobial activity of the samples will also be tested against common pathogenic microorganisms.

7.2 Experimental details

7.2.1 Plasma jet deposition system

The plasma jet consists of a pin and a mesh electrode placed in a quartz tube as described in chapter 4. Investigations based on optical emission spectroscopy revealed that the nitrogen plasma contains abundant excited states of nitrogen molecules $N_2(C^3\Pi_u, B^3\Pi_g, A^3\Pi_u)$, and ionized nitrogen species $N_2^+(B^2\Sigma_u, X^2\Sigma_g)$. A plasma jet generated in N_2 (7000 sccm) with admixing of O_2 (20 sccm) and tetramethyldisiloxane (TMDSO, Sigma Aldrich) as the organosilicon precursor has been used for the deposition of organosilicon matrix as discussed in chapter 5. The PET substrate is placed 10 mm away from the nozzle, where the gas tem-

perature decreases to 310 K which is of practical importance for PET non-woven fabrics. The plasma head is mounted on a robotic arm (Stepcraft 300, Germany) in order to achieve a large scale treatment. The uniformity of the scanning process for large area deposition has been confirmed using silicon wafers as substrate.

7.2.2   Preparation of silver loaded PET fabrics

Nano-silver non-woven PET fabrics were prepared using a three step procedure as shown in figure 7.1. Non-woven PET fabrics (DuPont, Spain) were cut into a size of 3 cm $\times$ 3 cm before the silver immobilization process. At first, an organosilicon thin film was deposited on the surface of the fabrics using the plasma deposition system. This 70 nm layer is used as a reservation layer for the silver immobilization and to control the silver nanoparticles adhesion to the PET fibres. The thickness of the reservation and barrier layers in this work was determined in the set of independent experiments on silicon wafer as it was described in chapter 5.

In the following steps, the samples with the plasma-polymerized layer on top were immersed into a suspension of AgNPs in ethanol and raised for drying. Silver nanoparticles (SSNANO, USA) of 20 nm size with a purity of 99.95% (trace metal basis) are used throughout the experiments as purchased. The color of the fabric changed from white to gray after the incorporation of the AgNPs. In the final step of the process, a second layer of organosilicon film was deposited using the plasma jet system. This second layer is used as a barrier to prevent the release of AgNPs. Two different thicknesses of the barrier layer film (10 and 50 nm) will be tested in the present study.
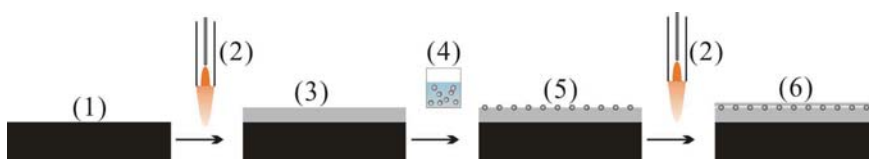
Figure 7.1: Scheme of the fabrication process for nan-osilver non-woven fabrics. (1) original sample of non-woven PET fabric; (2) plasma jet system for thin film deposition, detail of the experimental setup is given as a supplement information; (3) 1st step: plasma deposition of the reservation layer for silver nanoparticles immobilization and to control the silver nanoparticles adhesion to the PET fibres.; (4) prepared AgNPs dispersion; (5) 2nd step: AgNPs adhesion on the surface of the samples by immersing into the dispersion; (6) 3rd step: plasma deposition of the barrier layer.

7.2.3   Surface Characterization of silver loaded PET fabrics

The surface chemistry of the samples is determined by X-ray photoelectron spectroscopy (XPS) on a Versaprobe II system as described in section 3.3.3. The pressure in the analyzing chamber is maintained below 10^{-6} Pa during analysis and the photoelectrons are detected with a hemispherical analyzer positioned at an angle of 45° with respect to the normal of the sample surface. Elements present on the PET surfaces are identified from XPS survey scans, which have been performed on 3 different analyzing areas (200 μm x 600 μm) per sample. The obtained elements are quantified with Multipak software using a Shirley background and applying the relative sensitivity factors supplied by the manufacturer of the XPS instrument. Multipak software is also applied to curve fit the high resolution C1s peaks after the hydrocarbon component of the C1s spectrum (285.0 eV) is used to calibrate the energy scale. In a next step, the peaks were deconvoluted using Gaussian-Lorentzian peak shapes and the full-width at half maximum (FWHM) of each line shape was constrained between 1.3 and 1.8 eV.

SEM analysis is performed in order to investigate the morphology of the Ag-NPs in the PET samples. The samples are Au coated with a JFC-1300 Auto Fine Coater (JEOL, Belgium) in order to avoid charge effects. After applying the gold coating, the PET fabrics are studied with an InTouch Scope JSM-6010 SEM device (JEOL, Belgium).

7.2.4   Antimicrobial efficiency of the silver loaded PET fabrics

In order to evaluate the bactericide activity, all those materials have been tested through a method of standard antibacterial dilution test with protocol introduced in section 3.4.1. Since different microorganisms have been employed in this chapter, the detail information will be presented at the corresponding sections.

7.3   Plasma polymerization on non-woven PET fabrics

Plasma polymerization is capable of producing ultra-thin, polymer-like layers with a defined, regular structure on the top surface of flat materials. However, in this work, non-woven porous materials are exposed to a plasma polymerization process. Therefore, it is very important to study the penetration efficiency of the plasma polymerization process through the PET non-woven after the deposition of the first organosilicon layer. For this purpose, plasma polymerized PET samples are examined with XPS on two sides: the top side which is directly exposed to the plasma and the bottom side, which is in close contact with the sample holder.

Samples	C [at.%]	O [at.%]	Si [at.%]
Raw fabric	73.4 ± 0.7	26.6 ± 0.8	0
Top side of treated sample	24.4 ± 0.8	54.0 ± 0.7	21.6 ± 0.6
Bottom side of treated sample	25.1 ± 1.1	53.4 ± 0.9	21.4 ± 0.7

Table 7.1: Atomic composition of raw fabric, top side and bottom side of treated samples.

The atomic composition of the untreated and the plasma treated PET non-woven fabric is determined using XPS and is shown in table 7.1. The raw fabric is composed of 73.4% carbon and 26.6% oxygen. For the samples after plasma polymerization, the surfaces on the top and bottom sides show the same components: carbon, oxygen and silicon. It is noteworthy that the concentrations of the elements on both sides are almost identical. Thus, the plasma clearly penetrates into the structure of the fabric and plasma deposition can be achieved in the non-woven bulk as well as on the bottom side of the fabric. This can be explained by the efficient transfer of active plasma species and monomer's fragments by the vertical gas flow along the plasma jet.

Figure 7.2 shows the C1s spectra and Si2p spectra of the raw fabric and the top/bottom side of the plasma treated PET non-woven. These high resolution XPS spectra can be utilized to analyze the chemical state of the elements present on the surfaces. As shown in figure 7.2 (a), the profiles of the C1s peak reveal differences between the raw fabric on the one hand and the treated fabrics on the other hand which suggests the presence of completely different bonds on the surface after plasma polymerization. The C1s spectrum of the original PET fabric can be decomposed into three components: a component at 285.0 ± 0.1 eV due to C-C or C-H bonds, a component at 286.5 ± 0.1 eV due to C-O bonds and a component at 289.1 ± 0.1 eV due to O-C=O bonds. In contrast, the C1s spectra of the plasma treated samples have a completely different profile: these surfaces no longer contain O-C=O bonds at 289.1 eV but do contain a small peak at 283.1 eV suggesting the presence of Si-C bonds. These C1s spectra thus indicate that the fabric surface has been covered with an organosilicon layer due to the plasma polymerization process. As shown in Figure 7.2 (b), the raw fabric does not contain any Si2p peak. However, this peak is present for the plasma polymerized samples suggesting again the successful deposition of an organosilicon film on the PET fabric. The Si2p spectra shown in figure 7.2 (b) can be deconvoluted into 4 components: a component at $105.\text{eV} \pm 0.1$ eV due to $(CH_3)_3SiO$, a component at 102.2 ± 0.1 eV due to $(CH_3)_2SiO_2$, a component at 102.8 ± 0.1 eV due to CH_3SiO_3 and a component at 103.4 ± 0.1 eV due to SiO_4 [135]. Starting from pure TMDSO, one would expect to only observe a peak at 102.2 eV but due to the addition of a small amount of oxygen in the discharge gas, a mixture of different silicon bonds is present in the plasma deposited films. It is also important to note that the C1s

and Si2p spectra of the top and bottom side of the plasma treated fabric have almost identical profiles confirming uniform chemical composition of the deposits throughout the PET fabric.
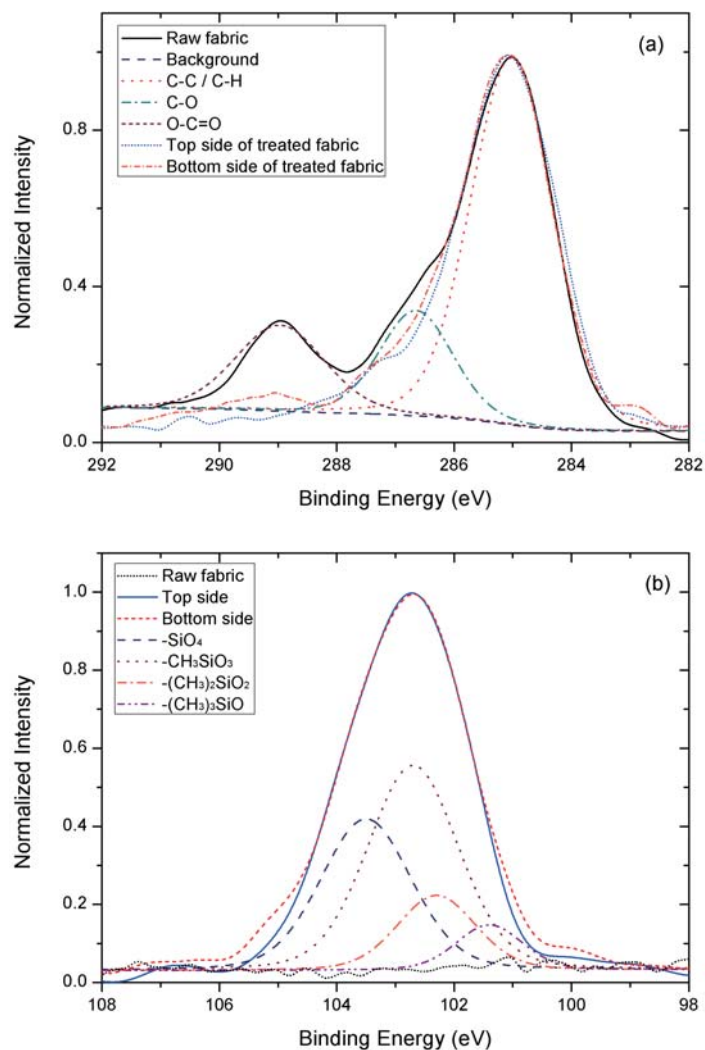
Figure 7.2: (a) High resolution C1s spectra for the raw PET fabric with the top and bottom side surface of plasma-polymerized fabrics. The C1s peak of raw PET fabric has been deconvoluted considering 3 groups; (b) High resolution Si2p spectra for the raw PET fabric with the top and bottom side surface of plasma-polymerized fabrics. The Si2p peak for plasma treated surface has been deconvoluted considering 4 groups.

7.4   Preparation of nanosilver non-woven fabrics with different barrier layers

7.4.1   Chemistry and morphology of the treated materials at different process steps

The chemical composition of the samples in different experimental steps was analyzed with XPS as shown in figure 7.3. In table 7.2, the corresponding results are presented. In the dipping and drying step, silver has been incorporated into the fabrics with a silver concentration of 1.9% on the surface. Oxygen and silicon concentrations decrease after incorporation of the AgNPs which is in good agreement with the observation in chapter 6. Silver concentration on the surface is reduced to 1.1% and 0.5% after deposition of a 10 nm and 50 nm barrier layer respectively. In our opinion, this effect is due to the blocking of the silver signal by the barrier layer surface. It is well know that XPS can be used to study the chemistry of the top 10 nm of a surface. As a result, one would expect to detect no silver concentration when a 10 nm or a 50 nm barrier layer is deposited on top of the AgNPs. However, in table 7.2, a small silver concentration is still present on the samples with the barrier layers on top. This effect can be attributed to the presence of cracks, pores or thin covering places on the points of AgNPs incorporation. While the reasons for the formation of the cracks and pores are not yet completely clear, it could be the result of thermal stress induced during the plasma deposition since a strong temperature gradient exists between the gas phase and the cold substrate. The presence of those imperfections in the barrier layer can be indirectly observed by the change of the Si signal in the XPS measurements. In the dipping and drying step, the silicon concentration is reduced from 21.6% to 15.2% due to the incorporation of the AgNPs. With the deposition of a 10 nm barrier layer, the Si concentration recovered to 19.9%. This value is lower than the value for the initial organosilicon film (21.6%) which suggests that the surface of the AgNPs was not completely covered by the 10 nm organosilicon film and that some imperfection areas are present in the thin barrier layer. Increasing the thickness of the barrier layer to 50 nm causes a further increase of the silicon percentage to 21.1%, which is close to the initial value due to the reduction of those imperfections. Thus, the imperfections in the 10 nm barrier layer can be clearly detected by XPS and can be considerably reduced by increasing the barrier thickness to 50 nm. Correspondingly, the thickness of the barrier layer is expected to be a key parameter in the control of the coating performance and the release of silver through imperfections.

Analysis of AgNPs incorporation on PET fibers was carried out with SEM. Figure 7.4 represents the surface morphology of the samples at different fabrication steps: (a) raw PET fabric, (b) deposition of a reservation layer; (c) incor-
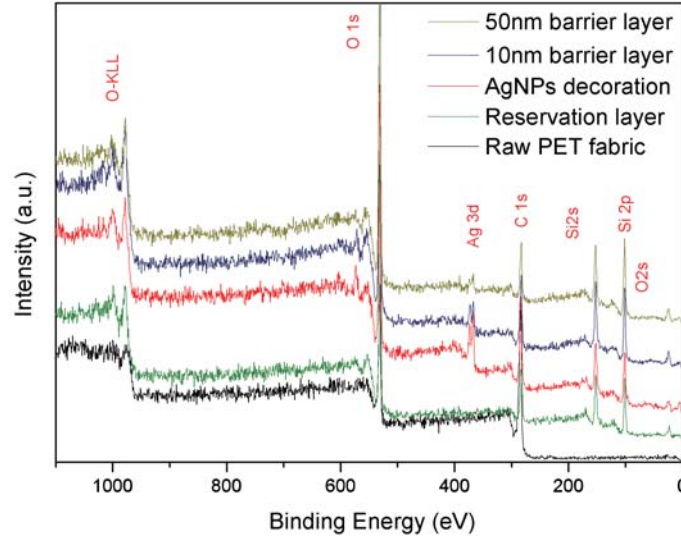
Figure 7.3: Survey spectra of the PET fabrics at different process steps.

Samples	C [at.%]	O [at.%]	Si [at.%]	Ag [at.%]
Raw fabric	73.4 ± 0.7	26.6 ± 0.8	0	0
With 1st layer	24.4 ± 0.8	54.0 ± 0.7	21.6 ± 0.6	0
AgNPs incorporation	37.9 ± 0.5	45.2 ± 0.7	15.2 ± 0.8	1.9 ± 0.3
With 10 nm 2nd layer	25.3 ± 0.6	53.7 ± 1.0	19.9 ± 0.8	1.1 ± 0.2
With 50 nm 2nd layer	24.7 ± 0.4	53.8 ± 0.8	21.1 ± 1.0	0.5 ± 0.1

Table 7.2: Atomic composition of the samples at different experimental steps and with variation of barrier layer thickness.

poration of AgNPs; (d) deposition of a barrier layer (50 nm). SEM figures with two different magnifications, i.e. $\times$ 1000 and $\times$ 10000, are presented on the left and right side respectively. The raw PET fabric consists of fibers with an average diameter of approximately 10 μm having a smooth surface as shown in figure 7.4 (a). After being treated with the first plasma deposition process (figure 7.4 (b)), the surface of the PET fibers is completely covered by a film. Figure 7.4 (c) is made after the dipping and drying step. Magnification of the surface reveals successful incorporation of silver particles on the fibers with a diameter of approximately a few tens of nanometers. A dramatic change of the surface morphology is observed after the barrier layer deposition. The surface of the PET fibers shown in figure 7.4 (d) is more smooth, which indicates the covering of the incorporated particles by a new film layer.
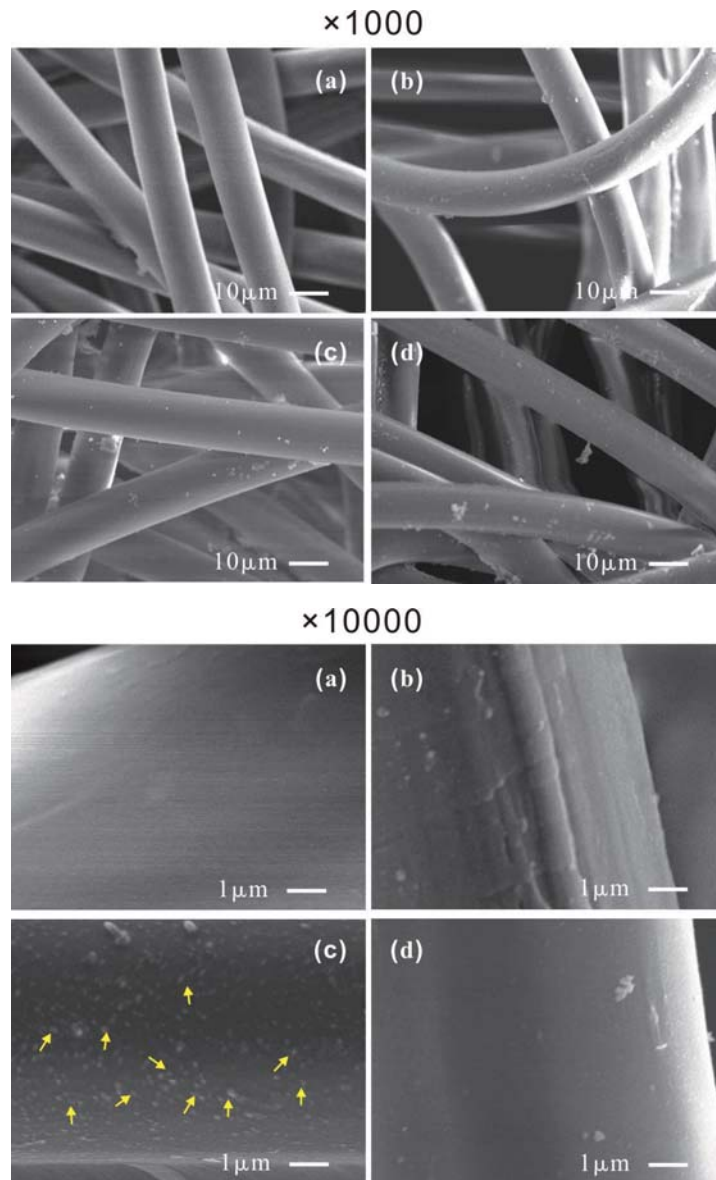
×1000

×10000

Figure 7.4: SEM images of the samples at different preparation steps. Two sets of SEM images with magnification of ×1000 (acceleration voltage:15 kV) and × 10000 (acceleration voltage 10 kV). (a) SEM images of original PET fabric; (b) the fabrics with a reservation layer, (c) the fabric after incorporation of AgNPs (labeled by some arrows on the image with ×10000 magnification), (d) the fabric with a 50 nm barrier layer.

7.4.2   Antimicrobial efficiency of the treated PET materials

To test the antimicrobial efficiency of the PET fabrics, the following test organisms were used: Pseudomonas aeruginosa (*P. aeruginosa*) ATCC 9027, Staphylococcus aureus (*S. aureus*) Mu50 and Candida albicans (*C. albicans*) SC5314, which are corresponding to a gram-positive bacteria, a gram-negative bacteria and a fungus respectively. *P. aeruginosa* infections are a serious problem in patients hospitalized with cancer, cystic fibrosis and burns; with high fatality rates [350]. *P. aeruginosa* is naturally resistant to a wide range of antibiotics. *S. aureus* is a pathogenic microorganism causing many diseases such as toxic shock syndrome, superficial skin lesions, deep-seated infections and is the leading overall cause of hospital acquired (nosocomial) infection of surgical wounds [350]. Moreover, it is resistant to a great number of antimicrobial agents [351]. *C. albicans* is the most common cause of opportunistic fungal infections and it can cause infections that range from superficial infections of the skin to life-threatening systemic infections [352]. Since all of the three microorganisms are considered as common potential pathogens for infections, those three aforementioned microorganisms were selected for evaluation of the antimicrobial efficiency in this research.

Before the assay, all samples were sterilized by a 30 minutes UV exposure. The microorganisms were grown on Tryptic Soy Agar (TSA) (Oxoid, Drongen, Belgium) (*P. aeruginosa* and *S. aureus*) or Sabouraud agar (Sab) (BD, Franklin Lakes, NJ) (*C. albicans*) under aerobic conditions at 37 ^{o}C. Using a sterile forceps, the samples were placed in the wells of a 24-well microtiter plate and subsequently 1 ml of the cell suspension, containing approx. 10^4 colony forming units (CFU)/ml was added. The plates were incubated for 24 h at 37C. Following incubation, the samples were transferred to 10 ml 0.9% (w/v) NaCl and subjected to three cycles of 30 s vortex mixing and 30 s sonication. Tenfold serial dilutions were made in 0.9% (w/v) NaCl and the number of CFU was determined by plate counting. To this end, one ml of each dilution was plated on TSA or Sab and the plates were incubated at 37C for 48 h. Percent reduction of organisms which indicates biostatic efficiency resulting from contact with the sample was determined using the formula 3.2. The control samples in this section are corresponding to samples with the deposition of the first film layer.

The antimicrobial properties of the samples were tested against P. *aeruginosa*, *S. aureus* and *C. albicans*. Initial sample with a 70 nm organosilicon film having no antimicrobial activity was used as a control. Antimicrobial capability of the treated PET fabrics without a barrier layer and with a 10 nm and 50 nm barrier layer is shown in figure 7.5. All samples with AgNPs exhibit antimicrobial activity against the three microorganisms, which clearly indicated that the growth of microorganisms in medium was affected by the presence of AgNPs. All treated PET fabrics show higher efficiency against *S. aureus* and lower against *P. aeruginosa*, which is in agreement with the results on commercially available silver-containing

dresses [353]. The samples with AgNPs but without a barrier layer have shown highest reduction of more than 90% of *S. aureus* and *C. albicans* and 80% of *P. aeruginosa*. Presence of the barrier layer results in a decrease of the antimicrobial efficiency to almost 50% reduction in the case of a 50 nm barrier layer. Such a strong effect of barrier layer can be linked to the way how AgNPs induce the antimicrobial effect.
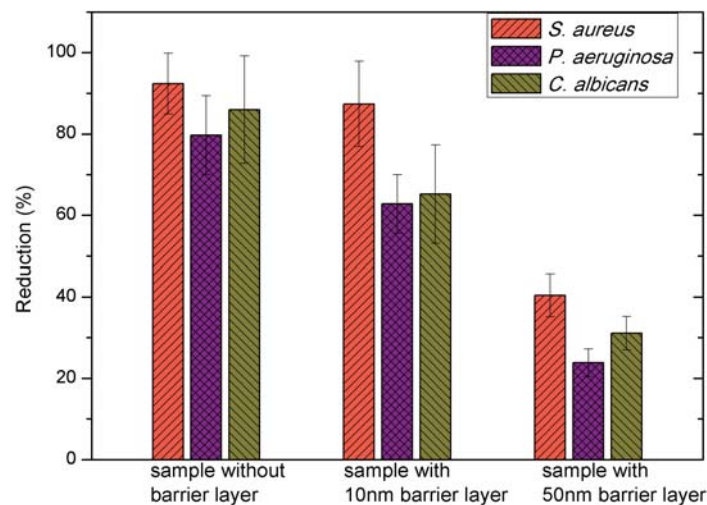
Figure 7.5: The reductions of the bacteria with the control sample, the treated sample with a 10 nm barrier layer and the sample with a 50 nm barrier layer against three microorganisms.

At present, the exact mechanism of antimicrobial activity of silver is not clear. The release of silver ions is believed to be the main contribution to the effect. Ionic silver has a strong affinity to electron donor groups in biological molecules containing sulphur, oxygen or nitrogen. It is therefore able to bind to thiol (-SH) groups in enzymes, and inactivates them and destroys cell membranes as well [354]. The DNA replication could also be inactivated due to the interaction with silver ions, as suggested by Thiel and Jung [355, 356]. It is well-known that silver nanoparticles can be oxidized after contact with the surrounding aqueous medium, either at the material-liquid interface or after water uptake by the polymer matrix. This results in the generation of silver ions, which diffuse to the liquid medium through the barrier layer, as shown in figure 7.6. On the scheme the first layer, the reservation layer, is used for AgNPs immobilization and to control the silver nanoparticles adhesion to the PET fibres. The second layer, the barrier layer, is used for precise control over the release of silver ions. The generation of silver ions is proposed as 2 steps processes through silver oxidation.

For the sample without the barrier layer, AgNPs on the materials have suffi-
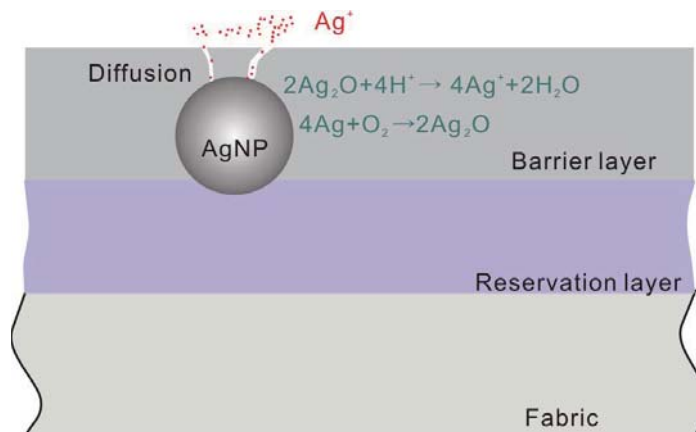
Figure 7.6: Scheme of silver ions generation and diffusion into a liquid medium.

cient contact with the medium. Therefore, they can provide a fast release of silver ions into the medium and exhibit the strongest antimicrobial activity against microorganisms. When a barrier film is deposited, the direct contact between AgNPs and the medium is hampered and the release of silver ions from AgNPs is reduced. In this case, the Ag^+ release is only possible through small cracks and pores in the barrier layer as it was shown in chapter 6. Moreover, the thickness of the barrier layer significantly influences the antimicrobial efficiency which is in contrast with work of Polux et al [357]. In their study, a heptylamine (HA) matrix was used for the loading of AgNPs and it showed that the thickness has no significant effect on the release of Ag ions due to the nanoporous morphology structure of HA, which enables Ag ions to diffuse through it freely. In the plasma deposition experiments performed in our work, increasing the thickness of barrier layers leads to a reduction in the number of cracks and pores in the organosilicon matrix which can be a way to control antimicrobial efficiency and to obtain prolonged antibacterial effect in the end-user product.

Additionally to the control of the antibacterial efficiency through deposition of a barrier coating, it is also of crucial importance for applications to avoid any release of AgNPs during the life time of the textiles and/or under mechanical stress which occurs during wearing and washing of articles. The efficiency of the produced PET samples under mechanical stress will therefore be examined in detail in the following section.

7.4.3   Antimicrobial efficiency under mechanical stress

As mentioned, direct contact of AgNPs with cells should be completely avoided due to their potential toxicity. Cytotoxic effect of silver nanoparticles is medi-

ated by the generation of oxidative stress resulting in a wide variety of physiologic and cellular events including stress, inflammation, DNA damage and apoptosis. In order to have those toxic effects, silver nanoparticles have to penetrate membrane and react with organelles, such as mitochondria. In our approach, the fixing AgNPs inside the coatings prevent the nanoparticles-cells reactions and further intracellular impact can be avoided. Therefore, we expect that the cytotoxicity of silver nanoparticles in the nanocomposite film is reduced. In this part, the durability of incorporated AgNPs in the materials is evaluated through a washing test of the samples after 1, 3, 5 and 10 washing cycles for 40 minutes each in a 200 ml of deionized water. All the samples were dried after washing in a vacuum prior to analysis. Figure 7.7 shows silver concentration on the top surface of three different samples after several washing cycles. The concentration shown in figure 7.7 is the average of 9 different locations on each sample. For the samples without a barrier layer, the silver concentration dramatically fluctuated with washing cycle. The interesting fact is that the concentration shows a steady rise to more than 3% for the first 3 washing cycles. Further washing processes lead to the reduction of silver concentration to about 1.3% and 0.4% after 5 and 10 washing cycles respectively.
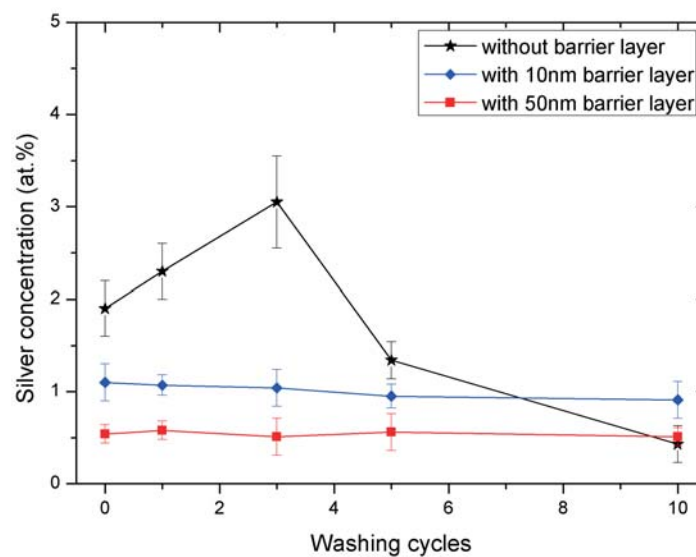
Figure 7.7: Silver concentrations of the samples after mechanical washing cycles. The silver contents were performed using the average of 9 different locations on each sample by XPS technique.

The effect at the beginning of washing can be explained by loosening of fibers in the non-woven structure and fast desorption of physically absorbed particles with migration from bulk of the material to the surface. Correspondingly, the
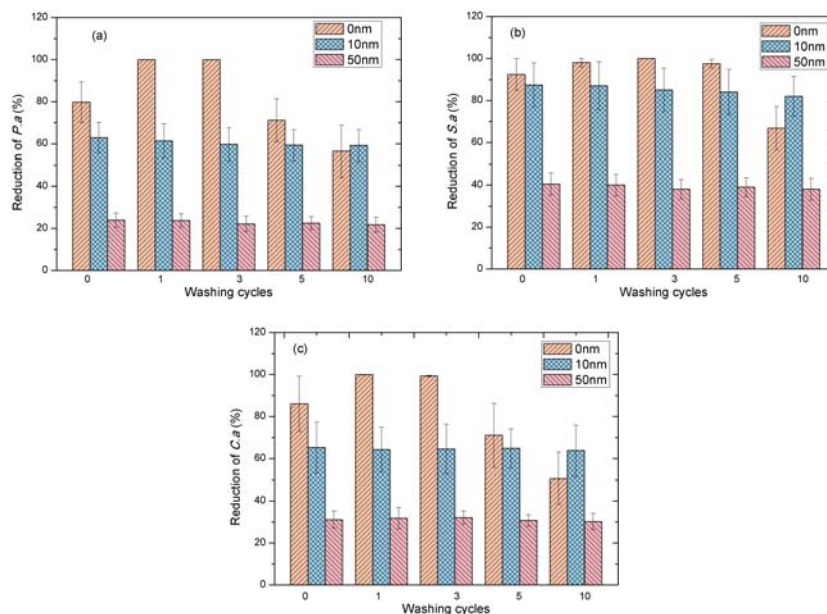
Figure 7.8: Antimicrobial activities of samples (without a barrier layer, with a 10 nm barrier layer and a 50 nm barrier layer.) after mechanical washing cycles against (a) P. aeruginosa*; (b)* S. aureus*; (c)* C. albicans*.*

increase of Ag signal in XPS analysis for the material without barrier layer is attributed to the release of free AgNPs. The reduction of silver concentration in the following washing cycles is due to the loss of nanoparticles absorption on fibers surface and spreading in the water. In samples without barrier layer, silver thus exhibits non-uniform kinetics of release at the first 5 washing cycles. This confirms the dramatic desorption and separation of AgNPs from this fabric. For the samples with 10 nm and 50 nm barrier layers, silver concentration on the surface has almost negligible fluctuations for all washing cycles. This conclusion clearly proves our conceptions to the use of barrier layers to prevent any release of AgNPs from the matrix.

The antimicrobial activity of treated fabrics with AgNPs in the absence and presence of a barrier layer was evaluated against *P. aeruginosa*, *S. aureus* and *C. albicans* after a series of washing cycles. The test results presented in figure 7.8 show that the general tendency of antimicrobial reduction is in perfect agreement with the XPS measurements of silver concentrations. For the samples without a barrier layer (orange bars in figure 7.8), a 100% reduction for the three microorganisms has been achieved after the first washing cycle. According to the XPS results in figure 7.8, this is due to a higher amount of AgNPs on the surface of the samples. This loose physical absorption of AgNPs can even cause the immigra-

tion of AgNPs into the bacterial suspension and result in a very high antimicrobial effect. This effect should however always be eliminated in any application. Moreover, after 5 times of washing, the antimicrobial activity reduced significantly due to the dramatic loss of AgNPs. For the samples with barrier layers (10 nm as blue bars and 50 nm as pink bars), the antimicrobial activity is maintained on a constant level and agrees with the XPS results, which confirms the stability of AgNPs bonding to the fibers and the positive effect of a barrier layer.

It is expected that samples with comparable silver concentrations would have similar antimicrobial activity. However, this is not always the case as observed for the samples after washing tests. According to the XPS analysis (figure 7.7), there were 0.4% and 0.5% of Ag on the samples without a barrier layer and the samples with a 50 nm barrier layer after 10 washing cycles respectively. However, as shown in figure 7.8, the bacterial reduction against three microorganisms of the sample without a barrier layer (orange bars) is higher than that of the sample with a 50 nm barrier layer (pink bars). In our opinion this phenomenon can be explained by the effect of the barrier layer preventing oxidation of AgNPs in liquid medium and release of silver ions. For the sample without a barrier layer after 10 washing cycles, all AgNPs on the surface were in direct contact with the medium and were affected by oxidation during the washing process which led to a high release of silver ions. While for the sample with a 50 nm barrier layer after 10 washing cycles, the release channels were limited to the cracks and pores on the barrier layer. Thus, even with comparable silver concentration on the surface for those two samples, the bacterial reduction was lower for the sample with a 50 nm barrier layer. Summarizing, barrier layer thickness has to be less than 50 nm if a high level of antimicrobial efficiency is required for the samples.

7.5 Preparation of nanosilver non-woven fabrics with various silver contents

The above section reveals that double layer immobilization of AgNPs in non-woven fabrics using an organosilicon matrix can provide a good way to control the release of silver ions with a high and lasting antimicrobial activity. In this section, fabrics with various incorporated silver AgNPs will be prepared and characterized. The preparation protocol is also the three-step process as depicted in figure 7.1, but with four different concentrations of the AgNPs dispersions (concentration of AgNPs in ethanol: 1 mg/ml, 2mg/ml, 5mg/ml, and 10mg/ml).

The top layer of 10 nm thickness was used as a barrier to prevent release of nanoparticles from the surface as described in section 7.4. The antimicrobial activity of the nano-silver fabrics was tested against *S. aureus* and *E. coli* by dilution method. The effect of silver concentration on the lag phase, the specific cell growth

rate, and the cell concentration has been studied and discussed based on bacterial growth curves as introduced in section 3.4.2.

7.5.1   Chemistry and morphology of the treated materials with various silver contents

In this work, four different concentrations of the AgNPs dispersions (concentration of AgNPs in ethanol: 1 mg/ml, 2mg/ml, 5mg/ml, and 10mg/ml) were prepared in order to easily control the amounts of incorporated silver onto the materials. All samples were structured by a 70 nm of reservation layer, then incorporated with AgNPs and coved by a 10 nm organosilicon film which is serviced as a barrier to prevent release of nanoparticles. The chemical compositions of the samples prepared with four different concentrations of AgNPs dispersions are determined with XPS and presented in figure 7.9.
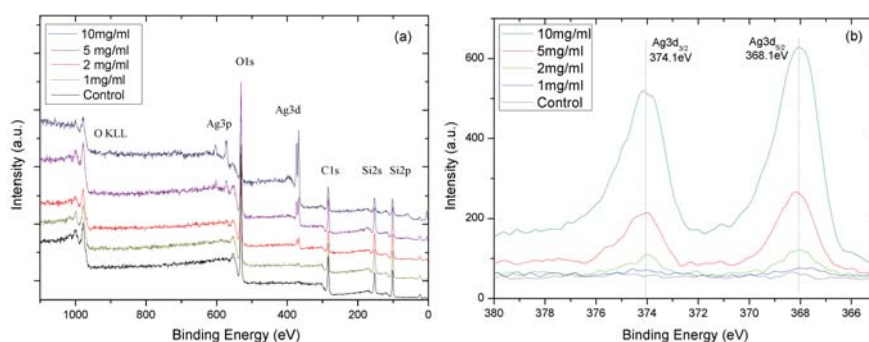
Figure 7.9: (a) XPS survey spectra of control samples and silver treated samples, (b) high-resolution XPS spectra of Ag3d for control samples and silver treated samples.

The XPS survey spectra acquired from the control sample and the silver treated samples in figure 7.9 (a) reveal peaks corresponding to Si, C, Ag, and O. The intensity of Ag 3d peak increases which indicates that the control of AgNPs incorporation can be achieved by the variation of the concentration of AgNPs dispersion. The silver concentrations, determined from the XPS survey spectra of the samples prepared with 10 mg/ml, 5 mg/ml, 2 mg/ml, 1 mg/ml AgNPs dispersions, are 7 $\pm$ 0.6, 1.9 $\pm$ 0.4, 0.9 $\pm$ 0.3, and 0.1 $\pm$ 0.2 at.%, respectively. It is well known that XPS can be used to study the chemistry of top surface within few nanometers. The appearance of Ag signal for the samples with covered barrier layers indicates the present of approaches for X-ray signal to reach silver. And it is believed to be cracks, pores or thin covering layer in the place of AgNPs incorporation. The high resolution spectra of the Ag 3d peaks in figure 7.9 (b) reveal that the binding energies of Ag 3d5/2 and Ag 3d3/2 of the silver nanoparticles are between 367 eV and 370 eV and between 374 eV and 375.5eV, respectively. A spin-orbit separation of
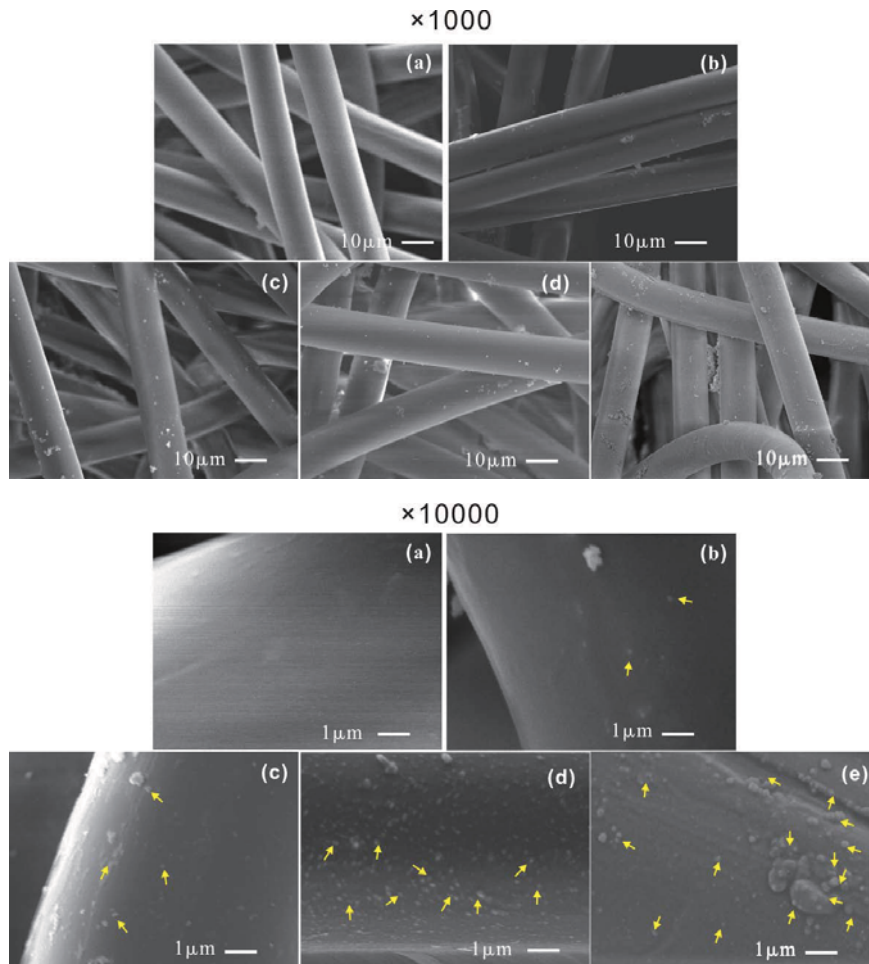
Figure 7.10: SEM image of the control sample (a) and the samples treated with 1 mg/ml (b), 2 mg/ml (c), 5 mg/ml (d) and 10 mg/ml (e) of AgNPs dispersion. The arrows on the image with × 10000 magnification indicate some AgNPs.

Ag 3d5/2 and Ag 3d3/2 peaks is 6.0 eV indicating the presence of metallic silver nanoparticles in the film. The energies are in good agreement with the reported values for the binding energies of silver nanoparticles [203]. While, comparing to the binding energy of Ag 3d5/2 for bulk metal Ag at 368.2 eV, a positive chemical shift observed for Ag 3d5/2 (at 368.1 eV) suggests that silver nanoparticles are small oxidized in the process.

Figure 7.10 represents the SEM image of the raw samples and the samples prepared with four various AgNPs suspensions at two magnifications, i.e. × 1000 and × 10000. The raw PET fabric consists of fibers with an average diameter of

approximately 10 μm and a smooth surface as shown in figure 7.10 (a). Figures 7.10 (b-e) suggest the covering of the PET fabrics after the treatment. As labeled by the yellow arrows in the high magnification figures, AgNPs were uniformly incorporated on the PET surface.

7.5.2   Antimicrobial efficiency of the treated PET materials with various silver contents

Antibacterial activity of the treated fabrics was tested by using macrodilution method against Escherichia coli (*E.Coli*) and Staphylococcus aureus (*S.aureus*). The samples were immersed in bacterial suspensions of culture (10^6 CFU/ml), and then were incubated at 37 ^{o}C for 24 h to analyze the number of colony forming units (CFU). Reduction of microorganisms R which indicates biostatic efficiency resulting from contact with the samples was determined by the formula 3.2. The sample with only first layer deposition was used as a control. The kinetics of bacterial growth in tryptic soy broth (TSB) was studied through the optical density of cultured medium at = 600 nm as introduced in section 3.4.2.

The capability of the fabrics to prevent viable bacteria colonization was verified by plate counting technique (PCT). Figure 7.11 shows typical colonization by *E.coli* and *S. aureus* on Mueller Hinton (MH) agar plates from the liquid medium cultured with samples containing different amount of AgNPs. All silver treated PET fabrics exhibited antibacterial activity against both bacteria, which clearly indicated that the growth of microorganisms in medium was affected by the presence of AgNPs on the fabrics. The numbers of survived colonies of *E. coli* and *S. aureus* on the agar plates decreased for the samples with higher silver concentration.

The bacterial reduction of *E. coli* and *S. aureus* is presented in figure 7.12. The trend indicates that the silver treated fabrics were more effective against *E. coli* than *S. aureus*. A great reduction of the bacterial growth was observed on the fabric samples prepared with 5 mg/ml of AgNPs dispersion. The reduction rates of *E. coli* and *S. aureus* achieved 100% and 99.7%, respectively. There was no cultivated and grown bacterium for the samples prepared with 10 mg/ml of AgNPs dispersion.

As introduced in section 3.4.2, the growth of bacteria in liquid culture medium should normally follow an exponential and can be divided into four major phase: lag phase, exponential phase, stationary phase and decline phase. The growth profiles are displayed in figure 7.13 for *E. coli* and *S. aureus* in TSB medium. In this work, only first three phases will be discussed which provide a clue to understand the kinetic details of the growth or inhibition [358]. Typically, the bacterial growth curves in this work can be divided into three major phases, which provide a clue to understand the kinetic details of the growth or inhibition [358]. Three main microbial growth kinetic parameters can be estimated : the lag time
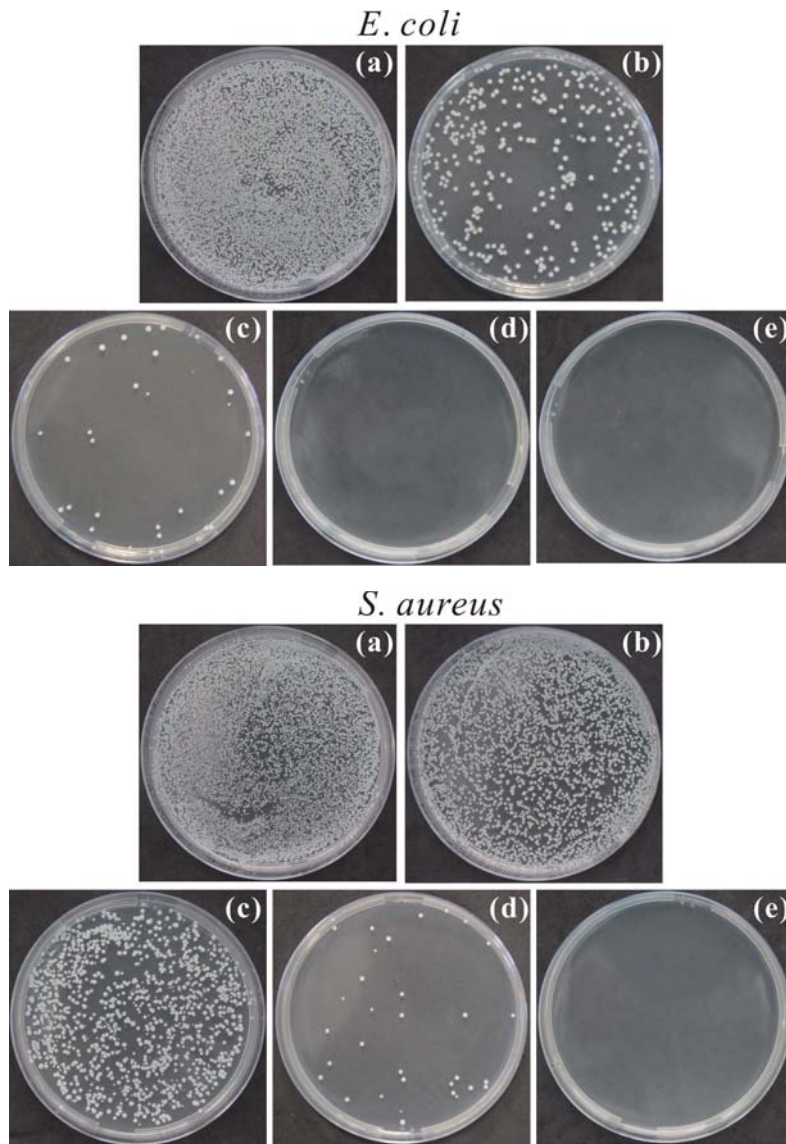
Figure 7.11: Photographs of E. coli *colonies and* S. aureus *on MH agar plates incubated with different samples: (a) control, (b-e) samples prepared with 1 mg/ml, 2 mg/ml, 5 mg/ml and 10 mg/ml of AgNPs dispersion, respectively.*

(T_{lag}); the specific cell growth rate during the exponential growth phase (μ); and the final cell concentration (C_f) as suggested by Han et al. [292]. The main kinetic parameters for growth curves are listed in Table 7.3, where a strongly correlation
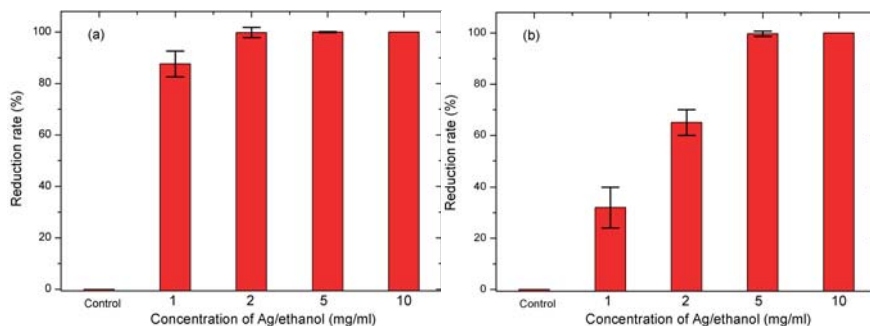
Figure 7.12: Antibacterial efficiency of the samples against E. coli *(a) and* S. aureus *(b).*
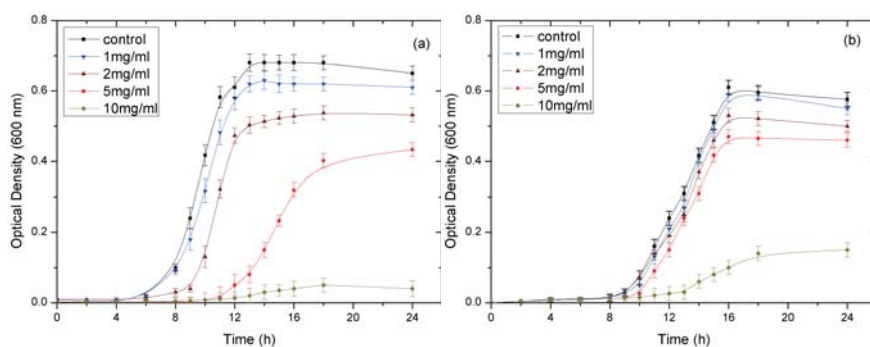
Figure 7.13: Bacterial dynamic growth curve in TSB medium with samples prepared with different concentration of silver dispersion. (a) E. coli*; (b)*S. aureus*.*

to concentration with deposited silver was observed.

For the fabrics prepared with 1 mg/ml AgNPs dispersion, there was no change in the lag time for two strains. The growth rate and final cell concentration of *E. coli* were reduced by 16.96% and 8.82%, respectively. Conversely, the same concentration exhibited only weak activity against *S. aureus* with 3% reduction in T_{lag} and (μ). The increase of the concentration of AgNPs dispersion (2 mg/ml and 5 mg/ml) with deposition to the fabrics exhibited a delay in lag time For the fabrics treated with 10 mg/ml AgNPs dispersion, the growth of *E. coli* were completely inhibited, and growth of *S. aureus* was significantly reduced. *S. aureus* were more resistant to and showed higher growth rates contrary to *E. coli*. The reason for this could be found the peptidoglycan in the cell walls of Gram-positive bacteria which provides higher cell protection for penetration of silver ions into the cytoplasm, since it is much thicker than that in the Gram-negative ones [336]. For this reason, the optimize dosage of AgNPs has to be deposited in order to improve performance on new fabric against both types of bacteria.

AgNPs dispersion	Strains	μ (h^{-1})	reduction of μ(%)	C$_f$ (OD$_{600}$)	reduction of C$_f$
Control	*E.coli*	0.374	-	0.68	-
1mg/ml	*E.coli*	0.311	16.96	0.62	8.82
2mg/ml	*E.coli*	0.255	31.76	0.54	20.88
5mg/ml	*E.coli*	0.207	44.55	0.43	36.32
10mg/ml	*E.coli*	0.015	95.99	0.05	92.65
Control	S. aureus	0.248	-	0.61	-
1mg/ml	*S. aureus*	0.239	3.19	0.59	3.28
2mg/ml	*S. aureus*	0.211	14.93	0.53	10.17
5mg/ml	*S. aureus*	0.188	24.16	0.47	11.32
10mg/ml	*S. aureus*	0.045	81.05	0.14	72.28

Table 7.3: Effect of incorporated silver on the specific growth rate and final cell concentration of E.coli *and* S. aureus*.*

7.6   Conclusions

In this chapter, antimicrobial nano-silver PET fabrics were prepared through a three step process based on atmospheric pressure plasma deposition process. It was revealed that plasma can penetrate through non-woven fabric structure and that uniform double side deposition can be achieved. AgNPs were imbedded between two layers of organosilicon films: a reservation layer (1st layer) and a barrier layer (2nd layer). Variation of the barrier layer thickness is proposed as a novel precise method to control release of silver ions and antimicrobial activity of the substrate. SEM and XPS results show that AgNPs can be uniformly distributed in PET materials. Antimicrobial tests against *P. aeruginosa*, *S. aureus* and *C. albicans* revealed that samples with a 10 nm barrier layer have stronger activity than those with a 50 nm barrier layer. Durability of silver nanoparticles bonding in the matrix was also investigated as an important factor through washing process. Silver concentration in samples without a barrier layer showed significant fluctuation after several washing cycles. This is explained by desorption of physically absorbed AgNPs from non-woven materials and migration to the medium during washing process. For samples with a barrier layer, however, effective immobilization of silver in the matrix was confirmed with stability of antibacterial effect even after 10 washing cycles. Besides, control of antibacterial activity of PET fabrics is obtained by variation of immobilized silver concentration in double layer coatings. Effect of silver concentration on key microbial growth kinetic parameters, i.e. lag time, reduction rate and final cell concentration is studied through bacterial growth curves. Results suggest that the methods for immobilization of AgNPs and control of silver content in non-woven fabrics might present a new route to preparation of complex topology structure materials with high and lasting antimicrobial activity.

8

Characteristics of a planar RF atmospheric pressure plasma source

8.1 Introduction

In the previous chapters, main focus has been put on the development of new coatings using plasma jet process. In fact, acceptance of the new technology by industry is directly related to possibility of upscale the system for deposition and production of new materials on large scale. Therefore, it is crucial important to develop methods to upscale the plasma system, as it is the fundamental for industrial application of plasma deposited coatings. As overviewed in chapter 2, numerous types of plasma jets have been developed in the past years. However, dimensions of developed APPJs nozzles and the DC plasma jet investigated in this thesis are mostly very small (sub-millimeter to several millimeters), which is a major drawback and limitation for some large-scale applications, such as surface modification and film deposition [93–95]. To overcome this barrier, two main strategies have been developed to obtain an up-scaled plasma jet source working in ambient air: (1) plasma jet arrays consisting of a number of individual plasma jets, (2) plasma jets with large cross section. The first approach can enlarge the overall dimension of plasma jets by combining small plasma jet devices together. There are one-dimension (1D) and two-dimension (2D) arrangements of identical plasma jets. However, uniform treatment is difficult to achieve due to complex gas and plasma distribution in working units of arrays [114]. Another disadvantage of the use of plasma jet arrays is complex interaction between individual jets, as has been ob-

served by many researchers [111]. Final point of concerns is requirement of very high gas flow to sustain a jet array and use of multiple the power supplies or external circuit for ignition of an array. As illustration of the problem we can consider upscale of N2 DC plasma jet to 15 cm wide plasma source. Operation of the array will use at least 10 jets with total gas flow of around 80 l/min and total loss of electrical power in ballast resistors will be about 1 kW.

The second strategy to produce plasma with large cross section is mostly achieved by enlargement of electrodes surface. Development of such new plasma source can be considered interesting in many fields including plasma medicine and plasma deposition. Unfortunately, current knowledge of such discharges physics is very limited and most research on the subject has been based on optical emission spectroscopy (OES) and electrical measurements, e.g. Lissajous figures.

In this chapter, a barrier discharge large scale plasma source excited by RF voltage of 13.56 MHz is developed and investigated with time resolved emission spectroscopy, absolute spectroscopy and high speed intensified charged coupled device (ICCD) camera. In contrast to most plasma jets, the source is characterized by an afterglow with a width of about 30 mm, which can be easily upscaled to any industrial demands. In this study the source is characterized by the main parameters: electrons density ne, electrons temperature T_e, gas temperature T_gas. Also physics of discharge generation and afterglow formation is investigated. The aim of study is to improve the understanding on plasma temporal dynamics in active zone and outside afterglow, and to provide a suitable plasma source for large scale processes including plasma deposition of antibacterial coatings.

8.2   Experimental details

Structure of the plasma device and experimental arrangement are schematically shown in figure 8.1. The plasma device consists of two parallel planar electrodes with a length of 30 mm. The high voltage (HV) electrode, coved by a 0.5 mm thick dielectric material in order to prevent formation of filamentary discharge, is connected to a radio frequency generator (Advanced Energy Cesar 133RF) through a matching box. The ground electrode is put 2 mm away from the dielectric plate. A compact stainless steel house is used to hold the electrodes. Argon gas with flow rate of 8 slm is used as working gas. It is noted that the electrode assembly was made airtight, thus preventing air leakage into the discharge region. When RF high voltages are applied to the HV electrode and Ar is supplied to the device, discharge is ignited and produces diffuse plasma, which can fill the entire discharge space. Meanwhile, a brush-shape homogeneous plasma afterglow is formed in the ambient air.

Waveforms of applied voltage and discharge current are recorded by a 4-channel oscilloscope (Lecroy Wavesurfer 64Xs) using a radio frequency probe (SOLAYL
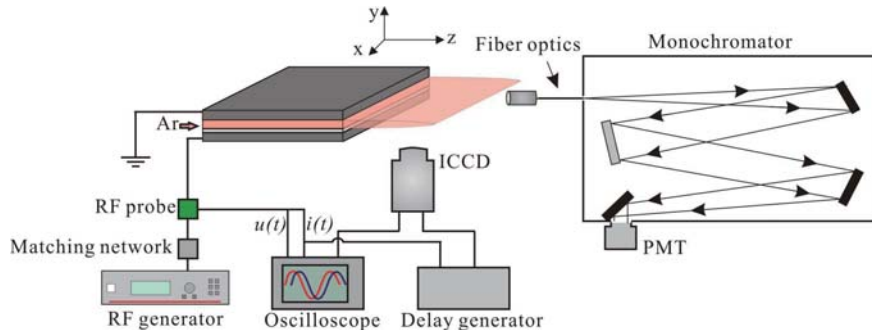
Figure 8.1: Schematic diagram of device structure and experimental setup.

Vigilant-Sensor). Optical emission spectrum is collected by two different spectrometers through fiber optics. For a survey emission spectrum (250 - 850 nm), a S2000 Ocean Optics spectrometer with moderate resolution of 0.8 nm full width at half maxima (FWHM) is used. In order to obtain gas temperature high resolution spectra of OH (A-X) bands are measured by an Avantes 3648 spectrometer with resolution of 0.05 nm FWHM. Discharge generation mechanism is studied by synchronizing the detector (PMT tube or ICCD camera) with plasma discharge current. Temporal resolved emission of two main species: OH radicals and Ar excited 2p states is detected with Hamamatsu R928 photomultiplier tube (PMT) in combination with a SR430 photon counter. Time resolved discharge dynamics are also studied by use of a Hamamatsu ICCD camera (C8484). ICCD camera gating time is synchronized to the discharge current using a delay generator (Stanford Instrument DG535). Exposure time of the ICCD camera is fixed at 5 ns.
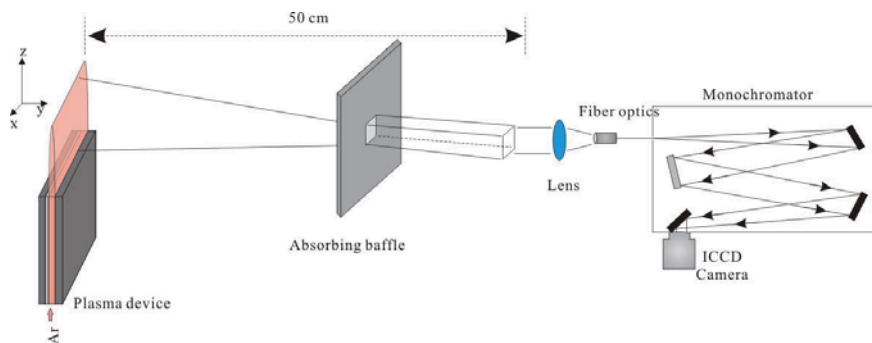
Figure 8.2: Schematic diagram of experimental setup for absolute OES measurements.

The optical system is absolutely calibrated with an Oriel model 63355 tungsten-D2 lamp and corresponding plasma irradiance in $Wm^{-2}nm^{-1}$ is measured. The experimental arrangement for absolute OES measurement is schematically shown

in figure 8.2. The plasma device is put 50 cm away from one plane plate with a $1 \times 1\ cm^2$ aperture. An absorbing baffle with a square aperture of $0.8 \times 0.8\ cm^2$ is placed between the jet source and the plane plate, and used to project the discharge emission light through the aperture on the plate. All three parts are centered precisely on the same optical axis with help of a He-Ne visible laser beam. A UV-vis lens is used to collect the $1 \times 1\ cm^2$ light into the optical fiber connected to the monochromator-ICCD OES system. All experimental arrangements mentioned above are fixed and applied identically for the tungsten lamp for calibration purpose. In this way, spectral irradiance $I_{P,\lambda}(\lambda)$ from the plasma device at a distance of 50 cm can be calibrated by:

$$I_{P,\lambda}(\lambda) = \frac{h_{P,\lambda}(\lambda)}{h_{L,\lambda}(\lambda)} I_{I,\lambda}(\lambda) \tag{8.1}$$

Where $I_{L,\lambda}(Wm^{-2}nm^{-1})$ is spectra irradiance from the calibration lamp at same distance of 50 cm, $h_{P,\lambda}(\lambda)$ and $h_{L,\lambda}(\lambda)$ are relative emission intensities from plasma and tungsten lamp measured by the same OES system, respectively. In calibration, settings (slit width, grating, exposure time of ICCD, etc) of the OES system are kept the same for measurements of both plasma and lamp.

8.3   Results and discussion

8.3.1   Visual view of RF-DBD plasma source

In order to investigate plasma performance, images of the RF-DBD plasma jet were taken. Attention is given to plasma discharge region as well as afterglow re-
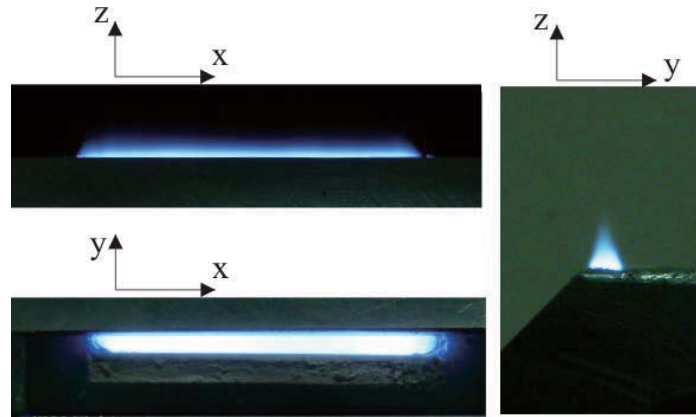
Figure 8.3: Front view and side view of plasma discharge region and afterglow region of the plasma jet with 8 slm of argon flow and with 25 W of dissipated power.

gion. Figure 8.3 shows front view and side view of both regions with 8 slm argon flow and 25 W dissipated power. As can be seen, the plasma in discharge zone exhibits a homogeneous and bright white emission, which indicates uniform and intense plasma is generated in between the electrodes. Due to flowing of working gas through the nozzle, an afterglow with brash-shape is formed in ambient air. Unlike conventional atmospheric plasma sources which are usually characterized by small dimensions, the brush-shaped plasma shows uniform distribution and has larger dimension than typical plasma jets. These features provide great potential for surface cleaning and modification, particularly to objects with complicated structures and large surface area. In addition, since the laminar plasma takes thin and broad (both in width and in height) shape, larger plasma surface area is exposed to ambient air, which can greatly improve release of heat, leading to gas temperature reduction.

In general, afterglow is characterized as a uniform and long plasma volume. Afterglow width in x-axial direction is 30 mm, similar to of the exit, and reduced to around 28 mm in frontier of the afterglow. Similarly, afterglow has a dimension of 2 mm in y-axial, reducing gradually in z-axial direction, and eliminated completely after a certain distance (length of the afterglow). For conditions in figure 8.3, the afterglow length is about 8 mm. It is noticed that emission intensity of the afterglow decreased along with gas flow, and the color of the afterglow changed from white to light blue probably due to presence of N_2 and OH emission in those parts of the jet.

8.3.2   Electrical property

Typical waveforms of applied voltage and discharge current of the RF-DBD plasma source are shown in figure 8.4. Both discharge current and applied voltage are almost perfectly sinusoidal. These waveforms are similar to those found in typical RF atmospheric pressure glow discharge with bare electrodes [359, 360]. In contrast, their sinusoidal character is distinctly different from atmospheric DBD generated at kilohertz frequency where discharge current is distinctively non-sinusoidal and short high current pulses of some hundreds of nanoseconds are normally presented in the current waveform indicating formation of microdiscahrges or filaments [43, 151]. In RF plasma source the peak values of the current and voltage are 0.72 A and 211 V respectively, with the current leading the voltage by a phase shift of around 70°. Both waveforms are smooth, consistent with the temporally uniform discharge emission. In addition, the nearly sinusoidal waveforms indicate the capacitive nature of the RF planar discharge.

Considering the dynamic generation of RF discharge, we noted that application of RF high-voltage with input power of about 70 W is required to ignite strongly filamentary γ mode discharge. Discharge can be transferred in a diffuse mode,

filling the entire discharge space by decrease of input power to 20 - 30 W. In diffuse α mode, a brush-shape homogenous plasma afterglow with total length of up to 8 mm can be generated along the slit in ambient air.

A current/power diagram of the discharge is shown in figure 8.5. Total RMS current in glow-like mode depends on applied voltage and is about 0.33 - 0.48 A. Due to lower potential of afterglow, the discharge effluent can be touched by hand without any risks of electrical shock. It is found that only 50 % or less of total current is attributed to plasma current, while the rest is displacement current. Power required to sustain the discharge in diffuse mode can be varied in a range of 15 - 28 W with less than 1 W of reflected power but at least 50 % of input power is dissipated in the system due to capacitive loss in α mode as shown in figure 8.5. Increase of discharge current to more than 0.5 A (RMS value) leads to sharp drop in plasma resistance, power increase and transformation of diffuse plasma to filamentary discharge.

8.3.3   Optical emission spectroscopy

8.3.3.1   Optical emission spectra overview

To identify various reactive species produced in the plasma afterglow, optical emission spectroscopy has been performed. Figure 8.6 shows typical overview emission spectra of argon plasma afterglow in surrounding air. The spectrum is measured in the afterglow region located about 2 mm in front of the slit. The
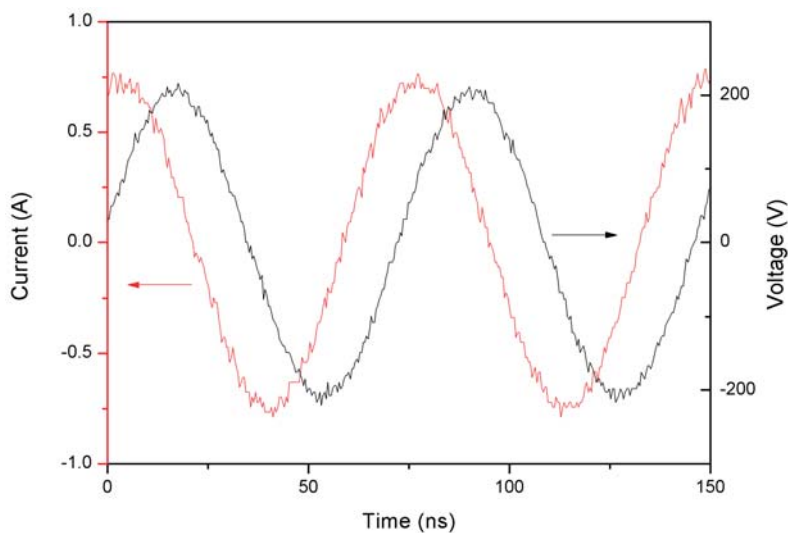
Figure 8.4: Typical waveforms of applied voltage and discharge current of the RF-DBD plasma source.
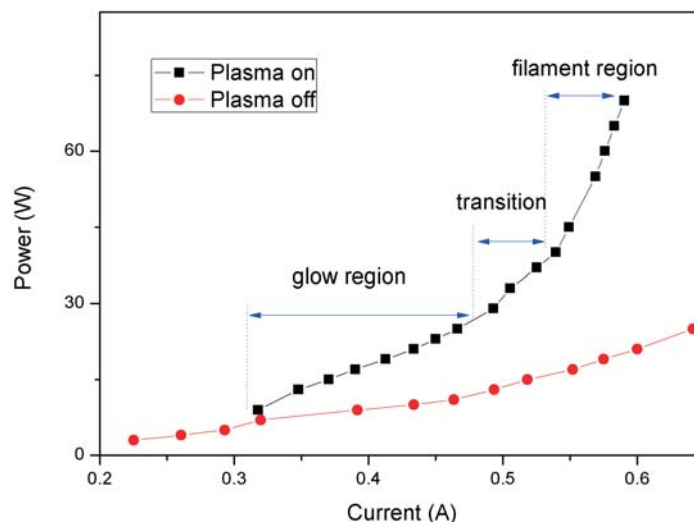
Figure 8.5: Discharge power vs. RMS discharge current when plasma is ON and when plasma is OFF (no Ar gas is applied).

identified spectra lines and molecular bands are summarized in table 8.1. As can be seen, upper wavelength region between 700 and 850 nm contains mainly lines emitted by argon atoms excited in 4p states (Ar($4p \rightarrow 4s$)transitions). Besides argon atomic spectra lines, molecular bands of inevitable impurities are observed: OH($A^2\Sigma \rightarrow X^2\Pi$), N$_2$($C^3\Pi_u \rightarrow B^3\Pi_g$) and O($5p \rightarrow 5s$). Also, afterglow exhibits strong continuum radiation in the range of 300-750 nm due to Bremsstrahlung radiation [361,362]. Appearance of OH emission is mainly caused by H$_2$O impurity in the main stream of argon gas as observed in other works [249]. N$_2$ and atomic oxygen emission is attributed to air diffusion into the argon gas stream due to propagation of the jet in ambient air. Presence of molecular bands of OH radicals and N$_2$ excited states allows estimating gas temperature of the afterglow. The continuous emission with absolute calibration can be used to determine electron density and electron temperature as will be shown later.

It is known that in Ar plasmas with small admixture of molecular gases (nitrogen, oxygen and water), production mechanisms of excited species are very complex, as reported in [363–365]. Dominant generation processes of excited species (Ar(4p), Ar(4s), O(3p), N$_2$(C), OH(A)) in the argon plasma jet device are listed in table 8.2. Due to their short lifetime, Ar(4p) states do not transport far from where they are formed before radiating [366]. Therefore, we can assume that Ar(4p) observed in afterglow region is produced onsite. The generation process of Ar(4p) by cascade transition is negligible due to the absent of emission by transitions from upper levels to Ar(4p). Direct electron excitation from ground state and step ex-
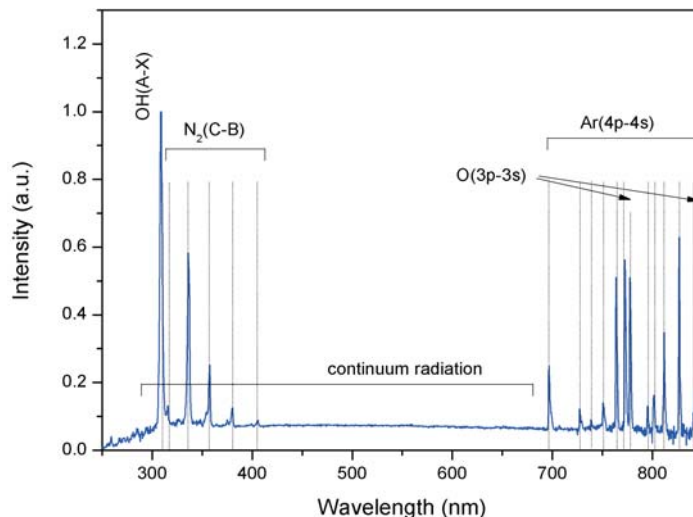
Figure 8.6: Overview of emission spectra of the plasma afterglows.

citation from Ar(4s) are the two main transitions for Ar(4p)generation. Atomic oxygen can be generated due to oxygen molecules dissociation by excited argon state (Ar(4s) and Ar(4p)) and by electrons. Electron step-excitation and pooling reaction related to metastable $N_2(A)$ are considered and may play a role in producing excited state $N_2(C)$ while plasma propagates in surrounding air. Besides being produced by $N_2(C-B)$ transition, $N_2(B)$ can also be generated by processes similar to $N_2(C)$ production. OH(A) radicals can be produced either by electronic dissociation and excitation of H_2O or due to collisions with long lived species, e.g. argon 4s metastable states.

Since reactive species are the main agents facilitating reactions in plasma treatments and plasma deposition, deposit uniformity and film growth rate is strongly affected by spatial profiles of these reactive species in the afterglow. Distribution of reactive species is influenced by plasma operational parameters, including electrical field and electron density as well as source operational parameters, e.g. gas flow and input RF power. For plasma sources with a large dimension, non-uniform distribution of active species in afterglow has been observed in a DC brush plasma device [119] and a DBD brush plasma device [371]. In the DC brush plasma device [119], appearance of peaks at the two edges was attributed to the arrangement of two electrodes at the edges, where cathode and anode glow were formed by energetic electrons. On the other hand, formation of the non-uniform afterglow by in DBD brush plasma device [371] was explained by different mixing ratios of surrounding air with the gas stream, which could result in different reaction possibilities. In this work, optical emission of OH(337.8 nm), N_2 (337.1 nm), O

Species	$\lambda(nm)$	Transition	E(eV)
OH	309	$OH(A^2\Sigma \to X^2\Pi)$	4.0
N_2	315.9; 337.1; 357.7; 380.5; 405.8	$N_2(C^3\Pi_u \to B^3\Pi_g)$	11.0
Ar I	696.5	$3s^23p^5(^2P^0_{1/2}4p - 3s^23p^5(^2P^0_{3/2})4s$	13.33
Ar I	706.7	$3s^23p^5(^2P^0_{1/2}4p - 3s^23p^5(^2P^0_{3/2})4s$	13.3
Ar I	727.3	$3s^23p^5(^2P^0_{1/2}4p - 3s^23p^5(^2P^0_{3/2})4s$	13.33
Ar I	738.4	$3s^23p^5(^2P^0_{1/2}4p - 3s^23p^5(^2P^0_{3/2})4s$	13.3
Ar I	751.5	$3s^23p^5(^2P^0_{3/2}4p - 3s^23p^5(^2P^0_{3/2})4s$	13.27
Ar I	763.5	$3s^23p^5(^2P^0_{3/2}4p - 3s^23p^5(^2P^0_{3/2})4s$	13.17
Ar I	772.4	$3s^23p^5(^2P^0_{1/2}4p - 3s^23p^5(^2P^0_{1/2})4s$	13.15
Ar I	794.8	$3s^23p^5(^2P^0_{1/2}4p - 3s^23p^5(^2P^0_{1/2})4s$	13.28
Ar I	801.5	$3s^23p^5(^2P^0_{3/2}4p - 3s^23p^5(^2P^0_{3/2})4s$	13.1
Ar I	811.5	$3s^23p^5(^2P^0_{3/2}4p - 3s^23p^5(^2P^0_{3/2})4s$	13.08
Ar I	826.5	$3s^23p^5(^2P^0_{1/2}4p - 3s^23p^5(^2P^0_{1/2})4s$	13.33
Ar I	842.5	$3s^23p^5(^2P^0_{3/2}4p - 3s^23p^5(^2P^0_{3/2})4s$	13.09
O I	777.2	$2s^22p^3(^4S^0)3p - 2s^22p^3(^4S^0)3s$	10.74
O I	844.6	$2s^22p^3(^4S^0)3p - 2s^22p^3(^4S^0)3s$	10.99

Table 8.1: Most intensive emission lines in the spectrum of the plasma jet.

Excited species	Generation Processes	Rate	Ref.
Ar(4p)	Ar+e→Ar(4p) +e	$\sigma(\varepsilon)$	[367]
	Ar(4s)+e→Ar(4s)+e	$\sigma(\varepsilon)$	[367]
Ar(4s)	Ar+e → Ar(4s)+e	$\sigma(\varepsilon)$	[367]
	Ar(4p) → Ar(4s) + hν	$2.5 \times 10^{-7}s^{-1}$	[363]
O(3p)	Ar(4p)/Ar(4s)+O_2 → O+O+Ar	$5.8 \times 10^{-11}cm^3s^{-1}$	[364, 365]
	Ar(4p)/Ar(4s)+O(3s)→O(3p)+Ar	$5.8 \times 10^{-11} \times (T)^{1/2}$	[363]
	O_2+e→O(3p)+O(3p)+e	$\sigma(\varepsilon)$	[363]
N_2(C)	N_2(X)+e→N_2(C)+e	$\sigma(\varepsilon)$	[363]
	N_2(A)+e→N_2(C)+e	$\sigma(\varepsilon)$	[306]
	N_2(A)+N_2(A)→N_2(C)+N_2(X)	$1.5 \times 10^{-10}cm^3s^{-1}$	[368]
	N_2(X)+Ar(4p)/Ar(4s)→N_2(C)+Ar	$10^{-11} \sim 10^{-10}$	[369]
OH(A)	H_2O+e→ OH(A)+H+e	$\sigma(\varepsilon)$	[363]
	H_2O+Ar(4p)/Ar(4s)→OH(A)+H+Ar	$10^{-10}cm^3s^{-1}$	[370]

Table 8.2: Main generation processes of active species in the argon plasma jet device. $\sigma(\varepsilon)$ is cross section of the corresponding reaction, and ε is electron energy.

(777.2 nm) and Ar (772.4 nm) are spatially examined in transverse direction, e.g. x direction. Figure 8.7 shows that all reactive species present a near-symmetrical

distribution of emission profile, with small fluctuations in the center region. This suggests that reactive species are uniformly distributed in transverse direction. The flat distribution of reactive species is mainly attributed to the uniform electric field in the discharge chamber and the laminar gas flow.

8.3.3.2   Gas temperature determination

From a technological point of view, one of the important parameters in plasma jet device application is the gas temperature in the afterglow, which is dependent on the fraction of molecular species in the jet. In atmospheric pressure plasma, rotational temperature Trot is supposed to be equal to gas temperature (T_{gas}) based on the assumption that molecules in rotational states and surrounding neutral gases molecules are in equilibrium due to the frequent collisions of heavy particles [236, 237]. As indicated in survey spectra (figure 8.6), the presence of molecular bands of OH radicals and N_2 excited states could be used to estimate gas temperature. As known, the energy transfer in between Ar metastables and ground state N_2 leads to the excitation of excited state N_2(C) at high rotational levels, resulting in a non-Boltzmann rotational distribution of nitrogen [249]. Thus, it is difficult to interpret the emission of N_2 bands and to estimate the rotational temperature. Therefore,
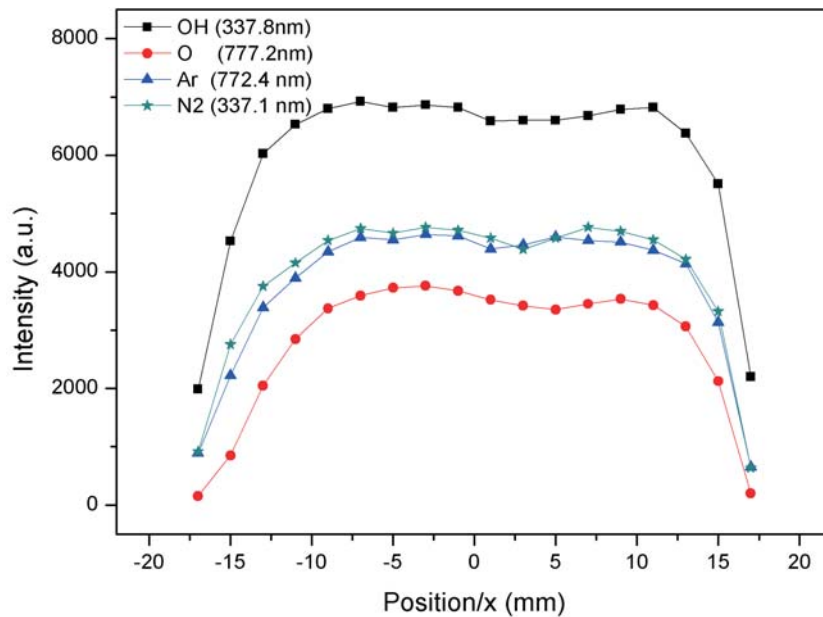
Figure 8.7: Emission profiles of OH molecular line at 307.8 nm, N2 molecular line at 337.1nm, atomic oxygen line at 777.2 nm and atomic argon line at 763.7 nm along x axis.

OH($A^2\Sigma \to X^2\Pi$, $\Delta\upsilon = 0$) band has been used in the present work for the gas temperature determination.

From technological point of view, one of the important parameters in plasma jet device application is gas temperature in the afterglow, which depends on the fraction of molecular species in the jet. In atmospheric pressure plasma, rotational temperature T_{rot} is supposed to be equal to gas temperature (T_{gas}) based on the assumption that molecules in rotational states and surrounding neutral gases molecules are in equilibrium due to frequent collisions of heavy particles [236, 237]. As indicated in survey spectra (figure 8.6), presence of molecular bands of OH radicals and N_2 excited states could be used to estimate gas temperature. As known, energy transfer in between Ar metastables and ground state N_2 leads to the excitation of excited state $N_2(C)$ at high rotational levels, resulting in a non-Boltzmann rotational distribution of nitrogen [249]. Thus, it is difficult to interpret N_2 bands emission and to estimate rotational temperature. Therefore, OH($A^2\Sigma \to X^2\Pi$, $\Delta\upsilon = 0$)band has been used in the present work for gas temperature determination.

In order to determine rotational temperature (T_{rot}), the numerical calculation of discharge spectra at various temperatures has been used. Simulation is carried out using the Lifbase package [242]. For comparison, all simulated and experimental spectra are normalized in intensity for the (0-0) band head. The experimental spectrum is compared with simulated spectra for various rotational temperatures. Good agreement between the measured spectrum and the synthetic
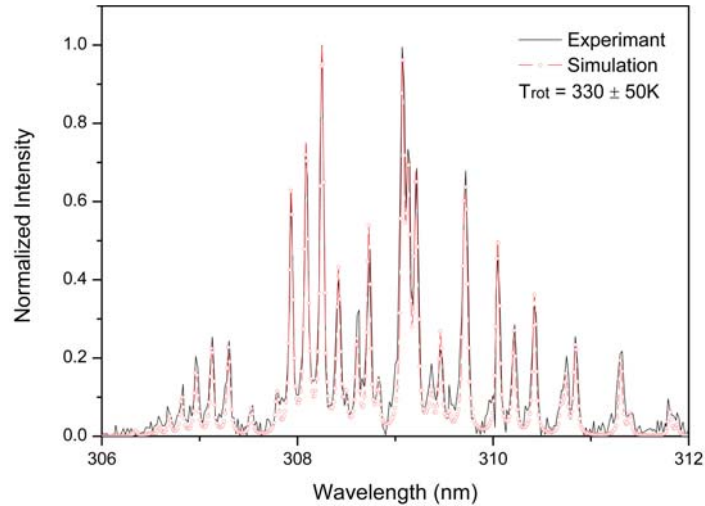
Figure 8.8: *The best fitting of OH band by the simulation with T_{rot} = 330 ± 50 K. Spectral resolution 0.05 nm, the instrumental function is Voigt with 70 % Lorentzian contribution.*

one provides a fast and reliable way to estimate gas temperature. Figure 8.8 shows a typical fitting synthetic spectrum to the experimental spectrum of the OH($A^2\Sigma \rightarrow X^2\Pi$, $\Delta v = 0$) band transition from 306 nm to 312 nm, with rotational temperature of 330 ± 50 K. This Trot value agrees well with measurements by the IR thermometer that gives temperature of 340 K. This clearly indicates low working temperature of the plasma source which is important for possible biomedical application and thermal-sensitive material treatment. Additionally, gas temperature profile along transverse direction agrees well with that of optical emissions which is shown in figure 8.7.

8.3.3.3 Calculation of electron density and electron temperature

As shown in figure 8.6 the RF plasma source designed here emits strong continuum Bremsstrahlung radiation appearing due to electron-atom and electron-ions interaction [361]. Presence of the continuum in the emission provides a fast way to measure two important plasma parameters: electron density and electron temperature. In fact, absolute value of plasma emissivity in $W \times nm^{-1}m^{-3}sr^{-1}$ due to the Bremsstrahlung radiation can be calculated as a sum of the contribution from free electron-atom interactions $\epsilon_{ea}(\lambda, T_e, n_e)$, from recombination of electrons and ions $\epsilon_{ei}^{fb}(\lambda, T_e, n_e)$ and from free-free interaction of electrons and ions $\epsilon_{ei}^{ff}(\lambda, T_e, n_e)$. In approximation of Maxwellian energy distribution of electron energy, the continuum contributions can be expressed as [361, 362]:

$$\epsilon_{ea}(\lambda, T_e, n_e) = C_{ea}\frac{n_e n_{Ar}}{\lambda^2(k_B T_e)^{3/2}}$$

$$\int_{hc/\lambda}^{\infty} Q_{ea}^{mom}(E)(1 - \frac{hc}{2\lambda E})\sqrt{1 - \frac{hc}{\lambda E}}e^{-\frac{E}{k_b T_e}}E^2 dE \qquad (8.2)$$

$$\epsilon_{ei}^{fb}(\lambda, T_e, n_e) = C_1 Z^2 \frac{n_e n_i}{\lambda^2 \sqrt{T_e}}(1 - e^{-\frac{hc}{\lambda k_b T_e}})\xi_{ei}^{fb}(\lambda, T_e) \qquad (8.3)$$

$$\epsilon_{ei}^{ff}(\lambda, T_e, n_e) = C_1 Z^2 \frac{n_e n_i}{\lambda^2 \sqrt{T_e}}(e^{-\frac{hc}{\lambda k_b T_e}})\xi_{ei}^{ff}(\lambda, T_e) \qquad (8.4)$$

where n_{Ar} is Ar atoms density, λ is wavelength, E is electrons energy, k_B is the Boltzmann constant ($1.38065 \times 10^{-23}m^2kgs^{-2}K^{-1}$), h is the Planck constant ($4.13567 \times 10^{-15}eV \cdot s$), n_i is ion density, Z is ion charge and $Q_{ea}^{mom}(E)$ is the momentum transfer cross section for electron atoms collisions. The constants in eqs.(8.2, 8.3, 8.4) are: $C_{ea} = 0.10779 \times \alpha h / (m_e^{3/2}c) \, Wm^2 J^{-3/2} \, sr^{-1}$ with $\alpha = e^2/(2hc\varepsilon_0)$, ε_0 is the permittivity of vacuum, $C_1 = 1.6321 \times 10^{-43}$ $Jm^4K^{1/2}s^{-1}sr^{-1}$. ξ_{ei}^{fb} and ξ_{ei}^{ff} are the Biberman factors. As following from eqs. (8.2, 8.3, 8.4), emissivity of the plasma continuum depends on electron density and electron temperature. Correspondingly, both plasma parameters can be estimated based on eqs. (8.2, 8.3, 8.4), if absolute value of the plasma continuum is

measured. Considering free electron-atom interactions, recombination of electrons and ions and free-free interaction of electrons and ions, figure 8.9 shows a typical calculation of the absolute value of the plasma emissivity in the range of 300 - 650 nm for the plasma jet. As can be seen, contribution of electron-atom interactions is almost three orders higher than that of recombination of electrons and ions and free-free interaction of electrons and ions.

In the current work, plasma irradiance in units $W/nm \times m^2$ has been obtained through calibration of the spectrometer. Next, this irradiance has been compared with results of the calculations based on eqs. (8.2, 8.3, 8.4) and n_e with T_e have been determined. In contrast to works [257, 361, 362], all contributions from ϵ_{ea}, ϵ_{ei}^{ff} and ϵ_{ei}^{fb} are considered in the work and the integral in eq.8.2:

$$\int_{hc/\lambda}^{\infty} Q_{ea}^{mom}(E)(1 - \frac{hc}{2\lambda E})\sqrt{1 - \frac{hc}{\lambda E}}e^{-\frac{E}{k_b T_e}} E^2 dE$$

has been calculated numerically. ϵ_{ea}, ϵ_{ei}^{ff} and ϵ_{ei}^{fb} values have been calculated in Python electron densities in the rage of 10^{11} to $10^{15} cm^{-3}$ and T_e varying from 0.5 to 4 eV. The required value of Q_{ea}^{mom} is taken from [361], and so called Biberman factor ξ_{ei}^{ff} is considered as a constant in the wavelength range of 300-700 nm, whereas ξ_{ei}^{fb} is taken from [372]. Best fitting of the experimental results for RF plasma of 20 W has been obtained with $n_e = 1.9 \pm 1 \times 10^{14} cm^{-3}$ and $T_e = 1.75 \pm 0.25$ eV. The electron density measured through absolute value of the continuum is in a good agreement with results obtained by different techniques [235] for RF atmospheric pressure plasma jets. This electron temperature is higher than the typical value of Ar excitation temperature T_{exc} of 1 eV measured in the plasma jets by line-ratio technique [233]. It has to be noted here that the so called excitation temperature measured by means of the line-ratio method is actually not electron temperature and a special procedure has to be used to make a correction in estimation of T_e from T_{exc}. The value of T_e found here is in agreement with scarce direct measurements of Te by Thomson scattering on a plasma jet source of 14.5 MHz where T_e has been found to be about 1.2 - 1.5 eV [373].

8.3.4 Temporal and spatial kinetics of the plasma

8.3.4.1 Temporally resolved spectroscopy of the plasma discharge

The RF discharge is sustained through application of 13.56 MHz frequency HV. Therefore discharge dynamics on ns scale are important to understand the physics behind the discharge. Besides being used for identification of reactive species and estimation of plasma parameters as shown above, optical emission spectroscopy is also a useful tool to study plasma dynamics. Time resolved spectroscopy has been used here to have a detailed insight into physics of discharge generation.
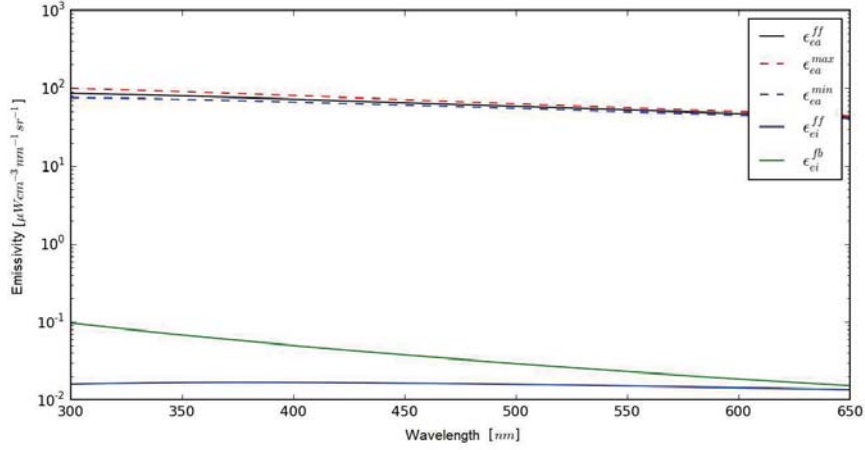
Figure 8.9: Contribution of free electron-atom interactions, recombination of electrons and ions and free-free interaction of electrons and ions to the absolute value of the plasma emissivity (with T_e = 1.75 eV and $n_e=10^{14} cm^{-3}$).
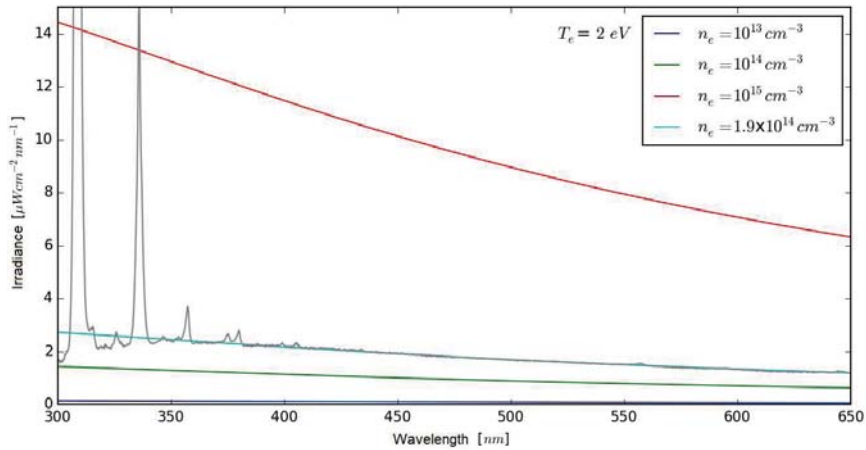
Figure 8.10: The best fitting of plasma irradiance with results of the calculations

Figure 8.11 shows typical temporal behavior of the optical emission intensities of four emission lines: OH radicals (309 nm), continuum radiation (450 nm and 600 nm), and Ar I (763.5 nm), for two discharge periods. The negative value of the signal corresponds to the output signal of the PMT tube detection of discharge emission. One of the important observations is presence of offset for all registered lines. To clear the offset emission, a gray area is drawn in figure 8.11 to outline emission intensity in the plasma. In general, plasma in RF device ex-
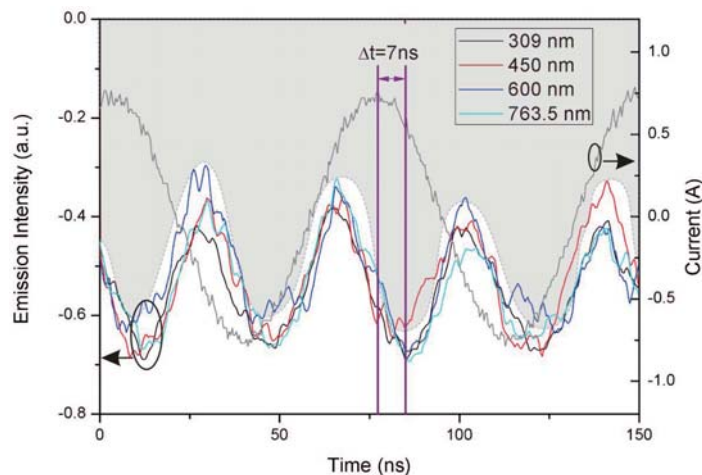
Figure 8.11: Time resolved spatial integrated PMT signal of different lines and continuum radiation of the discharge plotted over the current waveform. Temporal resolution is better than 5 ns. The signal is 50 times averaged.

hibits continuous emission over time. The emitting intensities at four wavelengths (309 nm, 450 nm, 600 nm, and 763.5 nm) fluctuate with time but never reach zero value. So the offset in emission indicates presence of discharge even at the time when discharge current and electrical field reach zero value. It is different from the behavior of plasma jets excited by AC voltage (frequency of some kHz) or pulsed voltage [283]. Discontinuous phenomenon, always observed in plasma jet sources with a low driving frequency (AC or pulsed), has been found and investigated by fast imaging techniques and time resolved spectroscopy [278, 374]. In a period of driving voltage, temporal behavior of optical emission intensity of reactive species is mostly represented in form of short emission peaks of some ns. Emission intensity firstly increases from the baseline and reaches its highest value, which corresponds to an ionization wave front (also known as plasma bullet), and decreases dramatically to the baseline right after pass of ionization wave. Kim et al. [375] noticed that plasma properties are different for driving frequency of 2 MHz and higher. Therefore, about two megahertz represents the plasma ion frequency. Both electrons and ions can follow the external electric field at exciting frequency under 2 MHz. However when the exciting frequency of the external electric field is above 2 MHz, only electrons can respond to the field.

In this RF plasma source, the fluctuating emission intensities with the offset indicate that plasma periodically develops with the driving voltage. For each period of voltage, plasma grows from weak to intense and decreases to weak with a double frequency of the applied voltage. Even at the moment of lowest intensity, plasma still exhibits considerable emission.

Emission of all lines follows the current waveform with phase shift about 7 ns. In every half period of RF cycle, 2 strong discharges are observed just before and 7 ns after current reaches its maximum. The observed phase shift is attributed to capacitive coupling of the RF power where certain time is required for charge accumulation and RF sheath formation.

8.3.4.2   Temporal and spatial resolved images

Detailed spatially resolved images of discharge emission are presented in figure 8.12 for total emission in the full range (250 - 900 nm), OH radicals emission with a narrow band filter of 309 nm and Ar I line at 753 nm. The ICCD camera gating unit is synchronized to the discharge current with trigger time showing in figure 8.11 (a). Exposure time of the ICCD camera is fixed at 5 ns.

The detailed spatially resolved images of the discharge emission are presented in figure 8.12 for the total emission in the full range (250 - 900 nm), OH radicals emission with a narrow band filter of 309 nm and Ar I line at 753 nm. The ICCD camera gating unit is synchronized to the discharge current with the trigger time showing in figure 8.12 (a). The exposure time of the ICCD camera is fixed at 5 ns.

Temporal discharge dynamics in figure 8.12 correspond to the time resolved signal of PMT in figure 8.11 with 3 ns difference due to delay in the ICCD gate unit. At the moment of 7 ns (frames t=10 ns) after current reaches 0.75 A, the emission maximum is observed. Glow-like discharge fills the whole gap with stronger radiation close to the edges of the device where electrical field is higher. 30 ns later a second strong emission pulse appears see, figure 8.12 frame at 37 ns. OH(A-X) emission has similar dynamics to the full range emission with less pronounced increase of the radiation at 10 and 47 ns. In contrast, the signal from Ar I states is different. Strong emission is observed at the layer of about 100-140 μm at 10 ns nearby the electrode. Emission is always stronger at the cathode. We attribute this strong emission layer to formation of a RF sheath. Indeed, the experimental measured sheath thickness s of 100-140 μm is in a good agreement with theoretical estimation of 107 μm based on the following expression [376, 377]:

$$s = \frac{1.52\varepsilon_0 A}{C_t} = \frac{1.52\varepsilon_0 A 2\pi f V}{I\sqrt{1 + \tan(\Phi)^{-2}}} \tag{8.5}$$

where A is cross section of the discharge, C_t is total capacitance of the plasma, f is voltage frequency, V is voltage across the gap, and Φ is voltage/current phase shift in radials.

A similar sheath region has been observed in planar RF discharge by Laimer [378]. In contrast to his observation, emission in the sheath is decreasing during 10 ns (see frame t=28 ns, Ar I, figure 8.12) and is almost symmetrical structure of the two sheath regions is formed in the gap at 28 ns and later on at 65 ns time.
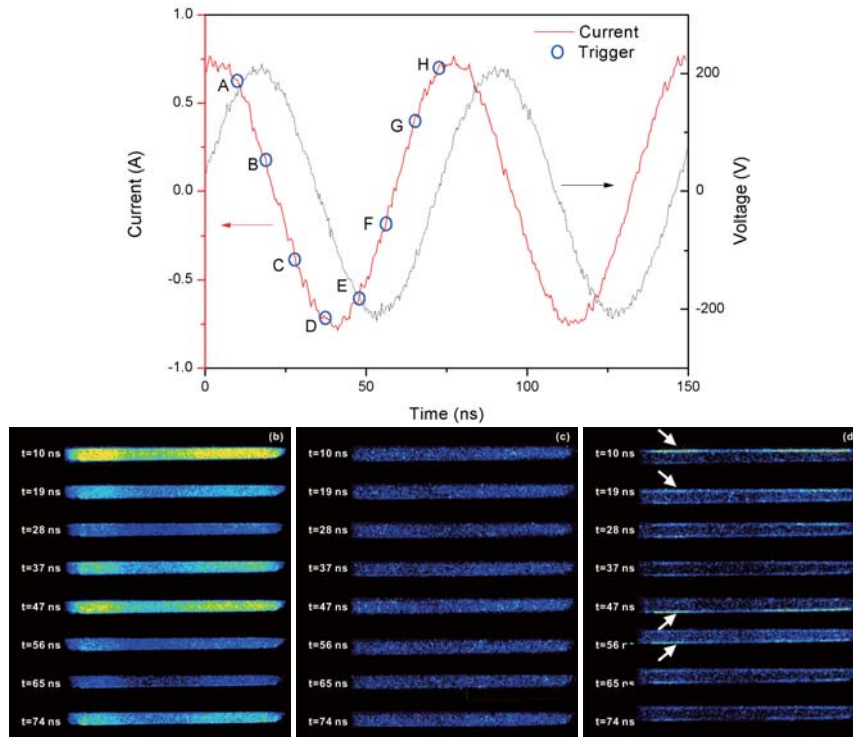
Figure 8.12: Temporal and spatially resolved ICCD images of the discharge with 5 ns resolution. (a) The blue points on voltage/current waveform correspond to the moment of the camera triggering. (b)ICCD photographs of the discharge in full spectrum range. (c) ICCD photographs of OH emission at 309 nm. (d) ICCD photographs of the Ar I emission at 753 nm. Arrows shows formation of the strong Ar I emission in the RF sheath.

Ar I emission in the bulk is much weaker and follows the applied voltage waveform. The observed difference between luminescence of Ar I and OH(A) indicates the importance of the sheath region in formation and sustainment of the RF atmospheric pressure planar discharge. The difference also suggests OH(A) production in the discharge is different from Ar I excitation pathways, which is important since OH(A) and OH(X) radicals are considered a key species in biomedical applications and plasma deposition at atmospheric pressure.

In addition to study the discharge dynamics in the interelectodes gap, the temporal-spatial resolved images of the afterglow emission are captured. The evolution of OH (309 nm) and Ar I (753 nm) emission in the afterglow is difficult to analyze due to their weak emission. As can be seen in figure 8.13, the afterglow develops a uniform emission along transverse direction. The time evolution
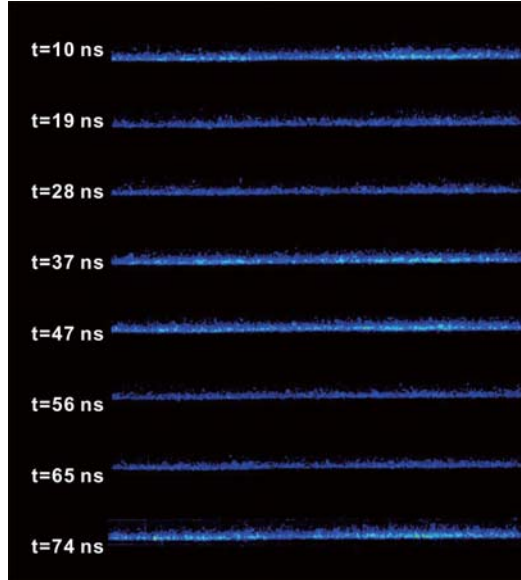
Figure 8.13: Temporal and spatially resolved ICCD images of the afterglow with 5 ns resolution.

of emission intensity in afterglow follows that in the discharge region (figure 8.12 (b)).

8.4 Conclusions

In summary, a 30 mm wide diffuse RF planar plasma source working at atmospheric pressure argon is developed and studied in this chapter. The source is proposed as a possible candidate for use in large scale application of plasma for deposition of coatings on textile materials. Main discharge parameters are determined by electrical diagnostics, OES and time resolved images. Two discharge modes, diffuse α mode and filament γ mode discharge, can be sustained in the plasma source depending on dissipated power. In diffuse α mode, a brush-shape homogenous plasma afterglow with the total length of up to 8 mm can be generated along the slit in ambient air.

From OES, emission of plasma afterglow is dominated by Ar(4p $\rightarrow$ 4s) transitions, OH($A^2\Sigma \rightarrow X^2\Pi$), N$_2$($C^3\Pi_u \rightarrow B^3\Pi_g$) and O(5p $\rightarrow$ 5s). Based on simulation of the rotational temperature of OH radicals, gas temperature is determined as 330 K. With absolute calibrated spectroscopy, electrons density and electron temperature are estimated from the absolute value of continuum radiation, about $1.9 \pm 1 \times 10^{14} cm^{-3}$ and 1.75 eV respectively. Time resolved intensity

of plasma emission indicates that plasma is sustained through formation of two strong emission peaks appearing with 27.12 MHz frequency. ICCD images show that production of Ar excited states appears in the RF sheath region of 100-140 μm close to the electrodes whereas OH(A-X) emission is almost uniformly distributed in the gap.

Based on of study the discharge physics it is concluded that the source developed here can be alternative to "traditional plasma jets". Use of RF planar source conception in plasma deposition provides a simple way to upscale plasma deposition method to industrial demands and large scale applications.

9

General conclusions and outlook

Plasma technology for thin film polymerization has been extensively studied over the past few decades. Many processes have been proposed and implemented in lab and industrial scale application. New techniques of polymerization processes using atmospheric pressure plasma jets (APPJ) are particularly attractive due to portable designs of the plasma sources, short processing time, considerably high deposition rates and capabilities for coating on objects with complex morphologies and structures. Moreover, success of the plasma jets use for polymerization on various substrates can be attributed to the fact that heat sensitive materials can be used in deposition because of low temperature at the jet downstream.

In this work, efforts were given to preparation of new kind of antibacterial nanocomposite films via plasma jet process. Starting point of the work was to develop a non-equilibrium atmospheric pressure plasma jet device. Direct current plasma jet with nitrogen/air as working gas was developed and constructed for plasma polymerization combining advantage of its simple apparatus requirement and stable discharge performance. General characterization of the DC plasma jet has been carried out through study of discharge electrical properties, emission spectroscopy, mass spectroscopy, and ozone measurements. Organosilicon films deposition using the DC plasma jet was investigated as function of oxygen addition in the plasma feed gas and discharge power. The plasma process has been optimized in terms of film quality and chemical composition. The plasma deposition process has been modified in order to produce antibacterial nanocomposite films on flat and non-woven textile materials. Chemistry, morphology and antibacterial activity of these materials were analyzed by XPS, SEM, GD-OES

methods and a variety of antibacterial tests with and without mechanical load on the samples.Finally, to explore the possibility of plasma deposition system up-scale, a special kind of barrier discharge plasma source excited by RF voltage was developed and characterized by means of absolute spectroscopy as well as temporal and spatial images for possible application in plasma assisted deposition of nanocomposite coating.

Characterization of a DC plasma jet

A non-equilibrium atmospheric pressure DC plasma jet in nitrogen and air gas was developed and investigated in terms of plasma properties and generation of active species in active zone and afterglow. Influence of working gas composition and discharge current on plasma parameters and afterglow properties were studied. Depending on discharge current, two discharge modes were determined. At low current, discharge was sustained in self-pulsing regime and at current higher than 10 mA, plasma behaved as a constricted glow discharge without voltage and current oscillations. Optical emission spectroscopy was employed to analyze reactive species, and to determine gas and vibrational temperature of the jet in active zone and in afterglow. Vibrational temperature of nitrogen and air discharge was much higher than gas temperature, which indicated strong non-equilibrium conditions in the plasma. A significant difference of long living reactive species in afterglow of N_2 and air plasma jet was founded: O_3 was only found in afterglow of the N_2 plasma jet, whereas NO was only found in the afterglow of air plasma jet. Space-resolved ozone and nitric oxide densities were determined in each afterglow.

Plasma polymerization of basic organosilicon films and antimicrobial nanocomposite films

Plasma polymerization of organosilicon films has attracted considerable attention due to their use for vapor and gas barrier creation, wear and friction reduction, corrosion protection, biocompatibility and hydrophobicity of surfaces. Organosilicon film deposition has been performed for the first time here with DC plasma jet working with nitrogen, where the film is proposed as matrix for nanocomposite fabrication with antibacterial properties.

Firstly, organosilicon film deposition by atmospheric pressure nitrogen DC plasma jet with TMDSO as precursor was investigated. Effect of O_2 content and discharge power on film deposition rate and chemical properties of the films was thoroughly studied. It was found that oxygen addition and power increase could enhance deposition rate due to effective monomer decomposition and dissociation by the plasma. It was shown by FTIR and XPS measurements that the deposited film could be tuned in content of organic and inorganic components to specific requirements by variation of oxygen admixing and discharge power.

The organosilicon film has been used in a new method of nanocomposite thin film fabrication with incorporation of AgNPs. The method has been applied on flat surface materials in a single step plasma jet process. AgNPs were directly fed into the DC plasma jet and participated in the deposition process on substrate surface. It was found that control of morphology of AgNPs in the films could be achieved by variation of AgNPs feeding rate. It was found that silver content in the films can be controlled from few percent to more than 30% by variation of plasma operation parameters. Antibacterial activity of nanocomposite film has been tested using *E. coli* and *S. aureus* strains.

The method of antibacterial nanocomposites deposition has been extended to PET non-woven fabrics as a three step process based on atmospheric pressure plasma deposition. In this approach, AgNPs were firmly immobilized via a double layer of plasma deposited organic films: a reservation layer (1st layer) and a barrier layer (2nd layer). It was revealed that plasma could penetrate through non-woven fabric structure and achieve uniform deposition on both sides of the fabric. The barrier layer could not only prevent release of AgNPs, which was confirmed through washing tests, but could also be used to control release of silver ions, which was proved by antibacterial test. It was shown that this new kind of coatings prepared by plasma deposition of nano-silver exhibits strong antibacterial activity against different microorganisms.

Characterization of upscaled RF-DBD plasma jet

With the success in nanocomposite antibacterial film development, it is important to explore methods to upscale the process for industrial requirements. Therefore, a plasma jet source with large scale dimensions was developed based on the concept of barrier discharge. A brush shaped plasma jet, excited by RF voltage, was characterized with time-resolved emission spectroscopy, absolute spectroscopy and high speed ICCD camera. In contrast to most plasma jets, the source has a wide afterglow with width of about 30 mm and can be easily upscaled to any industrial demands. Gas temperature estimated by emission spectroscopy is about 330 K. With absolute calibrated spectroscopy, electrons density and electron temperature are estimated from absolute value of continuum radiation to be about $\times 10^{14}$ cm^{-3} and 1.75 ± 0.25 eV, respectively. ICCD images show that Ar excited states production appeared in the RF sheath region of 100-140 μm close to the electrodes whereas OH(A) emission was almost uniformly distributed in the gap. It is proposed that use of the RF planar source concept in plasma deposition provides a simple way to upscale plasma deposition method to industrial demands and large scale applications.

Outlook

The work presented in this dissertation proves the potential of nanocomposite film polymerization by means of a plasma jet. This can be beneficial for fabrication of novel functional materials in many practical applications, such as antibacterial medical and hygienical materials. Also, results on the non-woven fabrics are of great importance for medical sector and healthcare industry. Final goal of this work is to develop a plasma jet system and related methods for fabrication of proper functional nanocomposite films, which can also be industrialized for mass-production. In such case, there are two main open questions for the future.

- Firstly, development of a proper plasma source is important for future work. In our work, a DC plasma jet has been used to sustain non-equilibrium plasma due to its simple, reliable operation and low operational costs, but the source dimensions are a considerable drawback for industrial use. In the last chapter, we develop a plasma source with larger dimension in order to upscale the process. However, investigation on how to use this plasma jet as sources for plasma polymerization, and how to achieve good quality films has to be done.

- Secondly, relationship between film chemical properties and antibacterial activity should be further explored. Influence of surface morphology, film chemical composition, and nanoparticle propertis (size, shape and type) on bactericide activity is an interesting topic for the future. Moreover, control of surface morphology, for instance formation of imperfections in nanocomposite film, is also an interesting and important point.

Due to the interdisciplinary nature of this topic, collaborations between scientists of different fields are necessary for future success in the use of functional nanocomposite films for real life application.

References

[1] Alexander Fridman and Lawrence A Kennedy. *Plasma physics and engineering*. CRC press, 2004.

[2] Seung-Lok Park, Jae-Duk Moon, Seug-Hoon Lee, and Soo-Yeon Shin. Effective ozone generation utilizing a meshed-plate electrode in a dielectric-barrier discharge type ozone generator. *Journal of Electrostatics*, 64(5):275–282, 2006.

[3] Arne M Vandenbroucke, Rino Morent, Nathalie De Geyter, and Christophe Leys. Non-thermal plasmas for non-catalytic and catalytic voc abatement. *Journal of hazardous materials*, 195:30–54, 2011.

[4] Gregory Fridman, Gary Friedman, Alexander Gutsol, Anatoly B Shekhter, Victor N Vasilets, and Alexander Fridman. Applied plasma medicine. *Plasma Processes and Polymers*, 5(6):503–533, 2008.

[5] Nathalie De Geyter, Rino Morent, Sandra Van Vlierberghe, M Frere-Trentesaux, Peter Dubruel, and E Payen. Effect of electrode geometry on the uniformity of plasma-polymerized methyl methacrylate coatings. *Progress in Organic Coatings*, 70(4):293–299, 2011.

[6] Vijay Nehra, Ashok Kumar, and HK Dwivedi. Atmospheric non-thermal plasma sources. *Int J Eng*, 2(1):53–68, 2008.

[7] Ulrich Kogelschatz. Filamentary, patterned, and diffuse barrier discharges. *Plasma Science, IEEE Transactions on*, 30(4):1400–1408, 2002.

[8] H-E Wagner, R Brandenburg, KV Kozlov, A Sonnenfeld, P Michel, and JF Behnke. The barrier discharge: basic properties and applications to surface treatment. *Vacuum*, 71(3):417–436, 2003.

[9] Klaus Dieter Weltmann, Eckhard Kindel, Thomas von Woedtke, Marcel Hähnel, Manfred Stieber, and Ronny Brandenburg. Atmospheric-pressure plasma sources: Prospective tools for plasma medicine. *Pure and Applied Chemistry*, 82(6):1223–1237, 2010.

[10] K-D Weltmann, E Kindel, R Brandenburg, Ch Meyer, R Bussiahn, Ch Wilke, and Th Von Woedtke. Atmospheric pressure plasma jet for medical therapy: plasma parameters and risk estimation. *Contributions to Plasma Physics*, 49(9):631–640, 2009.

[11] GY Park, SJ Park, MY Choi, IG Koo, JH Byun, JW Hong, JY Sim, GJ Collins, and JK Lee. Atmospheric-pressure plasma sources for biomedical applications. *Plasma Sources Science and Technology*, 21(4):043001, 2012.

[12] Geoff Lloyd, Gary Friedman, Syed Jafri, Greg Schultz, Alex Fridman, and Keith Harding. Gas plasma: medical uses and developments in wound care. *Plasma Processes and Polymers*, 7(3-4):194–211, 2010.

[13] Michael G Kong, G Kroesen, G Morfill, T Nosenko, Toshimi Shimizu, J Van Dijk, and JL Zimmermann. Plasma medicine: an introductory review. *New Journal of Physics*, 11(11):115012, 2009.

[14] Th Von Woedtke, S Reuter, K Masur, and K-D Weltmann. Plasmas for medicine. *Physics Reports*, 530(4):291–320, 2013.

[15] David B Graves. Low temperature plasma biomedicine: A tutorial reviewa). *Physics of Plasmas*, 21(8):080901, 2014.

[16] James L Walsh and Michael G Kong. Contrasting characteristics of linear-field and cross-field atmospheric plasma jets. *Applied Physics Letters*, 93(11):111501, 2008.

[17] X Lu, M Laroussi, and V Puech. On atmospheric-pressure non-equilibrium plasma jets and plasma bullets. *Plasma Sources Science and Technology*, 21(3):034005, 2012.

[18] Mounir Laroussi and Tamer Akan. Arc-free atmospheric pressure cold plasma jets: A review. *Plasma Processes and Polymers*, 4(9):777–788, 2007.

[19] Johann Laimer and Herbert Störi. Recent advances in the research on non-equilibrium atmospheric pressure plasma jets. *Plasma processes and polymers*, 4(3):266–274, 2007.

[20] Yu Akishev, M Grushin, I Kochetov, V Karal'Nik, A Napartovich, and N Trushkin. Negative corona, glow and spark discharges in ambient air and transitions between them. *Plasma Sources Science and Technology*, 14(2):S18, 2005.

[21] Yu Akishev, M Grushin, V Karalnik, A Petryakov, and N Trushkin. On basic processes sustaining constricted glow discharge in longitudinal n_2 flow at atmospheric pressure. *Journal of Physics D: Applied Physics*, 43(21):215202, 2010.

[22] Yu Akishev, M Grushin, V Karalnik, A Petryakov, and N Trushkin. Non-equilibrium constricted dc glow discharge in N_2 flow at atmospheric pressure: stable and unstable regimes. *Journal of Physics D: Applied Physics*, 43(7):075202, 2010.

[23] D Dudek, N Bibinov, J Engemann, and P Awakowicz. Direct current plasma jet needle source. *Journal of Physics D: Applied Physics*, 40(23):7367, 2007.

[24] Jia Li, Natsuko Sakai, Masato Watanabe, Eiki Hotta, and Masaaki Wachi. Study on plasma agent effect of a direct-current atmospheric pressure oxygen-plasma jet on inactivation of E. coli using bacterial mutants. *Plasma Science, IEEE Transactions on*, 41(4):935–941, 2013.

[25] YuBin Xian, ShuQun Wu, Zhan Wang, QuanJun Huang, XinPei Lu, and Juergen F Kolb. Discharge dynamics and modes of an atmospheric pressure non-equilibrium air plasma jet. *Plasma Processes and Polymers*, 10(4):372–378, 2013.

[26] YuBin Xian, XinPei Lu, ShuQun Wu, Paul K Chu, and Yuan Pan. Are all atmospheric pressure cold plasma jets electrically driven? *Applied Physics Letters*, 100(12):123702, 2012.

[27] JF Kolb, A-A H Mohamed, RO Price, RJ Swanson, A Bowman, RL Chiavarini, M Stacey, and KH Schoenbach. Cold atmospheric pressure air plasma jet for medical applications. *Applied Physics Letters*, 92(24):241501, 2008.

[28] WeiDong Zhu and Jose L Lopez. A DC non-thermal atmospheric-pressure plasma microjet. *Plasma Sources Science and Technology*, 21(3):034018, 2012.

[29] Fuxiang Liu, Peng Sun, Na Bai, Ye Tian, Haixia Zhou, Shicheng Wei, Yanheng Zhou, Jue Zhang, Weidong Zhu, Kurt Becker, et al. Inactivation of bacteria in an aqueous environment by a direct-current, cold-atmospheric-pressure air plasma microjet. *Plasma Processes and Polymers*, 7(3-4):231–236, 2010.

[30] Hongqing Feng, Peng Sun, Yufeng Chai, Guohua Tong, Jue Zhang, Weidong Zhu, and Jing Fang. The interaction of a direct-current cold

atmospheric-pressure air plasma with bacteria. *Plasma Science, IEEE Transactions on*, 37(1):121–127, 2009.

[31] Peng Sun, Jie Pan, Ye Tian, Na Bai, Haiyan Wu, Lingxuan Wang, Cailan Yu, Jue Zhang, Weidong Zhu, Kurt H Becker, et al. Tooth whitening with hydrogen peroxide assisted by a direct-current cold atmospheric-pressure air plasma microjet. *Plasma Science, IEEE Transactions on*, 38(8):1892–1896, 2010.

[32] Jie Pan, Peng Sun, Ye Tian, Haixia Zhou, Haiyan Wu, Na Bai, Fuxiang Liu, Weidong Zhu, Jue Zhang, Kurt H Becker, et al. A novel method of tooth whitening using cold plasma microjet driven by direct current in atmospheric-pressure air. *Plasma Science, IEEE Transactions on*, 38(11):3143–3151, 2010.

[33] S Wu, Z Wang, Q Huang, Xinpei Lu, and K Ostrikov. Open-air direct current plasma jet: Scaling up, uniformity, and cellular control. *Physics of Plasmas*, 19(10):103503, 2012.

[34] Weiman Jiang, Jie Tang, Yishan Wang, Wei Zhao, and Yixiang Duan. Characterization of argon direct-current glow discharge with a longitudinal electric field applied at ambient air. *Scientific reports*, 4, 2014.

[35] M Teschke, J Kedzierski, EG Finantu-Dinu, D Korzec, and J Engemann. High-speed photographs of a dielectric barrier atmospheric pressure plasma jet. *Plasma Science, IEEE Transactions on*, 33(2):310–311, 2005.

[36] Hyun Woo Lee, Seoul Hee Nam, Abdel-Aleam H Mohamed, Gyoo Cheon Kim, and Jae Koo Lee. Atmospheric pressure plasma jet composed of three electrodes: application to tooth bleaching. *Plasma Processes and Polymers*, 7(3-4):274–280, 2010.

[37] Seoul Hee Nam, Hyun Woo Lee, Soo Hyun Cho, Jae Koo Lee, Young Chan Jeon, and Gyoo Cheon Kim. High-efficiency tooth bleaching using non-thermal atmospheric pressure plasma with low concentration of hydrogen peroxide. *Journal of Applied Oral Science*, 21(3):265–270, 2013.

[38] Qing Li, Jiang-Tao Li, Wen-Chao Zhu, Xi-Ming Zhu, and Yi-Kang Pu. Effects of gas flow rate on the length of atmospheric pressure nonequilibrium plasma jets. *Applied Physics Letters*, 95(14):141502, 2009.

[39] Abdollah Sarani, Anton Yu Nikiforov, and Christophe Leys. Atmospheric pressure plasma jet in ar and ar/h$_2$o mixtures: Optical emission spectroscopy and temperature measurements. *Physics of Plasmas*, 17(6):063504, 2010.

[40] Nathalie De Geyter, Abdollah Sarani, Tinneke Jacobs, A Yu Nikiforov, Tim Desmet, and Peter Dubruel. Surface modification of poly-ε-caprolactone with an atmospheric pressure plasma jet. *Plasma Chemistry and Plasma Processing*, 33(1):165–175, 2013.

[41] Leila Taghizadeh, Gilles Brackman, Anton Nikiforov, Joost van der Mullen, Christophe Leys, and Tom Coenye. Inactivation of biofilms using a low power atmospheric pressure argon plasma jet; the role of entrained nitrogen. *Plasma Processes and Polymers*, 12(1):75–81, 2015.

[42] Abdollah Sarani, Anton Yu Nikiforov, Nathalie De Geyter, Rino Morent, and Christophe Leys. Surface modification of polypropylene with an atmospheric pressure plasma jet sustained in argon and an argon/water vapour mixture. *Applied Surface Science*, 257(20):8737–8741, 2011.

[43] Iu Onyshchenko, Nathalie De Geyter, Anton Yu Nikiforov, and Rino Morent. Atmospheric pressure plasma penetration inside flexible polymeric tubes. *Plasma Processes and Polymers*, 2015.

[44] A Van Deynse, P Cools, C Leys, N De Geyter, and R Morent. Surface activation of polyethylene with an argon atmospheric pressure plasma jet: Influence of applied power and flow rate. *Applied Surface Science*, 328:269–278, 2015.

[45] XinPei Lu, ZhongHe Jiang, Qing Xiong, ZhiYuan Tang, XiWei Hu, and Yuan Pan. An 11cm long atmospheric pressure cold plasma plume for applications of plasma medicine. *Applied Physics Letters*, 92(8):081502, 2008.

[46] Guangliang Chen, Wenjun Zhao, Shihua Chen, Mingyan Zhou, Wenran Feng, Weichao Gu, and Si-ze Yang. Preparation of nanocones for immobilizing DNA probe by a low-temperature plasma plume. *Applied physics letters*, 89(12):121501, 2006.

[47] Guangliang Chen, Mingyan Zhou, Zhaoxia Zhang, Guohua Lv, Sylvain Massey, Wilson Smith, and Michael Tatoulian. Acrylic acid polymer coatings on silk fibers by room-temperature apgd plasma jets. *Plasma Processes and Polymers*, 8(8):701–708, 2011.

[48] Yong Cheol Hong and Han Sup Uhm. Microplasma jet at atmospheric pressure. *Applied physics letters*, 89(22):221504, 2006.

[49] Hideomi Koinuma, Hiroyuki Ohkubo, Takuya Hashimoto, Kiyoto Inomata, Tadashi Shiraishi, Akiharu Miyanaga, and Shigenori Hayashi. Development and application of a microbeam plasma generator. *Applied physics letters*, 60(7):816–817, 1992.

[50] Kiyoto Inomata, Nobuyuki Aoki, and Hideomi Koinuma. Production of fullerenes by low temperature plasma chemical vaper deposition under atmospheric pressure. *Japanese journal of applied physics*, 33(2A):L197, 1994.

[51] Bong-ju Lee, Yukihiro Kusano, Nobuko Kato, Kazuo Naito, Takao Horiuchi, and Hideomi Koinuma. Oxygen plasma treatment of rubber surface by the atmospheric pressure cold plasma torch. *Japanese journal of applied physics*, 36(5R):2888, 1997.

[52] Kristian Wende, Susanne Straßenburg, Beate Haertel, Manuela Harms, Sarah Holtz, Annemarie Barton, Kai Masur, Thomas von Woedtke, and Ulrike Lindequist. Atmospheric pressure plasma jet treatment evokes transient oxidative stress in hacat keratinocytes and influences cell physiology. *Cell biology international*, 38(4):412–425, 2014.

[53] Maxi Hoentsch, Thomas von Woedtke, Klaus-Dieter Weltmann, and J Barbara Nebe. Time-dependent effects of low-temperature atmospheric-pressure argon plasma on epithelial cell attachment, viability and tight junction formation in vitro. *Journal of Physics D: Applied Physics*, 45(2):025206, 2012.

[54] Rutger Matthes, Ina Koban, Claudia Bender, Kai Masur, Eckhard Kindel, Klaus-Dieter Weltmann, Thomas Kocher, Axel Kramer, and Nils-Olaf Hübner. Antimicrobial efficacy of an atmospheric pressure plasma jet against biofilms of pseudomonas aeruginosa and staphylococcus epidermidis. *Plasma Processes and Polymers*, 10(2):161–166, 2013.

[55] Oleksandr Galmiz, Monika Stupavska, Harm Wulff, Holger Kersten, Antonin Brablec, and Mirko Cernak. Deposition of Zn-containing films using atmospheric pressure plasma jet. *Open Chemistry*, 13(1), 2015.

[56] Dan Bee Kim, JK Rhee, B Gweon, SY Moon, and W Choe. Comparative study of atmospheric pressure low and radio frequency microjet plasmas produced in a single electrode configuration. *Applied Physics Letters*, 91(15):151502–151502, 2007.

[57] JY Jeong, SE Babayan, VJ Tu, J Park, I Henins, RF Hicks, and GS Selwyn. Etching materials with an atmospheric-pressure plasma jet. *Plasma Sources Science and Technology*, 7(3):282, 1998.

[58] SE Babayan, JY Jeong, VJ Tu, J Park, GS Selwyn, and RF Hicks. Deposition of silicon dioxide films with an atmospheric-pressure plasma jet. *Plasma Sources Science and Technology*, 7(3):286, 1998.

[59] Guo Li, He-Ping Li, Li-Yan Wang, Sen Wang, Hong-Xin Zhao, Wen-Ting Sun, Xin-Hui Xing, and Cheng-Yu Bao. Genetic effects of radio-frequency, atmospheric-pressure glow discharges with helium. *Applied physics letters*, 92(22):221504, 2008.

[60] V Schulz-von der Gathen, L Schaper, N Knake, St Reuter, K Niemi, T Gans, and J Winter. Spatially resolved diagnostics on a microscale atmospheric pressure plasma jet. *Journal of Physics D: Applied Physics*, 41(19):194004, 2008.

[61] Dirk Ellerweg, Jan Benedikt, Achim von Keudell, Nikolas Knake, and Volker Schulz-von der Gathen. Characterization of the effluent of a he/o$_2$ microscale atmospheric pressure plasma jet by quantitative molecular beam mass spectrometry. *New Journal of Physics*, 12(1):013021, 2010.

[62] Daniel Schröder, Sebastian Burhenn, Teresa de los Arcos, and Volker Schulz-von der Gathen. Characteristics of a propagating, self-pulsing, constricted γ-mode-like discharge. *Journal of Physics D: Applied Physics*, 48(5):055206, 2015.

[63] B Niermann, A Kanitz, M Böke, and J Winter. Impurity intrusion in radio-frequency micro-plasma jets operated in ambient air. *Journal of Physics D: Applied Physics*, 44(32):325201, 2011.

[64] Stefan Spiekermeier, Daniel Schröder, Volker Schulz-von der Gathen, Marc Böke, and Jörg Winter. Helium metastable density evolution in a self-pulsing μ-appj. *Journal of Physics D: Applied Physics*, 48(3):035203, 2015.

[65] Zhen-hua Bi, Yong-xin Liu, Wei Jiang, Xiang Xu, and You-nian Wang. A brief review of dual-frequency capacitively coupled discharges. *Current Applied Physics*, 11(5):S2–S8, 2011.

[66] Yong-Jie Zhou, Qiang-Hua Yuan, Fei Li, Xiao-Min Wang, Gui-Qin Yin, and Chen-Zhong Dong. Nonequilibrium atmospheric pressure plasma jet using a combination of 50 kHz/2 MHz dual-frequency power sources. *Physics of Plasmas*, 20(11):113502, 2013.

[67] Z Cao, QY Nie, and MG Kong. A cold atmospheric pressure plasma jet controlled with spatially separated dual-frequency excitations. *Journal of Physics D: Applied Physics*, 42(22):222003, 2009.

[68] M Jasiński, D Czylkowski, B Hrycak, M Dors, and J Mizeraczyk. Atmospheric pressure microwave plasma source for hydrogen production. *international journal of hydrogen energy*, 38(26):11473–11483, 2013.

[69] Chuji Wang and Wei Wu. Simultaneous measurements of OH (A) and OH (X) radicals in microwave plasma jet-assisted combustion of methane/air mixtures around the lean-burn limit using optical emission spectroscopy and cavity ringdown spectroscopy. *Journal of Physics D: Applied Physics*, 46(46):464008, 2013.

[70] G Wattieaux, M Yousfi, and N Merbahi. Optical emission spectroscopy for quantification of ultraviolet radiations and biocide active species in microwave argon plasma jet at atmospheric pressure. *Spectrochimica Acta Part B: Atomic Spectroscopy*, 89:66–76, 2013.

[71] Jun Choi, Abdel-Aleam H Mohamed, Sung Kil Kang, Kyung Chul Woo, Kyong Tai Kim, and Jae Koo Lee. 900-MHz nonthermal atmospheric pressure plasma jet for biomedical applications. *Plasma Processes and Polymers*, 7(3-4):258–263, 2010.

[72] J Choi, F Iza, HJ Do, JK Lee, and MH Cho. Microwave-excited atmospheric-pressure microplasmas based on a coaxial transmission line resonator. *Plasma Sources Science and Technology*, 18(2):025029, 2009.

[73] Myoung Soo Kim, Ho Young Kim, Hyun Kook Shin, Hyoung Cheol Kwon, Jae Yoon Sim, Jae Koo Lee, et al. Comparative study between atmospheric microwave and low-frequency plasmas: Production efficiency of reactive species and their effectiveness. *Japanese Journal of Applied Physics*, 53(5S1):05FR02, 2014.

[74] Young H Na, Gyungsoon Park, Eun H Choi, and Han S Uhm. Effects of the physical parameters of a microwave plasma jet on the inactivation of fungal spores. *Thin Solid Films*, 547:125–131, 2013.

[75] Robert Stonies, Susanne Schermer, Edgar Voges, and José AC Broekaert. A new small microwave plasma torch. *Plasma Sources Science and Technology*, 13(4):604, 2004.

[76] Tetsuji Shimizu, Bernd Steffes, Rene Pompl, Ferdinand Jamitzky, Wolfram Bunk, Katrin Ramrath, Matthias Georgi, Wilhelm Stolz, Hans-Ulrich Schmidt, Takuya Urayama, et al. Characterization of microwave plasma torch for decontamination. *Plasma Processes and Polymers*, 5(6):577–582, 2008.

[77] R Tiede, J Hirschberg, G Daeschlein, T von Woedtke, W Vioel, and S Emmert. Plasma applications: a dermatological view. *Contributions to Plasma Physics*, 54(2):118–130, 2014.

[78] Cheng Zhang, Tao Shao, Ruixue Wang, Zhongsheng Zhou, Yixiao Zhou, and Ping Yan. A comparison between characteristics of atmospheric-pressure plasma jets sustained by nanosecond-and microsecond-pulse generators in helium. *Physics of Plasmas*, 21(10):103505, 2014.

[79] JL Walsh and MG Kong. Portable nanosecond pulsed air plasma jet. *Applied Physics Letters*, 99(8):081501, 2011.

[80] Andrada Lazea-Stoyanova, Angela Vlad, Aurel Mihai Vlaicu, Valentin Serban Teodorescu, and Gheorghe Dinescu. Synthesis of copper particles by non-thermal atmospheric pressure plasma jet. *Plasma Processes and Polymers*, 2015.

[81] XinPei Lu, ZhongHe Jiang, Qing Xiong, ZhiYuan Tang, and Yuan Pan. A single electrode room-temperature plasma jet device for biomedical applications. *Applied Physics Letters*, 92(15):151504, 2008.

[82] Erdinc Karakas, Mehmet Arda Akman, and Mounir Laroussi. The evolution of atmospheric-pressure low-temperature plasma jets: jet current measurements. *Plasma Sources Science and Technology*, 21(3):034016, 2012.

[83] Q Xiong, X Lu, K Ostrikov, Z Xiong, Y Xian, F Zhou, C Zou, J Hu, W Gong, and Z Jiang. Length control of he atmospheric plasma jet plumes: effects of discharge parameters and ambient air. *Physics of Plasmas*, 16(4):043505, 2009.

[84] Qing Xiong, Xinpei Lu, Jinhui Liu, Y Xian, Z Xiong, F Zou, C Zou, W Gong, J Hu, K Chen, et al. Temporal and spatial resolved optical emission behaviors of a cold atmospheric pressure plasma jet. *Journal of Applied Physics*, 106(8):083302, 2009.

[85] Q Xiong, XP Lu, K Ostrikov, Y Xian, C Zou, Z Xiong, and Y Pan. Pulsed dc-and sine-wave-excited cold atmospheric plasma plumes: A comparative analysis. *Physics of Plasmas*, 17(4):043506, 2010.

[86] C Jiang, MT Chen, and MA Gundersen. Polarity-induced asymmetric effects of nanosecond pulsed plasma jets. *Journal of Physics D: Applied Physics*, 42(23):232002, 2009.

[87] Michael Noeske, Jost Degenhardt, Silke Strudthoff, and Uwe Lommatzsch. Plasma jet treatment of five polymers at atmospheric pressure: surface modifications and the relevance for adhesion. *International Journal of Adhesion and Adhesives*, 24(2):171–177, 2004.

[88] Yao-wen Hsu, Hsin-Chieh Li, Yao-Jhen Yang, and Cheng-che Hsu. Deposition of zinc oxide thin films by an atmospheric pressure plasma jet. *Thin Solid Films*, 519(10):3095–3099, 2011.

[89] Delphine Merche, Nicolas Vandencasteele, and François Reniers. Atmospheric plasmas for thin film deposition: A critical review. *Thin Solid Films*, 520(13):4219–4236, 2012.

[90] Jürgen Schlegel, Julia Köritzer, and Veronika Boxhammer. Plasma in cancer treatment. *Clinical Plasma Medicine*, 1(2):2–7, 2013.

[91] Davide Mariotti and R Mohan Sankaran. Microplasmas for nanomaterials synthesis. *Journal of Physics D: Applied Physics*, 43(32):323001, 2010.

[92] Ruixue Wang, Shasha Zuo, Weidong Zhu, Shan Wu, Weifeng Nian, Jue Zhang, and Jing Fang. Microplasma-assisted growth of colloidal silver nanoparticles for enhanced antibacterial activity. *Plasma Processes and Polymers*, 11(1):44–51, 2014.

[93] Yixiang Duan, C Huang, and QS Yu. Cold plasma brush generated at atmospheric pressure. *Review of scientific instruments*, 78(1):015104, 2007.

[94] Xinpei Lu, S Wu, Paul K Chu, D Liu, and Y Pan. An atmospheric-pressure plasma brush driven by sub-microsecond voltage pulses. *Plasma Sources Science and Technology*, 20(6):065009, 2011.

[95] Qiu-Yue Nie, Z Cao, Chun-Sheng Ren, De Zhen Wang, and Michael G Kong. A two-dimensional cold atmospheric plasma jet array for uniform treatment of large-area surfaces for plasma medicine. *New Journal of Physics*, 11(11):115015, 2009.

[96] Ho Young Kim, Sung Kil Kang, Hyoung Cheol Kwon, Hyun Woo Lee, and Jae Koo Lee. Gas temperature effect on reactive species generation from the atmospheric pressure air plasma. *Plasma Processes and Polymers*, 10(8):686–697, 2013.

[97] Marcel Šimor, Pavel Vojtek, Mirko Černák, Antonın Brablec, et al. Atmospheric-pressure diffuse coplanar surface discharge for surface treatments. *Applied Physics Letters*, 81(15):2716–2718, 2002.

[98] D Li, DX Liu, QY Nie, HP Li, HL Chen, and MG Kong. Array of surface-confined glow discharges in atmospheric pressure helium: Modes and dynamics. *Applied Physics Letters*, 104(20):204101, 2014.

[99] Z Cao, James L Walsh, and Michael G Kong. Atmospheric plasma jet array in parallel electric and gas flow fields for three-dimensional surface treatment. *Applied Physics Letters*, 94(2):021501, 2009.

[100] Sun Ja Kim, Tae Hun Chung, Hea Min Joh, J-H Cha, In Sub Eom, and H-J Lee. Characteristics of multiple plasma plumes and formation of bullets in an atmospheric-pressure plasma jet array. *Plasma Science, IEEE Transactions on*, 43(3):753–759, 2015.

[101] X Pei, Z Wang, Q Huang, S Wu, and X Lu. Dynamics of a plasma jet array. *Plasma Science, IEEE Transactions on*, 39(11):2276–2277, 2011.

[102] Z Cao, Q Nie, DL Bayliss, James L Walsh, Chun-Sheng Ren, De Zhen Wang, and Michael G Kong. Spatially extended atmospheric plasma arrays. *Plasma Sources Science and Technology*, 19(2):025003, 2010.

[103] Qian-Qian Fan, Mu-Yang Qian, Chun-Sheng Ren, Dezhen Wang, and Xiaoqiong Wen. Discharge characteristics of a cold-atmospheric-plasma jet array generated with single-electrode configuration. *Plasma Science, IEEE Transactions on*, 40(6):1724–1729, 2012.

[104] Jae Young Kim, John Ballato, and Sung-O Kim. Intense and energetic atmospheric pressure plasma jet arrays. *Plasma Processes and Polymers*, 9(3):253–260, 2012.

[105] Sung-O Kim, Jae Young Kim, Do Yeob Kim, John Ballato, et al. Intense plasma emission induced by jet-to-jet coupling in atmospheric pressure plasma arrays. *Applied Physics Letters*, 101(17):173503, 2012.

[106] Jae Young Kim and Sung-O Kim. Intense plasma emission from atmospheric-pressure plasma jet array by jet-to-jet coupling. *Plasma Science, IEEE Transactions on*, 39(11):2278–2279, 2011.

[107] Do Yeob Kim, Jae Young Kim, Hyuk Chang, Min Su Kim, Jae-Young Leem, John Ballato, and Sung-O Kim. Low-temperature growth of multiple-stack high-density zno nanoflowers/nanorods on plastic substrates. *Nanotechnology*, 23(48):485606, 2012.

[108] PP Sun, JH Cho, C-H Park, S-J Park, and JG Eden. Close-packed arrays of plasma jets emanating from microchannels in a transparent polymer. *Plasma Science, IEEE Transactions on*, 40(11):2946–2950, 2012.

[109] Chan Hum Park, Joong Seob Lee, Ji Heui Kim, Dong-Kyu Kim, Ok Joo Lee, Hyung Woo Ju, Bo Mi Moon, Jin Hoon Cho, Min Hwan Kim, Peter Peng Sun, et al. Wound healing with nonthermal microplasma jets generated in arrays of hourglass microcavity devices. *Journal of Physics D: Applied Physics*, 47(43):435402, 2014.

[110] Plasma Science Committee et al. *Plasma Science:: From Fundamental Research to Technological Applications*. National Academies Press, 1995.

[111] Seiji Samukawa, Masaru Hori, Shahid Rauf, Kunihide Tachibana, Peter Bruggeman, Gerrit Kroesen, J Christopher Whitehead, Anthony B Murphy, Alexander F Gutsol, Svetlana Starikovskaia, et al. The 2012 plasma roadmap. *Journal of Physics D: Applied Physics*, 45(25):253001, 2012.

[112] Chen Qian, J Yang, M Kang, et al. Investigation on atmospheric pressure plasma jet array in ar. 2014.

[113] Cheng Zhang, Tao Shao, Yixiao Zhou, Zhi Fang, Ping Yan, and Wenjin Yang. Effect of O_2 additive on spatial uniformity of atmospheric-pressure helium plasma jet array driven by microsecond-duration pulses. *Applied Physics Letters*, 105(4):044102–044102, 2014.

[114] M Ghasemi, P Olszewski, JW Bradley, and JL Walsh. Interaction of multiple plasma plumes in an atmospheric pressure plasma jet array. *Journal of Physics D: Applied Physics*, 46(5):052001, 2013.

[115] Jaeyoung Park, I Henins, HW Herrmann, GS Selwyn, JY Jeong, RF Hicks, D Shim, and CS Chang. An atmospheric pressure plasma source. *Applied Physics Letters*, 76(3):288–290, 2000.

[116] Jaeyoung Park, I Henins, HW Herrmann, GS Selwyn, and RF Hicks. Discharge phenomena of an atmospheric pressure radio-frequency capacitive plasma source. *Journal of Applied Physics*, 89(1):20–28, 2001.

[117] Johann Laimer, Stefan Haslinger, Walter Meissl, J Hell, and Herbert Störi. Investigation of an atmospheric pressure radio-frequency capacitive plasma jet. *Vacuum*, 79(3):209–214, 2005.

[118] Johann Laimer and Herbert Störi. Glow discharges observed in capacitive radio-frequency atmospheric-pressure plasma jets. *Plasma Processes and Polymers*, 3(8):573–586, 2006.

[119] Jie Tang, Wenqing Cao, Wei Zhao, Yishan Wang, and Yixiang Duan. Characterization of stable brush-shaped large-volume plasma generated at ambient air. *Physics of Plasmas*, 19(1):013501, 2012.

[120] Jie Tang, Shibo Li, Wei Zhao, Yishan Wang, and Yixiang Duan. Development of a stable dielectric-barrier discharge enhanced laminar plasma jet generated at atmospheric pressure. *Applied Physics Letters*, 100(25):253505, 2012.

[121] Xuemei Li, Jie Tang, Xuefang Zhan, Xin Yuan, Zhongjun Zhao, Yanyue Yan, and Yixiang Duan. A dielectric-barrier discharge enhanced plasma brush array at atmospheric pressure. *Applied Physics Letters*, 103(3):033519, 2013.

[122] Weiman Jiang, Jie Tang, Yishan Wang, Wei Zhao, and Yixiang Duan. A low-power magnetic-field-assisted plasma jet generated by dielectric-barrier discharge enhanced direct-current glow discharge at atmospheric pressure. *Applied Physics Letters*, 104(1):013505, 2014.

[123] Xuechen Li, Runfu Liu, Pengying Jia, Wenting Bao, and Yong Shang. Self-pulsing discharge of a plasma brush operated in atmospheric-pressure argon. *EPL (Europhysics Letters)*, 102(5):55003, 2013.

[124] J Heinlin, G Isbary, W Stolz, G Morfill, M Landthaler, T Shimizu, B Steffes, T Nosenko, JL Zimmermann, and S Karrer. Plasma applications in medicine with a special focus on dermatology. *Journal of the European Academy of Dermatology and Venereology*, 25(1):1–11, 2011.

[125] G Isbary, JL Zimmermann, T Shimizu, Y-F Li, GE Morfill, HM Thomas, B Steffes, J Heinlin, S Karrer, and W Stolz. Non-thermal plasmamore than five years of clinical experience. *Clinical Plasma Medicine*, 1(1):19–23, 2013.

[126] Svetlana A Ermolaeva, Alexander F Varfolomeev, Marina Yu Chernukha, Dmitry S Yurov, Mikhail M Vasiliev, Anastasya A Kaminskaya, Mikhail M Moisenovich, Julia M Romanova, Arcady N Murashev, Irina I Selezneva, et al. Bactericidal effects of non-thermal argon plasma in vitro, in biofilms and in the animal model of infected wounds. *Journal of medical microbiology*, 60(1):75–83, 2011.

[127] Mounir Laroussi. Low-temperature plasma jet for biomedical applications: A review. *Plasma Science, IEEE Transactions on*, 43(3):703–712, 2015.

[128] Jeroen Vandamme, Anton Nikiforov, Klaas Dujardin, Christophe Leys, Luc De Cooman, and Jim Van Durme. Critical evaluation of non-thermal plasma as an innovative accelerated lipid oxidation technique in fish oil. *Food Research International*, 72:115–125, 2015.

[129] Ivona Elez Garofulić, Anet Režek Jambrak, Slobodan Milošević, Verica Dragović-Uzelac, Zoran Zorić, and Zoran Herceg. The effect of gas phase plasma treatment on the anthocyanin and phenolic acid content of sour cherry marasca (prunus cerasus var. marasca) juice. *LWT-Food Science and Technology*, 2014.

[130] Iu Onyshchenko, Anton Yu Nikiforov, Nathalie De Geyter, and Rino Morent. Local analysis of pet surface functionalization by an atmospheric pressure plasma jet. *Plasma Processes and Polymers*, 2015.

[131] L Chandana, P Manoj Kumar Reddy, and Ch Subrahmanyam. Atmospheric pressure non-thermal plasma jet for the degradation of methylene blue in aqueous medium. *Chemical Engineering Journal*, 2015.

[132] María Hijosa-Valsero, Ricardo Molina, Anna Montràs, Michael Müller, and Josep M Bayona. Decontamination of waterborne chemical pollutants by using atmospheric pressure nonthermal plasma: a review. *Environmental Technology Reviews*, 3(1):71–91, 2014.

[133] Davide Mariotti, Jenish Patel, Vladimir Švrček, and Paul Maguire. Plasma–liquid interactions at atmospheric pressure for nanomaterials synthesis and surface engineering. *Plasma Processes and Polymers*, 9(11-12):1074–1085, 2012.

[134] Naoki Shirai, Satoshi Uchida, and Fumiyoshi Tochikubo. Synthesis of metal nanoparticles by dual plasma electrolysis using atmospheric dc glow discharge in contact with liquid. *Japanese Journal of Applied Physics*, 53(4):046202, 2014.

[135] Rino Morent, Nathalie De Geyter, Sandra Van Vlierberghe, Peter Dubruel, Christophe Leys, L Gengembre, Etienne Schacht, and E Payen. Deposition of hmdso-based coatings on pet substrates using an atmospheric pressure dielectric barrier discharge. *Progress in Organic Coatings*, 64(2):304–310, 2009.

[136] Shashi Kishor Pankaj, C Bueno-Ferrer, NN Misra, V Milosavljević, CP O'Donnell, Paula Bourke, KM Keener, and PJ Cullen. Applications of cold plasma technology in food packaging. *Trends in Food Science & Technology*, 35(1):5–17, 2014.

[137] G Da Ponte, E Sardella, F Fanelli, A Van Hoeck, R d'Agostino, S Paulussen, and P Favia. Atmospheric pressure plasma deposition of organic films of biomedical interest. *Surface and Coatings Technology*, 205:S525–S528, 2011.

[138] Rino Morent, Nathalie De Geyter, Tinneke Jacobs, Sandra Van Vlierberghe, Peter Dubruel, Christophe Leys, and Etienne Schacht. Plasma-polymerization of hmdso using an atmospheric pressure dielectric barrier discharge. *Plasma Processes and Polymers*, 6(S1):S537–S542, 2009.

[139] Fiorenza Fanelli. Thin film deposition and surface modification with atmospheric pressure dielectric barrier discharges. *Surface and Coatings Technology*, 205(5):1536–1543, 2010.

[140] Sergei E Alexandrov and Michael L Hitchman. Chemical vapor deposition enhanced by atmospheric pressure non-thermal non-equilibrium plasmas. *Chemical Vapor Deposition*, 11(11-12):457–468, 2005.

[141] Francoise Massines, Christian Sarra-Bournet, Fiorenza Fanelli, Nicolas Naudé, and Nicolas Gherardi. Atmospheric pressure low temperature direct plasma technology: Status and challenges for thin film deposition. *Plasma Processes and Polymers*, 9(11-12):1041–1073, 2012.

[142] Jason D Whittle, Robert D Short, David A Steele, James W Bradley, Paul M Bryant, Faiq Jan, Hynek Biederman, Anton A Serov, Andrei Choukurov, Andrew L Hook, et al. Variability in plasma polymerization processes–an international round-robin study. *Plasma Processes and Polymers*, 10(9):767–778, 2013.

[143] Cheng-Yang Wu, Ren-Mao Liao, Li-Wei Lai, Ming-Shin Jeng, and Day-Shan Liu. Organosilicon/silicon oxide gas barrier structure encapsulated flexible plastic substrate by using plasma-enhanced chemical vapor deposition. *Surface and Coatings Technology*, 206(22):4685–4691, 2012.

[144] I Blaszczyk-Lezak and AM Wrobel. Silicon carbonitride by remote microwave plasma CVD from organosilicon precursor: Physical and mechanical properties of deposited Si:C:N films. *Applied surface science*, 253(18):7404–7411, 2007.

[145] Lan Zhou, Guo-Hua Lv, Chao Ji, and Si-Ze Yang. Application of plasma polymerized siloxane films for the corrosion protection of titanium alloy. *Thin Solid Films*, 520(7):2505–2509, 2012.

[146] Tohru Hayakawa, Masao Yoshinari, and Kimiya Nemoto. Characterization and protein-adsorption behavior of deposited organic thin film onto titanium by plasma polymerization with hexamethyldisiloxane. *Biomaterials*, 25(1):119–127, 2004.

[147] MC Kim and C-P Klages. One-step process to deposit a soft superhydrophobic film by filamentary dielectric barrier discharge-assisted cvd using hmctso as a precursor. *Surface and Coatings Technology*, 204(4):428–432, 2009.

[148] Rino Morent, Nathalie De Geyter, Sandra Van Vlierberghe, Peter Dubruel, Christophe Leys, and Etienne Schacht. Organic–inorganic behaviour of hmdso films plasma-polymerized at atmospheric pressure. *Surface and Coatings Technology*, 203(10):1366–1372, 2009.

[149] HK Yasuda. *Plasma polymerization*. Academic press, 2012.

[150] Nathalie De Geyter, Rino Morent, Sandra Van Vlierberghe, Peter Dubruel, Christophe Leys, L Gengembre, Etienne Schacht, and E Payen. Deposition of polymethyl methacrylate on polypropylene substrates using an atmospheric pressure dielectric barrier discharge. *Progress in Organic Coatings*, 64(2):230–237, 2009.

[151] Rino Morent, Nathalie De Geyter, Sandra Van Vlierberghe, Els Vanderleyden, Peter Dubruel, Christophe Leys, and Etienne Schacht. Deposition of polyacrylic acid films by means of an atmospheric pressure dielectric barrier discharge. *Plasma Chemistry and Plasma Processing*, 29(2):103–117, 2009.

[152] Pieter Cools, Stijn Van Vrekhem, Nathalie De Geyter, and Rino Morent. The use of DBD plasma treatment and polymerization for the enhancement of biomedical uhmwpe. *Thin Solid Films*, 572:251–259, 2014.

[153] R Reuter, N Gherardi, and J Benedikt. Effect of N_2 dielectric barrier discharge treatment on the composition of very thin SiO_2-like films deposited from hexamethyldisiloxane at atmospheric pressure. *Applied Physics Letters*, 101(19):194104–194104, 2012.

[154] Nicolas D Boscher, Florian Hilt, David Duday, Gilles Frache, Thierry Fouquet, and Patrick Choquet. Atmospheric pressure plasma initiated chemical vapor deposition using ultra-short square pulse dielectric barrier discharge. *Plasma Processes and Polymers*, 12(1):66–74, 2015.

[155] F Hilt, D Duday, N Gherardi, G Frache, J Didierjean, and P Choquet. Plasma polymerisation of an allyl organophosphate monomer by atmospheric pressure pulsed-pecvd: insights into the growth mechanisms. *RSC Advances*, 5(6):4277–4285, 2015.

[156] Nicolas D Boscher, Patrick Choquet, David Duday, and Stéphane Verdier. Advantages of a pulsed electrical excitation mode on the corrosion performance of organosilicon thin films deposited on aluminium foil by atmospheric pressure dielectric barrier discharge. *Plasma Processes and Polymers*, 7(2):163–171, 2010.

[157] Jörg Friedrich. Mechanisms of plasma polymerization–reviewed from a chemical point of view. *Plasma Processes and Polymers*, 8(9):783–802, 2011.

[158] Riccardo A Siliprandi, Stefano Zanini, Elisa Grimoldi, Francesco S Fumagalli, Ruggero Barni, and Claudia Riccardi. Atmospheric pressure plasma discharge for polysiloxane thin films deposition and comparison with low

pressure process. *Plasma Chemistry and Plasma Processing*, 31(2):353–372, 2011.

[159] Julien Petersen, Rony Bechara, Julien Bardon, Thierry Fouquet, Fabio Ziarelli, Laurence Daheron, Vincent Ball, Valérie Toniazzo, Marc Michel, Aziz Dinia, et al. Atmospheric plasma deposition process: A versatile tool for the design of tunable siloxanes-based plasma polymer films. *Plasma Processes and Polymers*, 8(10):895–903, 2011.

[160] Sergey A Starostin, Mariadriana Creatore, Jan B Bouwstra, Mauritius van de Sanden, and Hindrik W de Vries. Towards roll-to-roll deposition of high quality moisture barrier films on polymers by atmospheric pressure plasma assisted process. *Plasma Processes and Polymers*, 2014.

[161] Alexandros Kakaroglou, Bernard Nisol, Kitty Baert, Iris De Graeve, François Reniers, Guy Van Assche, and Herman Terryn. Evaluation of the yasuda parameter for the atmospheric plasma deposition of allyl methacrylate. *RSC Advances*, 5(35):27449–27457, 2015.

[162] Axel Sonnenfeld, TM Tun, Lenka Zajíčková, KV Kozlov, H-E Wagner, JF Behnke, and R Hippler. Deposition process based on organosilicon precursors in dielectric barrier discharges at atmospheric pressurea comparison. *Plasmas and polymers*, 6(4):237–266, 2001.

[163] Fiorenza Fanelli, Sara Lovascio, Riccardo d'Agostino, Farzaneh Arefi-Khonsari, and Francesco Fracassi. Ar/HMDSO/O_2 fed atmospheric pressure dbds: Thin film deposition and GC-MS investigation of by-products. *Plasma Processes and Polymers*, 7(7):535–543, 2010.

[164] Fiorenza Fanelli, Sara Lovascio, Riccardo d'Agostino, and Francesco Fracassi. Insights into the atmospheric pressure plasma-enhanced chemical vapor deposition of thin films from methyldisiloxane precursors. *Plasma Processes and Polymers*, 9(11-12):1132–1143, 2012.

[165] Katja Rügner, Rüdiger Reuter, Dirk Ellerweg, Teresa de los Arcos, Achim von Keudell, and Jan Benedikt. Insight into the reaction scheme of SiO_2 film deposition at atmospheric pressure. *Plasma Processes and Polymers*, 10(12):1061–1073, 2013.

[166] Igor Vinogradov and Achim Lunk. Film deposition in the dielectric barrier discharge at atmospheric pressure in He/O_2/HMDSO and He/N_2O/HMDSO mixtures. *Plasma Processes and Polymers*, 6(S1):S514–S518, 2009.

[167] SE Babayan, JY Jeong, A Schütze, VJ Tu, Maryam Moravej, GS Selwyn, and RF Hicks. Deposition of silicon dioxide films with a non-equilibrium

atmospheric-pressure plasma jet. *Plasma Sources Science and Technology*, 10(4):573, 2001.

[168] Uwe Lommatzsch and Jörg Ihde. Plasma polymerization of hmdso with an atmospheric pressure plasma jet for corrosion protection of aluminum and low-adhesion surfaces. *Plasma Processes and Polymers*, 6(10):642–648, 2009.

[169] V Raballand, J Benedikt, and A Von Keudell. Deposition of carbon-free silicon dioxide from pure hexamethyldisiloxane using an atmospheric microplasma jet. *Applied Physics Letters*, 92(9):091502, 2008.

[170] Chun Huang, Shin-Yi Wu, Ching-Yuan Tsai, and Wei-Ting Liu. The growth of organosilicon film using a hexamethyldisilazane/oxygen atmospheric pressure plasma jet. *Thin Solid Films*, 529:292–295, 2013.

[171] Shih-Hsien Yang, Chi-Hung Liu, Chun-Hsien Su, and Hui Chen. Atmospheric-pressure plasma deposition of SiO_x films for super-hydrophobic application. *Thin solid films*, 517(17):5284–5287, 2009.

[172] J Schäfer, R Foest, F Sigeneger, D Loffhagen, K-D Weltmann, U Martens, and R Hippler. Study of thin film formation from silicon-containing precursors produced by an RF non-thermal plasma jet at atmospheric pressure. *Contributions to Plasma Physics*, 52(10):872–880, 2012.

[173] J Schäfer, R Foest, A Quade, A Ohl, and KD Weltmann. Local deposition of SiO_x plasma polymer films by a miniaturized atmospheric pressure plasma jet (appj). *Journal of Physics D: Applied Physics*, 41(19):194010, 2008.

[174] Jan Schäfer, Rüdiger Foest, Antje Quade, Andreas Ohl, and Klaus-Dieter Weltmann. Chemical composition of SiO_x films deposited by an atmospheric pressure plasma jet (APPJ). *Plasma Processes and Polymers*, 6(S1):S519–S524, 2009.

[175] J Schäfer, R Foest, A Quade, A Ohl, J Meichsner, and KD Weltmann. Carbon-free SiO_x films deposited from octamethylcyclotetrasiloxane (OM-CTS) by an atmospheric pressure plasma jet (APPJ). *The European Physical Journal D-Atomic, Molecular, Optical and Plasma Physics*, 54(2):211–217, 2009.

[176] J Schäfer, R Foest, A Ohl, and KD Weltmann. Miniaturized non-thermal atmospheric pressure plasma jetcharacterization of self-organized regimes. *Plasma Physics and Controlled Fusion*, 51(12):124045, 2009.

[177] Yosuke Ito, Keiichiro Urabe, Nobuhiko Takano, and Kunihide Tachibana. High speed deposition of SiO_2 films with plasma jet based on capillary dielectric barrier discharge at atmospheric pressure. *Applied physics express*, 1(6):067009, 2008.

[178] Yosuke Ito, Osamu Sakai, and Kunihide Tachibana. Study of plasma enhanced chemical vapor deposition of ZnO films by non-thermal plasma jet at atmospheric pressure. *Thin Solid Films*, 518(13):3513–3516, 2010.

[179] C Dominguez-Wong, GM Loredo-Becerra, CC Quintero-González, ME Noriega-Treviño, ME Compeán-Jasso, N Niño-Martínez, I DeAlba-Montero, and Facundo Ruiz. Evaluation of the antibacterial activity of an indoor waterborne architectural coating containing Ag/TiO_2 under different relative humidity environments. *Materials Letters*, 134:103–106, 2014.

[180] Rasika Tankhiwale and SK Bajpai. Preparation, characterization and antibacterial applications of ZnO-nanoparticles coated polyethylene films for food packaging. *Colloids and Surfaces B: Biointerfaces*, 90:16–20, 2012.

[181] Rajdip Bandyopadhyaya, M Venkata Sivaiah, and PA Shankar. Silver-embedded granular activated carbon as an antibacterial medium for water purification. *Journal of chemical technology and biotechnology*, 83(8):1177–1180, 2008.

[182] Krasimir Vasilev, Jessica Cook, and Hans J Griesser. Antibacterial surfaces for biomedical devices. 2009.

[183] J Kellogg Parsons, Ioannis Varkarakis, Koon H Rha, Thomas W Jarrett, Peter A Pinto, and Louis R Kavoussi. Complications of abdominal urologic laparoscopy: longitudinal five-year analysis. *Urology*, 63(1):27–32, 2004.

[184] Koichi Ogura, Hideo Yasunaga, Hiromasa Horiguchi, Kazuhiko Ohe, Yusuke Shinoda, Sakae Tanaka, and Hirotaka Kawano. Impact of hospital volume on postoperative complications and in-hospital mortality after musculoskeletal tumor surgery. *The Journal of Bone & Joint Surgery*, 95(18):1684–1691, 2013.

[185] Iolanda Francolini and Gianfranco Donelli. Prevention and control of biofilm-based medical-device-related infections. *FEMS Immunology & Medical Microbiology*, 59(3):227–238, 2010.

[186] Menno LW Knetsch and Leo H Koole. New strategies in the development of antimicrobial coatings: the example of increasing usage of silver and silver nanoparticles. *Polymers*, 3(1):340–366, 2011.

[187] Krasimir Vasilev, Stefani S Griesser, and Hans J Griesser. Antibacterial surfaces and coatings produced by plasma techniques. *Plasma Processes and Polymers*, 8(11):1010–1023, 2011.

[188] Ajay Vikram Singh, Varun Vyas, Rajendra Patil, Vimal Sharma, Pasquale Emanuele Scopelliti, Gero Bongiorno, Alessandro Podesta, Cristina Lenardi, Wasudev Namdev Gade, and Paolo Milani. Quantitative characterization of the influence of the nanoscale morphology of nanostructured surfaces on bacterial adhesion and biofilm formation. *PLoS One*, 6(9):e25029, 2011.

[189] K Anselme, P Davidson, AM Popa, M Giazzon, M Liley, and L Ploux. The interaction of cells and bacteria with surfaces structured at the nanometre scale. *Acta biomaterialia*, 6(10):3824–3846, 2010.

[190] Indrani Banerjee, Ravindra C Pangule, and Ravi S Kane. Antifouling coatings: recent developments in the design of surfaces that prevent fouling by proteins, bacteria, and marine organisms. *Advanced Materials*, 23(6):690–718, 2011.

[191] Ahmed Kerkeni, Nemeshwaree Behary, Pascal Dhulster, Nour-Eddine Chihib, and Anne Perwuelz. Study on the effect of plasma treatment of woven polyester fabrics with respect to nisin adsorption and antibacterial activity. *Journal of Applied Polymer Science*, 129(2):866–873, 2013.

[192] Inigo Braceras, Joseba Oyarbide, Patxi Azpiroz, Nerea Briz, Enrique Ipinazar, Noelia Alvarez, Garbine Atorrasagasti, Raluca M Fratila, and Jesus M Aizpurua. "Plasma-click" based strategy for obtaining antibacterial surfaces on implants. *Plasma Processes and Polymers*, 10(4):328–335, 2013.

[193] Jafar Hasan, Russell J Crawford, and Elena P Ivanova. Antibacterial surfaces: the quest for a new generation of biomaterials. *Trends in biotechnology*, 31(5):295–304, 2013.

[194] Maria Jose Garcia-Fernandez, Laura Martinez-Calvo, Juan-Carlos Ruiz, Michael R Wertheimer, Angel Concheiro, and Carmen Alvarez-Lorenzo. Loading and release of drugs from oxygen-rich plasma polymer coatings. *Plasma Processes and Polymers*, 9(5):540–549, 2012.

[195] Tadas S Sileika, Hyung-Do Kim, Piotr Maniak, and Phillip B Messersmith. Antibacterial performance of polydopamine-modified polymer surfaces containing passive and active components. *ACS applied materials & interfaces*, 3(12):4602–4610, 2011.

[196] Yu-Bin Chang, Pei-Chi Tu, Mien-Win Wu, Tien-Hsiang Hsueh, and Shan-hui Hsu. A study on chitosan modification of polyester fabrics by atmospheric pressure plasma and its antibacterial effects. *Fibers and Polymers*, 9(3):307–311, 2008.

[197] Siriporn Theapsak, Anyarat Watthanaphanit, and Ratana Rujiravanit. Preparation of chitosan-coated polyethylene packaging films by dbd plasma treatment. *ACS applied materials & interfaces*, 4(5):2474–2482, 2012.

[198] Pannee Sophonvachiraporn, Ratana Rujiravanit, Thammanoon Sreethawong, Seiichi Tokura, and Sumaeth Chavadej. Surface characterization and antimicrobial activity of chitosan-deposited dbd plasma-modified woven pet surface. *Plasma Chemistry and Plasma Processing*, 31(1):233–249, 2011.

[199] Layal Karam, Charafeddine Jama, Anne-Sophie Mamede, Ahmad Fahs, Guy Louarn, Pascal Dhulster, and Nour-Eddine Chihib. Study of nisin adsorption on plasma-treated polymer surfaces for setting up materials with antibacterial properties. *Reactive and Functional Polymers*, 73(11):1473–1479, 2013.

[200] David Duday, Christelle Vreuls, Maryline Moreno, Gilles Frache, Nicolas D Boscher, Germaine Zocchi, Catherine Archambeau, Cécile Van De Weerdt, Joseph Martial, and Patrick Choquet. Atmospheric pressure plasma modified surfaces for immobilization of antimicrobial nisin peptides. *Surface and Coatings Technology*, 218:152–161, 2013.

[201] Mirjana Kostić, Nina Radić, Bratislav M Obradović, Suzana Dimitrijević, Milorad M Kuraica, and Petar Škundrić. Silver-loaded cotton/polyester fabric modified by dielectric barrier discharge treatment. *Plasma Processes and Polymers*, 6(1):58–67, 2009.

[202] Ana Kramar, Vadym Prysiazhnyi, B Dojčinović, K Mihajlovski, BM Obradović, MM Kuraica, and Mirjana Kostić. Antimicrobial viscose fabric prepared by treatment in DBD and subsequent deposition of silver and copper ionsinvestigation of plasma aging effect. *Surface and Coatings Technology*, 234:92–99, 2013.

[203] Nguyen Khanh Vu, Andrea Zille, Fernando Ribeiro Oliveira, Noémia Carneiro, and Antonio Pedro Souto. Effect of particle size on silver nanoparticle deposition onto dielectric barrier discharge (DBD) plasma functionalized polyamide fabric. *Plasma Processes and Polymers*, 10(3):285–296, 2013.

[204] Nina Radić, Bratislav M Obradović, Mirjana Kostić, Biljana Dojčinović, Markéta Hudcová, Milorad M Kuraica, and Mirko Černák. Deposition of

gold nanoparticles on polypropylene nonwoven pretreated by dielectric barrier discharge and diffuse coplanar surface barrier discharge. *Plasma Chemistry and Plasma Processing*, 33(1):201–218, 2013.

[205] Yoann De Rancourt, Benoit Couturaud, André Mas, and Jean Jacques Robin. Synthesis of antibacterial surfaces by plasma grafting of zinc oxide based nanocomposites onto polypropylene. *Journal of colloid and interface science*, 402:320–326, 2013.

[206] Marija Gorjanc, Vili Bukošek, Marija Gorenšek, and Miran Mozetič. CF_4 plasma and silver functionalized cotton. *Textile research journal*, page 0040517510376268, 2010.

[207] Shima Taheri, Alex Cavallaro, Susan N Christo, Louise E Smith, Peter Majewski, Mary Barton, John D Hayball, and Krasimir Vasilev. Substrate independent silver nanoparticle based antibacterial coatings. *Biomaterials*, 35(16):4601–4609, 2014.

[208] Shima Taheri, Grit Baier, Peter Majewski, Mary Barton, Renate Förch, Katharina Landfester, and Krasimir Vasilev. Synthesis and surface immobilization of antibacterial hybrid silver-poly (l-lactide) nanoparticles. *Nanotechnology*, 25(30):305102, 2014.

[209] Bernard Despax and Patrice Raynaud. Deposition of "polysiloxane" thin films containing silver particles by an RF asymmetrical discharge. *Plasma Processes and Polymers*, 4(2):127–134, 2007.

[210] Gaëlle Guillemot, Bernard Despax, Patrice Raynaud, Sandrine Zanna, Philippe Marcus, Philippe Schmitz, and Muriel Mercier-Bonin. Plasma deposition of silver nanoparticles onto stainless steel for the prevention of fungal biofilms: a case study on saccharomyces cerevisiae. *Plasma Processes and Polymers*, 5(3):228–238, 2008.

[211] Claire Saulou, Bernard Despax, Patrice Raynaud, Sandrine Zanna, Philippe Marcus, and Muriel Mercier-Bonin. Plasma deposition of organosilicon polymer thin films with embedded nanosilver for prevention of microbial adhesion. *Applied Surface Science*, 256(3):S35–S39, 2009.

[212] Claire Saulou, Bernard Despax, Patrice Raynaud, Sandrine Zanna, Antoine Seyeux, Philippe Marcus, Jean-Nicolas Audinot, and Muriel Mercier-Bonin. Plasma-mediated nanosilver-organosilicon composite films deposited on stainless steel: Synthesis, surface characterization, and evaluation of anti-adhesive and anti-microbial properties on the model yeast saccharomyces cerevisiae. *Plasma Processes and Polymers*, 9(3):324–338, 2012.

[213] C Saulou, F Jamme, C Maranges, I Fourquaux, B Despax, P Raynaud, P Dumas, and M Mercier-Bonin. Synchrotron FTIR microspectroscopy of the yeast saccharomyces cerevisiae after exposure to plasma-deposited nanosilver-containing coating. *Analytical and bioanalytical chemistry*, 396(4):1441–1450, 2010.

[214] S Zanna, C Saulou, M Mercier-Bonin, B Despax, P Raynaud, A Seyeux, and P Marcus. Ageing of plasma-mediated coatings with embedded silver nanoparticles on stainless steel: An XPS and ToF-SIMS investigation. *Applied Surface Science*, 256(22):6499–6505, 2010.

[215] B Despax, C Saulou, P Raynaud, L Datas, and M Mercier-Bonin. Transmission electron microscopy for elucidating the impact of silver-based treatments (ionic silver versus nanosilver-containing coating) on the model yeast saccharomyces cerevisiae. *Nanotechnology*, 22(17):175101, 2011.

[216] Enrico Körner, Myriam H Aguirre, Giuseppino Fortunato, Axel Ritter, Jürgen Rühe, and Dirk Hegemann. Formation and distribution of silver nanoparticles in a functional plasma polymer matrix and related Ag^+ release properties. *Plasma Processes and Polymers*, 7(7):619–625, 2010.

[217] Enrico Körner, Barbara Hanselmann, Peter Cierniak, and Dirk Hegemann. Tailor-made silver release properties of silver-containing functional plasma polymer coatings adjusted through a macroscopic kinetics approach. *Plasma Chemistry and Plasma Processing*, 32(3):619–627, 2012.

[218] Stefanie Lischer, Enrico Körner, Dawn J Balazs, Dakang Shen, Peter Wick, Kathrin Grieder, Dieter Haas, Manfred Heuberger, and Dirk Hegemann. Antibacterial burst-release from minimal Ag-containing plasma polymer coatings. *Journal of The Royal Society Interface*, page rsif20100596, 2011.

[219] Martin Drábik, Josef Pešička, Hynek Biederman, and Dirk Hegemann. Long-term aging of Ag/a-C: H: O nanocomposite coatings in air and in aqueous environment. *Science and Technology of Advanced Materials*, 16(2):025005, 2015.

[220] Alain Daniel, Christophe Le Pen, Catherine Archambeau, and François Reniers. Use of a PECVD–PVD process for the deposition of copper containing organosilicon thin films on steel. *Applied surface science*, 256(3):S82–S85, 2009.

[221] Elena Dilonardo, Antonella Milella, Fabio Palumbo, Giancarlo Capitani, Riccardo d'Agostino, and Francesco Fracassi. One-step plasma deposition of platinum containing nanocomposite coatings. *Plasma Processes and Polymers*, 7(1):51–58, 2010.

[222] T Peter, S Rehders, U Schürmann, T Strunskus, V Zaporojtchenko, and F Faupel. High rate deposition system for metal-cluster/$SiO_xC_yH_z-$ polymer nanocomposite thin films. *Journal of nanoparticle research*, 15(6):1–8, 2013.

[223] Oliver Beier, Andreas Pfuch, Kerstin Horn, Jürgen Weisser, Matthias Schnabelrauch, and Arnd Schimanski. Low temperature deposition of antibacterially active silicon oxide layers containing silver nanoparticles, prepared by atmospheric pressure plasma chemical vapor deposition. *Plasma Processes and Polymers*, 10(1):77–87, 2013.

[224] Sebastian Spange, Andreas Pfuch, Cornelia Wiegand, Oliver Beier, Uta C Hipler, and Bernd Grünler. Atmospheric pressure plasma CVD as a tool to functionalise wound dressings. *Journal of Materials Science: Materials in Medicine*, 26(2):1–9, 2015.

[225] N Alissawi, T Peter, T Strunskus, C Ebbert, G Grundmeier, and F Faupel. Plasma-polymerized HMDSo coatings to adjust the silver ion release properties of Ag/polymer nanocomposites. *Journal of nanoparticle research*, 15(11):1–12, 2013.

[226] N Alissawi, V Zaporojtchenko, T Strunskus, T Hrkac, I Kocabas, B Erkartal, VSK Chakravadhanula, L Kienle, G Grundmeier, Dieter Garbe-Schönberg, et al. Tuning of the ion release properties of silver nanoparticles buried under a hydrophobic polymer barrier. *Journal of Nanoparticle Research*, 14(7):1–12, 2012.

[227] Krasimir Vasilev, Vasu Sah, Karine Anselme, Chi Ndi, Mihaela Mateescu, Bjorn Dollmann, Petr Martinek, Lydie Ploux, and Hans J Griesser. Tunable antibacterial coatings that support mammalian cell growth. *Nano letters*, 10(1):202–207, 2009.

[228] Krasimir Vasilev, Neil Poulter, Petr Martinek, and Hans J Griesser. Controlled release of levofloxacin sandwiched between two plasma polymerized layers on a solid carrier. *ACS applied materials & interfaces*, 3(12):4831–4836, 2011.

[229] Krasimir Vasilev. Nanoengineered plasma polymer films for biomaterial applications. *Plasma Chemistry and Plasma Processing*, 34(3):545–558, 2014.

[230] Emilia Kulaga, Lydie Ploux, and Vincent Roucoules. Effect of ageing and sterilization on plasma multilayer system. *Polymer Degradation and Stability*, 116:1–13, 2015.

[231] Emilia Kulaga, Lydie Ploux, Lavinia Balan, Gautier Schrodj, and Vincent Roucoules. Mechanically responsive antibacterial plasma polymer coatings for textile biomaterials. *Plasma Processes and Polymers*, 11(1):63–79, 2014.

[232] Aissam Airoudj, Emilia Kulaga, Vincent Roucoules, and Lydie Ploux. Mechanically switchable biocide plasma-polymer coatings for biomaterials. *Advanced Engineering Materials*, 13(10):B360–B368, 2011.

[233] U Fantz. Basics of plasma spectroscopy. *Plasma sources science and technology*, 15(4):S137, 2006.

[234] Giorgio Dilecce. Optical spectroscopy diagnostics of discharges at atmospheric pressure. *Plasma Sources Science and Technology*, 23(1):015011, 2014.

[235] A Yu Nikiforov, Ch Leys, MA Gonzalez, and JL Walsh. Electron density measurement in atmospheric pressure plasma jets: Stark broadening of hydrogenated and non-hydrogenated lines. *Plasma Sources Science and Technology*, 24(3):034001, 2015.

[236] Se Youn Moon, W Choe, and BK Kang. A uniform glow discharge plasma source at atmospheric pressure. *Applied Physics Letters*, 84(2):188–190, 2004.

[237] Mounir Laroussi and Xu Lu. Room-temperature atmospheric pressure plasma plume for biomedical applications. *Applied Physics Letters*, 87(11):113902, 2005.

[238] B Benstaali, P Boubert, BG Cheron, A Addou, and JL Brisset. Density and rotational temperature measurements of the OH and NO radicals produced by a gliding arc in humid air. *Plasma chemistry and plasma processing*, 22(4):553–571, 2002.

[239] Se Youn Moon and W Choe. A comparative study of rotational temperatures using diatomic OH, O_2 and N_2^+ molecular spectra emitted from atmospheric plasmas. *Spectrochimica Acta Part B: Atomic Spectroscopy*, 58(2):249–257, 2003.

[240] Géraldine Faure and SM Shkol'Nik. Determination of rotational and vibrational temperatures in a discharge with liquid non-metallic electrodes in air at atmospheric pressure. *Journal of Physics D: Applied Physics*, 31(10):1212, 1998.

[241] CO Laux, TG Spence, CH Kruger, and RN Zare. Optical diagnostics of atmospheric pressure air plasmas. *Plasma Sources Science and Technology*, 12(2):125, 2003.

[242] J Luque and DR Crosley. LIFBASE: Database and spectral simulation (version 1.5). *SRI international report MP*, pages 99–009, 1999.

[243] Li Li, Anton Nikiforov, Qing Xiong, N Britun, Rony Snyders, X Lu, and Christophe Leys. OH radicals distribution in an Ar-H_2O atmospheric plasma jet. *Physics of Plasmas*, 20(9):093502, 2013.

[244] Nimisha Srivastava and Chuji Wang. Effects of water addition on OH radical generation and plasma properties in an atmospheric argon microwave plasma jet. *Journal of Applied Physics*, 110(5):053304, 2011.

[245] Tiny Verreycken, Rob Mensink, Ruud Van Der Horst, Nader Sadeghi, and Peter J Bruggeman. Absolute OH density measurements in the effluent of a cold atmospheric-pressure Ar–H_2O RF plasma jet in air. *Plasma Sources Science and Technology*, 22(5):055014, 2013.

[246] Xuechen Li, Lifang Dong, Na Zhao, Zengqian Yin, Tongzhen Fang, and Long Wang. A simple device of generating glow discharge plasma in atmospheric pressure argon. *Applied Physics Letters*, 91(16):161507, 2007.

[247] Peter Bruggeman, Felipe Iza, Peter Guns, Daniel Lauwers, Michael G Kong, Yolanda Aranda Gonzalvo, Christophe Leys, and Daan C Schram. Electronic quenching of OH(A) by water in atmospheric pressure plasmas and its influence on the gas temperature determination by OH (A–X) emission. *Plasma Sources Science and Technology*, 19(1):015016, 2010.

[248] Peter Bruggeman, Daan C Schram, Michael G Kong, and Christophe Leys. Is the rotational temperature of OH(A–X) for discharges in and in contact with liquids a good diagnostic for determining the gas temperature? *Plasma Processes and Polymers*, 6(11):751–762, 2009.

[249] Qing Xiong, AY Nikiforov, XP Lu, and Christophe Leys. High-speed dispersed photographing of an open-air argon plasma plume by a grating–ICCD camera system. *Journal of Physics D: Applied Physics*, 43(41):415201, 2010.

[250] E Stoffels, AJ Flikweert, WW Stoffels, and GMW Kroesen. Plasma needle: a non-destructive atmospheric plasma source for fine surface treatment of (bio) materials. *Plasma Sources Science and Technology*, 11(4):383, 2002.

[251] N Masoud, K Martus, M Figus, and K Becker. Rotational and vibrational temperature measurements in a high-pressure cylindrical dielectric barrier discharge (C-DBD). *Contributions to Plasma Physics*, 45(1):32–39, 2005.

[252] A Yu Nikiforov, Abdollah Sarani, and Ch Leys. The influence of water vapor content on electrical and spectral properties of an atmospheric pressure plasma jet. *Plasma Sources Science and Technology*, 20(1):015014, 2011.

[253] Tian-Liang Zhao, Yong Xu, Yuan-Hong Song, Xiao-Song Li, Jing-Lin Liu, Jin-Bao Liu, and Ai-Min Zhu. Determination of vibrational and rotational temperatures in a gliding arc discharge by using overlapped molecular emission spectra. *Journal of Physics D: Applied Physics*, 46(34):345201, 2013.

[254] Baoguo Zhang, Jianquan Wang, Xinli Tian, Xiujian Tang, Wanglong Wang, and Pengxiao Wang. Spectroscopic diagnostics of plasma jet in microdetonation of striking arc machining of engineering ceramics. *Nuclear Instruments and Methods in Physics Research Section B: Beam Interactions with Materials and Atoms*, 307:353–356, 2013.

[255] Dana Skácelová and Pavel Slavicek. Characterization of plasma pencil pulsed discharge. *Plasma Science, IEEE Transactions on*, 40(11):2920–2924, 2012.

[256] S Förster, C Mohr, and W Viöl. Investigations of an atmospheric pressure plasma jet by optical emission spectroscopy. *Surface and Coatings Technology*, 200(1):827–830, 2005.

[257] E Iordanova, JM Palomares, Antonio Gamero, Antonio Sola, and JJAM van der Mullen. A novel method to determine the electron temperature and density from the absolute intensity of line and continuum emission: application to atmospheric microwave induced ar plasmas. *Journal of Physics D: Applied Physics*, 42(15):155208, 2009.

[258] Leila Taghizadeh, Joost van der Mullen, Anton Nikiforov, and Christophe Leys. Determination of the electron density in an argon plasma jet using absolute measurements of continuum radiation. *Plasma Processes and Polymers*, 2015.

[259] Leila Taghizadeh, Anton Nikiforov, Rino Morent, Joost van der Mullen, and Christophe Leys. Determination of the electron temperature of atmospheric pressure argon plasmas by absolute line intensities and a collisional radiative model. *Plasma Processes and Polymers*, 11(8):777–786, 2014.

[260] DE Kelleher, WL Wiese, V Helbig, RL Greene, and DH Oza. Advances in plasma broadening of atomic hydrogen. *Physica Scripta*, 1993(T47):75, 1993.

[261] Sven Hofmann, AFH Van Gessel, Tiny Verreycken, and P Bruggeman. Power dissipation, gas temperatures and electron densities of cold atmospheric pressure helium and argon rf plasma jets. *Plasma Sources Science and Technology*, 20(6):065010, 2011.

[262] BN Sismanoglu, J Amorim, JA Souza-Corrêa, C Oliveira, and MP Gomes. Optical emission spectroscopy diagnostics of an atmospheric pressure direct current microplasma jet. *Spectrochimica Acta Part B: Atomic Spectroscopy*, 64(11):1287–1293, 2009.

[263] BN Sismanoglu, KG Grigorov, R Caetano, MVO Rezende, and YD Hoyer. Spectroscopic measurements and electrical diagnostics of microhollow cathode discharges in argon flow at atmospheric pressure. *The European Physical Journal D-Atomic, Molecular, Optical and Plasma Physics*, 60(3):505–516, 2010.

[264] Muyang Qian, Chunsheng Ren, Dezhen Wang, Jialiang Zhang, and Guodong Wei. Stark broadening measurement of the electron density in an atmospheric pressure argon plasma jet with double-power electrodes. *Journal of Applied Physics*, 107(6):063303, 2010.

[265] Qing Xiong, Anton Nikiforov, N Britun, Rony Snyders, Christophe Leys, and X Lu. A simple profile-fitting method to determine the metastable and resonant densities in a cold atmospheric pressure argon plasma jet. *Journal of Applied Physics*, 110(7):073302, 2011.

[266] RS Patel, M Roy, GK Dutta, et al. Mass spectrometry-a review. *Veterinary World*, 5(3):185–192, 2012.

[267] J Benedikt, A Hecimovic, D Ellerweg, and A Von Keudell. Quadrupole mass spectrometry of reactive plasmas. *Journal of Physics D: Applied Physics*, 45(40):403001, 2012.

[268] S Nunomura and M Kondo. Characterization of high-pressure capacitively coupled hydrogen plasmas. *Journal of Applied Physics*, 102(9):093306, 2007.

[269] Hiroshi Muta, Shinichi Kishida, Masayoshi Tanaka, Yasuhiro Yamauchi, Tomoyoshi Baba, Yoshiaki Takeuchi, Hiromu Takatsuka, and Yoshinobu Kawai. Investigation of plasma parameters in a VHF plasma with narrow gap under high gaseous pressure. *Plasma Processes and Polymers*, 6(S1):S792–S795, 2009.

[270] Jan D Skalny, Tomas Mikoviny, Stefan Matejcik, and Nigel J Mason. An analysis of mass spectrometric study of negative ions extracted from negative corona discharge in air. *International Journal of Mass Spectrometry*, 233(1):317–324, 2004.

[271] Kanako Sekimoto and Mitsuo Takayama. Influence of needle voltage on the formation of negative core ions using atmospheric pressure corona discharge in air. *International Journal of Mass Spectrometry*, 261(1):38–44, 2007.

[272] Kenkichi Nagato, Yasunori Matsui, Takahiro Miyata, and Toshiyuki Yamauchi. An analysis of the evolution of negative ions produced by a corona ionizer in air. *International Journal of Mass Spectrometry*, 248(3):142–147, 2006.

[273] Peter Bruggeman, Felipe Iza, Daniël Lauwers, and Yolanda Aranda Gonzalvo. Mass spectrometry study of positive and negative ions in a capacitively coupled atmospheric pressure rf excited glow discharge in he–water mixtures. *Journal of Physics D: Applied Physics*, 43(1):012003, 2010.

[274] Jun-Seok Oh, Hiroshi Furuta, Akimitsu Hatta, and James W Bradley. Investigating the effect of additional gases in an atmospheric-pressure helium plasma jet using ambient mass spectrometry. *Japanese Journal of Applied Physics*, 54(1S):01AA03, 2015.

[275] E Stoffels, Y Aranda Gonzalvo, TD Whitmore, DL Seymour, and JA Rees. Mass spectrometric detection of short-living radicals produced by a plasma needle. *Plasma Sources Science and Technology*, 16(3):549, 2007.

[276] D Maletić, N Puač, S Lazović, G Malović, T Gans, V Schulz-von der Gathen, and Z Lj Petrović. Detection of atomic oxygen and nitrogen created in a radio-frequency-driven micro-scale atmospheric pressure plasma jet using mass spectrometry. *Plasma Physics and Controlled Fusion*, 54(12):124046, 2012.

[277] Julien Jarrige, Mounir Laroussi, and Erdinc Karakas. Formation and dynamics of plasma bullets in a non-thermal plasma jet: influence of the high-voltage parameters on the plume characteristics. *Plasma Sources Science and Technology*, 19(6):065005, 2010.

[278] Erdinc Karakas and Mounir Laroussi. Experimental studies on the plasma bullet propagation and its inhibition. *Journal of Applied Physics*, 108(6):063305, 2010.

[279] JP Boeuf, LL Yang, and LC Pitchford. Dynamics of a guided streamer ('plasma bullet') in a helium jet in air at atmospheric pressure. *Journal of Physics D: Applied Physics*, 46(1):015201, 2013.

[280] XinPei Lu, Qing Xiong, ZiLan Xiong, Jing Hu, Fei Zhou, WeiWei Gong, YuBin Xian, ChangLin Zhou, ZhiYuan Tang, ZhongHe Jiang, et al. A cold plasma cross made of three bullet-like plasma plumes. *Thin Solid Films*, 518(3):967–970, 2009.

[281] Longwei Chen, Peng Zhao, Xingsheng Shu, Jie Shen, and Yuedong Meng. On the mechanism of atmospheric pressure plasma plume. *Physics of Plasmas*, 17(8):083502, 2010.

[282] Deanna A Lacoste, Anne Bourdon, Koichi Kuribara, Keiichiro Urabe, Sven Stauss, and Kazuo Terashima. Pure air-plasma bullets propagating inside microcapillaries and in ambient air. *Plasma Sources Science and Technology*, 23(6):062006, 2014.

[283] Xianguo Lu, GV Naidis, M Laroussi, and K Ostrikov. Guided ionization waves: Theory and experiments. *Physics Reports*, 540(3):123–166, 2014.

[284] Anton Nikiforov, Li Li, N Britun, Rony Snyders, Patrick Vanraes, and Christophe Leys. Influence of air diffusion on the OH radicals and atomic O distribution in an atmospheric Ar (bio)plasma jet. *Plasma Sources Science and Technology*, 23(1):015015, 2014.

[285] AFH Van Gessel, EAD Carbone, PJ Bruggeman, and JJAM Van der Mullen. Laser scattering on an atmospheric pressure plasma jet: disentangling rayleigh, raman and thomson scattering. *Plasma Sources Science and Technology*, 21(1):015003, 2012.

[286] Eric Robert, Vanessa Sarron, Delphine Riès, Sébastien Dozias, Marc Vandamme, and Jean Michel Pouvesle. Characterization of pulsed atmospheric-pressure plasma streams (PAPS) generated by a plasma gun. *Plasma Sources Science and Technology*, 21(3):034017, 2012.

[287] Qing Xiong, A Yu Nikiforov, Li Li, Patrick Vanraes, N Britun, Rony Snyders, Xin P Lu, and Christophe Leys. Absolute OH density determination by laser induced fluorescence spectroscopy in an atmospheric pressure rf plasma jet. *The European Physical Journal D-Atomic, Molecular, Optical and Plasma Physics*, 66(11):1–8, 2012.

[288] Francis M Mirabella. *Internal reflection spectroscopy: Theory and applications*, volume 15. CRC Press, 1992.

[289] Kai Siegbahn, Ulrik Gelius, Hans Siegbahn, and Erik Olson. Angular distribution of electrons in ESCA spectra from a single crystal. *Physica Scripta*, 1(5-6):272, 1970.

[290] Mohammad J Hajipour, Katharina M Fromm, Ali Akbar Ashkarran, Dorleta Jimenez de Aberasturi, Idoia Ruiz de Larramendi, Teofilo Rojo, Vahid Serpooshan, Wolfgang J Parak, and Morteza Mahmoudi. Antibacterial properties of nanoparticles. *Trends in biotechnology*, 30(10):499–511, 2012.

[291] Connie R Mahon, Donald C Lehman, and George Manuselis Jr. *Textbook of diagnostic microbiology*. Elsevier Health Sciences, 2014.

[292] J Han, ME Castell-Perez, and RG Moreira. The influence of electron beam irradiation of antimicrobial-coated ldpe/polyamide films on antimicrobial activity and film properties. *LWT-Food Science and Technology*, 40(9):1545–1554, 2007.

[293] Donghwan Chung, Spyridon E Papadakis, and Kit L Yam. Evaluation of a polymer coating containing triclosan as the antimicrobial layer for packaging materials. *International journal of food science & technology*, 38(2):165–169, 2003.

[294] Joerg Liebmann, Joachim Scherer, Nikita Bibinov, Priyadarshini Rajasekaran, Reinhold Kovacs, Roland Gesche, Peter Awakowicz, and Victoria Kolb-Bachofen. Biological effects of nitric oxide generated by an atmospheric pressure gas-plasma on human skin cells. *Nitric Oxide*, 24(1):8–16, 2011.

[295] Yuri Akishev, Mikhail Grushin, Vladimir Karalnik, Igor Kochetov, Anatoly Napartovich, and Nikolay Trushkin. Generation of atmospheric pressure non-thermal plasma by diffusive and constricted discharges in air and nitrogen at the rest and flow. In *Journal of Physics: Conference Series*, volume 257, page 012014. IOP Publishing, 2010.

[296] Yu Akishev, O Goossens, T Callebaut, Christophe Leys, A Napartovich, and N Trushkin. The influence of electrode geometry and gas flow on corona-to-glow and glow-to-spark threshold currents in air. *Journal of Physics D: Applied Physics*, 34(18):2875, 2001.

[297] Eef Temmerman, Yuri Akishev, Nikolay Trushkin, Christophe Leys, and Jo Verschuren. Surface modification with a remote atmospheric pressure plasma: dc glow discharge and surface streamer regime. *Journal of Physics D: Applied Physics*, 38(4):505, 2005.

[298] Yukikazu Itikawa, M Hayashi, A Ichimura, K Onda, K Sakimoto, K Takayanagi, M Nakamura, H Nishimura, and T Takayanagi. Cross sections for collisions of electrons and photons with nitrogen molecules. *Journal of physical and chemical reference data*, 15(3):985–1010, 1986.

[299] DR Bates, AE Kingston, and RW Pt McWhirter. Recombination between electrons and atomic ions. i. optically thin plasmas. *Proceedings of the Royal Society of London. Series A. Mathematical and Physical Sciences*, 267(1330):297–312, 1962.

[300] Alexander Fridman. *Plasma chemistry*. Cambridge University Press, 2008.

[301] A Yu Nikiforov, Ch Leys, Li Li, Lucie Nemcova, and F Krcma. Physical properties and chemical efficiency of an underwater dc discharge generated in He, Ar, N_2 and air bubbles. *Plasma Sources Science and Technology*, 20(3):034008, 2011.

[302] Yu S Akishev, ME Grushin, VB Karal'nik, AV Petryakov, and NI Trushkin. Pink splash of active nitrogen in the discharge afterglow. *Plasma Physics Reports*, 33(9):757–773, 2007.

[303] Tom Callebaut, I Kochetov, Yu Akishev, A Napartovich, and Christophe Leys. Numerical simulation and experimental study of the corona and glow regime of a negative pin-to-plate discharge in flowing ambient air. *Plasma Sources Science and Technology*, 13(2):245, 2004.

[304] IA Kossyi, A Yu Kostinsky, AA Matveyev, and VP Silakov. Kinetic scheme of the non-equilibrium discharge in nitrogen-oxygen mixtures. *Plasma Sources Science and Technology*, 1(3):207, 1992.

[305] Gerhard Herzberg. *Molecular spectra and molecular structure: spectra of diatomic molecules*. van Nostrand, 1982.

[306] Ph Teulet, JP Sarrette, and AM Gomes. Calculation of electron impact inelastic cross sections and rate coefficients for diatomic molecules. application to air molecules. *Journal of Quantitative Spectroscopy and Radiative Transfer*, 62(5):549–569, 1999.

[307] DE Shemansky and AL Broadfoot. Excitation of N_2 and N_2^+ systems by electrons-i. absolute transition probabilities. *Journal of Quantitative Spectroscopy and Radiative Transfer*, 11(10):1385 – 1400, 1971.

[308] Eduard M Bazelyan and Yuri P Raizer. *Spark discharge*. CRC press, 1997.

[309] SC Hill and L Douglas Smoot. Modeling of nitrogen oxides formation and destruction in combustion systems. *Progress in energy and combustion science*, 26(4):417–458, 2000.

[310] Barry Twomey, Mahfujur Rahman, Gerry Byrne, Alan Hynes, Lesley-Ann O'Hare, Liam O'Neill, and Denis Dowling. Effect of plasma exposure on the chemistry and morphology of aerosol-assisted, plasma-deposited coatings. *Plasma processes and polymers*, 5(8):737–744, 2008.

[311] AS da Silva Sobrinho, M Latreche, G Czeremuszkin, JE Klemberg-Sapieha, and MR Wertheimer. Transparent barrier coatings on polyethylene terephthalate by single-and dual-frequency plasma-enhanced chemical vapor deposition. *Journal of Vacuum Science & Technology A*, 16(6):3190–3198, 1998.

[312] Nathalie De Geyter, Rino Morent, Sandra Van Vlierberghe, Peter Dubruel, Christophe Leys, and Etienne Schacht. Plasma polymerisation of siloxanes at atmospheric pressure. *Surface Engineering*, 27(8):627–633, 2011.

[313] T Belmonte, G Henrion, and T Gries. Nonequilibrium atmospheric plasma deposition. *Journal of thermal spray technology*, 20(4):744–759, 2011.

[314] Paul W May. Diamond thin films: a 21st-century material. *Philosophical Transactions of the Royal Society of London. Series A: Mathematical, Physical and Engineering Sciences*, 358(1766):473–495, 2000.

[315] Li Fu Hei, Jie Liu, Fan Xiu Lu, Cheng Ming Li, Jian Hua Song, and Guang Chao Chen. Effect of growth parameters on single crystal diamond deposition by dc arc plasma jet cvd. In *Advanced Materials Research*, volume 490, pages 3094–3099. Trans Tech Publ, 2012.

[316] Arias A. I. Oliva and V Lopez-Garduza, F.and Sosa. On the thickness measurement of metallic thin films. *Ingenieria*, 10(2):57–65, 2006.

[317] Ritalba Lamendola, Riccardo dAgostino, and Francesco Fracassi. Thin film deposition from hexamethyldisiloxane fed glow discharges. *Plasmas and polymers*, 2(3):147–164, 1997.

[318] Chun Huang and Qingsong Yu. Deposition of silicon oxide hard coatings by low-temperature radio-frequency plasmas. *Journal of applied polymer science*, 116(1):245–251, 2010.

[319] GR Nowling, M Yajima, SE Babayan, M Moravej, X Yang, W Hoffman, and RF Hicks. Chamberless plasma deposition of glass coatings on plastic. *Plasma Sources Science and Technology*, 14(3):477, 2005.

[320] George Socrates. *Infrared and Raman characteristic group frequencies: tables and charts*. John Wiley & Sons, 2004.

[321] Yung-Sen Lin, Mao-Syuan Weng, Tsair-Wang Chung, and Charming Huang. Enhanced surface hardness of flexible polycarbonate substrates using plasma-polymerized organosilicon oxynitride films by air plasma jet under atmospheric pressure. *Surface and Coatings Technology*, 205(13):3856–3864, 2011.

[322] Michael Deilmann, Mirko Grabowski, Sebastian Theiß, Nikita Bibinov, and Peter Awakowicz. Permeation mechanisms of pulsed microwave plasma deposited silicon oxide films for food packaging applications. *Journal of Physics D: Applied Physics*, 41(13):135207, 2008.

[323] Françoise Massines, Nicolas Gherardi, Antonella Fornelli, and Steve Martin. Atmospheric pressure plasma deposition of thin films by townsend dielectric barrier discharge. *Surface and Coatings Technology*, 200(5):1855–1861, 2005.

[324] Morgan R Alexander, RD Short, FR Jones, W Michaeli, and CJ Blomfield. A study of HMDSO/O_2 plasma deposits using a high-sensitivity and-energy resolution xps instrument: curve fitting of the Si 2p core level. *Applied surface science*, 137(1):179–183, 1999.

[325] J Musil. Hard and superhard nanocomposite coatings. *Surface and coatings technology*, 125(1):322–330, 2000.

[326] Pulickel M Ajayan, Linda S Schadler, and Paul V Braun. *Nanocomposite science and technology*. John Wiley & Sons, 2006.

[327] Stuart B Levy and Bonnie Marshall. Antibacterial resistance worldwide: causes, challenges and responses. *Nature medicine*, 10:S122–S129, 2004.

[328] Mahendra Rai, Alka Yadav, and Aniket Gade. Silver nanoparticles as a new generation of antimicrobials. *Biotechnology advances*, 27(1):76–83, 2009.

[329] Nicola Cioffi, Luisa Torsi, Nicoletta Ditaranto, Giuseppina Tantillo, Lina Ghibelli, Luigia Sabbatini, Teresa Bleve-Zacheo, Maria D'Alessio, P Giorgio Zambonin, and Enrico Traversa. Copper nanoparticle/polymer composites with antifungal and bacteriostatic properties. *Chemistry of Materials*, 17(21):5255–5262, 2005.

[330] Krishna R Raghupathi, Ranjit T Koodali, and Adhar C Manna. Size-dependent bacterial growth inhibition and mechanism of antibacterial activity of zinc oxide nanoparticles. *Langmuir*, 27(7):4020–4028, 2011.

[331] PV AshaRani, Grace Low Kah Mun, Manoor Prakash Hande, and Suresh Valiyaveettil. Cytotoxicity and genotoxicity of silver nanoparticles in human cells. *ACS nano*, 3(2):279–290, 2008.

[332] Xuefei Li, Liming Xu, Anliang Shao, Gang Wu, and Nobutaka Hanagata. Cytotoxic and genotoxic effects of silver nanoparticles on primary syrian hamster embryo (SHE) cells. *Journal of nanoscience and nanotechnology*, 13(1):161–170, 2013.

[333] Virendra Kumar, Claude Jolivalt, Jerome Pulpytel, Reza Jafari, and Farzaneh Arefi-Khonsari. Development of silver nanoparticle loaded antibacterial polymer mesh using plasma polymerization process. *Journal of Biomedical Materials Research Part A*, 101(4):1121–1132, 2013.

[334] Andreas Holländer, Michael Haupt, and Christian Oehr. On depth profiling of polymers by argon ion sputtering. *Plasma Processes and Polymers*, 4(9):773–776, 2007.

[335] Thomas Nelis and Richard Payling. *Glow discharge optical emission spectroscopy: a practical guide*, volume 7. Royal Society of Chemistry, 2003.

[336] QL Feng, Jian Wu, GQ Chen, FZ Cui, TN Kim, and JO Kim. A mechanistic study of the antibacterial effect of silver ions on escherichia coli and staphylococcus aureus. *Journal of biomedical materials research*, (52):662–8, 2001.

[337] Jun Sung Kim, Eunye Kuk, Kyeong Nam Yu, Jong-Ho Kim, Sung Jin Park, Hu Jang Lee, So Hyun Kim, Young Kyung Park, Yong Ho Park, Cheol-Yong Hwang, et al. Antimicrobial effects of silver nanoparticles. *Nanomedicine: Nanotechnology, Biology and Medicine*, 3(1):95–101, 2007.

[338] Stefan Marius, Hritcu Lucian, Mihasan Marius, Pricop Daniela, Gostin Irina, Olariu Romeo-Iulian, Dunca Simona, and Melnig Viorel. Enhanced antibacterial effect of silver nanoparticles obtained by electrochemical synthesis in poly (amide-hydroxyurethane) media. *Journal of Materials Science: Materials in Medicine*, 22(4):789–796, 2011.

[339] Dan-Qi Chen, Yu-Zhong Wang, Xiao-Ping Hu, De-Yi Wang, Ming-Hai Qu, and Bing Yang. Flame-retardant and anti-dripping effects of a novel char-forming flame retardant for the treatment of poly (ethylene terephthalate) fabrics. *Polymer Degradation and Stability*, 88(2):349–356, 2005.

[340] Marija Gorenšek, Marija Gorjanc, Vili Bukošek, Janez Kovač, Zoran Petrović, and Nevena Puač. Functionalization of polyester fabric by Ar/N_2 plasma and silver. *Textile research journal*, 80(16):1633–1642, 2010.

[341] Xiaoli Cheng, Kaikai Ma, Rong Li, Xuehong Ren, and TS Huang. Antimicrobial coating of modified chitosan onto cotton fabrics. *Applied Surface Science*, 309:138–143, 2014.

[342] Mohammad Shahid and Faqeer Mohammad. Green chemistry approaches to develop antimicrobial textiles based on sustainable biopolymersr a review. *Industrial & Engineering Chemistry Research*, 52(15):5245–5260, 2013.

[343] Ying-Hung Chen, Chiao-Chih Hsu, and Ju-Liang He. Antibacterial silver coating on poly (ethylene terephthalate) fabric by using high power impulse magnetron sputtering. *Surface and Coatings Technology*, 232:868–875, 2013.

[344] U Klueh, V Wagner, S Kelly, A Johnson, and JD Bryers. Efficacy of silver-coated fabric to prevent bacterial colonization and subsequent device-based biofilm formation. *Journal of biomedical materials research*, 53(6):621–631, 2000.

[345] SX Jiang, WF Qin, RH Guo, and L Zhang. Surface functionalization of nanostructured silver-coated polyester fabric by magnetron sputtering. *Surface and Coatings Technology*, 204(21):3662–3667, 2010.

[346] Sung Hoon Jeong, Yun Hwan Hwang, and Sung Chul Yi. Antibacterial properties of padded PP/PE nonwovens incorporating nano-sized silver colloids. *Journal of materials science*, 40(20):5413–5418, 2005.

[347] Hoon Joo Lee and Sung Hoon Jeong. Bacteriostasis of nanosized colloidal silver on polyester nonwovens. *Textile Research Journal*, 74(5):442–447, 2004.

[348] Ilana Perelshtein, Guy Applerot, Nina Perkas, Geoffrey Guibert, Serguei Mikhailov, and Aharon Gedanken. Sonochemical coating of silver nanoparticles on textile fabrics (nylon, polyester and cotton) and their antibacterial activity. *Nanotechnology*, 19(24):245705, 2008.

[349] Roya Dastjerdi, Majid Montazer, and Shadi Shahsavan. A new method to stabilize nanoparticles on textile surfaces. *Colloids and Surfaces A: Physicochemical and Engineering Aspects*, 345(1):202–210, 2009.

[350] David Greenwood, Richard CB Slack, Michael R Barer, and Will L Irving. *Medical Microbiology: A Guide to Microbial Infections: Pathogenesis, Immunity, Laboratory Diagnosis and Control. With STUDENT CONSULT Online Access*. Elsevier Health Sciences, 2012.

[351] Franklin D Lowy. Antimicrobial resistance: the example of staphylococcus aureus. *Journal of Clinical Investigation*, 111(9):1265, 2003.

[352] François L Mayer, Duncan Wilson, and Bernhard Hube. Candida albicans pathogenicity mechanisms. *Virulence*, 4(2):119–128, 2013.

[353] Joseph J Castellano, Susan M Shafii, Francis Ko, Guillermo Donate, Terry E Wright, Rudolph J Mannari, Wyatt G Payne, David J Smith, and Martin C Robson. Comparative evaluation of silver-containing antimicrobial dressings and drugs. *International Wound Journal*, 4(2):114–122, 2007.

[354] Zong-ming Xiu, Qing-bo Zhang, Hema L Puppala, Vicki L Colvin, and Pedro JJ Alvarez. Negligible particle-specific antibacterial activity of silver nanoparticles. *Nano letters*, 12(8):4271–4275, 2012.

[355] Woo Kyung Jung, Hye Cheong Koo, Ki Woo Kim, Sook Shin, So Hyun Kim, and Yong Ho Park. Antibacterial activity and mechanism of action of the silver ion in Staphylococcus aureus and Escherichia coli. *Applied and environmental microbiology*, 74(7):2171–2178, 2008.

[356] J Thiel, L Pakstis, S Buzby, M Raffi, C Ni, D emsp14J Pochan, and S Ismat Shah. Antibacterial properties of silver-doped titania. *Small*, 3(5):799–803, 2007.

[357] Lydie Ploux, Mihaela Mateescu, Karine Anselme, and Krasimir Vasilev. Antibacterial properties of silver-loaded plasma polymer coatings. *Journal of Nanomaterials*, 2012:6, 2012.

[358] Edward Luce. Koneman's color atlas and textbook of diagnostic microbiology. *Plastic and Reconstructive Surgery*, 125(1):414–415, 2010.

[359] He-Ping Li, Wen-Ting Sun, Hua-Bo Wang, Guo Li, and Cheng-Yu Bao. Electrical features of radio-frequency, atmospheric-pressure, bare-metallic-electrode glow discharges. *Plasma Chemistry and Plasma Processing*, 27(5):529–545, 2007.

[360] JJ Shi and Michael G Kong. Radio-frequency dielectric-barrier glow discharges in atmospheric argon. *Applied physics letters*, 90(11):111502, 2007.

[361] E Iordanova, N De Vries, M Guillemier, and JJAM van der Mullen. Absolute measurements of the continuum radiation to determine the electron density in a microwave-induced argon plasma. *Journal of Physics D: Applied Physics*, 41(1):015208, 2008.

[362] Elisabeth Restrepo and A Devia. Optical emission diagnostic of a pulsed arc discharge. *Journal of Vacuum Science & Technology A*, 22(2):377–382, 2004.

[363] Dmitriy A Shutov, Sergeiy A Smirnov, Elena Bobkova, and Vladimir V Rybkin. Ionization mechanism and chemical composition of an argon dc discharge with water cathode. *Plasma Chemistry and Plasma Processing*, 35(1):107–132, 2015.

[364] M Moravej, X Yang, RF Hicks, J Penelon, and SE Babayan. A radio-frequency nonequilibrium atmospheric pressure plasma operating with argon and oxygen. *Journal of applied physics*, 99(9):093305–093305, 2006.

[365] JT Gudmundsson and EG Thorsteinsson. Oxygen discharges diluted with argon: dissociation processes. *Plasma Sources Science and Technology*, 16(2):399, 2007.

[366] Mark J Kushner. Modelling of microdischarge devices: plasma and gas dynamics. *Journal of Physics D: Applied Physics*, 38(11):1633, 2005.

[367] Arati Dasgupta, M Blaha, and JL Giuliani. Electron-impact excitation from the ground and the metastable levels of ar i. *Physical review A*, 61(1):012703, 1999.

[368] Lawrence G Piper. State-to-state $N_2(A^3 \Sigma_u^+)$ energy-pooling reactions. i. the formation of $N_2(C^3\Pi_u)$ and the herman infrared system. *The Journal of chemical physics*, 88(1):231–239, 1988.

[369] A Bogaerts and R Gijbels. Modeling of metastable argon atoms in a direct-current glow discharge. *Physical Review A*, 52(5):3743, 1995.

[370] JE Velazco, JH Kolts, and DW Setser. Rate constants and quenching mechanisms for the metastable states of argon, krypton, and xenon. *The Journal of Chemical Physics*, 69(10):4357–4373, 1978.

[371] Qing Li, Hidemasa Takana, Yi-Kang Pu, and Hideya Nishiyama. An atmospheric pressure quasiuniform planar plasma jet generated by using a dielectric barrier configuration. *Applied Physics Letters*, 98(24):241501, 2011.

[372] BHP Broks, JG Keizer, RAB Zijlmans, and JJAM van der Mullen. Modelling of a pinched cascaded arc light source using argon. *Plasma Sources Science and Technology*, 15(4):865, 2006.

[373] Bram van Gessel, Ronny Brandenburg, and Peter Bruggeman. Electron properties and air mixing in radio frequency driven argon plasma jets at atmospheric pressure. *Applied Physics Letters*, 103(6):064103, 2013.

[374] Giichiro Uchida, Kosuke Takenaka, Kazufumi Kawabata, Atsushi Miyazaki, and Yuichi Setsuhara. Effects of driving voltage frequency on the discharge characteristics of atmospheric dielectric-barrier-discharge plasma jet. *Japanese Journal of Applied Physics*, 53(11S):11RA08, 2014.

[375] Dan Bee Kim, H Jung, B Gweon, SY Moon, JK Rhee, and W Choe. The driving frequency effects on the atmospheric pressure corona jet plasmas

from low frequency to radio frequency. *Physics of Plasmas*, 18(4):043503, 2011.

[376] M Moravej, X Yang, M Barankin, J Penelon, SE Babayan, and RF Hicks. Properties of an atmospheric pressure radio-frequency argon and nitrogen plasma. *Plasma Sources Science and Technology*, 15(2):204, 2006.

[377] Andrew J Wagner, Davide Mariotti, Konstantin J Yurchenko, and Tuhin K Das. Experimental study of a planar atmospheric-pressure plasma operating in the microplasma regime. *Physical Review E*, 80(6):065401, 2009.

[378] Johann Laimer, Alexander Puchhammer, and Herbert Störi. Plasma sheath dynamics in dielectric barrier-free atmospheric pressure radio-frequency glow discharges. *Plasma Processes and Polymers*, 6(S1):S253–S257, 2009.